Preprint accepted at Nature Geoscience on 15th May 2020 and made available under the CC-BY-NC-ND 4.0 license. © 2020

Global distribution of sediment-hosted metals controlled by craton edge stability

Mark J. Hoggard,[*,a,b] Karol Czarnota,[*,c,d] Fred D. Richards,[a,e] David L. Huston,[c] A. Lynton Jaques,[d] & Sia Ghelichkhan[d]

[a]Department of Earth and Planetary Sciences, Harvard University, USA.
[b]Lamont-Doherty Earth Observatory, Columbia University, USA.
[c]Geoscience Australia, Canberra, Australia.
[d]Research School of Earth Sciences, Australian National University, Canberra, Australia.
[e]Department of Earth Science and Engineering, Imperial College London, UK.

[*]www.mjhoggard.com; mark_hoggard@fas.harvard.edu; karol.czarnota@ga.gov.au

Cite as: Hoggard, M.J., K. Czarnota, F.D. Richards, D.L. Huston, A.L. Jaques, & S. Ghelichkhan (2020). Global distribution of sediment-hosted metals controlled by craton edge stability, *Nature Geoscience*, **13**(7), 504–510. https://doi.org/10.1038/s41561-020-0593-2

Sustainable development and the transition to a clean-energy economy drives ever-increasing demand for base metals, substantially outstripping the discovery rate of new deposits and necessitating dramatic improvements in exploration success. Rifting of the continents has formed widespread sedimentary basins, some of which contain large quantities of copper, lead and zinc. Despite over a century of research, the geological structure responsible for the spatial distribution of such fertile regions remains enigmatic. Here, we use statistical tests to compare deposit locations with new maps of lithospheric thickness, which outline the base of tectonic plates. We find that 85% of sediment-hosted base metals, including all giant deposits (>10 megatonnes of metal), occur within 200 km of the transition between thick and thin lithosphere. Rifting in this setting produces greater subsidence and lower basal heat flow, enlarging the depth extent of hydrothermal circulation available for forming giant deposits. Given that mineralisation ages span the last 2 billion years, this observation implies long-term lithospheric edge stability and a genetic link between deep Earth processes and near-surface hydrothermal mineral systems. This discovery provides an unprecedented global framework for identifying fertile regions for targeted mineral exploration, reducing the search-space for new deposits by two-thirds on this lithospheric thickness criterion alone.

Consumption of base metals (copper, lead, zinc and nickel) over the next ∼25 years is set to exceed the total produced in human history to date (Ali *et al.*, 2017; Schodde, 2017). Moreover, critical minerals (e.g. cobalt, indium and germanium) are often produced as by-products of base metal mining and are essential in many high-tech applications (Nassar *et al.*, 2015; Mudd *et al.*, 2018; IRENA, 2019; Dominish *et al.*, 2019; Sovacool *et al.*, 2020). A growing concern is that the rate of exploitation of existing reserves is outstripping discovery of new deposits, despite exploration expenditure tripling during the 2005–2012 minerals boom (Ali *et al.*, 2017; Schodde, 2017). To reverse this trend and supply the resources necessary to comply with policies such as the Paris Climate Agreement and United Nations' Sustainable Development Goals, improved techniques for locating new deposits are required, particularly those buried under shallow sedimentary cover or ice (The Uncover Group, 2012).

Narrowing the search-space for new deposits

In mineral exploration, initial area selection at continental scales is arguably the most important step, as successful identification of fertile regions can compensate for many subsequent errors (McCuaig *et al.*, 2010). Over the last two decades, the search for analogues of known deposits has progressed towards a more holistic determination of factors controlling deposit generation and preservation (Wyborn *et al.*, 1994; Bierlein *et al.*, 2006; McCuaig & Hronsky, 2014; Dentith *et al.*, 2018; Skirrow *et al.*, 2019). Mineral systems analysis has resulted in a growing acceptance that the spatial distribution of deposits associated with magmatic processes is controlled by lithospheric-scale structure (McCuaig *et al.*, 2010; Begg *et al.*, 2010; Griffin *et al.*, 2013). For example, porphyry copper deposits are generated by wet melting in the mantle wedge above a subducting slab, followed by emplacement of these melts into the shallow overlying crust and subsequent concentration by high-temperature hydrothermal circulation (Griffin *et al.*, 2013). Thus, by combining the plate tectonic setting with geological constraints on the location of key mineral system ingredients, the search-space for new magmatic deposits can be substantially reduced (Rosenbaum *et al.*, 2005; Butterworth *et al.*, 2016; O'Reilly *et al.*, 2017).

In the case of sediment-hosted deposits, most assessments to date have focused on their genesis within the context of Earth's secular evolution, as well as past tectonic and geographic settings (McCuaig *et al.*, 2018). The majority are found in failed rift and passive margin settings, and it is generally agreed that basin-scale hydrothermal circulation is required to scavenge sufficient metals to form giant deposits (Figure 1a; Leach *et al.*, 2010; Hitzman *et al.*, 2010; Manning & Emsbo, 2018). Metals are mobilised and transported by oxidised brines with moderate temperatures (80–250°C) and moderate-to-high salinity (10–30 wt.% NaCl), limiting their maximum age to the Great Oxidation Event at 2.4 Ga (Leach *et al.*, 2010; Hitzman *et al.*, 2010). These fluids are sourced from evaporites at low latitudes and remain buffered as they pass through voluminous oxidised terrestrial sediments, allowing them to scavenge lead from arkosic sandstones and felsic volcanics, as well as copper and zinc from mafic rocks (Leach *et al.*, 2010; Hitzman *et al.*, 2010). Transport along faults, either during rifting or basin inversion, focuses these fluids into oxidation-reduction interfaces, such as distal-facies black shales, where metals precipitate (Figures 1b and 1c; Huston *et al.*, 2016).

Preprint accepted at Nature Geoscience on 15th May 2020 and made available under the CC-BY-NC-ND 4.0 license. © 2020

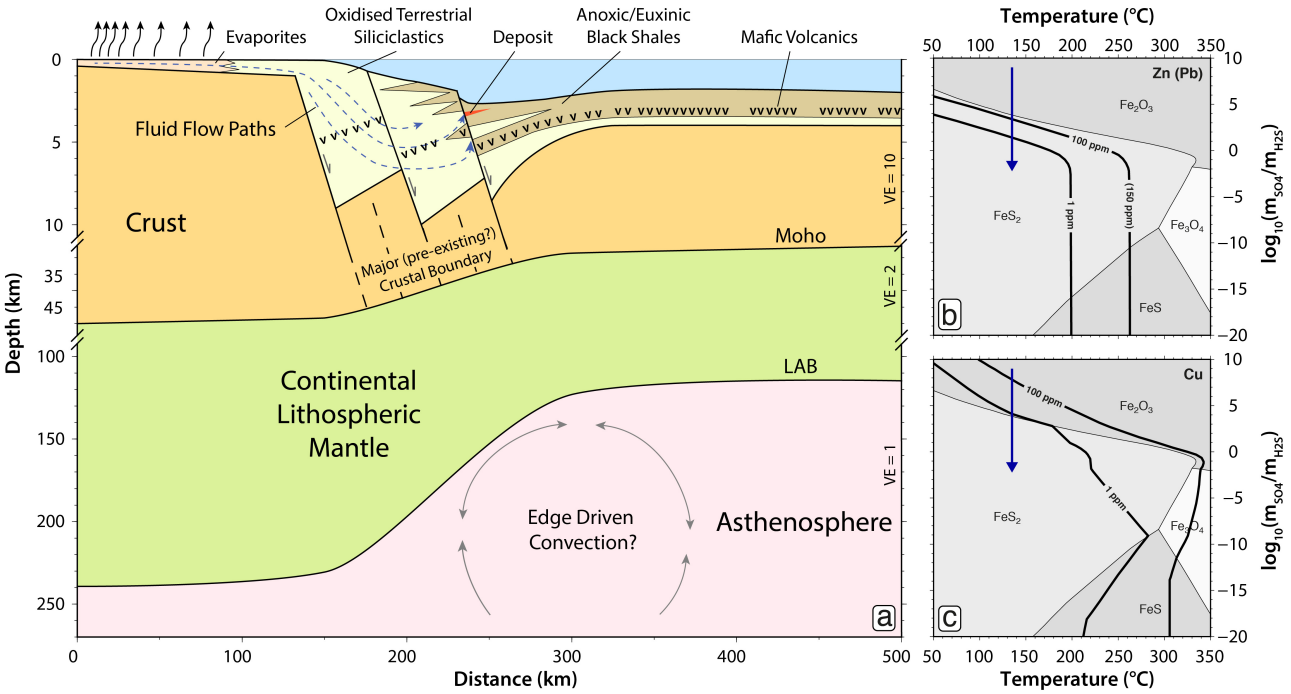

Figure 1: **Mineralisation system for genesis of sediment-hosted base metal deposits.** (**a**) Schematic illustration of deposit location in extensional rift settings. Basinal brines sourced from evaporites scavenge metals from oxidised terrestrial sediments and volcanics (v) on route to metal deposition sites in black shales (Manning & Emsbo, 2018). Notice variable vertical exaggeration (VE) and prominence of the lithosphere-asthenosphere boundary (LAB) edge illustrated at 1:1 scale. Schematic based on architectural constraints from the Australian Carpenteria Zinc Belt and Polish Fore-Sudetic Block. (**b**) Stability field of Fe–S–O minerals as a function of temperature and redox conditions; m_{SO_4} = molarity of sulphate; m_{H_2S} = molarity of sulphide; thick black lines = solubility of zinc (and lead) in brine, calculated for fluid salinity = 10 wt.% NaCl, total concentration of sulphur species = $10^{-2.5}$ M, and pH = 4.5 (Huston *et al.*, 2016); blue arrow = fluid path for metal precipitation by oxidation-reduction deposition mechanism. (**c**) Same for copper solubility.

Sediment-hosted base metal deposits are desirable due to their greater quantity of contained metal (in contrast to volcanogenic massive sulfides) and higher grades of ore (in comparison to porphyry copper), resulting in lower environmental degradation during extraction (Dominish *et al.*, 2019; Azadi *et al.*, 2020). However, narrowing the search-space for new sediment-hosted deposits has been less successful than for magmatic mineral systems. Sedimentary basins cover ∼75% of the continental surface, and the key ingredients of evaporites associated with brine formation, felsic and mafic volcanic rocks for sourcing metals, and organic rich shale precipitation sites, are widespread and do not substantially reduce this search-space. The first-order geological control that localises their spatial distribution throughout the continents remains unknown, severely limiting predictive power for identifying new targets. A classic example comes from the Carpentaria Zinc Belt in northern Australia, which contains several world class clastic-dominated lead-zinc deposits formed between 1.8–1.4 Ga (Figure 2a). These deposits lie along an arcuate trend that runs oblique to mapped geology and crustal geological boundaries, as demonstrated by gravity and magnetic datasets (Geoscience Australia, 2018).

Crucially, despite the absence of a clear crustal relationship, the linear distribution of sediment-hosted deposits in the Carpentaria Zinc Belt hints at an underlying regional-scale control. An important advance in understanding the genesis of magmatic mineral systems has come from probing their relationship with major crustal and lithospheric structures (Griffin *et al.*, 2013). Given that sedimentary basins are themselves the result of lithospheric scale processes, we therefore investigate both regional and global-scale links between sediment-hosted base-metal deposits and the most fundamental shallow mantle structure – the lithosphere-asthenosphere boundary (LAB).

Relationship with lithospheric structure

We begin by collating global inventories of six major base-metal mineral systems from published sources (Methods). Three are magmatic and three are sediment-hosted, which include sedimentary copper (Cu-sed), clastic-dominated lead-zinc (PbZn-CD, commonly also referred to as sedimentary exhalative), and Mississippi Valley-type lead-zinc (Pb-Zn-MVT). We next refine a method developed by Priestley & McKenzie (2013) for mapping the thermal LAB from seismic tomography, taking into consideration recent laboratory experiments concerning the effect of anelasticity on shear-wave velocities (Yamauchi & Takei, 2016; Methods). This benchmarking procedure is necessary in order to increase consistency between LAB maps obtained for different tomography models, which can image surprisingly variable seismic velocities. A high resolution regional LAB map over Australia is obtained from the FR12 model (Fishwick & Rawlinson, 2012) and is calibrated using nine local paleogeotherms derived from thermobarometry of mantle peridotite xenoliths and xenocrysts. To expand our analysis to other continents, a global LAB is also produced using the SL2013sv model (Schaeffer & Lebedev, 2013) and calibrated using multiple constraints, including the latest thermal structure of cooling oceanic lithosphere (Richards *et al.*, 2018). This global LAB exhibits a bi-modal thickness distribution, with peaks at 90 km and 190 km, separated by a minimum at 150 km (Supplementary Information).

Inspection of the Australian model reveals a striking correlation between major sediment-hosted mineral deposits and the edge of thick lithosphere, defined here by the 170 km thickness contour (Figure 2b). Major PbZn-CD and sedimentary copper deposits in the Carpentaria Zinc Belt overlie this contour, which runs obliquely to geological boundaries, such that intersections between these two features con-

Preprint accepted at Nature Geoscience on 15th May 2020 and made available under the CC-BY-NC-ND 4.0 license. © 2020

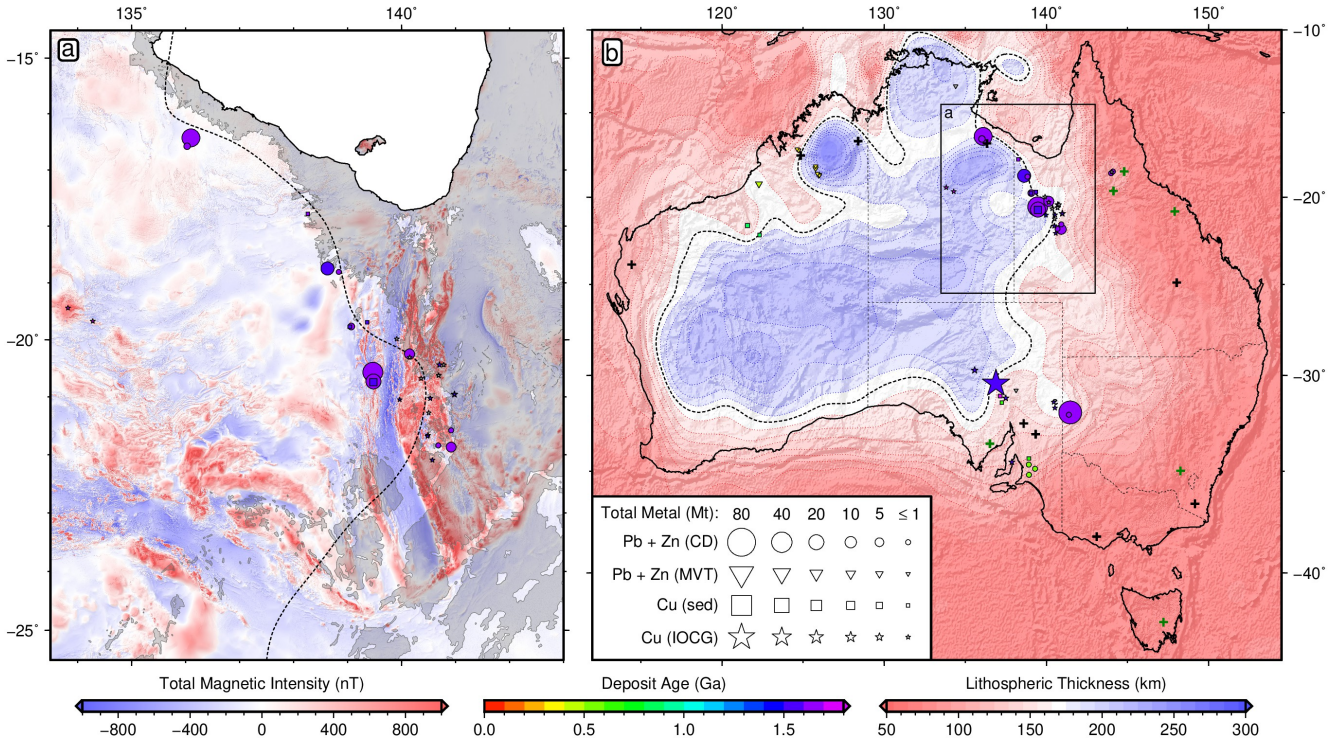

Figure 2: **Distribution of sediment-hosted and iron-oxide-copper-gold base metal deposits as a function of Australian lithospheric thickness.** (**a**) Carpentaria Zinc Belt; red/blue = variably reduced to pole aeromagnetic intensity data (Geoscience Australia, 2018); grey polygons = generalised outcrop of Cretaceous marine sediments in Eromanga and Carpentaria Basins (Raymond, 2018); black dashed contour = 170 km LAB thickness; symbols = deposit locations; symbol area proportional to estimate of total contained mass of metal (either lead plus zinc, or copper) in mega-tonnes (Mt); unknown deposit size given 1 Mt symbol; colour = ore body formation age (billion years); unknown age plotted in grey; circles = clastic-dominated lead-zinc (PbZn-CD); triangles = Mississippi Valley-type lead-zinc (PbZn-MVT); squares = sedimentary copper (Cu-sed); stars = iron-oxide-copper-gold (IOCG). (**b**) Australian LAB mapped by converting FR12 tomography (Fishwick & Rawlinson, 2012) to temperature using an anelasticity parameterisation (Yamauchi & Takei, 2016) calibrated on local paleogeotherms (Methods) and illuminated by free-air gravity anomalies (Geoscience Australia, 2018); black/green crosses = geotherms used as constraints/tests in anelasticity calibration (Supplementary Information); box = location of panel (a); large star in South Australia shows location of the Olympic Dam IOCG deposit.

sistently coincide with deposit locations. This behaviour is particularly useful for highlighting new prospective regions for exploration. Other observables that correlate with this lithospheric thickness change include variations in lead isotopes from Proterozoic galena and pyrite minerals (Huston *et al.*, 2019), long-wavelength gravity anomaly gradients (Hobbs *et al.*, 2000), changes in crustal character in deep reflection seismic profiles (Kennett *et al.*, 2016), a topographic ridge, and the western extent of Cretaceous marine sediments (Figure 2a). These latter two associations demonstrate the post-Proterozoic stability of this edge and its influence on local geology and topography. There is also a strong relationship with iron-oxide-copper-gold deposits, including the Olympic Dam mine in South Australia (84 Mt of copper, world's largest known uranium resource; Heinson *et al.*, 2018; Skirrow *et al.*, 2018; Curtis & Thiel, 2019). However, a lack of consensus on global classification schemes means that we have limited analysis of this deposit type to only Australia.

Extending our analysis globally further confirms the strength of this relationship (Figure 3). The link between the 170 km lithospheric thickness contour and location of all large sediment-hosted deposits holds regardless of deposit age, which spans the last 2 billion years. Given the 180–220 km cluster of LAB thicknesses is likely to represent standard cratonic lithosphere, the 170 km contour therefore demarcates the outer boundary of cratons. Within the PbZn-CD deposit class, those more strongly associated with abundant mafic rocks systematically occur on the thinner lithosphere side of the contour compared to their carbonate-rich counterparts (e.g. Carpenteria Zinc Belt and northwest North America). These observations are consistent with an extensional origin of the host basins.

To quantify these visual relationships, the shortest distance is calculated between each deposit and the 170 km LAB thickness contour and results are plotted in a cumulative distribution function (CDF). Weighting deposits by the mass of contained metal and substituting the Australian LAB from the global model with our high-resolution regional version substantially improves the correlation for PbZn-CD (Figure 4a). Globally, we observe that ∼95% of sedimentary copper, ∼90% of clastic-dominated lead-zinc and ∼70% of Mississippi Valley-type lead-zinc resources are located within a 200 km-wide corridor either side of the 170 km LAB thickness contour (Figure 4b). This region corresponds to only ∼35% of continental surface area. Given that this swath width is similar to the ∼280 km node spacing in SL2013sv, tighter constraints are only possible with higher resolution tomography models. For example, all giant deposits in Australia lie within 100 km of the 170 km contour for the higher resolution FR12 model. The significance of the relationship is globally examined using the *two-sample Kolmogorov-Smirnov test*, which estimates that the probability of these sediment-hosted deposits representing random continental locations is less than 1 in 10^{12} (Kolmogorov, 1933; Methods). This relationship holds true for three other global surface wave tomography models (Extended Data Figure 1).

All >10 mega-tonne sediment-hosted deposits are located along the boundary of thick lithosphere, but amongst the smaller deposits, there are some notable exceptions. Minor PbZn-CD outliers occur in Europe, the Caribbean, Indonesia and east China. Anomalous PbZn-MVT deposits are found in Ireland, east China and along the Tethys sub-

Preprint accepted at Nature Geoscience on 15th May 2020 and made available under the CC-BY-NC-ND 4.0 license. © 2020

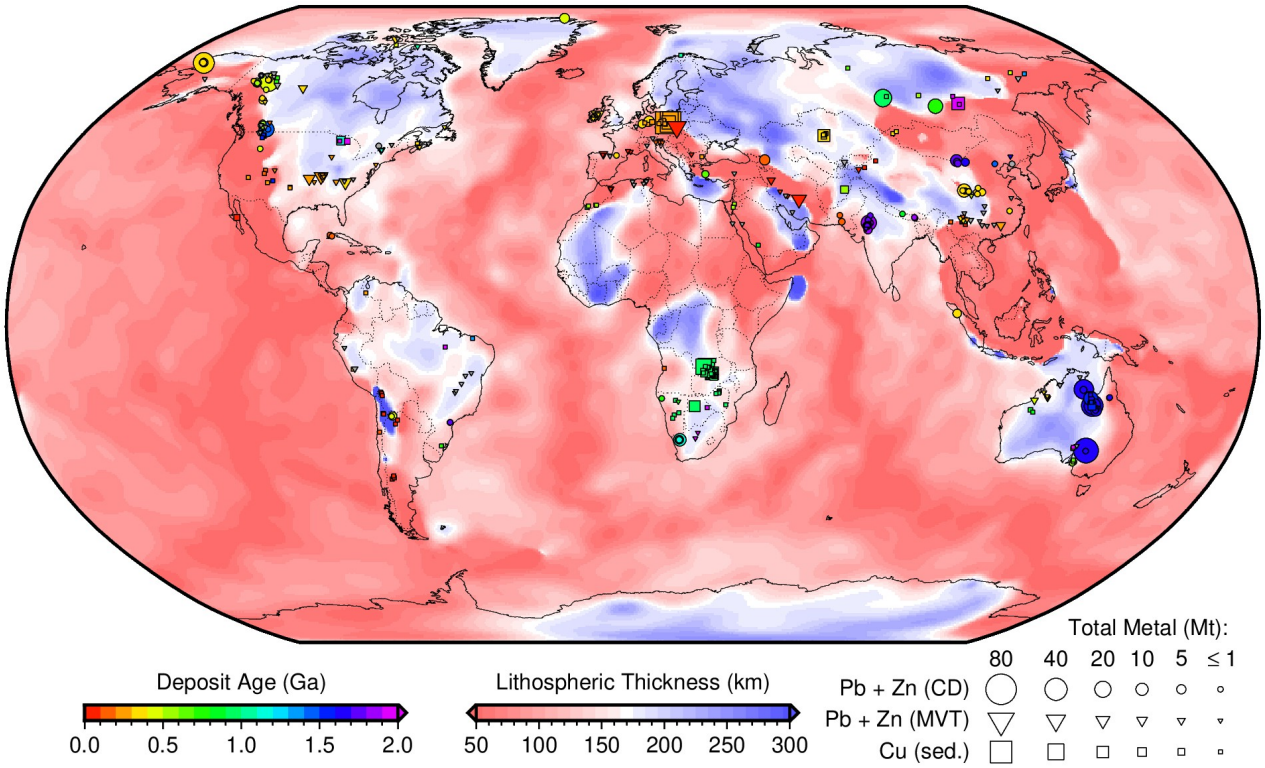

Figure 3: **Global distribution of sediment-hosted base metal deposits as a function of lithospheric thickness.** LAB derived from SL2013sv tomography model (Schaeffer & Lebedev, 2013) using a calibrated anelasticity parameterisation (Yamauchi & Takei, 2016; Methods). Symbols = deposit locations; symbol area proportional to estimate of total contained mass of metal (either lead plus zinc, or copper) in mega-tonnes (Mt); unknown deposit size given 1 Mt symbol; colour = ore body formation age (billion years); unknown age plotted in grey; circles = clastic-dominated lead-zinc (PbZn-CD); triangles = Mississippi Valley type lead-zinc (PbZn-MVT); squares = sedimentary copper (Cu-sed).

duction zone across Europe, whilst small sedimentary copper deposits occur in southwestern North America and southern South America. This observation indicates that minor sediment-hosted mineral systems can develop in a variety of basins, whilst giant deposits form only at the edges of cratonic lithosphere. PbZn-MVT deposits are generally more widely distributed, which likely reflects that a subset of these deposits are linked with orogenic processes along basin margins (Leach *et al.*, 2010), resulting in longer hydrothermal fluid flow paths. Nevertheless, not all sediment-hosted outliers were necessarily anomalies at the time of ore formation. The majority now occur in accretionary terranes, whereby plate tectonic processes may have rifted segments off thick lithosphere and transported them into subduction zone settings. Other areas, such as east China, are known to have undergone lithospheric thinning some time after deposit formation, based on thermobarometric constraints (Menzies *et al.*, 2007).

Regardless of age, sediment-hosted base-metal deposits predominantly cluster on the edges of present-day thick lithosphere. Therefore, many of these lithospheric steps appear to be remarkably robust on billion-year timescales, despite the assembly and disaggregation of several supercontinents, the impacts of large igneous provinces and the possible erosional effect of edge-driven convection (Currie & van Wijk, 2016). Deposit ages in northwestern North America span ~1.5–0.5 Ga, pointing to the stability and importance of this boundary in localising multiple deformational and ore-forming processes.

Mineral system implications

Our results indicate that the edges of thick lithosphere place first-order controls on the genesis of extensional basins and their associated mineral systems (Figure 1). Rifting causes localised thinning and produces a lateral transition from oxidising terrestrial environments into marine settings. This transition provides the optimal juxtaposition of the ingredients necessary for deposit formation. The adjacent unstretched cratons provide a bountiful source of oxidised sediments and extensive low-elevation platforms, which enhance evaporite formation. Proximal land masses also aid the development of restricted marine settings that are ideal for accumulating thick evaporite sequences (through periodic cycles of evaporation and flooding), and promote euxinic water conditions that are favourable for deposition of reducing shales that have high organic carbon content. Thinning of the lithosphere in the centre of the basin causes decompression melting, providing mafic and felsic volcanic rocks from which metals are scavenged. Intercalation of proximal and distal facies components is further modulated by transient vertical motions, generally thought to be associated with edge driven convection across lithospheric steps (Davies & Rawlinson, 2014). Nevertheless, these mineral system components are common to both rifts in thick lithosphere and regular passive margins, and the question remains — what is favourable about rifting cratonic lithosphere for formation of the shallow hydrothermal systems necessary to produce giant deposits?

From a geodynamic perspective, these lithospheric edges represent rheological contrasts that focus strain and localise repeated cycles of extensional deformation and basin contraction, thereby controlling both the spatial distribution of required lithologies and the focusing of mineralising fluids (Sloan *et al.*, 2011; Gibson *et al.*, 2016; O'Reilly *et al.*, 2017). Thick cratonic lithosphere is colder than standard continental lithosphere and has a larger seismogenic thickness, resulting in the development of deeper, longer, and more widely spaced normal faults during rifting (Biggs *et al.*, 2010). This architecture increases the horizontal aspect ratio of hydrothermal cells, providing greater sediment volumes for fluid–rock

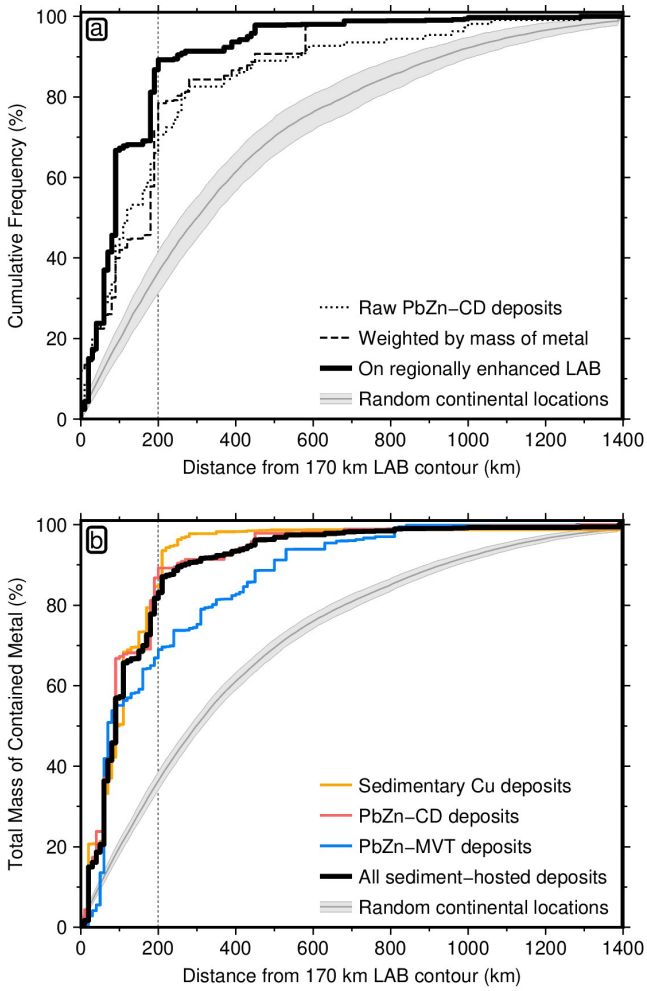

Figure 4: **Cumulative distribution functions for global sediment-hosted base metals.** (**a**) Different approaches for counting 109 clastic-dominated lead-zinc deposits (PbZn-CD). Dotted line = simple count of number of deposits with increasing distance from the 170 km contour in global LAB map (Figure 3); dashed line = weighting by contained mass of lead and zinc; solid black line = mass-weighted deposits where the Australian LAB from the global model has been replaced with the regionally enhanced map (Figure 2b); grey line/bounds = mean and standard deviation of 100 sets of equivalent number (109) of randomly drawn continental locations, with respect to regionally enhanced LAB. (**b**) Mass-weighted, regionally enhanced CDFs for 139 sedimentary copper deposits (Cu-sed), 109 PbZn-CD, 147 Mississippi Valley-type (PbZn-MVT), and combination of all three. Grey band as before for combined number of deposits (395).

interaction. These faults are active for longer periods of time, and the entire syn-rift phase of basin formation can last 50–100 Myr, in contrast to standard continental rifts that typically last ∼25 Myr, yielding a more extensive time window for mineralisation (Allen & Armitage, 2012). Furthermore, basins forming in continental interiors are more likely to be restricted, which is not only favourable for high siliciclastic supply and the formation of evaporites and reductants, but also results in laterally continuous sediment packages that trap hydrothermal fluid systems and potentially promote recirculation of brines (Hitzman *et al.*, 2010).

A key observation is that metal precipitation in sediment-hosted base metal deposits is generally driven by oxidation-reduction reactions, which become ineffective when brine temperatures exceed ∼ 250°C (Figures 1b and 1c; Huston *et al.*, 2016). As hydrothermal fluid temperatures are buffered by conditions towards the base of the sediment pile (often where the mafic metal source rocks are located), the basal temperature of the sedimentary pile must not substantially exceed this threshold value. Total extension in a basin can be estimated using a stretching factor, β, which is the ratio of original to final crustal thickness. Failed rifts on standard continental lithosphere such as the North Sea typically have $\beta \approx 2$, and simple thermal modelling assuming pure-shear rifting indicates that this produces ∼ 4 km of syn-rift sediment with basal temperatures cooler than ∼ 250°C (Figure 5a; Methods). Given that all the necessary ingredients occur within basins, the likelihood of developing a successful mineral system is higher for a larger sediment pile, which can be achieved by increasing the stretching factor. However, more extreme rifting causes the asthenosphere to upwell to substantially shallower depths, producing elevated basal heat flow that heats the sediment pile above this threshold and so inhibits metal precipitation (Figure 5b).

Two important differences occur during rifting of cratonic lithosphere. First, the greater initial thickness of the lithosphere results in a lower geothermal gradient, such that the basal heat flow spike during rifting is substantially lower than for standard continental rifts (Supplementary Information). Secondly, the density of cratonic lithosphere is reduced by up to ∼50 kg m^{-3} by chemical depletion compared to standard lithosphere (Jordan, 1978). This increased buoyancy reduces the dampening effect during syn-rift subsidence that is associated with replacing cold continental lithosphere with lower density asthenosphere, resulting in substantially larger thicknesses of syn-rift sediments for any given stretching factor. Assuming unlimited sediment supply, $\beta \approx 2$ yields a 8–9 km syn-rift sediment pile, the base of which stays cooler than the threshold ∼250°C (Figure 5c). Thus, rifting cratonic lithosphere produces more than twice the volume of mineral system ingredients without exceeding the thermal conditions necessary for successful precipitation, over a duration of time that can be up to a factor of four more extensive (Figure 5d and 5e). This mechanism explains why smaller deposits can occur in any extensional setting (e.g. Irish PbZn-MVT deposits), but giant deposits requiring the largest volumes of fluid-rock interaction are restricted to rift basins at the edges of the thickest lithosphere.

A final consideration is that a setting on the edge of thick lithosphere enhances the preservation potential of deposits through subsequent orogenic events and supercontinent cycles. For example, the Boleo Copper District in Baja California formed only three-million years ago and sits in shallow crust on thin lithosphere, resulting in poor long-term preservation potential. In contrast, the 1.7 Ga Broken Hill deposit in Australia (world's largest known lead deposit) has been metamorphosed to amphibolite–granulite facies, yet survives on the edge of the Curnamona part of the South Australian Craton.

Surprisingly, given the results of previous studies (e.g. Griffin *et al.*, 2013), deposits associated with magmatic systems generally exhibit a weaker association with the edge of cratonic lithosphere than sediment-hosted systems (Supplementary Information). Porphyry copper deposits are predominantly Cenozoic in age and are generally positioned on thin lithosphere (≤100 km). Their formation in subduction zone settings at shallow crustal depths leads to poor preservation potential within the geological record, making this association unsurprising. Volcanogenic massive sulphides have an episodic age distribution from 3.5 Ga to present. Their generation is thought to require moderate-degree partial melting of hydrated mantle in back-arc settings (Huston *et al.*, 2010). We observe that they spatially occur randomly on thick and thin lithosphere, but exhibit systematic temporal ordering, with the oldest positioned over thick lithosphere

Preprint accepted at Nature Geoscience on 15th May 2020 and made available under the CC-BY-NC-ND 4.0 license. © 2020

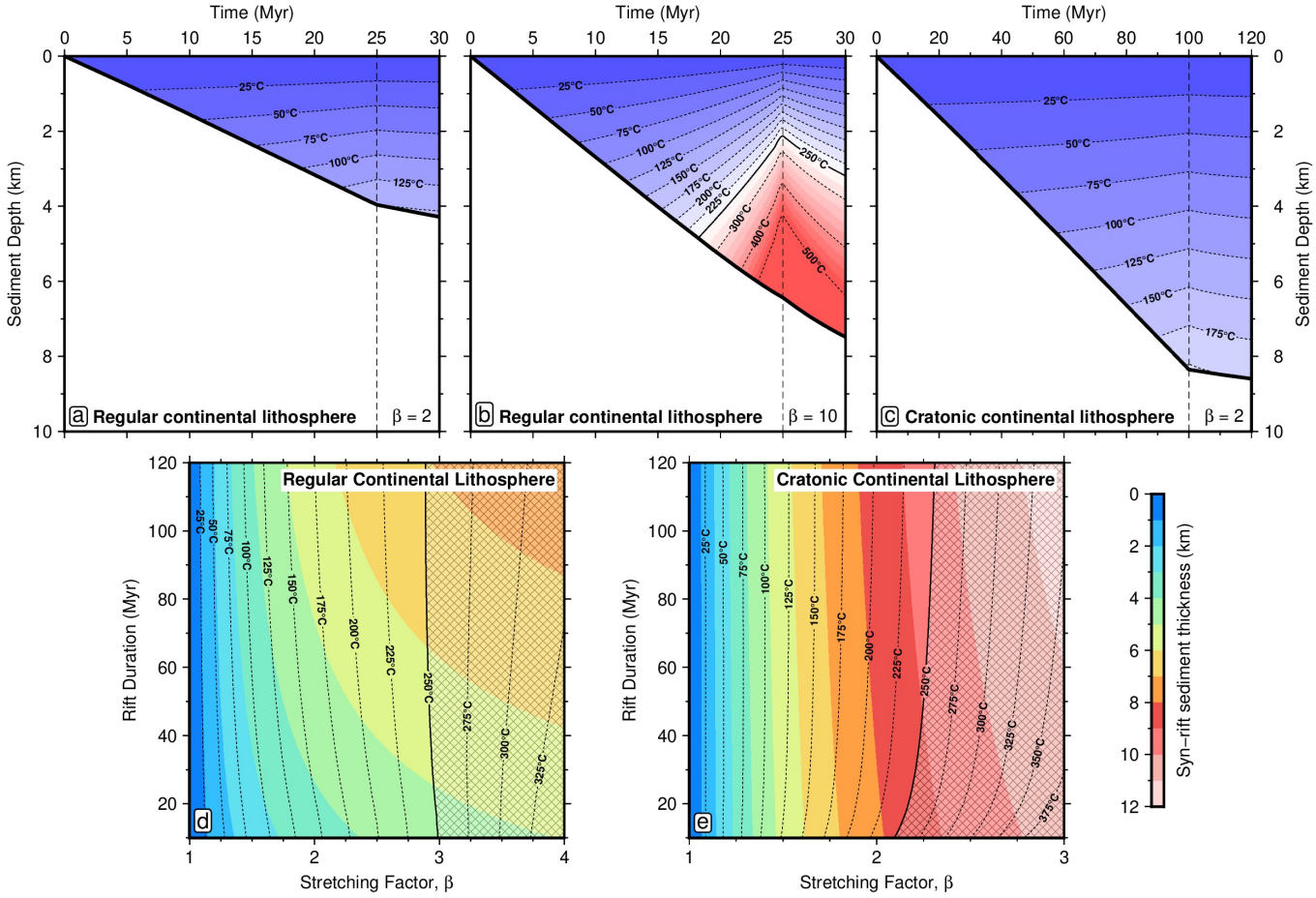

Figure 5: **Thermal modelling of basin subsidence histories.** (**a**) Syn-rift sedimentation for $\beta = 2$ rift of regular continental lithosphere; dashed line = rift duration; colours = temperature structure of the sediment pile. (**b**) Same for $\beta = 10$ rift of regular continental lithosphere. (**c**) Same for $\beta = 2$ rift of cratonic continental lithosphere. (**d**) Minerals system operating window for rifting of regular continental lithosphere; colours = syn-rift sediment thickness; contours = basal temperature of the sediment pile; hatched region = location where hydrothermal fluids typically become too hot for metal precipitation by oxidation-reduction mechanisms ($> 250°C$). (**e**) Same for cratonic continental lithosphere.

that are rimmed by progressively younger deposits, consistent with growth of cratons by accretion. Finally, magmatic nickel deposits are mostly Archean and Proterozoic in age and commonly occur on thick lithosphere ($\geq$150 km). Unlike other base metal deposits, their distribution is associated with edges of even thicker lithosphere ($\sim$200 km), broadly consistent with previous studies showing major lithospheric structural controls on these deposit locations (Begg *et al.*, 2010; Regis *et al.*, 2017; Alghamdi *et al.*, 2018). Their generation requires large fraction partial melting of peridotite, indicative of high mantle temperatures (more prevalent in a early, hotter Earth) and decompression melting at shallow depths (Arndt *et al.*, 2005). Therefore, their present distribution suggests lithospheric thickness must have locally increased since formation, simultaneously enhancing preservation potential.

In summary, this work illustrates a new and robust link between giant sediment-hosted base metal mineral systems and the edges of thick lithosphere. Approximately 55% of the world's lead, 45% of its zinc and 20% of known copper is found within $\sim$ 200 km of this boundary. We have demonstrated the value of regional seismic arrays to better resolve this edge and enhance the mineral exploration efforts required to sustain ongoing global development. Importantly, deposit ages indicate that, following rifting, the edges of thick-lithosphere are generally stable over billion-year timescales. The far-reaching geodynamic and societal implications of these observations highlight the need for extensive further research. To improve resolution of mapped lithospheric structure, higher fidelity seismic imaging needs to be coupled with enhanced mantle xenolith coverage and tighter constraints on seismic anelasticity from mineral physics experiments. More generally, these maps should be integrated with models of basin dynamics, surface processes and reactive transport modelling, and benchmarked against additional geological information, such as sedimentary facies variations, tectonic structures and alteration zones. These multiple research strands will yield fundamental new insights into sediment-hosted mineral systems and lead to substantial improvements in exploration success.

Methods

Deposit compilation. Our global inventory of 2166 major base metal deposits are categorised into six main classes. Three are sediment hosted: sedimentary copper (Cu-sed; contains ∼20% of all known copper); clastic-dominated lead-zinc (PbZn-CD; ∼43% of all lead and ∼33% of zinc); and Mississippi Valley-type lead-zinc (PbZn-MVT; ∼25% lead, ∼22% zinc). The other three are associated with magmatic systems: copper porphyry (Cu-por; contains ∼65% of all known copper); magmatic nickel-copper-platinum group elements (Ni-Cu-PGE; ∼45% nickel, ∼3% copper); and volcanogenic massive sulfides (VMS; ∼6% copper, ∼23% lead, ∼39% zinc).

For each deposit, we include the type (based on established classification schemes), location, age (direct measurement or inferred based on geological relationships) and total resource size by combining historical production with estimated resources. Our Cu-sed deposit dataset follows the classification scheme and compilation of Hitzman *et al.* (2005), cross-checked against Cox *et al.* (2007). Where these two compilations disagree on deposit size, the larger value has been used. Our PbZn-CD and PbZn-MVT deposit compilations extensively revise and build on the work of Taylor *et al.* (2009). References for each deposit type were manually checked and additional references have been included. We exploit the compilation of Sillitoe (2010) for Cu-por deposits. Our magmatic Ni-Cu-PGE compilation follows Hoatson *et al.* (2006), with deposit location populated from disparate sources. Our catalogue of VMS deposits is an extensive revision of the compilation by Franklin *et al.* (2005). Australian information for all the above deposit types, with the addition of 25 iron-oxide-copper-gold deposits, was updated using the authors' own knowledge building from the Geoscience Australia OZMin database (Sexton, 2011).

We have endeavoured to assemble the most complete deposit dataset possible by revising and extending pre-existing compilations. Our database can be found in the online Supplementary Datasets. Importantly, patchy or absent reporting of mineral deposit information from some countries inevitably means our global database is incomplete, but we do not believe that this will impact the veracity of our main conclusions.

Metal scavenging window. Following Cooke *et al.* (2000), we have selected a precipitation gradient from ∼100 ppm to 1 ppm for the metal scavenging window in Figure 1. Estimates of the metal concentration of mineralising brines are obtained from fluid inclusion studies contained within ore and other gangue minerals. Care must be taken that host minerals formed during the period of ore deposition and that analyses are not contaminated by metals contained within the mineral lattice itself, which is a particular problem in the early stages of LA-ICP-MS analysis when the laser initially vaporises a mixture of mineral and fluid inclusion to produce a mixed signal. Generally, inclusions from European sediment-hosted deposits and Irish and US MVTs hosted by quartz, calcite, and dolomite have values at the lower end of our range, whilst those in sphalerite can sometimes reach several hundred ppm of Pb (Appold *et al.*, 2004; Kostova *et al.*, 2004; Wilkinson *et al.*, 2005; Kotzeva *et al.*, 2011; Fusswinkel *et al.*, 2014). Values in the several thousands of ppm have been inferred in rare cases for single fluid inclusions (e.g. Wilkinson *et al.*, 2009; Davey, 2019) However, these high values are often found for inclusions with high homogenisation temperatures, whilst those fluids thought to be cooler than ∼ 250°C generally return concentrations an order of magnitude or more below 1000 ppm (Davey, 2019). While there remains debate on complexity and exact composition of mineralising fluids (Fusswinkel *et al.*, 2013; Schlegel *et al.*, 2018), for ores deposited via the reduction mechanism, our inference of an enlarged operating window in cratonic rift basins holds regardless of the exact fluid metal concentrations.

Choice of seismic tomography model. Our LAB maps are based on recent shear-wave velocity (V_S) models that contain a lot of surface wave data and have nominal vertical resolution on the order of 25–50 km (Priestley & McKenzie, 2006). For the global map, we use SL2013sv, which is an upper mantle-only model built from a combination of body and surface waves, including fundamental and higher modes (Schaeffer & Lebedev, 2013). Periods considered are 11–450 s, ∼750,000 seismograms are included, and misfits are calculated between synthetics and the full waveform up to the 18th overtone. Crucially, simultaneous inversion for the crustal model results in reduced smearing of slow crustal velocities down into the upper mantle in comparison to other models, thereby allowing us to use more depth slices in our V_S to temperature calibration. Checkerboard resolution tests indicate that features ∼600 km in diameter at lithospheric depths are generally well resolved. Finer features should be resolvable in regions with dense ray path coverage, such as North America, Europe and southeast Asia. The SL2013sv model utilises data from only 6 seismometers in Australia, so has limited resolution within this continent. Therefore, we also investigate the FR12 regional seismic tomography model to generate a high resolution map for the Australian continent (Fishwick & Rawlinson, 2012). FR12 is a radially isotropic V_S model derived from Rayleigh wave travel times (Fishwick *et al.*, 2008). Periods considered are 50–120 s and the fundamental and first four higher modes have been used where possible, leading to good sensitivity down to ∼250 km depths. It contains a greater number of source–receiver paths (>13,000) compared to other Australian models. However, it uses an *a priori* crustal model that remains fixed throughout the inversion, resulting in noticeable smearing of crustal velocities into the upper mantle. Checkerboard tests indicate that features ∼300 km in diameter at lithospheric depths are well resolved, and where higher mode information is included.

For comparison, we include LAB maps derived from three additional upper mantle seismic tomography datasets with global coverage in Extended Data Figure 1. These include the 3D2015-07Sv model of Debayle *et al.* (2016), the CAM2016 model of Ho *et al.* (2016) and Priestley *et al.* (2018), and a version of SL2013sv into which we have blended the regional updates SL2013NA in North America (Schaeffer & Lebedev, 2014), AF2019 in Africa (Celli *et al.*, 2020a), and SA2019 in South America and the South Atlantic Ocean (Celli *et al.*, 2020b) to produce a combined model SLNAAFSA. For the continental analyses in Australia, we also consider regional model AuSREM of Kennett *et al.* (2013) and Y14 of Yoshizawa (2014). Deposit locations are compared with all seven of our new LAB maps in the Supplementary Information, in addition to eleven previously published LAB maps derived from a mixture of heat flow data, seismic tomography datasets, and potential field data. Many giant sediment hosted mineral deposits lie along LAB edges defined by these other studies, testifying to the robustness of the observed relationship.

Parameterising anelasticity. Seismic tomography models provide images of the upper mantle and have been extensively used to constrain its thermomechanical structure, composition, and the depth of the lithosphere-asthenosphere boundary (Priestley & McKenzie, 2006; An & Shi, 2006; Goes *et al.*, 2012; Afonso *et al.*, 2016; Cammarano & Guerri, 2017; Klöcking *et al.*, 2018; Afonso *et al.*, 2019). For accurate mapping from V_S into temperature, it is essential to include the effect of anelasticity on this conversion (Karato, 1993; Cammarano *et al.*, 2003). When a viscoelastic material such as the mantle is cold, deformation associated with passage of acoustic energy is predominantly elastic, yielding a linear dependence of V_S on temperature referred to as the *anharmonic velocity*. As temperature increases, a special case of viscoelastic deformation known as *anelasticity* becomes increasingly important and gives rise to a strongly non-linear relationship between V_S and temperature. This behaviour has been extensively studied in laboratory experiments on silicates and organic analogues of mantle rocks, revealing that the strength of the anelastic regime varies with both the frequency of seismic waves and as a function of material properties, such as melting temperature and grain size (Jackson *et al.*, 2002; Sundberg & Cooper, 2010; McCarthy *et al.*, 2011; Takei *et al.*, 2014; Faul & Jackson, 2015). Several studies have attempted to parameterise these complex dependencies, and have been regularly updated as forced oscillation and creep experiments in the laboratory have been pushed towards increasingly realistic frequencies, pressures, temperatures, grain sizes and strain rates (Faul & Jackson, 2005; Jackson & Faul, 2010; Takei, 2017). In this study, we adopt the parameterisation of Yamauchi & Takei (2016), which includes effects of anelasticity in pre-melt conditions (temperatures above ∼ 90% of melting temperature) and is outlined in full in the Supplementary Information.

Xenolith and xenocryst thermobarometry. Temperature estimates across a range of depths are required to generate a series of V_S–temperature–pressure tie points in order to calibrate the regional seismic tomography models. We therefore assemble a suite of fifteen Australian paleogeotherms derived from thermobarometric analysis of mantle xenoliths and xenocrysts (Supplementary Information). These come from a range of settings within both thick and thin lithosphere. Localities with thin lithosphere tend to have data obtained from whole xenolith samples, typically hosted in basaltic volcanic products. For these cases, the compositions of multiple phases (garnet, clinopyroxene, orthopyroxene and olivine) can be obtained that all equilibrated under the same pressure-temperature (P–T) conditions. In these samples, we use

Preprint accepted at Nature Geoscience on 15th May 2020 and made available under the CC-BY-NC-ND 4.0 license. © 2020

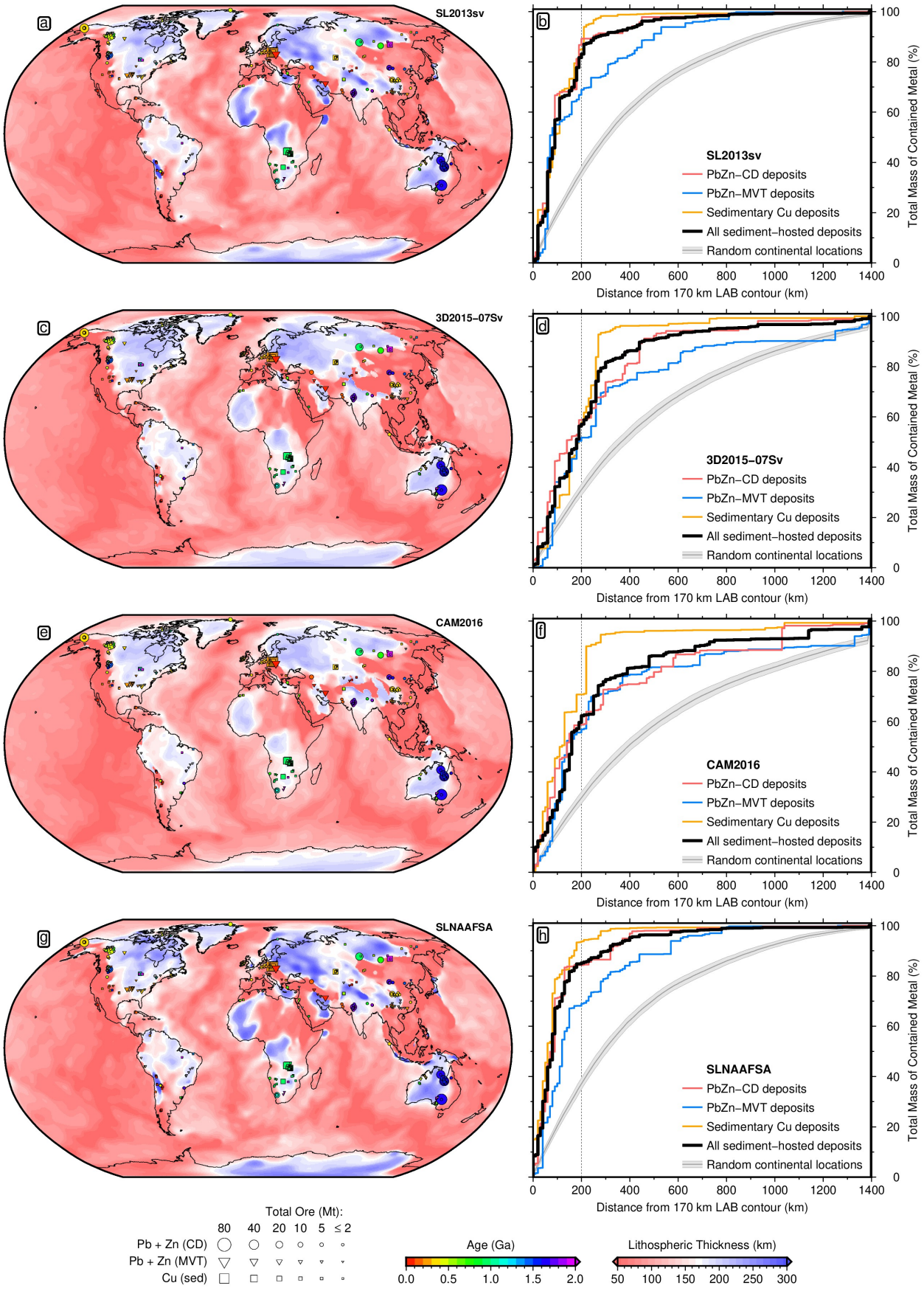

Extended Data Figure 1: **Global lithospheric thickness maps obtained from calibration of four upper mantle surface wave tomography models.** (**a**) SL2013sv model (Schaeffer & Lebedev, 2013). Symbols = deposit locations; area proportional to estimate of total contained mass of metal (either lead plus zinc, or copper) in mega-tonnes (Mt); unknown deposit size given 2 Mt symbol; colour = ore body formation age (billion years); unknown age plotted in grey; circles = clastic-dominated lead-zinc (PbZn-CD); triangles = Mississippi Valley type lead-zinc (PbZn-MVT); squares = sedimentary copper (Cu-sed). (**b**) Associated CDFs for sediment-hosted deposits and random continental locations. (**c**–**d**) Same for the 3D2015-07Sv model (Debayle *et al.*, 2016). (**e**–**f**) Same for the CAM2016 model (Ho *et al.*, 2016; Priestley *et al.*, 2018). (**g**–**h**) Same for the SLNAAFSA model, generated by blending regional updates from North America (SL2013NA), Africa (AF2019), and South America (SA2019) into the global SL2013sv model (Schaeffer & Lebedev, 2014; Celli *et al.*, 2020a,b). Note that CDFs for all tomography models show a significant difference from the distribution of random continental locations.

a thermometer that exploits exchange of calcium and magnesium between orthopyroxene and clinopyroxene (Taylor, 1998), and a barometer based upon aluminium exchange between orthopyroxene and garnet, given by Equation (5) of Nickel & Green (1985). This approach therefore requires compositions of garnet, diopside (clinopyroxene) and enstatite (orthopyroxene) for each xenolith, and we only use samples with all three of these minerals present. This barometer and thermometer pair both also depend upon the temperature and pressure, respectively. These two equations are therefore solved simultaneously by iteration to obtain equilibration P-T conditions. Samples are discarded if they fail more than one of the eight oxide, cation and equilibration checks suggested by Nimis & Grütter (2010).

Despite all samples containing garnet, a small number return depths as shallow as ∼25 km (see Bullenmerri, Monaro, Mt St Martin, and Sapphire Hill). The presence of garnet in xenoliths from shallow depths is well documented. The garnet-spinel transition can occur at pressures as low as 1 GPa (∼30 km depth) in pyroxenite and 1.5 GPa (∼45 km depth) in lherzolite, with the exact pressure of the transition depending on relative abundance of Cr and Al in each assemblage (Gasparik, 1984; Klemme, 2004; Nimis & Grütter, 2010). Our shallow samples are dominantly pyroxenites and mostly give pressures larger than the 1 GPa lower limit. Of these four sites with shallower samples, we select only Bullenmerri and Monaro for the anelasticity calibration, as these geotherms also contain samples at greater depths. In both cases, the deeper samples are consistent with the shallow results.

Analyses from locations on thicker lithosphere are predominantly obtained from heavy mineral concentrates generated during diamond exploration (plus rare diamond inclusions and occasional whole peridotite xenoliths), where the association of one mineral grain with any other has been lost. Thus, the approach outlined in the preceding paragraphs using multiple phases is unavailable, and we instead turn to single grain combined thermobarometers for deriving equilibration P-T conditions. For these samples, we use the chrome-in-diopside barometer that exploits the exchange of chromium between clinopyroxene and garnet (Equation (9) of Nimis & Taylor, 2000). It uses only diopside compositions, but requires that garnet was also present in the source region. The associated thermometer exploits enstatite-in-diopside, again using only diopside compositions but requiring that orthopyroxene was present within the source. The temperature is given by Equation (17) of Nimis & Taylor (2000). Again, these two equations must be solved by iteration to obtain P-T conditions for each diopside grain. Calibration on laboratory experiments has shown that this thermobarometer may become inaccurate at low pressures and at temperatures <700°C (Nimis & Grütter, 2010). We therefore only use P-T estimates derived from this thermobarometer that yield depths >60 km and pass both of the clinopyroxene cation and oxide checks.

There are two sources of error to consider for each suite of P-T estimates. The first is uncertainty in the microprobe analyses of elemental oxide concentrations in each of the mineral samples. For the three-mineral thermobarometer, this introduces uncertainty of ±30°C and ±10 km at low temperatures (∼700°C), reducing to ±10°C and ±3 km by ∼1200°C (Mather *et al.*, 2011). For the diopside-only thermobarometer, uncertainties are larger at ±70°C and ±12 km for low temperatures (∼600°C) and ±15°C and ±3 km for higher temperatures (∼1200°C) (Mather *et al.*, 2011). However, these uncertainties in pressure and temperature are positively correlated, such that samples broadly move up and down the geothermal gradient, with limited effect on the best fitting geotherm. The second and more significant source of uncertainty arises from error in the thermobarometers themselves, which are calibrated on laboratory samples over a range of pressure-temperature conditions and do not necessarily trade-off in the same manner. Quoted uncertainties are ±50°C and ±15 km for the three-mineral, and ±100°C and ±15 km for the diopside-only thermobarometer (Nimis & Taylor, 2000; Nimis & Grütter, 2010; Mather *et al.*, 2011).

Fitting a geotherm to P-T estimates. For each locality, P-T estimates derived from thermobarometry are entered into FITPLOT to constrain the best-fitting paleogeotherm (McKenzie *et al.*, 2005; Mather *et al.*, 2011; Supplementary Information). Within the crust, we adopt a constant conductivity of 2.5 W m^{-1} °C^{-1}, whilst a pressure- and temperature-dependent parameterisation is used within the mantle (Osako *et al.*, 2004). Bulk crustal radiogenic heat production is assumed to be 0.7 μW m^{-3}, with a standard deviation of 0.2 μW m^{-3} (Jaupart *et al.*, 2007). Crustal thickness at each location is obtained from the AusMoho model with standard deviation assigned as 10% of the total thickness (Kennett *et al.*, 2011). We assume a potential temperature of 1330 ± 50°C, which is consistent with both seismological observations and the thickness and geochemistry of mid-ocean ridge basalts, assuming a dry lherzolite source using a corner-flow melting parameterisation (Dalton *et al.*, 2014; Katz *et al.*, 2003; Shorttle *et al.*, 2014). Kinematic viscosity of the mantle is set to 2×10^{16} m^2 s^{-1}, with a standard deviation of 0.7 orders of magnitude, which is consistent with constraints from glacial isostatic adjustment (Lau *et al.*, 2016). Thermal parameters that are consistent with the melting parameterisation are used to calculate the adiabatic gradient, including a reference density of $\rho_0 = 3.3$ Mg m^{-3}, thermal expansivity of $\alpha = 3 \times 10^{-5}$ °C^{-1} and specific heat capacity of $C_P = 1187$ J kg^{-1} °C^{-1}. Uncertainty in the crustal thickness, radiogenic heat production, mantle potential temperature, and kinematic viscosity are propagated through FITPLOT using a Monte Carlo approach. 1000 combinations of these four parameters are randomly drawn assuming Gaussian distributions of the uncertainties. Geotherms are strongly consistent in the vicinity of P-T constraints, but can vary by ±50°C when greater than ∼30 km from a P-T estimate (Supplementary Information).

Calibrating V_S-to-temperature conversion. Some of the anelasticity parameters have been directly constrained by forced oscillation experiments on borneol (Yamauchi & Takei, 2016). Others, however, are material properties that must be independently determined. A widely adopted approach is to fix these parameters for a given mineral assemblage, often calculated using mineral physics tables and a thermodynamic Gibbs energy minimisation algorithm (Stixrude & Lithgow-Bertelloni, 2005; Connolly, 2009; Stixrude & Lithgow-Bertelloni, 2011; Holland & Powell, 2011; Cottaar *et al.*, 2014). In this manner, an anelastic conversion can be used in a forward sense to map between V_S and temperature (An & Shi, 2006; Cammarano *et al.*, 2009; Goes *et al.*, 2012; Dannberg *et al.*, 2017; Cammarano & Guerri, 2017). However, inferred temperature structures are variable as a result of uncertainty in the mantle's chemical composition and grain size, and differences in absolute V_S between tomography models arising from different reference models and regularisation schemes.

An alternative approach to constraining these material properties is to invert real-Earth observations of the relationship between temperature, shear-wave velocity, attenuation and viscosity in the upper mantle (Priestley & McKenzie, 2006; Afonso *et al.*, 2013a,b; Yamauchi & Takei, 2016). The general philosophy is that there are certain properties that are 'known' about Earth, including the typical thermal structure of oceanic lithosphere (Richards *et al.*, 2018), the average adiabatic gradient within the convecting mantle (Connolly, 2009), the attenuation structure of the upper mantle beneath old oceanic lithosphere (Dalton *et al.*, 2009), and the bulk diffusion creep viscosity of the upper mantle from studies of glacial isostatic adjustment (Lau *et al.*, 2016). Thus any thermal model inferred from shear-wave velocities should be compatible with these observations. This general approach was pioneered by Priestley & McKenzie (2006) and Priestley & McKenzie (2013). The approach has been further refined by (Richards *et al.*, 2020, under review) and we adopt their approach for calibration of global tomography models (see Supplementary Information).

For the Australian regional tomography models, we cannot use oceanic observations for calibration due to insufficient offshore coverage, and instead use the better constrained paleogeotherms derived from thermobarometry on mantle xenoliths (in combination with the adiabatic gradient). Away from three close together sites in South Australia in the vicinity of the Gawler Craton, it is notable that the global SL2013sv model provides a surprisingly good fit to the Australian paleogeotherms, despite being calibrated independently (Supplementary Information). This observation is unexpected for two reasons. First, the nominal resolution of the global model is lower than the local models. There are only six seismometers in Australia (located in the far west, north and east of the continent, with none in South Australia), and the density of crossing ray paths is much lower than in Europe, Asia, North, and South America (Schaeffer & Lebedev, 2013). Secondly, the Australian geotherms occur in continental lithosphere that is thought to be chemically depleted by melt extraction, reducing the quantity of garnet and clinopyroxene with respect to more fertile oceanic mantle. Nevertheless, the global model calibrated on fertile mantle constraints provides a good match to independent V_S–T–P observations in depleted continental lithosphere. This result implies that temperature plays the dominant role in controlling variations in seismic wave speed in the shallow mantle, whilst the effects of compositional variation are substantially smaller (Goes *et al.*,

2000; Priestley & McKenzie, 2006; Schutt & Lesher, 2006).

Mapping the lithosphere-asthenosphere boundary (LAB). A recent study on the thermal structure of oceanic lithosphere found that the 1175 ± 50°C isotherm provides a good match to seismological observations of the lithosphere-asthenosphere boundary (Richards *et al.*, 2018). In this study, we therefore adopt this isotherm as a proxy for lithospheric thickness beneath the continents. The temperature (T) as a function of depth (z) is extracted from the V_S model and $\frac{\partial T}{\partial z}$ is calculated over 25 km increments. Starting from the surface and progressing downwards, when temperature passes the 1175°C threshold, LAB depth is calculated using linear interpolation, with one important exception. In locations of thick crust, low V_S values at shallow depths arising from crustal bleeding can lead to lithospheric mantle being erroneously interpreted as hot. In the regional seismic tomography models, this crustal bleeding can be observed down to ∼125 km in some locations (see calibration Figure S7 in Supplementary Information). To circumvent this issue, when an inverted temperature gradient is found at shallow depths, we move on to deeper levels until temperature starts to increase with depth. This crustal bleeding is only considered down to 200 km. Maximum LAB depth is limited to 350 km or the deepest slice in the seismic tomography model. Our 1175°C isotherm LAB proxy is shallower than used in some other studies that define the LAB using the intersection of conductive and adiabatic temperature gradients in the thermal boundary layer (typically occurring at temperatures 1350–1450°C; McKenzie *et al.*, 2005; Mather *et al.*, 2011; Priestley & McKenzie, 2013). However, in addition to matching oceanic observations, the 1175°C isotherm corresponds to lower homologous temperatures, where uncertainty in anelastic parameters has a smaller impact on the recovered LAB.

As in previous studies using seismic tomography (e.g. Priestley & McKenzie, 2013; Steinberger & Becker, 2018; Priestley *et al.*, 2018; Afonso *et al.*, 2019), our LAB map exhibits regions of thick lithosphere in some subduction zones (e.g. west coast of South America, south Alaska and Japan). Many of these features are likely to represent subducting slabs rather than cratonic lithosphere. None of the giant (>10 Mt of contained metal) sediment-hosted deposits is found in these settings, although some minor sedimentary copper deposits do occur, particularly in the Andes. These deposits may well represent distal components of porphyry coppers, but we have left them in our sedimentary copper dataset in line with pre-existing classification schemes. It is possible to manually exclude potential slab-related features from the analysis utilising the Slab2 model(Hayes *et al.*, 2018; Supplementary Information). Doing so actually improves the results of statistical tests, with the chances of the relationship between sediment-hosted deposits and the edge of cratonic lithosphere being random reducing by a factor of three. This occurs because the continental area within 200 km of the 170 km LAB contour decreases from 34.3% to 31.0%, while only marginally increasing the proportion of small outlier deposits. Nevertheless, we have deliberately retained these regions in the main manuscript in order to avoid introducing subjectivity and bias into our LAB maps, as opinions are likely to differ on which features to exclude. Furthermore, some studies argue that over long periods of time, thick lithosphere may actually be generated at subduction zones by thrust stacking (Cook *et al.*, 1999). Thus, exclusion of these features is potentially unwarranted.

Test suites of random continental locations. In order to test the statistical significance of real deposit locations, a test suite of random points on a sphere have been generated by randomly selecting two variables, a and b, in the range 0–1 and converting into longitude, θ, and latitude, ϕ, using area-normalised relationships

$$\theta = 360 \times a \tag{1}$$

$$\phi = \frac{180}{\pi} \times \arcsin(2b - 1) \tag{2}$$

These are subsequently filtered to select only those points that lie onshore (Supplementary Information). For each location, the closest approach to the 170 km lithospheric thickness contour is calculated and the resulting distances are plotted in a cumulative distribution function (CDF).

Kolmogorov-Smirnov statistical tests. We use the *two-sample Kolmogorov-Smirnov test* to examine whether the difference between two cumulative distribution functions is significant, given their respective population sizes (Kolmogorov, 1933). The D-value is the maximum magnitude of the difference between two CDFs at any point. The test calculates the probability that a D-value of this magnitude might accidentally occur, had the two CDFs been randomly selected from the same underlying population. The probability, P, is approximated using

$$P \approx \exp\left(\frac{-2pqD^2}{p+q}\right) \tag{3}$$

where p and q are the number of samples in each CDF and D is the D-value expressed as a fraction between 0 and 1. For each Kolmogorov-Smirnov test, a number of random points are generated that is equivalent to the number of real deposits of that type (109 for PbZn-CD, 147 for PbZn-MVT and 139 for sedimentary copper). Given the low sample size for some of the deposit classes, the distribution of this random set can vary somewhat from the true average distribution of random continental locations. We therefore draw a test set in this manner 100 times and report the Kolmogorov-Smirnov statistics associated with each separate test within a histogram. For PbZn-CD deposits, the D-value between the real non-weighted, regionally enhanced CDF and each random CDF is individually calculated, yielding a mean and standard deviation of $D = 0.36 \pm 0.05$, with extremes of 0.26–0.46. For the combined sediment-hosted deposits in Figure 3, the equivalent values are $D = 0.27 \pm 0.02$ with extremes of 0.22–0.32. A D-value of 0.27 for the 395 combined sedimentary-hosted deposits suggests that the probability this CDF is drawn from randomly distributed continental points is less than 1 in 10^{12} (Supplementary Information).

Thermal modelling of lithospheric rifting. Rifting of continental lithosphere causes subsidence of the surface to form a basin that progressively infills with sediments. An initial syn-rift subsidence phase occurs during lateral extension and vertical thinning of the crust and lithospheric mantle, which is contemporaneous with normal faulting. Following cessation of extension, faulting stops and post-rift thermal subsidence occurs as hot, upwelled asthenospheric mantle conductively cools back to an equilibrium lithospheric thickness (McKenzie, 1978). To predict the subsidence and basal heat flow of the basin, we model the 1-dimensional thermal evolution of the lithosphere during rifting using a finite difference scheme. Following McKenzie (1978), we assume thinning occurs by pure shear and that vertical heat transfer dominates.

For each rift scenario, we select an initial lithospheric template. For regular continental lithosphere, the crustal thickness is set to 30 km and the total lithospheric thickness to 140 km, which matches results from plate cooling models of oceanic lithosphere (Richards *et al.*, 2018) and places the 1175°C isotherm at ∼ 120 km. Radiogenic heat production in the mantle is set to zero, whilst the crustal value is tuned to 1.0 μW m^{-3} such that the steady state geotherm yields a surface heat flow of ∼63 mW m^{-2}, which is the average for Phanerozoic continental lithosphere (Lucazeau, 2019) For cratonic lithosphere, we assume an initial crustal thickness of 50 km, lithospheric thickness of 280 km (1175°C isotherm at ∼ 240 km), and crustal radiogenic heat production of 0.57 μW m^{-3}, which yields an initial surface heat flux consistent with the average of ∼48 mW m^{-2} for Archean and cratonic areas (Lucazeau, 2019) Based on the typically low paleowater depth of sediments found in proximal portions of these basins and the high supply of clastic material from adjacent cratons, we assume the basin is constantly filled by sediments. We subsequently predict the temperature of the sediment pile using the basal heat flux and a constant sediment conductivity of 2.5 W m^{-1} K^{-1}, assuming a steady state conductive geotherm and negligible internal heat generation. Details of the finite difference scheme, thermal parameterisations, and individual model runs are given in the Supplementary Information.

References

Afonso, J. C., J. Fullea, W. L. Griffin, Y. Yang, A. G. Jones, J. A. Connolly, & S. Y. Reilly (2013a). 3-D multiobservable probabilistic inversion for the compositional and thermal structure of the lithosphere and upper mantle. I: A priori petrological information and geophysical observables. *Journal of Geophysical Research: Solid Earth*, 118, 2586–2617.

Afonso, J. C., J. Fullea, Y. Yang, J. A. Connolly, & A. G. Jones (2013b). 3-D multi-observable probabilistic inversion for the compositional and thermal structure of the lithosphere and upper mantle. II: General methodology and resolution analysis. *Journal of Geophysical Research: Solid Earth*, 118, 1650–1676.

Afonso, J. C., N. Rawlinson, Y. Yang, D. L. Schutt, A. G. Jones, J. Fullea, & W. L. Griffin (2016). 3-D multiobservable probabilistic inversion for the compositional and thermal structure of the lithosphere and upper mantle: III. Thermochemical tomography in the Western-

Central U.S. *Journal of Geophysical Research: Solid Earth*, 121, 7337–7370.

Afonso, J. C., F. Salajegheh, W. Szwillus, J. Ebbing, & C. Gaina (2019). A global reference model of the lithosphere and upper mantle from joint inversion and analysis of multiple data sets. *Geophysical Journal International*, 217, 1602–1628.

Alghamdi, A. H., A. R. Aitken, & M. C. Dentith (2018). The deep crustal structure of the Warakurna LIP, and insights on Proterozoic LIP processes and mineralisation. *Gondwana Research*, 56, 1–11.

Ali, S. H., D. Giurco, N. Arndt, E. Nickless, *et al.* (2017). Mineral supply for sustainable development requires resource governance. *Nature*, 543 (7645), 367–372.

Allen, P. A. & J. J. Armitage (2012). Cratonic basins. In: *Tectonics of Sedimentary Basins: Recent Advances* (edited by C. Busby & A. Azor), chap. 30, pp. 602–620. Blackwell Publishing Ltd, 1 edn.

An, M. & Y. Shi (2006). Lithospheric thickness of the Chinese continent. *Physics of the Earth and Planetary Interiors*, 159, 257–266.

Appold, M. S., T. J. Numelin, T. J. Shepherd, & S. R. Chenery (2004). Limits on the metal content of fluid inclusions in gangue minerals from the Viburnum Trend, southeast Missouri, determined by laser ablation ICP-MS. *Economic Geology*, 99, 185–198.

Arndt, N. T., C. M. Lesher, & G. K. Czamanske (2005). Mantle-derived magmas and magmatic Ni-Cu-(PGE) deposits. *Economic Geology 100th Anniversary Volume*, pp. 5–24.

Azadi, M., S. A. Northey, S. H. Ali, & M. Edraki (2020). Transparency on greenhouse gas emissions from mining to enable climate change mitigation. *Nature Geoscience*, 13, 100–104.

Begg, G. C., J. A. M. Hronsky, N. T. Arndt, W. L. Griffin, S. Y. O'Reilly, & N. Hayward (2010). Lithospheric, cratonic, and geodynamic setting of Ni-Cu-PGE sulfide deposits. *Economic Geology*, 105, 1057–1070.

Bierlein, F. P., D. I. Groves, R. J. Goldfarb, & B. Dubé (2006). Lithospheric controls on the formation of provinces hosting giant orogenic gold deposits. *Mineralium Deposita*, 40, 874–886.

Biggs, J., E. Nissen, T. Craig, J. Jackson, & D. P. Robinson (2010). Breaking up the hanging wall of a rift-border fault: The 2009 Karonga earthquakes, Malawi. *Geophysical Research Letters*, 37 (L11305).

Butterworth, N., D. Steinberg, R. D. Müller, S. Williams, A. S. Merdith, & S. Hardy (2016). Tectonic environments of South American porphyry copper magmatism through time revealed by spatiotemporal data mining. *Tectonics*, 35, 2847–2862.

Cammarano, F., S. Goes, P. Vacher, & D. Giardini (2003). Inferring upper-mantle temperatures from seismic velocities. *Physics of the Earth and Planetary Interiors*, 138, 197–222.

Cammarano, F. & M. Guerri (2017). Global thermal models of the lithosphere. *Geophysical Journal International*, 210, 56–72.

Cammarano, F., B. Romanowicz, L. Stixrude, C. Lithgow-Bertelloni, & W. Xu (2009). Inferring the thermochemical structure of the upper mantle from seismic data. *Geophysical Journal International*, 179, 1169–1185.

Celli, N. L., S. Lebedev, A. J. Schaeffer, & C. Gaina (2020a). African cratonic lithosphere carved by mantle plumes. *Nature Communications*, 11 (92).

Celli, N. L., S. Lebedev, A. J. Schaeffer, M. Ravenna, & C. Gaina (2020b). The upper mantle beneath the South Atlantic Ocean, South America and Africa from waveform tomography with massive data sets. *Geophysical Journal International*, 221, 178–204.

Connolly, J. A. (2009). The geodynamic equation of state: What and how. *Geochemistry, Geophysics, Geosystems*, 10 (Q10014).

Cook, F. A., A. J. Van Der Velden, K. W. Hall, & B. J. Roberts (1999). Frozen subduction in Canada's Northwest Territories: Lithoprobe deep lithospheric reflection profiling of the western Canadian Shield. *Tectonics*, 18 (1), 1–24.

Cooke, D. R., S. W. Bull, R. R. Large, & P. J. McGoldrick (2000). The importance of oxidized brines for the formation of Australian Proterozoic stratiform sediment-hosted Pb-Zn (sedex) deposits. *Economic Geology*, 95, 1–18.

Cottaar, S., T. Heister, I. Rose, & C. Unterborn (2014). BurnMan: A lower mantle mineral physics toolkit. *Geochemistry, Geophysics, Geosystems*, 15, 1164–1179.

Cox, D. P., D. A. Lindsey, D. A. Singer, B. C. Moring, & M. F. Diggles (2007). Sediment-hosted copper deposits of the world: Deposit models and database. *U.S. Geological Survey Open-File Report*, 03-107.

Currie, C. A. & J. van Wijk (2016). How craton margins are preserved: Insights from geodynamic models. *Journal of Geodynamics*, 100, 144–158.

Curtis, S. & S. Thiel (2019). Identifying lithospheric boundaries using magnetotellurics and Nd isotope geochemistry: An example from the Gawler Craton, Australia. *Precambrian Research*, 320, 403–423.

Dalton, C. A., G. Ekström, & A. M. Dziewonski (2009). Global seismological shear velocity and attenuation: A comparison with experimental observations. *Earth and Planetary Science Letters*, 284, 65–75.

Dalton, C. A., C. H. Langmuir, & A. Gale (2014). Geophysical and geochemical evidence for deep temperature variations beneath mid-ocean ridges. *Science*, 344, 80–83.

Dannberg, J., Z. Eilon, U. Faul, R. Gassmöller, P. Moulik, & R. Myhill (2017). The importance of grain size to mantle dynamics and seismological observations. *Geochemistry, Geophysics, Geosystems*, 18, 3034–3061.

Davey, J. (2019). *Anomalous metal enrichment of basin brines in the Zambian Copperbelt: A comparison of fluid chemistry in contrasting sediment-hosted copper systems.* Ph.D. thesis, University of Southampton.

Davies, D. R. & N. Rawlinson (2014). On the origin of recent intraplate volcanism in Australia. *Geology*, 42 (12), 1031–1034.

Debayle, E., F. Dubuffet, & S. Durand (2016). An automatically updated S-wave model of the upper mantle and the depth extent of azimuthal anisotropy. *Geophysical Research Letters*, 43, 674–682.

Dentith, M., H. Yuan, S. Johnson, R. Murdie, & P. Piña-Varas (2018). Application of deep-penetrating geophysical methods to mineral exploration: Examples from Western Australia. *Geophysics*, 83 (3), WC29–WC41.

Dominish, E., S. Teske, & N. Florin (2019). Responsible minerals sourcing for renewable energy. *Tech. rep.*, Institute for Sustainable Futures, University of Technology Sydney.

Faul, U. H. & I. Jackson (2005). The seismological signature of temperature and grain size variations in the upper mantle. *Earth and Planetary Science Letters*, 234, 119–134.

Faul, U. H. & I. Jackson (2015). Transient creep and strain energy dissipation: An experimental perspective. *Annual Review of Earth and Planetary Sciences*, 43, 541–569.

Fishwick, S., M. Heintz, B. L. N. Kennett, A. M. Reading, & K. Yoshizawa (2008). Steps in lithospheric thickness within eastern Australia, evidence from surface wave tomography. *Tectonics*, 27 (4009).

Fishwick, S. & N. Rawlinson (2012). 3-D structure of the Australian lithosphere from evolving seismic datasets. *Australian Journal of Earth Sciences*, 59, 809–826.

Franklin, J. M., H. L. Gibson, I. R. Jonasson, & A. G. Galley (2005). Volcanogenic massive sulfide deposits. *Economic Geology 100th Anniversary Volume*, pp. 523–560.

Fusswinkel, T., T. Wagner, M. Wälle, T. Wenzel, C. A. Heinrich, & G. Markl (2013). Fluid mixing forms basement-hosted Pb-Zn deposits: Insight from metal and halogen geochemistry of individual fluid inclusions. *Geology*, 41, 679–682.

Fusswinkel, T., T. Wagner, T. Wenzel, M. Wälle, & J. Lorenz (2014). Red bed and basement sourced fluids recorded in hydrothermal Mn-Fe-As veins, Sailauf (Germany): A LA-ICPMS fluid inclusion study. *Chemical Geology*, 363, 22–39.

Gasparik, T. (1984). Two-pyroxene thermobarometry with new experimental data in the system CaO–MgO–Al_2O_3–SiO_2. *Contributions to Mineralogy and Petrology*, 87, 87–97.

Geoscience Australia (2018). Geophysical Archive Data Delivery System (GADDS). URL `geoscience.gov.au/gadds`.

Gibson, G. M., A. J. Meixner, I. W. Withnall, R. J. Korsch, *et al.* (2016). Basin architecture and evolution in the Mount Isa mineral province, northern Australia: Constraints from deep seismic reflection profiling and implications for ore genesis. *Ore Geology Reviews*, 76, 414–441.

Goes, S., J. Armitage, N. Harmon, H. Smith, & R. Huismans (2012). Low seismic velocities below mid-ocean ridges: Attenuation versus melt retention. *Journal of Geophysical Research*, 117 (B12403).

Goes, S., R. Govers, & P. Vacher (2000). Shallow mantle temperatures under Europe from P and S wave tomography. *Journal of Geophysical Research*, 105 (B5), 11,153–11,169.

Griffin, W. L., G. C. Begg, & S. Y. O'Reilly (2013). Continental-root control on the genesis of magmatic ore deposits. *Nature Geoscience*, 6 (11), 905–910.

Hayes, G. P., G. L. Moore, D. E. Portner, M. Hearne, H. Flamme, M. Furtney, & G. M. Smoczyk (2018). Slab2, a comprehensive subduction zone geometry model. *Science*, 362, 58–61.

Heinson, G., Y. Didana, P. Soeffky, S. Thiel, & T. Wise (2018). The crustal geophysical signature of a world-class magmatic mineral system. *Scientific Reports*, 8 (10608).

Hitzman, M. W., R. Kirkham, D. Broughton, J. Thorson, & D. Selley (2005). The sediment-hosted stratiform Copper ore system. *Economic Geology 100th Anniversary Volume*, pp. 609–642.

Hitzman, M. W., D. Selley, & S. Bull (2010). Formation of sedimentary rock-hosted stratiform copper deposits through Earth history. *Economic Geology*, 105 (3), 627–639.

Ho, T., K. Priestley, & E. Debayle (2016). A global horizontal shear velocity model of the upper mantle from multimode love wave measurements. *Geophysical Journal International*, 207, 542–561.

Hoatson, D. M., S. Jaireth, & A. L. Jaques (2006). Nickel sulfide deposits in Australia: Characteristics, resources, and potential. *Ore Geology Reviews*, 29, 177–241.

Hobbs, B. E., A. Ord, N. J. Archibald, J. L. Walshe, Y. Zhang, M. Brown, & C. Zhao (2000). Geodynamic modelling as an exploration tool. In: *Australasian Institute of Mining and Metallurgy Publication Series*, pp. 34–49. Sydney.

Holland, T. J. & R. Powell (2011). An improved and extended internally consistent thermodynamic dataset for phases of petrological interest, involving a new equation of state for solids. *Journal of Metamorphic Geology*, 29, 333–383.

Huston, D. L., D. C. Champion, B. Ware, G. Carr, R. Maas, & S. Tessalina (2019). Preliminary national-scale lead isotope maps of Australia. *Geoscience Australia Record*, 01 (127263).

Huston, D. L., T. P. Mernagh, S. G. Hagemann, M. P. Doublier, *et al.* (2016). Tectono-metallogenic systems – The place of mineral systems within tectonic evolution, with an emphasis on Australian examples. *Ore Geology Reviews*, 76, 168–210.

Huston, D. L., S. Pehrsson, B. M. Eglington, & K. Zaw (2010). The geology and metallogeny of volcanic-hosted massive sulfide deposits: Variations through geologic time and with tectonic setting. *Economic Geology*, 105 (3), 571–591.

IRENA (2019). *Global energy transformation: A roadmap to 2050*. Abu Dhabi.

Jackson, I. & U. H. Faul (2010). Grainsize-sensitive viscoelastic relaxation in olivine: Towards a robust laboratory-based model for seismological application. *Physics of the Earth and Planetary Interiors*, 183, 151–163.

Jackson, I., J. D. Fitz Gerald, U. H. Faul, & B. H. Tan (2002). Grain-size-sensitive seismic wave attenuation in polycrystalline olivine. *Journal of Geophysical Research*, 107 (B12), 2360.

Jaupart, C., S. Labrosse, & J. C. Mareschal (2007). Temperatures, heat and energy in the mantle of the Earth. *Treatise on Geophysics*, 7, 253–303.

Jordan, T. H. (1978). Composition and development of the continental tectosphere. *Nature*, 274, 544–548.

Karato, S. (1993). Importance of anelasticity in the interpretation of seismic tomography. *Geophysical Research Letters*, 20 (15), 1623–1626.

Katz, R. F., M. Spiegelman, & C. H. Langmuir (2003). A new parameterization of hydrous mantle melting. *Geochemistry, Geophysics, Geosystems*, 4 (1073).

Kennett, B. L. N., A. Fichtner, S. Fishwick, & K. Yoshizawa (2013). Australian seismological reference model (AuSREM): Mantle component. *Geophysical Journal International*, 192, 871–887.

Kennett, B. L. N., M. Salmon, E. Saygin, & A. W. Group (2011). AusMoho: The variation of Moho depth in Australia. *Geophysical Journal International*, 187 (2), 946–958.

Kennett, B. L. N., E. Saygin, T. Fomin, & R. Blewett (2016). *Deep crustal seismic reflection profiling: Australia 1978-2015*. ANU Press and Commonwealth of Australia (Geoscience Australia), Canberra.

Klemme, S. (2004). The influence of Cr on the garnet-spinel transition in the Earth's mantle: Experiments in the system MgO–Cr_2O_3–SiO_2 and thermodynamic modelling. *Lithos*, 77 (1-4 SPEC. ISS.), 639–646.

Klöcking, M., N. J. White, J. Maclennan, D. McKenzie, & J. G. Fitton (2018). Quantitative relationships between basalt geochemistry, shear wave velocity, and asthenospheric temperature beneath western North America. *Geochemistry, Geophysics, Geosystems*, 19, 3376–3404.

Kolmogorov, A. N. (1933). Sulla determinazione empirica di una legge di distribuzione. *Giornale dell'Istituto Italiano degli Attuari*, 4, 83–91.

Kostova, B., T. Pettke, T. Driesner, P. Petrov, & C. A. Heinrich (2004). LA-ICP-MS study of fluid inclusions in quartz from the Yuzhna Petrovitsa deposit, Madan ore field, Bulgaria. *Schweizerische Mineralogische und Petrographische Mitteilungen*, 84, 25–36.

Kotzeva, B. G., M. Guillong, E. Stefanova, & N. B. Piperov (2011). LA-ICP-MS analysis of single fluid inclusions in a quartz crystal (Madan ore district, Bulgaria). *Journal of Geochemical Exploration*, 108, 163–175.

Lau, H. C., J. X. Mitrovica, J. Austermann, O. Crawford, D. Al-Attar, & K. Latychev (2016). Inferences of mantle viscosity based on ice age data sets: Radial structure. *Journal of Geophysical Research: Solid Earth*, 121 (10), 6991–7012.

Leach, D. L., D. C. Bradley, D. L. Huston, S. A. Pisarevsky, R. D. Taylor, & S. J. Gardoll (2010). Sediment-hosted lead-zinc deposits in Earth history. *Economic Geology*, 105 (3), 593–625.

Lucazeau, F. (2019). Analysis and mapping of an updated terrestrial heat flow data set. *Geochemistry, Geophysics, Geosystems*, 20, 4001–4024.

Manning, A. H. & P. Emsbo (2018). Testing the potential role of brine reflux in the formation of sedimentary exhalative (sedex) ore deposits. *Ore Geology Reviews*, 102, 862–874.

Mather, K. A., D. G. Pearson, D. P. McKenzie, B. A. Kjarsgaard, & K. Priestley (2011). Constraints on the depth and thermal history of cratonic lithosphere from peridotite xenoliths, xenocrysts and seismology. *Lithos*, 125, 729–742.

McCarthy, C., Y. Takei, & T. Hiraga (2011). Experimental study of attenuation and dispersion over a broad frequency range: 2. The universal scaling of polycrystalline materials. *Journal of Geophysical Research*, 116 (B09207).

McCuaig, T. C., S. Beresford, & J. Hronsky (2010). Translating the mineral systems approach into an effective exploration targeting system. *Ore Geology Reviews*, 38, 128–138.

McCuaig, T. C. & J. M. A. Hronsky (2014). The mineral system concept: The key to exploration targeting. In: *Society of Economic Geologists Special Publication 18*, pp. 153–175. Society of Economic Geologists.

McCuaig, T. C., S. Scarselli, T. O. Connor, S. Busuttil, & N. Mccormack (2018). The power of a systems approach to mineral and petroleum exploration in sedimentary basins. In: *SEG Special Publication 21*, chap. 3, pp. 39–62. Society of Economic Geologists.

McKenzie, D. P. (1978). Some remarks on the development of sedimentary basins. *Earth and Planetary Science Letters*, 40, 25–32.

McKenzie, D. P., J. Jackson, & K. Priestley (2005). Thermal structure of oceanic and continental lithosphere. *Earth and Planetary Science Letters*, 233, 337–349.

Menzies, M., Y. Xu, H. Zhang, & W. Fan (2007). Integration of geology, geophysics and geochemistry: A key to understanding the North China Craton. *Lithos*, 96, 1–21.

Mudd, G. M., T. T. Werner, Z. H. Weng, M. Yellishetty, Y. Yuan, S. R. B. McAlpine, R. Skirrow, & K. Czarnota (2018). Critical minerals in Australia: A review of opportunities and research needs. *Tech. rep.*, Geoscience Australia.

Nassar, N. T., T. E. Graedel, & E. M. Harper (2015). By-product metals are technologically essential but have problematic supply. *Science Advances*, 1 (1400180).

Nickel, K. G. & D. H. Green (1985). Empirical geothermobarometry for garnet peridotites and implications for the nature of the lithosphere, kimberlites and diamonds. *Earth and Planetary Science Letters*, 73, 158–170.

Nimis, P. & H. Grütter (2010). Internally consistent geothermometers for garnet peridotites and pyroxenites. *Contributions to Mineralogy and Petrology*, 159, 411–427.

Nimis, P. & W. R. Taylor (2000). Single clinopyroxene thermobarometry for garnet peridotites. Part I. Calibration and testing of a Cr-in-Cpx barometer and an enstatite-in-Cpx thermometer. *Contributions to Mineralogy and Petrology*, 139, 541–554.

O'Reilly, S. Y., W. L. Griffin, & N. J. Pearson (2017). Geodynamic and geophysical consequences of stealth(y) mantle metasomatism: Craton evolution and metallogeny. In: *11th International Kimberlite Conference*, 4537.

Osako, M., E. Ito, & A. Yoneda (2004). Simultaneous measurements of thermal conductivity and thermal diffusivity for garnet and olivine under high pressure. *Physics of the Earth and Planetary Interiors*, 143-144, 311–320.

Priestley, K., D. McKenzie, & T. Ho (2018). A lithosphere-asthenosphere boundary – A global model derived from multimode surface-wave tomography and petrology. In: *Geophysical Monograph 239, Lithospheric Discontinuities* (edited by H. Yuan & B. Romanowicz), chap. 6, pp. 111–123. John Wiley and Sons, Washington D.C.

Priestley, K. & D. P. McKenzie (2006). The thermal structure of the lithosphere from shear wave velocities. *Earth and Planetary Science Letters*, 244, 285–301.

Priestley, K. & D. P. McKenzie (2013). The relationship between shear wave velocity, temperature, attenuation and viscosity in the shallow part of the mantle. *Earth and Planetary Science Letters*, 381, 78–91.

Raymond, O. (2018). Australian Geological Provinces 2018.01 edition. *Geoscience Australia Dataset*, eCat Id: 116823. URL `pid.geoscience.gov.au/dataset/ga/116823`.

Regis, D., P. Acosta-Gongora, W. J. Davis, B. Knox, S. J. Pehrsson, E. Martel, & L. Hulbert (2017). Evidence for Neoarchean Ni-Cu-bearing mafic intrusions along a major lithospheric structure: A case study from the south Rae craton (Canada). *Precambrian Research*, 302, 312–339.

Richards, F. D., M. J. Hoggard, L. R. Cowton, & N. J. White (2018). Reassessing the thermal structure of oceanic lithosphere with revised global inventories of basement depths and heat flow measurements. *Journal of Geophysical Research: Solid Earth*, 123, 9136–9161.

Richards, F. D., M. J. Hoggard, N. J. White, & S. Ghelichkhan (2020). Quantifying the relationship between short-wavelength dynamic topography and thermomechanical structure of the upper mantle using calibrated parameterization of anelasticity. *Journal of Geophysical Research: Solid Earth*.

Rosenbaum, G., D. Giles, M. Saxon, P. G. Betts, R. F. Weinberg, & C. Duboz (2005). Subduction of the Nazca Ridge and the Inca Plateau: Insights into the formation of ore deposits in Peru. *Earth and Planetary Science Letters*, 239, 18–32.

Schaeffer, A. J. & S. Lebedev (2013). Global shear speed structure of the upper mantle and transition zone. *Geophysical Journal International*, 194, 417–449.

Schaeffer, A. J. & S. Lebedev (2014). Imaging the North American continent using waveform inversion of global and USArray data. *Earth and Planetary Science Letters*, 402, 26–41.

Schlegel, T. U., T. Wagner, M. Wälle, & C. A. Heinrich (2018). Hematite breccia-hosted iron oxide copper-gold deposits require magmatic fluid components exposed to atmospheric oxidation: Evidence from Prominent Hill, Gawler Craton, South Australia. *Economic Geology*, 113, 597–644.

Schodde, R. (2017). Long term trends in global exploration – Are we finding enough metal? In: *11th Fennoscandian Exploration and Mining Conference, 31st October 2017*. Levi, Finland. URL `minexconsulting.com/publications/oct2017b`.

Schutt, D. L. & C. E. Lesher (2006). Effects of melt depletion on the density and seismic velocity of garnet and spinel lherzolite. *Journal of Geophysical Research*, 111 (B05401).

Sexton, J. (2011). Australian mineral occurrences collection. *Geoscience Australia Dataset*, eCat Id 73131. URL `pid.geoscience.gov.au/dataset/ga/73131`.

Shorttle, O., J. Maclennan, & S. Lambart (2014). Quantifying lithological variability in the mantle. *Earth and Planetary Science Letters*, 395, 24–40.

Sillitoe, R. H. (2010). Porphyry copper systems. *Economic Geology*, 105, 3–41.

Skirrow, R. G., J. Murr, A. Schofield, D. L. Huston, *et al.* (2019). Mapping iron oxide Cu-Au (IOCG) mineral potential in Australia using a knowledge-driven mineral systems-based approach. *Ore Geology Reviews*, 113 (103011).

Skirrow, R. G., S. E. van der Wielen, D. C. Champion, K. Czarnota, & S. Thiel (2018). Lithospheric architecture and mantle metasomatism linked to Iron Oxide Cu-Au ore formation: Multidisciplinary evidence from the Olympic Dam region, South Australia. *Geochemistry, Geophysics, Geosystems*, 19 (8), 2673–2705.

Sloan, R. A., J. A. Jackson, D. P. McKenzie, & K. Priestley (2011). Earthquake depth distributions in central Asia, and their relations with lithosphere thickness, shortening and extension. *Geophysical Journal International*, 185 (1), 1–29.

Sovacool, B. B. K., S. H. Ali, M. Bazilian, B. Radley, B. Nemery, J. Okatz, & D. Mulvaney (2020). Sustainable minerals and metals for a low-carbon future. *Science*, 367 (6473), 30–33.

Steinberger, B. & T. W. Becker (2018). A comparison of lithospheric thickness models. *Tectonophysics*, 746, 325–338.

Stixrude, L. & C. Lithgow-Bertelloni (2005). Thermodynamics of mantle minerals - I. Physical properties. *Geophysical Journal International*, 162, 610–632.

Stixrude, L. & C. Lithgow-Bertelloni (2011). Thermodynamics of mantle minerals - II. Phase equilibria. *Geophysical Journal International*, 184, 1180–1213.

Sundberg, M. & R. F. Cooper (2010). A composite viscoelastic model for incorporating grain boundary sliding and transient diffusion creep: Correlating creep and attenuation responses for materials with a fine grain size. *Philosophical Magazine*, 90 (20), 2817–2840.

Takei, Y. (2017). Effects of partial melting on seismic velocity and attenuation: A new insight from experiments. *Annual Review of Earth and Planetary Sciences*, 45, 447–470.

Takei, Y., F. Karasawa, & H. Yamauchi (2014). Temperature, grain size, and chemical controls on polycrystal anelasticity over a broad frequency range extending into the seismic range. *Journal of Geophysical Research: Solid Earth*, 119, 5414–5443.

Taylor, R. D., D. L. Leach, D. C. Bradley, & S. A. Pisarevsky (2009). Compilation of mineral resource data for Mississippi Valley-type and clastic-dominated sediment-hosted lead-zinc deposits. *U.S. Geological Survey Open-File Report*, 1297.

Taylor, W. R. (1998). An experimental test of some geothermometer and geobarometer formulations for upper mantle peridotites with application to the thermobarometry of fertile lherzolite and garnet websterite. *Neues Jahrbuch für Mineralogie - Abhandlungen*, 172 (2-3), 381–408.

The Uncover Group (2012). Searching the deep Earth: A vision for exploration geoscience in Australia. *Tech. rep.*, Australian Academy of Science.

Wilkinson, J. J., C. E. Everett, A. J. Boyce, S. A. Gleeson, & D. M. Rye (2005). Intracratonic crustal seawater circulation and the genesis of subseafloor zinc-lead mineralization in the Irish orefield. *Geology*, 33, 805–808.

Wilkinson, J. J., B. Stoffell, C. C. Wilkinson, T. E. Jeffries, & M. S. Appold (2009). Anomalously metal-rich fluids form hydrothermal ore deposits. *Science*, 323, 764–767.

Wyborn, L. A. I., C. A. Heinrich, & A. L. Jaques (1994). Australian Proterozoic mineral systems: Essential ingredients and mappable criteria. *Australian Institute of Mining and Metallurgy Annual Conference*, pp. 109–115.

Yamauchi, H. & Y. Takei (2016). Polycrystal anelasticity at near-solidus temperatures. *Journal of Geophysical Research: Solid Earth*, 121 (11), 7790–7820.

Yoshizawa, K. (2014). Radially anisotropic 3-D shear wave structure of the Australian lithosphere and asthenosphere from multi-mode surface waves. *Physics of the Earth and Planetary Interiors*, 235, 33–48.

Corresponding authors: Correspondence should be addressed to M. Hoggard (mark_hoggard@fas.harvard.edu) and K. Czarnota (karol.czarnota@ga.gov.au).

Acknowledgments: This work is a contribution to the Australian Government's Exploring for the Future program. We are grateful to B. Steinberger, N. Rawlinson, K. Yoshizawa and B. Kennett for sharing lithospheric thickness maps. We thank J.C. Afonso, E. Bastrakov, G. Begg, R. Blewett, A. Bufe, D. Champion, R. Davies, B. Delbridge, A. Dickinson, M. Doublier, R. Fu, S. Goes, A. Gorbatov, B. Hodgin, B. Holtzman, C. Jiang, J. Kingslake, S. Liu, Z. Ma, T. Mackey, P. McFadden, D. McKenzie, D. Müller, P. Nimis, C. O'Malley, E. Powell, K. Priestley, R. Remm, T. Schlegel, D. Schutt, O. Shorttle, R. Skirrow, E. Smith, S. Stephenson, Y. Takei, C.-Y. Tien, N. White, & J. Winterbourne for their assistance and discussions. S. Lebedev provided helpful feedback on an early draft of this work. MH acknowledges support from the National Aeronautics and Space Administration (grant NNX17AE17G) and the Donors of the American Chemical Society Petroleum Research Fund (59062-DNI8). FR acknowledges support from the Schmidt Science Fellows program, in partnership with the Rhodes Trust. KC and DH publish with permission of the CEO of Geoscience Australia. Geoscience Australia eCat ID 132624. MH is indebted to J. Austermann & J. Mitrovica for personal guidance and affording him the freedom to pursue this research.

Author contributions: This relationship was discovered by KC, and the study was conceived and designed by KC and MH. DH, KC, FR and MH compiled deposit databases. LJ collated Australian xenolith data. Thermobarometry and paleogeotherm modelling was done by LJ, FR and MH. FR and MH developed shear-wave to temperature conversion scheme. FR calibrated anelasticity parameterisations. MH generated lithospheric thickness maps, performed statistical tests, made figures and compiled supplementary information. SG, MH and KC investigated implications of rifting continental lithosphere. The paper was written by KC and MH, with guidance from all authors.

Data availability: All data, including digital versions of lithospheric thickness maps and deposit databases, are available in the manuscript or the Supplementary Information, and on the OSF database (*https://osf.io/twksd*).

Competing interests: The authors declare no competing financial interests.

Supplementary Information for

"*Global distribution of sediment-hosted metals controlled by craton edge stability*"

Mark J. Hoggard,[*,1,2] Karol Czarnota,[*,3,4] Fred D. Richards,[1,5]
David L. Huston,[3] A. Lynton Jaques,[4] & Sia Ghelichkhan[4]

*mark_hoggard@fas.harvard.edu; karol.czarnota@ga.gov.au

1. Department of Earth and Planetary Sciences, Harvard University, Cambridge, USA.
2. Lamont-Doherty Earth Observatory, Columbia University, New York, USA.
3. Geoscience Australia, Canberra, Australia.
4. Research School of Earth Sciences, Australian National University, Canberra, Australia.
5. Department of Earth Science and Engineering, Imperial College London, UK.

Contents

Additional Supporting Information (Files uploaded separately)

1. Four global lithospheric thickness maps dervied from SL2013sv, 3D2015-07Sv, CAM2016, and SLNAAFSA in NetCDF, GeoTIFF, and CSV formats.
2. Three Australian lithospheric thickness maps derived from FR12, AuSREM, and Y14 in NetCDF, GeoTIFF, and CSV formats.
3. Database of deposit compilations in Excel spreadsheet.
4. Locations and mineral compositions for xenocryst/xenolith thermobarometry with optimal FITPLOT paleogeotherms in Excel spreadsheet.

1 Summary of selected seismic tomography models

Our LAB maps are based on recent, high-resolution shear wave tomography models that are constructed from large quantities of surface wave data. For the global map, we use vertically polarized shear wave velocity from SL2013sv upper mantle-only model, which represents the isotropic component of their azimuthally anisotropic velocities (Schaeffer & Lebedev, 2013). The model is constructed from a combination of body and surface waves, including fundamental and higher modes. Periods considered are 11–450 s, $\sim 750,000$ seismograms are included, and misfits are calculated between synthetics and the full waveform up to the 18^{th} overtone. Crucially, simultaneous inversion for the crustal model results in minimal smearing of slow crustal velocities down into the upper mantle, thereby allowing us to use more depth slices in our V_S to temperature calibration. Checkerboard resolution tests indicate that features ~ 600 km in diameter at lithospheric depths are generally well resolved. Finer features should be resolvable in regions with dense ray path coverage, such as North America, Europe and southeast Asia.

The SL2013sv model contains only 6 seismometers in Australia, so has limited resolution within this continent. Therefore, we also investigate three regional seismic tomography models to generate high resolution maps for the Australian continent. The main model used throughout this paper is the radially isotropic V_S model FR12 of Fishwick

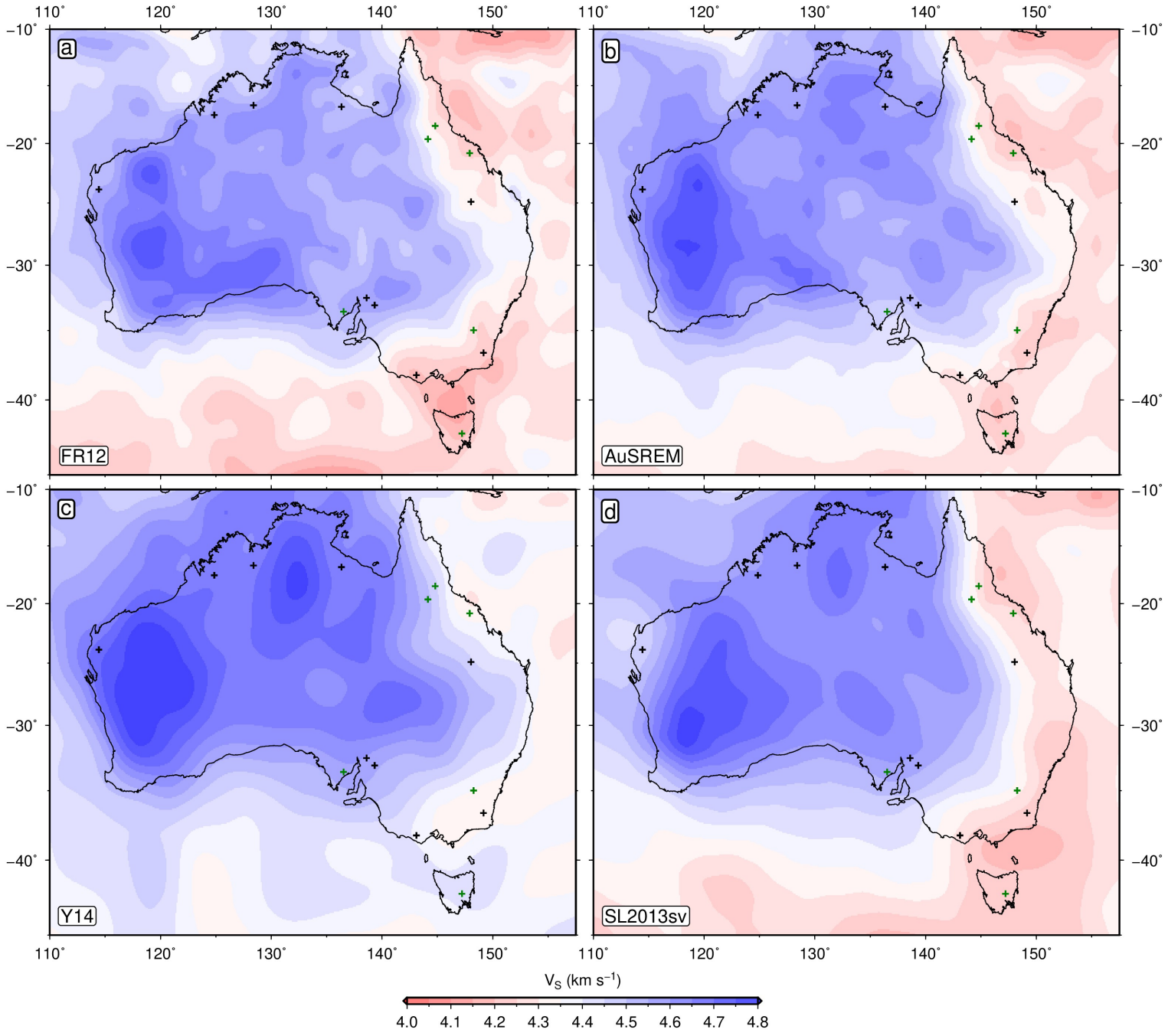

Figure S1: **100 km depth slice through Australian seismic tomography models.** Black/green crosses = paleogeotherms used as constraints/tests in anelasticity calibration. (a) FR12 = regional isotropic V_S (Fishwick & Rawlinson, 2012). (b) AuSREM = regional V_{SV} (Kennett *et al.*, 2013). (c) Y14 = regional V_{SV} (Yoshizawa, 2014). (d) SL2013sv = global V_{SV} (Schaeffer & Lebedev, 2013).

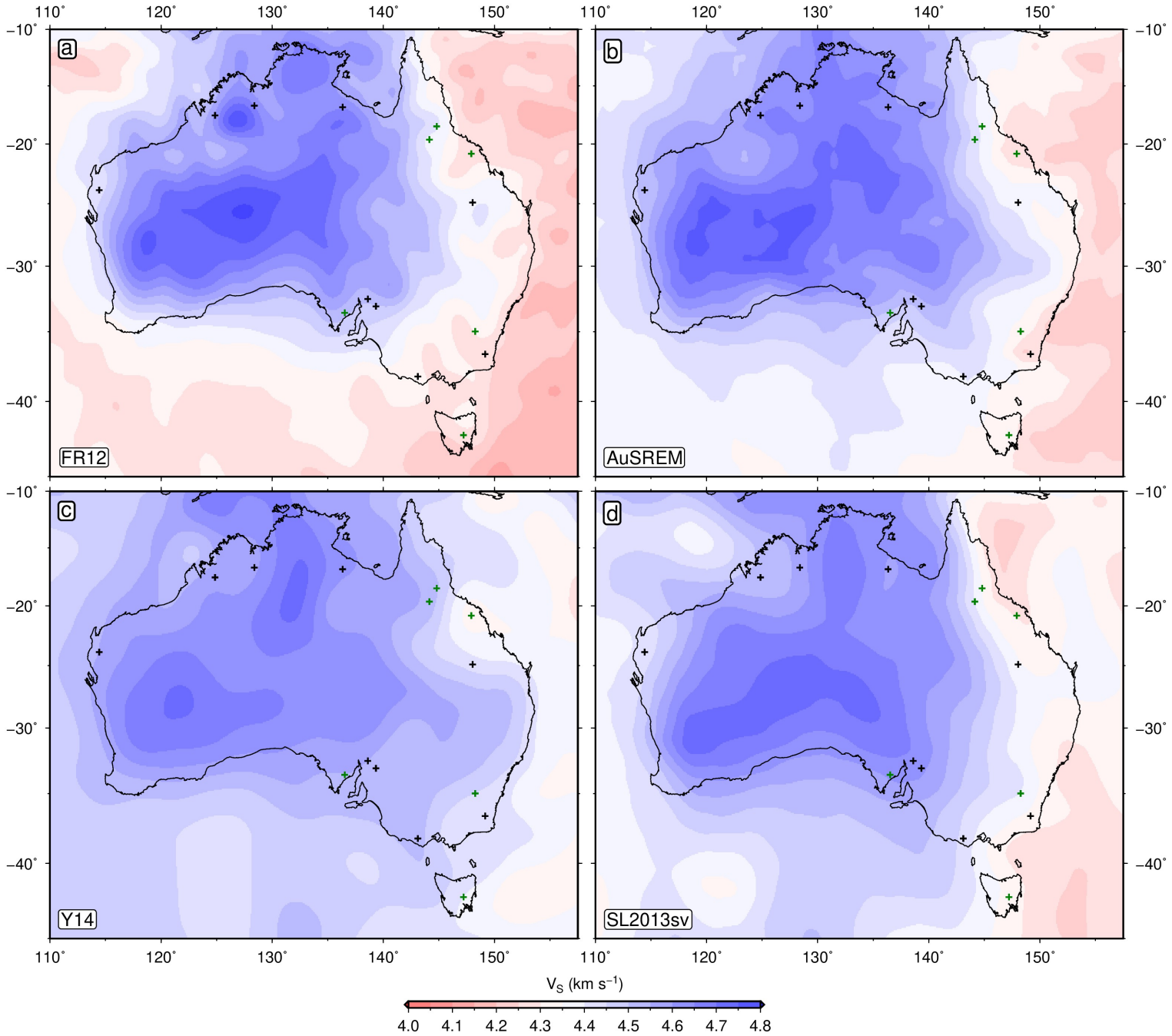

Figure S2: **175 km depth slice through Australian seismic tomography models.** Black/green crosses = paleogeotherms used as constraints/tests in anelasticity calibration. (a) FR12 = regional isotropic V_S (Fishwick & Rawlinson, 2012). (b) AuSREM = regional V_{SV} (Kennett *et al.*, 2013). (c) Y14 = regional V_{SV} (Yoshizawa, 2014). (d) SL2013sv = global V_{SV} (Schaeffer & Lebedev, 2013).

& Rawlinson (2012), which is derived from Rayleigh wave travel times (Fishwick *et al.*, 2008). Periods considered are 50–120 s and the fundamental and first four higher modes have been used where possible, leading to good sensitivity down to $\sim$ 250 km depths. It contains a greater number of source–receiver paths ($> 13,000$) compared to other Australian models. However, it uses an *a priori* crustal model that remains fixed throughout the inversion, resulting in noticeable smearing of crustal velocities into the upper mantle. Checkerboard tests indicate that features $\sim$ 300 km in diameter at lithospheric depths are well resolved.

The second regional model is AuSREM and is a hybrid model constructed by linear combination of several previous studies (Kennett *et al.*, 2013). It combines FR12 with YK04 and AMSAN.19 (Yoshizawa & Kennett, 2004; Fichtner *et al.*, 2010). YK04 is a radially anisotropic Rayleigh wave model using $>$ 8000 ray paths for the fundamental mode and $\sim$ 2000 for the first three higher modes, yielding a maximum period range of 40–150 s. It includes off-great circle and finite frequency effects, but also uses a fixed crustal model. AMSAN.19 is a radially anisotropic, 3D waveform, spectral element model that uses an inversion scheme based on the adjoint approach (Fichtner *et al.*, 2009a,b). Periods considered are 30–200 s and a fixed crustal model is used. Due to the computationally intensive methodology, $\sim 3,000$ waveforms are used in this inversion.

The third and final regional model considered in this study is the radially anisotropic Y14 (Yoshizawa, 2014). It

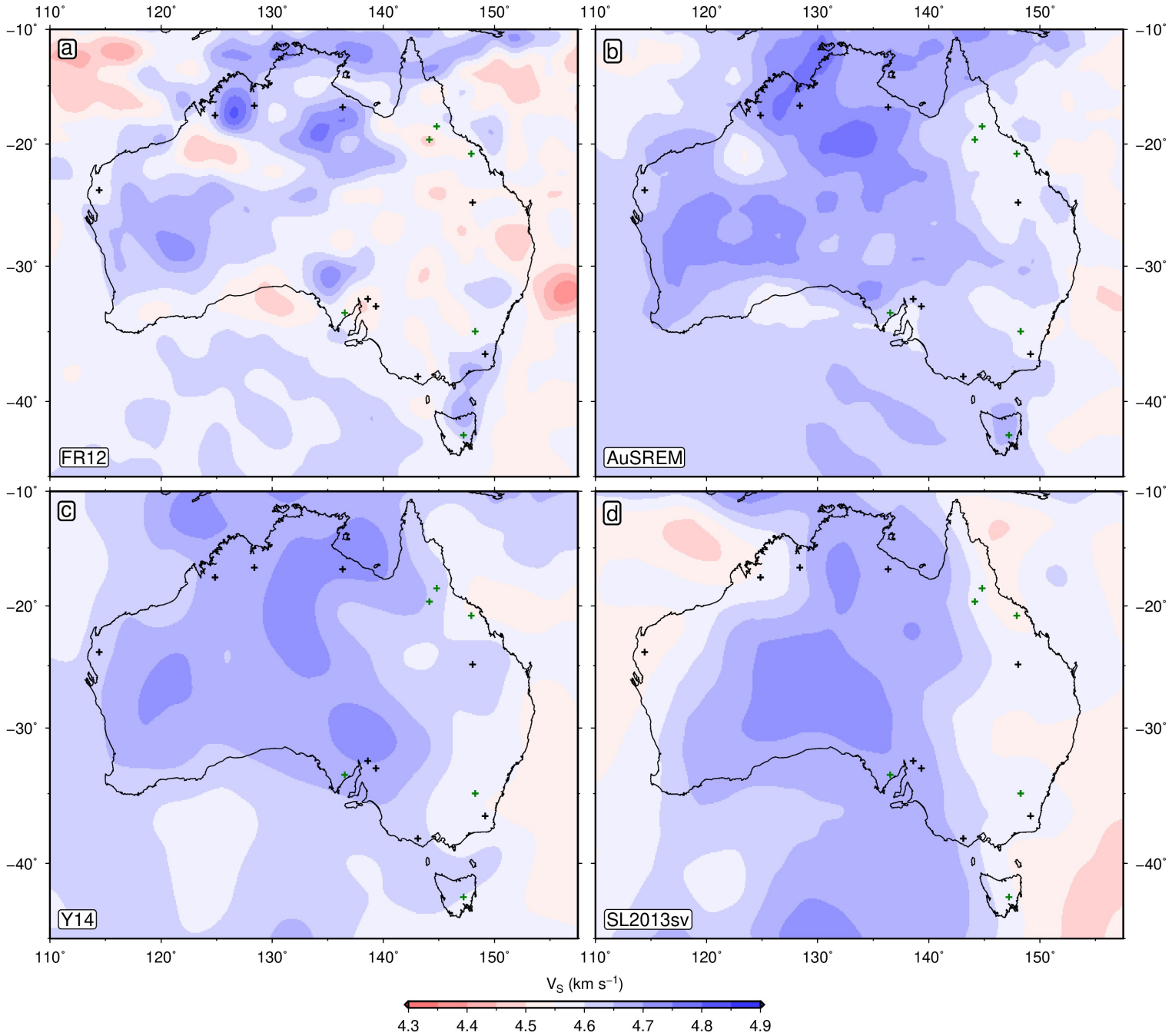

Figure S3: **250 km depth slice through Australian seismic tomography models.** Black/green crosses = paleogeotherms used as constraints/tests in anelasticity calibration. (a) FR12 = regional isotropic V_S (Fishwick & Rawlinson, 2012). (b) AuSREM = regional V_{SV} (Kennett *et al.*, 2013). (c) Y14 = regional V_{SV} (Yoshizawa, 2014). (d) SL2013sv = global V_{SV} (Schaeffer & Lebedev, 2013).

combines Rayleigh waves (8000 fundamental, $\sim$ 2500 higher mode) and Love waves (approximately two-thirds as many) with periods $\sim$ 25–200s, corrected for local crustal structure using a fixed crustal model. It adopts the same three-step inversion procedure as YK04 (Yoshizawa & Kennett, 2004). All three models are plotted alongside the global SL2013sv model in Figures S1, S2 and S3. At any given location within the continent, V_S varies between models by $\sim$ 0.1 km s^{-1}.

2 Parameterisation for anelasticity at seismic frequencies

As introduced in the Methods section, we have adopted the parameterisation of Yamauchi & Takei (2016) to convert shear wave velocity into temperature, which includes effects of anelasticity in pre-melt conditions (temperatures above $\sim 90\%$ of melting temperature). V_S is defined as

$$V_S = \frac{1}{\sqrt{\rho J_1}} \left(\frac{1 + \sqrt{1 + (J_2/J_1)^2}}{2} \right)^{-\frac{1}{2}} \simeq \frac{1}{\sqrt{\rho J_1}} \tag{1}$$

where ρ is the density and J_1 and J_2 represent real and imaginary components of the complex compliance, J^*, which is a quantity describing the sinusoidal strain resulting from the application of a unit sinusoidal stress. J_1 represents the strain amplitude in phase with the driving stress, whilst the J_2 component is $\frac{\pi}{2}$ out of phase, resulting in dissipation. These terms contain a high temperature background absorption band and and an additional low temperature absorption peak, expressed as

$$J_1(\tau'_S) = J_U \left[1 + \frac{A_B[\tau'_S]^{\alpha_B}}{\alpha_B} + \frac{\sqrt{2\pi}}{2} A_P \, \sigma_P \left\{ 1 - \mathrm{erf} \left(\frac{\ln[\tau'_P/\tau'_S]}{\sqrt{2}\sigma_P} \right) \right\} \right] \tag{2}$$

$$J_2(\tau'_S) = J_U \frac{\pi}{2} \left[A_B[\tau'_S]^{\alpha_B} + A_P \exp\left(-\frac{\ln^2[\tau'_P/\tau'_S]}{2\sigma_P^2} \right) \right] + J_U \tau'_S \tag{3}$$

where J_U is the unrelaxed compliance and the third term on the right of Equation (3) represents viscous relaxation. $A_B = 0.664$ and $\alpha_B = 0.38$ represent the amplitude and slope of the high temperature background stress relaxation, whilst A_P and σ_P represent the amplitude and width of the relaxation peak superimposed on the background trend and are given by

$$A_P(T') = \begin{cases} 0.01 & \text{for } T' < 0.91 \\ 0.01 + 0.4(T' - 0.91) & \text{for } 0.91 \leq T' < 0.96 \\ 0.03 & \text{for } 0.96 \leq T' < 1 \\ 0.03 + \beta(\phi_m) & \text{for } T' \geq 1 \end{cases} \tag{4}$$

and

$$\sigma_P(T') = \begin{cases} 4 & \text{for } T' < 0.92 \\ 4 + 37.5(T' - 0.92) & \text{for } 0.92 \leq T' < 1 \\ 7 & \text{for } T' \geq 1 \end{cases} \tag{5}$$

where $T' = \frac{T}{T_s}$ is homologous temperature, with T the temperature and T_s the solidus temperature, both in Kelvin. ϕ_m is the melt fraction and $\beta(\phi_m)$ describes the direct poroelastic effect of melt, which is assumed to be not important within the upper mantle where only very low volumes of melt are expected to be retained ($\sim 0.1\%$; McKenzie, 2000; Takei, 2017). For this case, J_U is the inverse of the unrelaxed shear modulus, $\mu_U(P,T)$, such that

$$J_U(P,T)^{-1} = \mu_U(P,T) = \mu_U^0 + \frac{\partial \mu_U}{\partial T}(T - T_0) + \frac{\partial \mu_U}{\partial P}(P - P_0) \tag{6}$$

where μ_U^0 is the unrelaxed shear modulus at surface pressure-temperature conditions, the differential terms are assumed to be constant and the pressure, P, in GPa is linearly related to the depth, z, in km by $P = \frac{z}{30}$. The normalised shear wave period, τ'_S, in Equations (2) and (3) is equal to $\frac{\tau_S}{2\pi\tau_M}$, where $\tau_M = \frac{\eta}{\mu_U}$ is the normalised Maxwell relaxation timescale and $\tau_S = \frac{z}{1.4}$ is the Rayleigh wave period most sensitive to ambient velocity structure at that depth (Forsyth, 1992). τ'_P represents the normalised shear-wave period associated with the centre of the low temperature relaxation peak, assumed to be 6×10^{-5}. The steady-state diffusion creep viscosity, η, is

$$\eta = \eta_r \left(\frac{d}{d_r} \right)^m \exp\left[\frac{E_a}{R} \left(\frac{1}{T} - \frac{1}{T_r} \right) \right] \exp\left[\frac{V_a}{R} \left(\frac{P}{T} - \frac{P_r}{T_r} \right) \right] A_\eta \tag{7}$$

where d is the grain size, m the grain size exponent (assumed to be 3 for this diffusion creep deformation mechanism), R the gas constant, E_a the activation energy and V_a the activation volume. Subscripts $[X]_r$ refer to reference values, assumed to be $d_r = 1$ mm, $P_r = 1.5$ GPa and $T_r = 1200°$C for the upper mantle. In this study, we make the simplifying assumption that $d = d_r$, which indicates an endmember scenario whereby lateral changes in V_S within the upper mantle arise purely from variations in temperature rather than grain size. It is also possible that grain size may vary significantly within the shallow mantle, but remains poorly constrained (Behn *et al.*, 2009; Dannberg *et al.*, 2017). A_η represents the extra reduction of viscosity due to an increase in E_a near the solidus, expressed as

$$A_\eta(T') = \begin{cases} 1 & \text{for } T' < T'_\eta \\ \exp\left[-\frac{(T'-T'_\eta)}{T'(1-T'_\eta)}\ln(\gamma)\right] & \text{for } T'_\eta \leq T' < 1 \\ \gamma^{-1}\exp(\lambda\phi) & \text{for } T' \geq 1 \end{cases} \tag{8}$$

where $T'_\eta = 0.94$ is the homologous temperature above which the effective activation energy increases beyond its original value and $\gamma = 5$ is the factor of additional viscosity reduction. $\lambda\phi$ describes the direct effect of melt on viscosity, also assumed to be negligible at low melt volumes. The solidus temperature, T_s, is fixed to a value of 1326°C at 50 km equivalent to the dry peridotite solidus of Hirschmann (2000), and linearly increases below this depth according to

$$T_s(z) = 1599 + \frac{\partial T_s}{\partial z}(z - 50) \tag{9}$$

where $\frac{\partial T_s}{\partial z}$ is the solidus gradient. We use a temperature-dependent, compressible density, $\rho(P,T)$, following the approach of Grose & Afonso (2013). First, we define a linear temperature-dependence on thermal expansivity, $\alpha(T)$, such that

$$\alpha(T) = \alpha_0 + \alpha_1 T \tag{10}$$

where $\alpha_0 = 2.832 \times 10^{-5}$ K^{-1} and $\alpha_1 = 0.758 \times 10^{-8}$ K^{-2} are constants calibrated from mineral physics experiments (Bouhifd *et al.*, 1996). To include pressure-dependence, the isothermal volume change, $(V_0/V)_T$ is calculated at each pressure using a Brent minimisation algorithm and the third-order Birch-Murnaghan equation of state

$$P = \frac{3}{2}K_0\left[\left(\frac{V_0}{V}\right)_T^{\frac{7}{3}} - \left(\frac{V_0}{V}\right)_T^{\frac{5}{3}}\right]\left\{1 + \frac{3}{4}(K'_T - 4)\left[\left(\frac{V_0}{V}\right)_T^{\frac{2}{3}} - 1\right]\right\} \tag{11}$$

where $K_0 = 130$ GPa is the bulk modulus at zero pressure and $K'_T = 4.8$ is the pressure-derivative of the isothermal bulk modulus. The associated isothermal density change with pressure, $\rho(P)$, is given by

$$\rho(P) = \rho_0\left(\frac{V_0}{V}\right)_T \tag{12}$$

where $\rho_0 = 3.33$ Mg m^{-3} is the density of mantle at surface pressure and temperature. The effect of pressure on thermal expansivity is included according to

$$\frac{\alpha(P,T)}{\alpha(T)} = \left(\frac{V_0}{V}\right)_T \exp\left\{(\delta_T + 1)\left[\left(\frac{V_0}{V}\right)_T^{-1} - 1\right]\right\} \tag{13}$$

where $\delta_T = 6$ is the Anderson-Grüneisen parameter. Thus, the final density, $\rho(P,T)$, can be calculated using

$$\rho(P,T) = \rho_0\left(\frac{V_0}{V}\right)_T\left\{1 - \left[\frac{\alpha(P,T)}{\alpha(T)}\right]\left[\alpha_0(T - T_0) + \frac{\alpha_1}{2}(T^2 - T_0^2)\right]\right\} \tag{14}$$

where $T_0 = 273$ K is temperature at the surface. In a similar manner to Equation (1), the shear-wave attenuation, Q_S^{-1}, can be defined as

$$Q_S^{-1} = \frac{J_2}{J_1}\left(\frac{1 + \sqrt{1 + (J_2/J_1)^2}}{2}\right)^{-1} \simeq \frac{J_2}{J_1} \tag{15}$$

3 Thermobarometry of mantle xenoliths and xenocrysts

In order to calibrate the anelasticity parameterisation for Australian regional seismic tomography models, a series of local V_S-T-P tie points are required. For temperature estimates, we have assembled a suite of Australian paleogeotherms derived from thermobarometric analysis of mantle xenoliths and xenocrysts from fifteen locations in thick and thin lithosphere (Figure S4; Nickel & Green, 1985; Nimis & Taylor, 2000; Taylor, 1998). As outlined in the methods, the resulting P-T estimates are entered into FITPLOT to generate palaeogeotherms (Figure S5; Mather *et al.*, 2011).

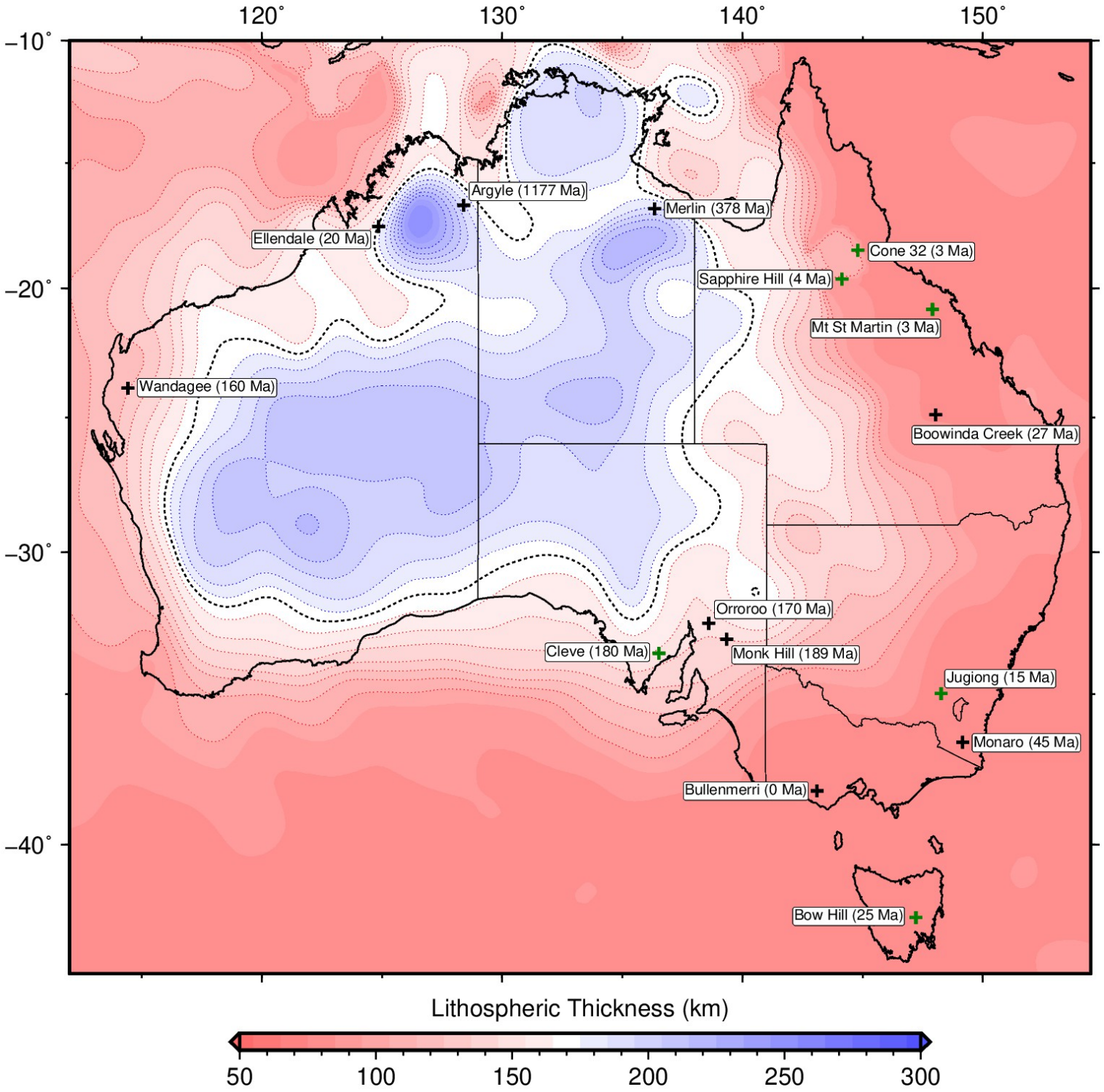

Figure S4: **Location of Australian xenolith and xenocryst suites.** Labels give site name and age (in million years); black crosses = locations used to constrain anelasticity calibration, green crosses = locations used to visually test validity of results; red/blue colours = lithospheric thickness (from Figure 2b), derived from FR12 seismic tomography model (Fishwick & Rawlinson, 2012).

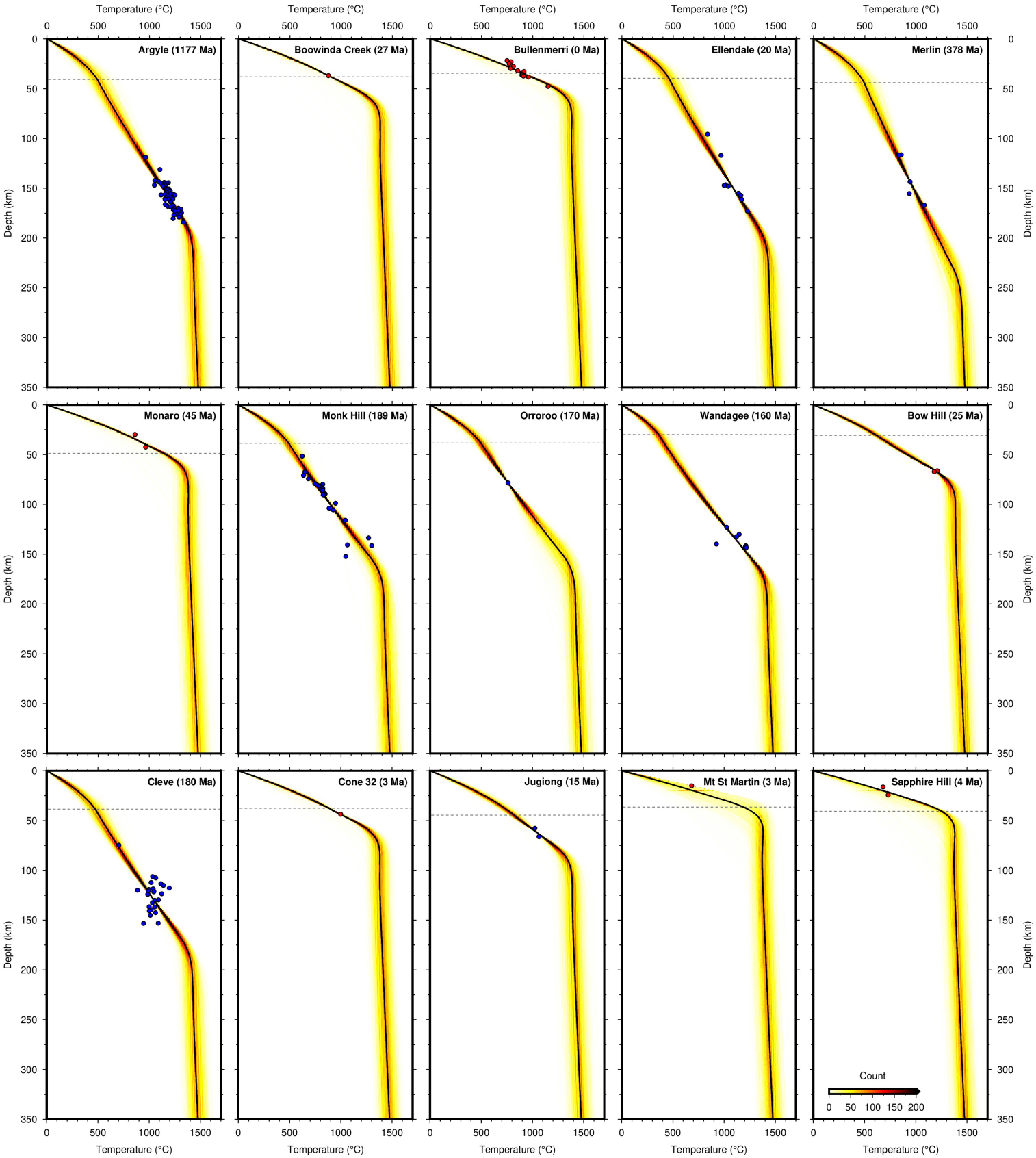

Figure S5: **Australian paleogeotherms derived from xenolith and xenocryst thermobarometry.** Labels give site name and age (in million years) from Figure S4; red circles = P-T estimates derived from multiphase thermobarometry (Nickel & Green, 1985; Taylor, 1998); blue circles = P-T estimates derived from single chrome diopside thermobarometry (Nimis & Taylor, 2000); dashed line = crustal thickness from AusMoho (Kennett *et al.*, 2011); solid line = FITPLOT optimal paleogeotherm (Mather *et al.*, 2011); coloured band = spread of 1000 geotherms from Monte Carlo FITPLOT analysis (Methods).

4 Inverse calibration of anelasticity parameterisation

Anelasticity parameters A_B, α_B, τ'_P, $\beta(\phi_m)$, γ, T'_η and $\lambda\phi$ have been directly constrained by forced oscillation experiments on borneol (Yamauchi & Takei, 2016). However, μ_U^0, $\frac{\partial \mu_U}{\partial T}$, $\frac{\partial \mu_U}{\partial P}$, η_r, E_a, V_a and $T_S(z)$ are material properties that must be independently determined. As outlined in the Methods, we adopt the methodology of Richards *et al.* (2020) to invert a suite of observational constraints. First, the SL2013sv global V_S model is stacked in oceanic regions to calculate average V_S as a function of depth and lithospheric age (Schaeffer & Lebedev, 2013). The age grid and optimal thermal model for a cooling oceanic plate are taken from Richards *et al.* (2018).

Due to the limited vertical resolution of tomographic models (25–50 km), we extract a suite of V_S versus temperature tie-points by taking the average V_S between 75 km and 100 km and cross-plotting it with temperature obtained from the thermal model at 87.5 km, which marks the midpoint of this depth range. A second curve is obtained using the 100 km and 125 km depth slices. Misfit, H_1, between predicted and observed V_S is

$$H_1 = \sqrt{\frac{1}{N}\sum_{i=1}^{N}\frac{1}{M}\sum_{j=1}^{M}\left(\frac{V_{ij}^o - V_{ij}^c}{\sigma_{ij}}\right)^2} \tag{16}$$

where V_{ij}^o are observed shear-wave velocities with associated standard deviation σ_{ij}, V_{ij}^c is the prediction from Equation (1), $M = 76$ is the number of age bins at a given depth and N is the number of depth slices (two in this case). A second suite of tie-points is created by assuming that temperatures are isentropic at depths well below the upper thermal boundary layer. We calculate average V_S as a function of depth over oceanic regions in the global model, and over the whole spatial domain in regional models. Over the depth range 225–400 km, beyond which the resolving power of surface waves drops significantly, these values are combined with an isentrope calculated for a potential temperature of 1333 °C and an adiabatic gradient determined using a reference density of $\rho_0 = 3.3$ Mg m^{-3}, thermal expansivity of $\alpha = 3 \times 10^{-5}$ °C^{-1} and specific heat capacity of $C_P = 1187$ J kg^{-1} °C^{-1}. Misfit for the isentrope, H_2, is

$$H_2 = \sqrt{\frac{1}{N}\sum_{i=1}^{N}\left(\frac{V_i^o - V_i^c}{\sigma_i}\right)^2} \tag{17}$$

It has been observed that over the depth range 150–400 km, both V_S and Q_S^{-1} are relatively consistent for oceanic ages $\geq$ 100 Ma (Adenis *et al.*, 2017). Over this age range, we stack the QRFSI12 attenuation model of Dalton *et al.* (2009), generating a suite of Q_S^{-1} to V_S tie-points as a function of depth. Equations (1) and (15) are coupled such that average temperature is obtained from the average V_S, rather than assuming isentropic temperatures extend up to 150 km. Misfit, H_3, between observed and predicted attenuation is

$$H_3 = \sqrt{\frac{1}{N}\sum_{i=1}^{N}\left(\frac{Q_i^{-1\ o} - Q_i^{-1\ c}}{\sigma_i}\right)^2} \tag{18}$$

We also adopt a bulk diffusion creep viscosity of $\eta_{ref} = 3\times10^{20}$ Pa s for the upper mantle ($\sim$ 100–670 km) obtained from glacial isostatic adjustment studies (Lau *et al.*, 2016), and compare it to the average predicted value for 225–400 km depths obtained from Equation (7). Misfit, H_4, is calculated using

$$H_4 = \sqrt{\frac{1}{\log_{10}[\sigma_i]^2}\left(\left\{\frac{1}{N}\sum_{i=1}^{N}\log_{10}[\eta_i^c]\right\} - \log_{10}[\eta_{ref}]\right)^2} \tag{19}$$

where η_i^c is predicted viscosity and the viscosity uncertainty, σ_i, is assumed to be one order of magnitude. Finally, for calibration of regional tomography models where these global oceanic observations are unavailable, we take the better constrained paleogeotherms derived from thermobarometry on mantle xenoliths. Argyle, Boowinda Creek, Bullenmerri, Ellendale, Merlin, Monaro, Monk Hill, Orroroo and Wandagee are used to directly constrain each anelasticity model. None of these paleogeotherms show evidence of having been perturbed by heating events immediately prior to xenolith entrainment, and we therefore take the calculated P-T conditions to represent ambient mantle conditions immediately

Table 1: Optimal anelasticity parameters for each seismic tomography model.

Model	μ_U^0 (GPa)	$\frac{\partial \mu_U}{\partial T}$ (MPa °C^{-1})	$\frac{\partial \mu_U}{\partial P}$	η_r (Pa s)	E_a (kJ mol^{-1})	V_a (cm^3 mol^{-1})	$\frac{\partial T_s}{\partial z}$ (°C km^{-1})
SL2013sv	78.2	-20.0	2.67	4.45×10^{22}	400	0.092	0.919
CAM2016	78.5	-19.8	2.38	9.99×10^{22}	467	0.012	0.886
3D2015-07Sv	74.1	-16.0	2.29	1.45×10^{22}	300	0.000	0.895
SLNAAFSA[a]	74.8	-16.5	2.47	1.17×10^{21}	104	0.009	1.011
FR12	69.0	-11.7	2.83	1.31×10^{22}	963	0.000	4.500
AuSREM	70.5	-9.6	2.18	9.31×10^{22}	1000	1.831	1.249
Y14	73.3	-10.1	1.67	1.18×10^{21}	100	30.00	4.500

[a] blend of SL2013sv, SL2013NA, AF2019, and SA2019 (Schaeffer & Lebedev, 2013, 2014; Celli *et al.*, 2020a,b).

prior to entrainment. Paleogeotherms derived from three-mineral thermobarometer P-T estimates that are either very shallow (Mt St Martin) or pass only seven of the eight oxide and cation checks (Bow Hill, Cone 32, Sapphire Hill) are considered less robust and only used to visually check results of the conversion, as are diopside-only estimates that have a very narrow depth range (Jugiong) or exhibit large spread (Cleve). For each paleogeotherm, we extract temperatures every 5 km from the base of the thermal boundary layer up to either 125 km in regions with thick lithosphere, or 50 km for those with thin (< 100 km) lithosphere. These variable top depths minimise the impact of potential crustal bleeding artefacts. Extracting $V_S(z)$ values at each paleogeotherm location yields a suite of V_S to temperature tie-points. Misfit, H_5, is calculated from

$$H_5 = \sqrt{\frac{1}{N}\sum_{i=1}^{N}\frac{1}{M}\sum_{j=1}^{M}\left(\frac{V_{ij}^o - V_{ij}^c}{\sigma_{ij}}\right)^2} \tag{20}$$

where M is the number of paleogeotherms, N is the number of tie-points associated with each geotherm and σ_{ij} reflects uncertainty in the V_S measurement, assumed to be a constant 0.1 km s^{-1} which captures typical variations between different tomography models at a given location. Combined misfit, H, is given by

$$H = \frac{w_1 H_1 + w_2 H_2 + w_3 H_3 + w_4 H_4 + w_5 H_5}{w_1 + w_2 + w_3 + w_4 + w_5} \tag{21}$$

where w represents weighting applied to each misfit constraint. H is minimised in two steps. Initially, a parameter sweep is performed to identify the approximate location of the global minimum. μ_U^0 is varied between 69–82 GPa (in increments of 1 GPa), $\frac{\partial \mu}{\partial T}$ between −20 and −8 MPa °C^{-1} (2 MPa °C^{-1} increments), $\frac{\partial \mu}{\partial P}$ between 1.5–2.9 (0.2 increments), η_r between 10^{17}–10^{23} Pa s ($10^{0.5}$ Pa s increments), E_a between 100–1000 kJ mol^{-1} (100 kJ mol^{-1} increments), V_a between 0–30 cm^3 mol^{-1} (2 cm^3 mol^{-1} increments) and $\frac{\partial T_s}{\partial z}$ between 0–4.5 °C km^{-1} (0.25 °C km^{-1} increments). These extrema are chosen to exceed the range of previous parameter estimates obtained from laboratory experiments and other studies (Priestley & McKenzie, 2013; Yamauchi & Takei, 2016; Jain *et al.*, 2018). Secondly, Powell's conjugate gradient algorithm is used to further minimise H using best-fitting parameters from the initial sweep as the starting point (Press *et al.*, 1992). There are two broad sets of parameter trade-offs. The first occurs between parameters controlling anharmonic velocities (μ_U^0, $\frac{\partial \mu}{\partial T}$, and $\frac{\partial \mu_U}{\partial P}$). The second is between parameters controlling anelastic effects (η_r, E_a, V_a, and $\frac{\partial T_s}{\partial z}$). The change in misfit value, H, along each of these trade-offs is minor, such that multiple parameter combinations yield similar conversions between V_S and temperature (Richards *et al.*, 2020). This effect means that whilst the uncertainty on each anelastic parameter may be high for a given tomography model, the resulting mantle temperature structures remain largely consistent.

For calibration of the four global models, we set $w_1 = 10$, $w_2 = 1$, $w_3 = 2$, $w_4 = 2$ and $w_5 = 0$. In the case of SL2013sv, the minimum misfit is $H = 0.568$ and occurs when $\mu_U^0 = 78.2$ GPa, $\frac{\partial \mu_U}{\partial T} = -20.0$ MPa °C^{-1}, $\frac{\partial \mu_U}{\partial P} = 2.67$, $\eta_r = 4.45 \times 10^{22}$ Pa s, $E_a = 400$ kJ mol^{-1}, $V_a = 0.092$ cm^3 mol^{-1} and $\frac{\partial T_s}{\partial z} = 0.919$ °C km^{-1}. These parameters are then used to convert the full three-dimensional V_S model to temperature. Optimal anelasticity parameters for each of the calibrated seismic tomography models are listed in Table 1. For comparison, the optimal misfit for CAM2016 is $H = 0.929$ and for 3D2015-07Sv is $H = 0.887$, which is partly why we prefer the SL2013sv model. Our blended global model SLNAAFSA achieves the lowest optimal misfit of $H = 0.533$.

For Australian regional models, we constrain the calibration using the nine most reliable paleogeotherms. All

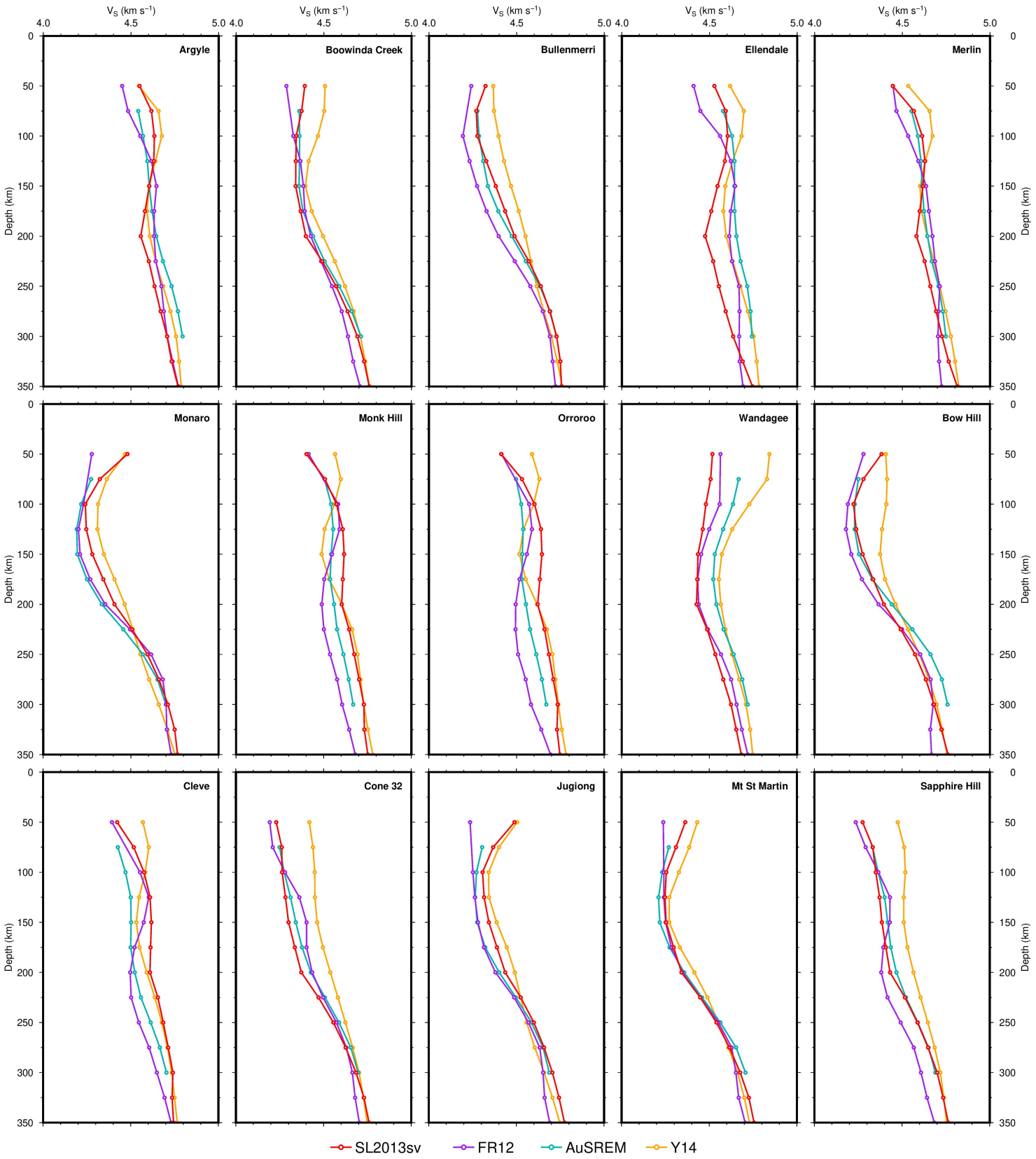

Figure S6: **$\mathbf{V}_S$ as a function of depth at sites of fifteen Australian paleogeotherms.** Labels give site name (locations in Figure S4); red = global SL2013sv modelSchaeffer & Lebedev (2013); purple = regional FR12 modelFishwick & Rawlinson (2012); blue = regional AuSREM modelKennett *et al.* (2013); orange = regional Y14 modelYoshizawa (2014).

weights are set to zero except for $w_2 = 1$ and $w_5 = 10$. The minimum misfit for FR12 is $H = 0.590$ and occurs when $\mu_U^0 = 69.0$ GPa, $\frac{\partial \mu_U}{\partial T} = -11.7$ MPa °C^{-1}, $\frac{\partial \mu_U}{\partial P} = 2.83$, $\eta_r = 1.31 \times 10^{22}$ Pa s, $E_a = 1000$ kJ mol^{-1}, $V_a = 0$ cm^3 mol^{-1} and $\frac{\partial T_s}{\partial z} = 4.50$ °C km^{-1}.

The predicted geotherm from each tomography model is compared to the paleogeotherms in Figures S6 and S7. Note that the global model SL2013sv yields good fits to paleogeotherms away from south Australia (Monk Hill, Orroroo and Cleve), despite being lower resolution than the local models and being calibrated completely independently of this information (red lines in Figure S7). Conversely, regional models often provide a poorer fit to the full range of the paleogeotherms and can exhibit substantial crustal bleeding artefacts at depths shallower than $\sim$ 125 km.

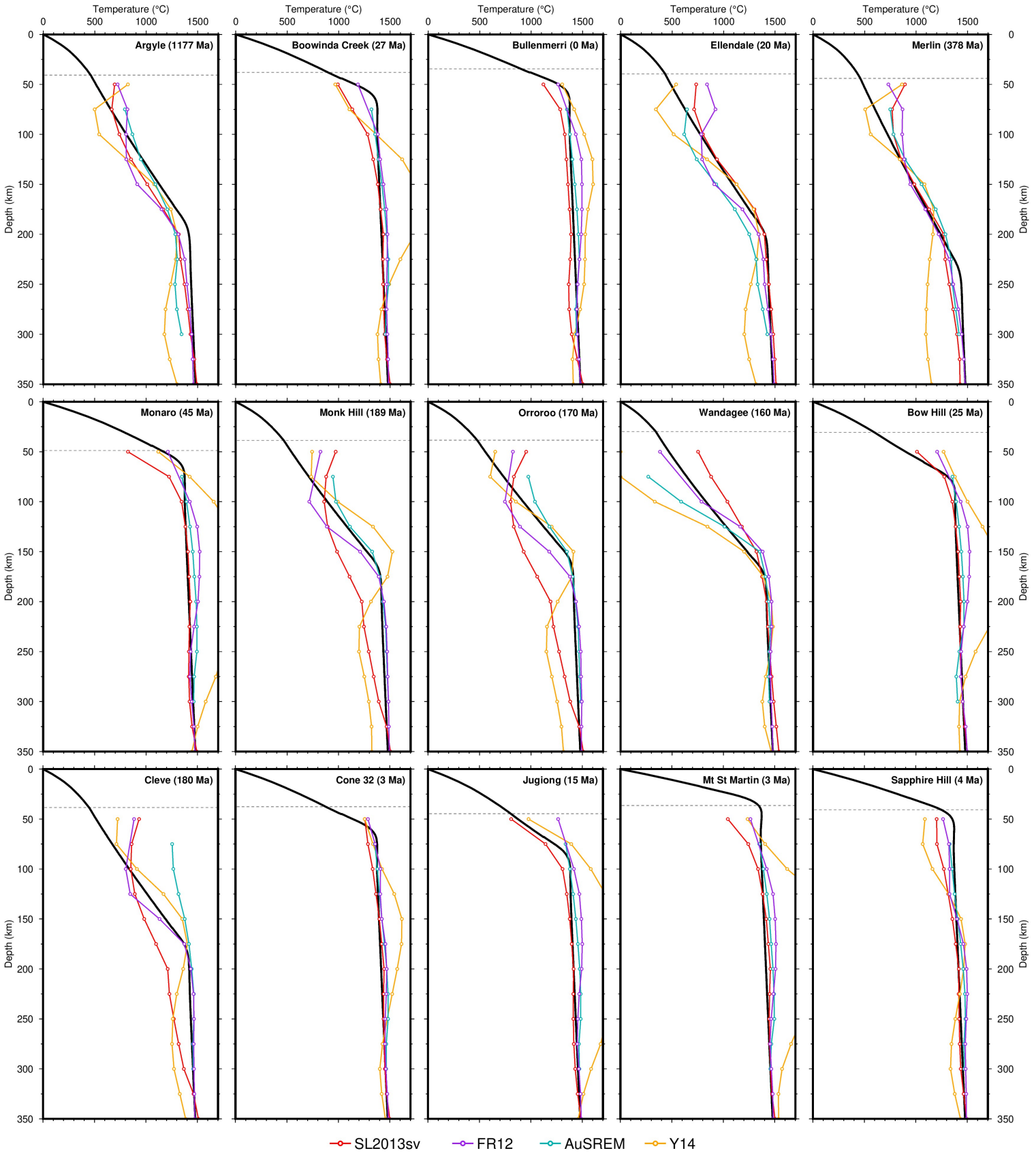

Figure S7: **Calibration of anelasticity parameterisation on Australian paleogeotherms.** Labels give site name and inferred age of paleogeotherms in million years (locations in Figure S4); sites Argyle to Wandagee are used to constrain calibration; sites Bow Hill to Sapphire Hill are used to visually check output; dashed line = crustal thickness from AusMohoKennett *et al.* (2011); solid line = optimal FITPLOT geotherm from Figure S5; purple = regional FR12 modelFishwick & Rawlinson (2012); blue = regional AuSREM modelKennett *et al.* (2013); orange = regional Y14 modelYoshizawa (2014); red = global SL2013sv modelSchaeffer & Lebedev (2013), for comparison, calibrated independently of palaeogeotherm constraints.

It is important to note that of the nine geotherms used to calibrate the anelasticity parameterisation for the regional FR12 model, two are only constrained by a single P-T estimate (Orroroo and Boowinda Creek). We have therefore tested the effect of removing these two sites from the calibration scheme. As Figure S8 shows, there is no discernible effect on the inferred temperature structure. Given this result and that these two samples pass all of the thermobarometry cation and oxide tests, we have chosen to keep Orroroo and Boowinda Creek within the set of nine geotherms used in calibration of local tomography models.

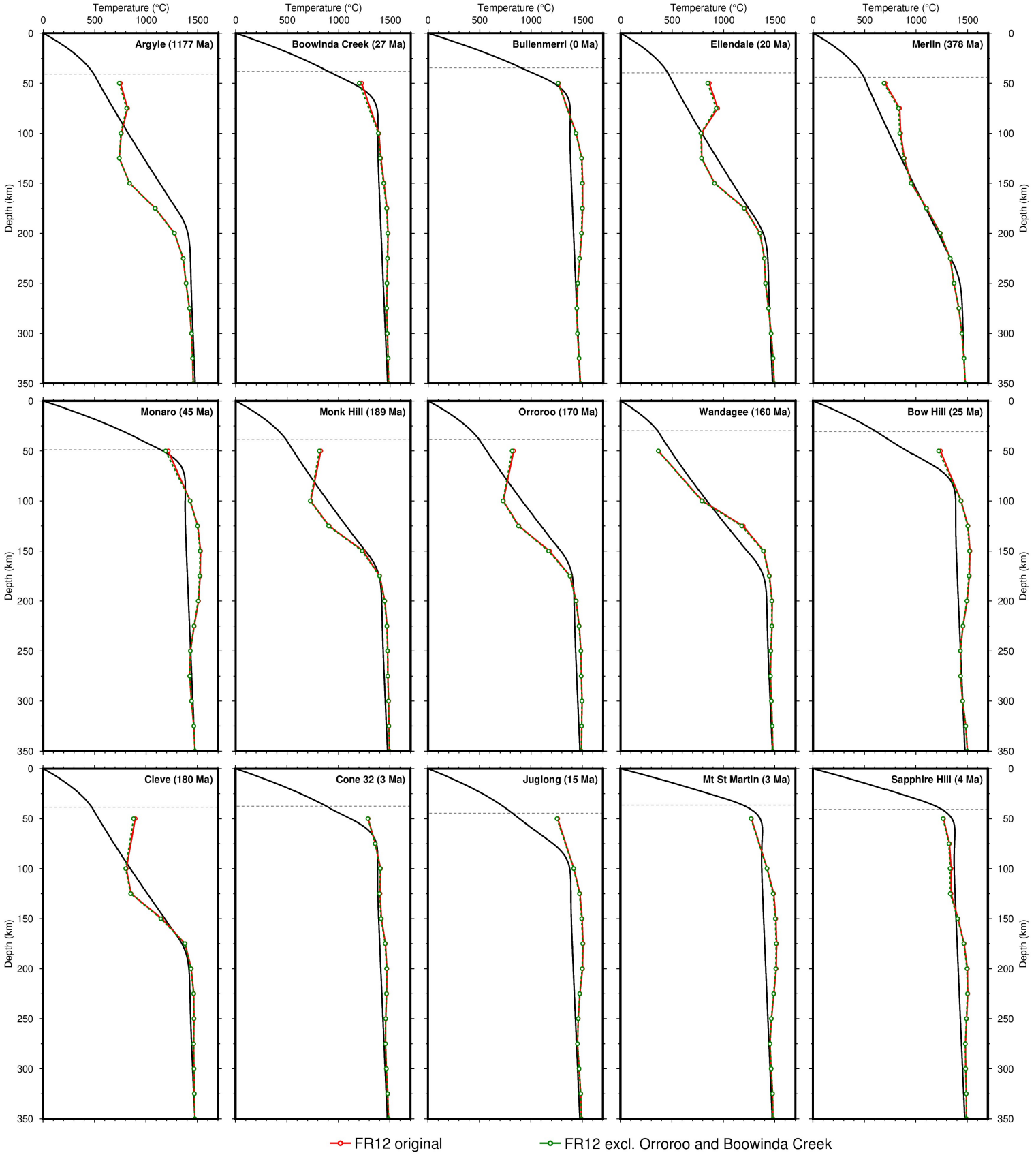

Figure S8: **Calibration of anelasticity parameterisation on Australian paleogeotherms.** Labels give site name and inferred age of paleogeotherms in million years (locations in Figure S4); red line = FR12 model calibrated using sites Argyle through Wandagee; green line = same but excluding Boowinda Creek and Orroroo from the calibrations set.

5 Global lithospheric thickness maps

We have calibrated two other recent surface wave tomography models that each have global coverage (3D2015-07Sv and CAM2016; Debayle *et al.*, 2016; Priestley *et al.*, 2018). In addition, we have generated a higher resolution version of SL2013sv, referred to as SLNAAFSA, by blending in three regional updates including SL2013NA in North America, AF2019 in Africa, and SA2019 in the South Atlantic Ocean (Schaeffer & Lebedev, 2014; Celli *et al.*, 2020a,b). The lithospheric thickness maps for all four global models are visually similar and are shown in the extended data figure of the manuscript and available in ASCII, GeoTIFF and GMT NetCDF formats in the online Supplementary Information. All four exhibit robust relationships with sediment-hosted deposits.

A histogram of global lithospheric thickness derived from the SL2013sv model is shown in Figure S9 and reveals a bi-modal population, with peaks at $\sim$ 90 km and $\sim$ 190 km, separated by a minimum at 150 km. There is also a noticeable drop-off deeper than 200 km, which we attribute to a change in the gradient of V_S with depth in the initial starting profile used to construct the tomography model.

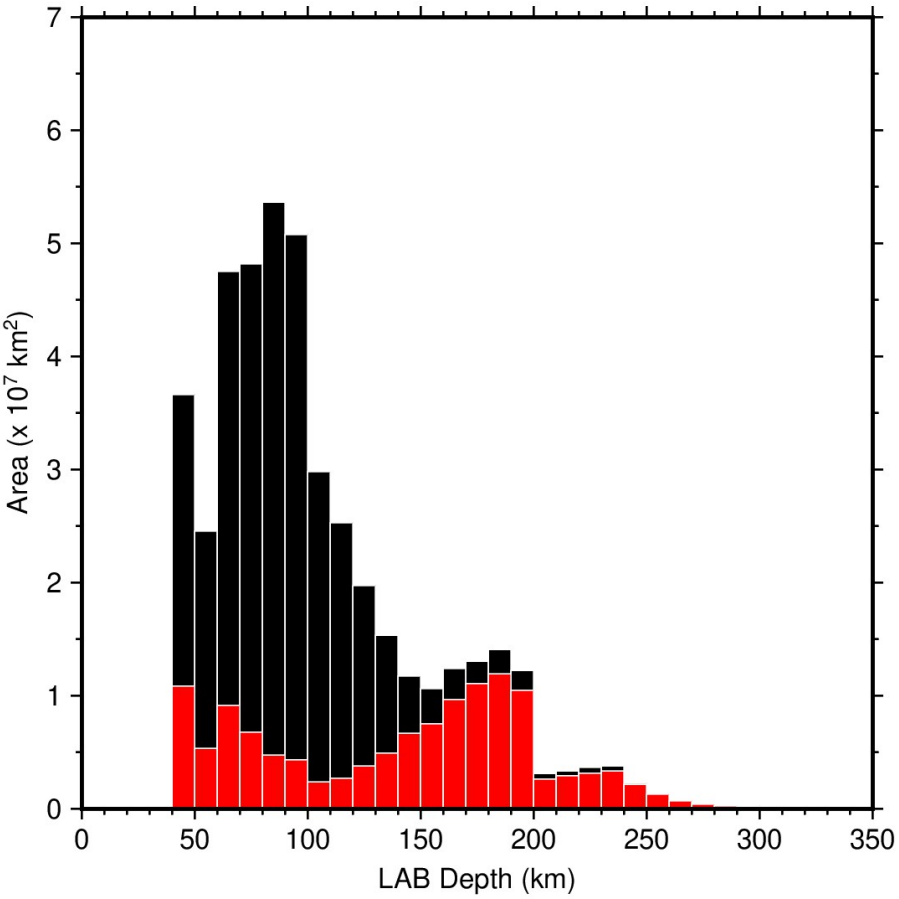

Figure S9: **Area-weighted histogram of global LAB depths.** LAB derived from the SL2013sv tomography model (Schaeffer & Lebedev, 2013); black bars = oceanic regions; red bars = continental regions.

For comparison, we also provide seven previously published global lithosphere-asthenosphere boundary (LAB) maps derived from a mixture of heat flow data, seismic tomography datasets, and potential field data. Interestingly, many giant sediment hosted mineral deposits lie along LAB edges defined by these other studies, testifying to the robustness of the observed relationship.

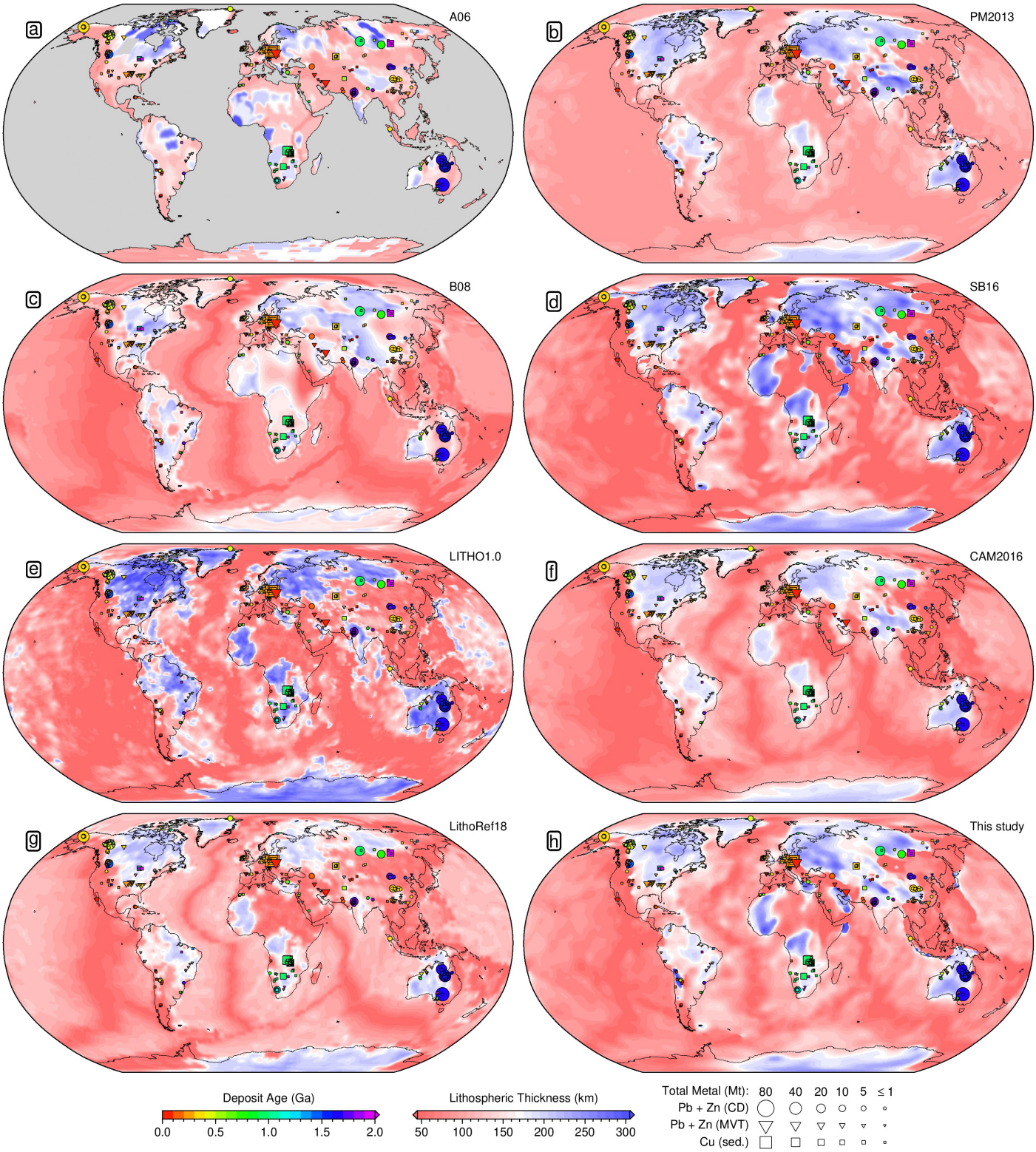

Figure S10: **Previously published global maps of depth to the lithosphere-asthenosphere boundary.** Symbols = sediment-hosted deposit locations; area proportional to estimate of total contained mass of metal (Mt = megatonnes); unknown deposit size given 1 Mt symbol; colour = ore body formation age (billion years); unknown age plotted in grey; circles = clastic-dominated lead-zinc (PbZn-CD); triangles = Mississippi Valley type lead-zinc (PbZn-MVT); squares = sedimentary copper (Cu-sed). (a) LAB derived from surface heat flow measurements (Artemieva, 2006); (b) LAB derived from surface wave tomography (Priestley & McKenzie, 2013); (c) LAB derived from vertical shear-wave travel time anomalies in the continents (Bird *et al.*, 2008); (d) LAB derived by Steinberger & Becker (2018) from SL2013sv tomography model (Schaeffer & Lebedev, 2013); (e) LAB derived from surface wave tomography (Pasyanos *et al.*, 2014); (f) LAB derived from surface wave tomography (Priestley *et al.*, 2018); (g) LAB derived from joint inversion of seismic, potential field and geochemical data (Afonso *et al.*, 2019); (h) LAB derived in this study using SL2013sv tomography model (Schaeffer & Lebedev, 2013).

6 Australian lithospheric thickness maps

For each of the Australian regional seismic tomography models considered in this study, we have individually calibrated and mapped out the LAB in a consistent manner. The resulting maps for Australia are shown in Figure S11, whilst in Figure S12 we compare our preferred FR12 regional model to previously published maps of LAB depth beneath Australia.

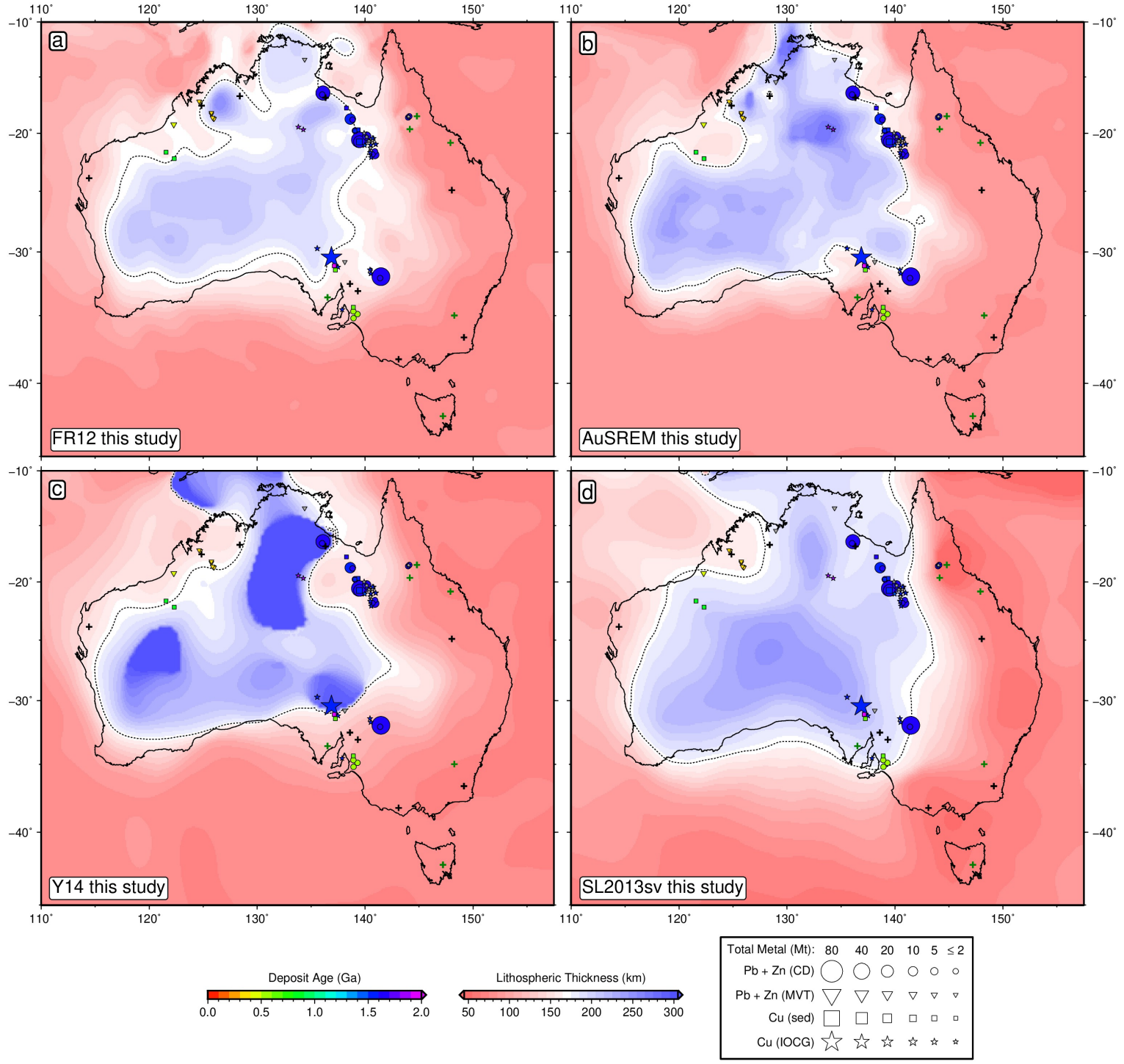

Figure S11: **Depth to lithosphere-asthenosphere boundary from individually calibrated Australian seismic tomography models.** Black contour = 170 km LAB thickness; green/black crosses = paleogeotherms used/unused in anelasticity calibration; other symbols = sediment-hosted deposit locations; area proportional to estimate of total contained mass of metal (Mt = megatonnes); unknown deposit size given 2 Mt symbol; colour = ore body formation age (billion years); unknown age plotted in grey; circles = clastic-dominated lead-zinc (PbZn-CD); triangles = Mississippi Valley type lead-zinc (PbZn-MVT); squares = sedimentary copper (Cu-sed); stars = iron-oxide-copper-gold (IOCG). (a) regional calibration of FR12 (Fishwick & Rawlinson, 2012). (b) regional calibration of AuSREM (Kennett *et al.*, 2013). (c) regional calibration of Y14 (Yoshizawa, 2014). (d) global calibration of SL2013sv (Schaeffer & Lebedev, 2013).

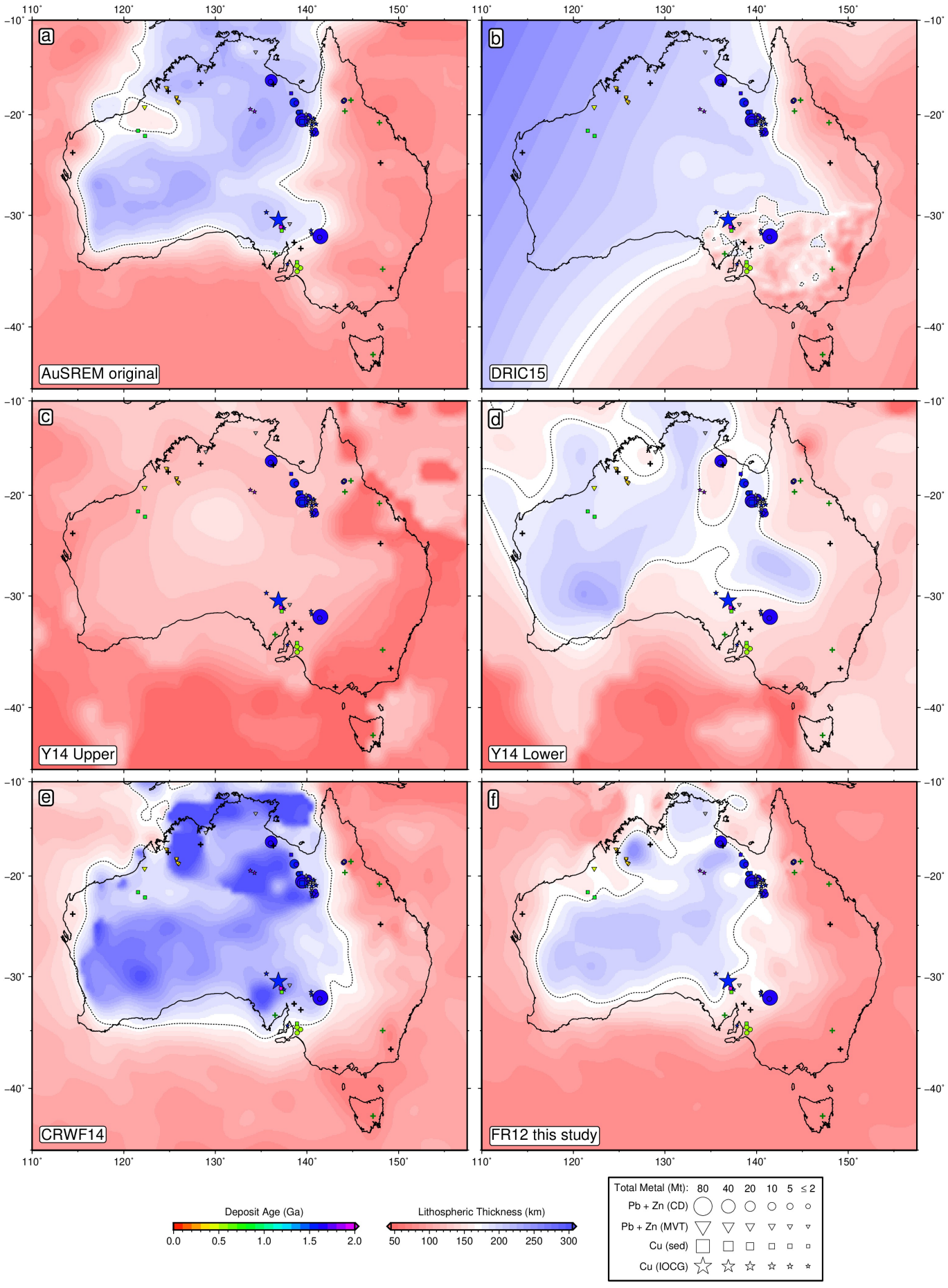

Figure S12: **Depth to lithosphere-asthenosphere boundary beneath Australia from previous studies.** Black contour = 170 km LAB thickness; green/white crosses = paleogeotherms used/unused in anelasticity calibration; other symbols = sediment-hosted deposit locations; area proportional to estimate of total contained mass of metal (Mt = megatonnes); unknown deposit size given 2 Mt symbol; colour = ore body formation age (billion years); unknown age plotted in grey; circles = clastic-dominated lead-zinc (PbZn-CD); triangles = Mississippi Valley type lead-zinc (PbZn-MVT); squares = sedimentary copper (Cu-sed); stars = iron-oxide-copper-gold (IOCG). (a) Original AuSREM (Kennett *et al.*, 2013). (b) DRIC15 (Davies *et al.*, 2015). (c) Upper bound of Y14 (Yoshizawa, 2014). (d) Lower bound of Y14 (Yoshizawa, 2014). (e) CRWF14, derived using FR12 tomography (Czarnota *et al.*, 2014; Fishwick & Rawlinson, 2012). (f) FR12 LAB model generated in this study.

7 Kolmogorov-Smirnov Statistical Tests

In order to test the statistical significance of real deposit locations, test suites of random points on a sphere are generated (Methods). Example test suites of 100, 1000 and 10,000 points are shown in Figure S13.

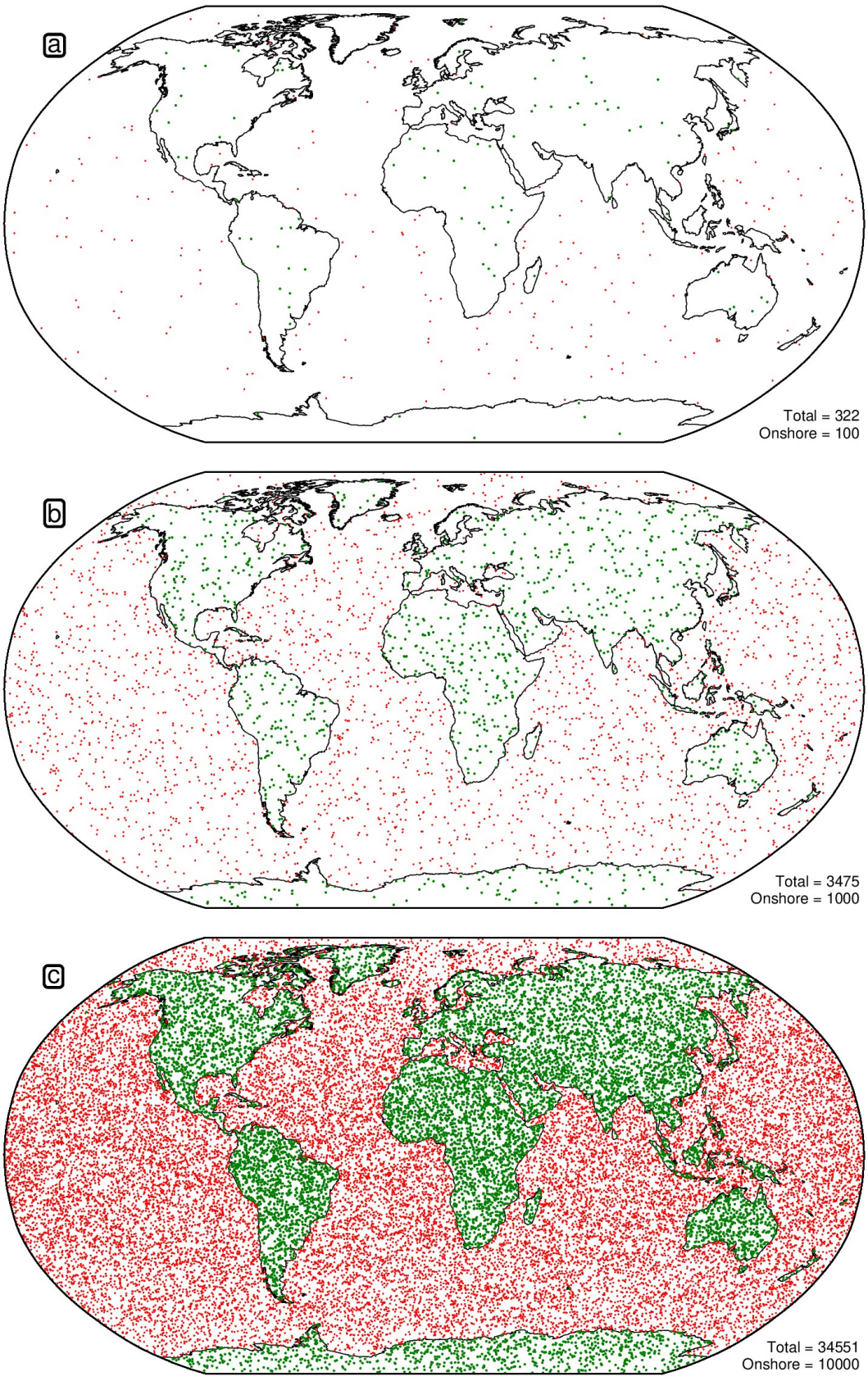

Figure S13: **Distribution of random points on the surface of a sphere.** Green circles = onshore points; red = offshore. (a) Example set of 100 onshore points. (b) Example set of 1000 onshore points. (c) Example set of 10,000 onshore points.

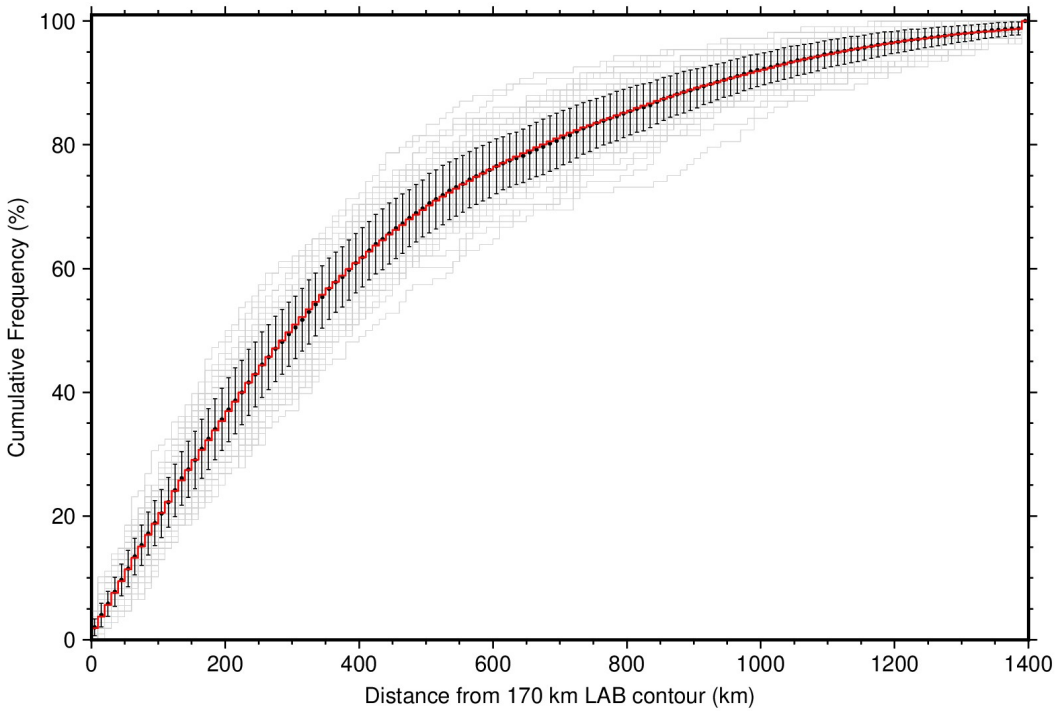

Figure S14: **Cumulative distribution functions for random continental points with distance from the SL2013sv-derived 170 km LAB thickness contour.** Grey lines = 100 CDFs for a set of 109 random points in the continents; black points with error bars = mean and standard deviation of all 100 CDFs within each 10 km bin; red line = CDF for a set of 10,000 random continental points.

For each Kolmogorov-Smirnov test, a number of random points are generated that is equivalent to the number of real deposits of that type (109 for PbZn-CD, 147 for PbZn-MVT and 139 for Cu-sed). Given the low sample size for some of the deposit classes, the distribution of this random set can vary somewhat from the true average distribution of continental locations. We therefore draw a test set in this manner 100 times (Figure S14). These random CDFs are relatively consistent but have some outliers. The D-value and Kolmogorov-Smirnov statistic between each random CDF and the real one is calculated and reported within a histogram (Figure S15).

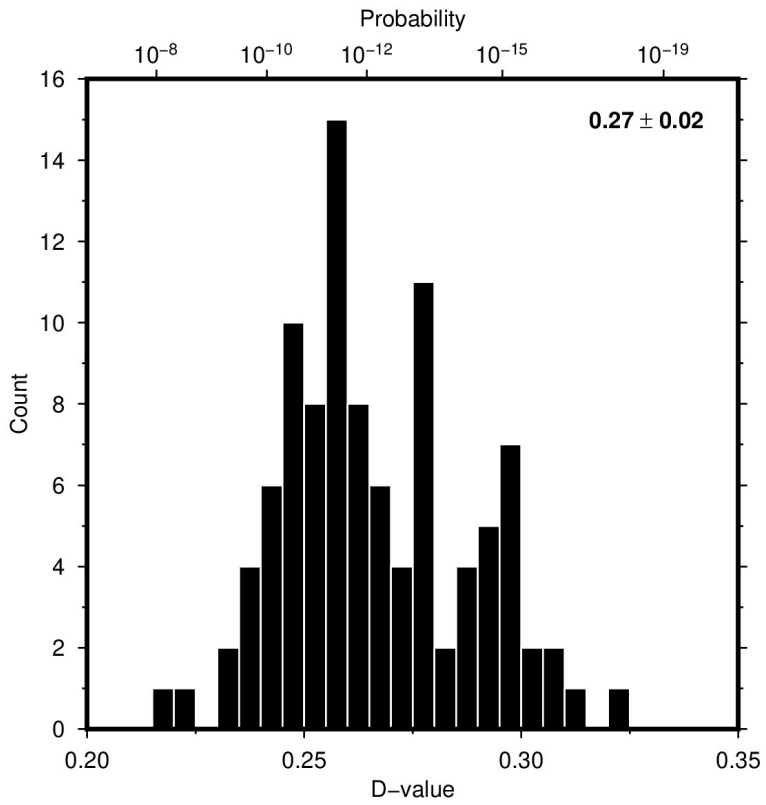

Figure S15: **D-values for all 395 sediment-hosted base metal deposits.** Histogram of D-values for ensemble of 100 random CDFs calculated for each random test set compared with the non-mass-weighted, locally enhanced CDF; inset lists mean and standard deviation of D-values; associated probabilities shown across top.

8 Effect of subducting slabs on deposit statistics

The relationship between seismic wavespeed and temperature results in a tomography model at depths > 150 km imaging cold subducting slabs as fast velocities, in addition to those associated with thick, cold cratonic lithosphere. Thus it is possible that some of the features imaged in our LAB maps are not related to cratonic lithosphere. Examples include features along the Andean, Caribbean, Aleutian, Japanese, Philippines, Indonesian, and eastern Mediterranean subduction zones (Figure S16).

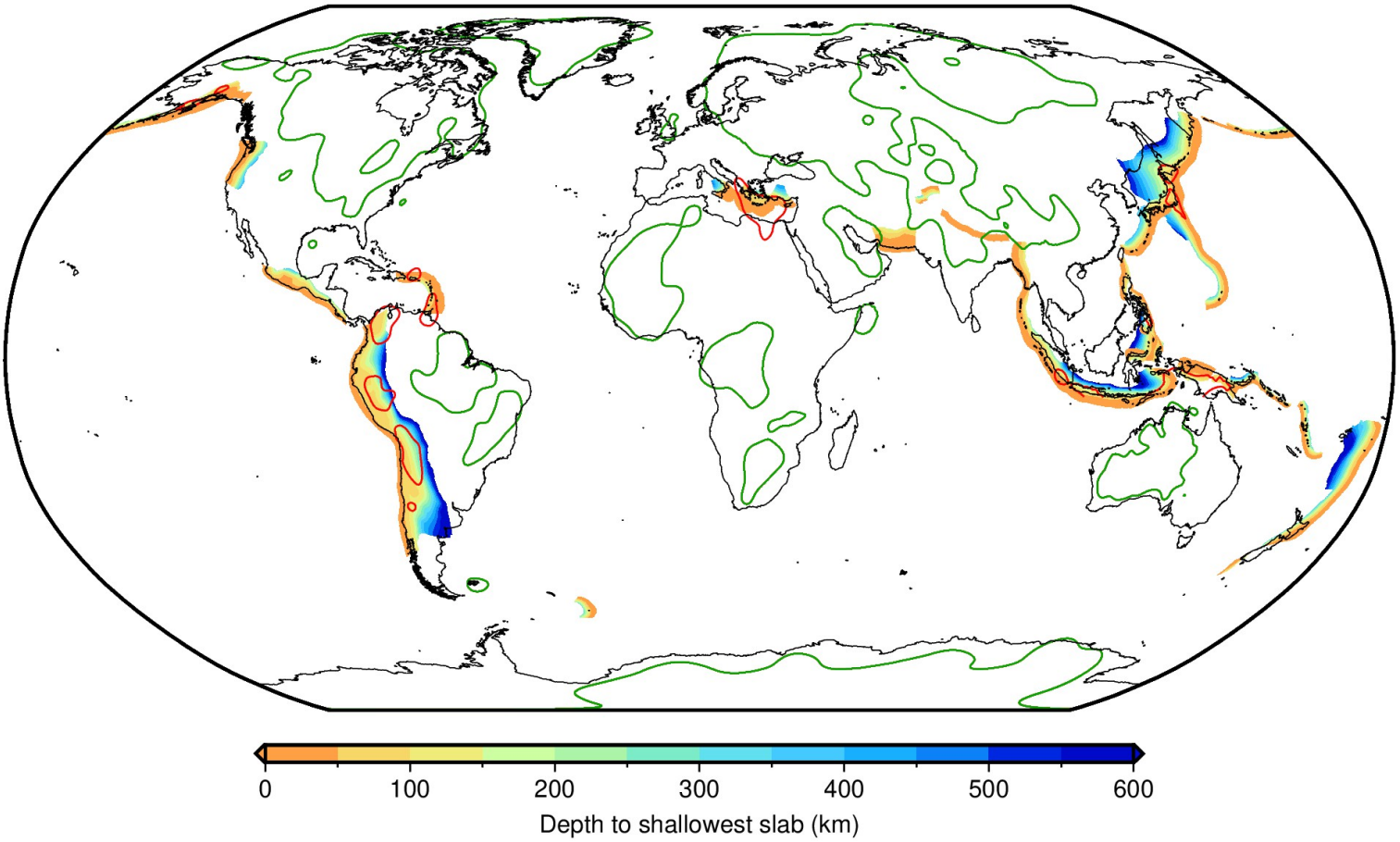

Figure S16: **Subduction zones and areas of thick lithosphere.** Depth of shallowest subducting slabs in the global Slab2 model (Hayes *et al.*, 2018); red lines = 170 km thickness contours in LAB derived from SL2013sv that are potentially related to subducting slabs; green lines = other contours of thick cratonic lithosphere.

None of the giant (> 10 Mt contained metal) sediment-hosted deposits are located at these subduction zones. Nevertheless, some of the smaller deposits can be, such as those in South America, Indonesia and Turkey. We have therefore manually excised 170 km LAB contours that may potentially be related to slabs (red polygons on Figure S16) and repeated the statistical tests.

The CDF for all sediment-hosted base metal deposits is essentially unchanged by this procedure, with ∼ 85% of total metal still found within 200 km of the 170 km contour (Figure S17c). However, the deposit statistics are actually improved, with the D-value increasing from 0.270 ± 0.020 to 0.276 ± 0.022, changing the probability of the relationship occurring by random chance from 1 in 3.35 trillion to 1 in 10.6 trillion. The reason for this is that the reduction in contour extent results in fewer random continental locations falling near the line, with the percentage of total continental area within 200 km of the 170 km LAB thickness contour dropping from 34.3% to 31.0%.

Nevertheless, we have chosen to use the full, non-excised LAB in the paper. Manual identification of potential slabs is a subjective process, with results dependent upon an individual's opinion. Furthermore, it is possible that rifted cratonic fragments may be transported into subduction zone settings (Cook *et al.*, 1999), and thus not all of these subduction zone features are necessarily anomalous. We therefore prefer to keep our testing of the veracity of the observed relationship between LAB thickness and ore deposit locations as objective as possible.

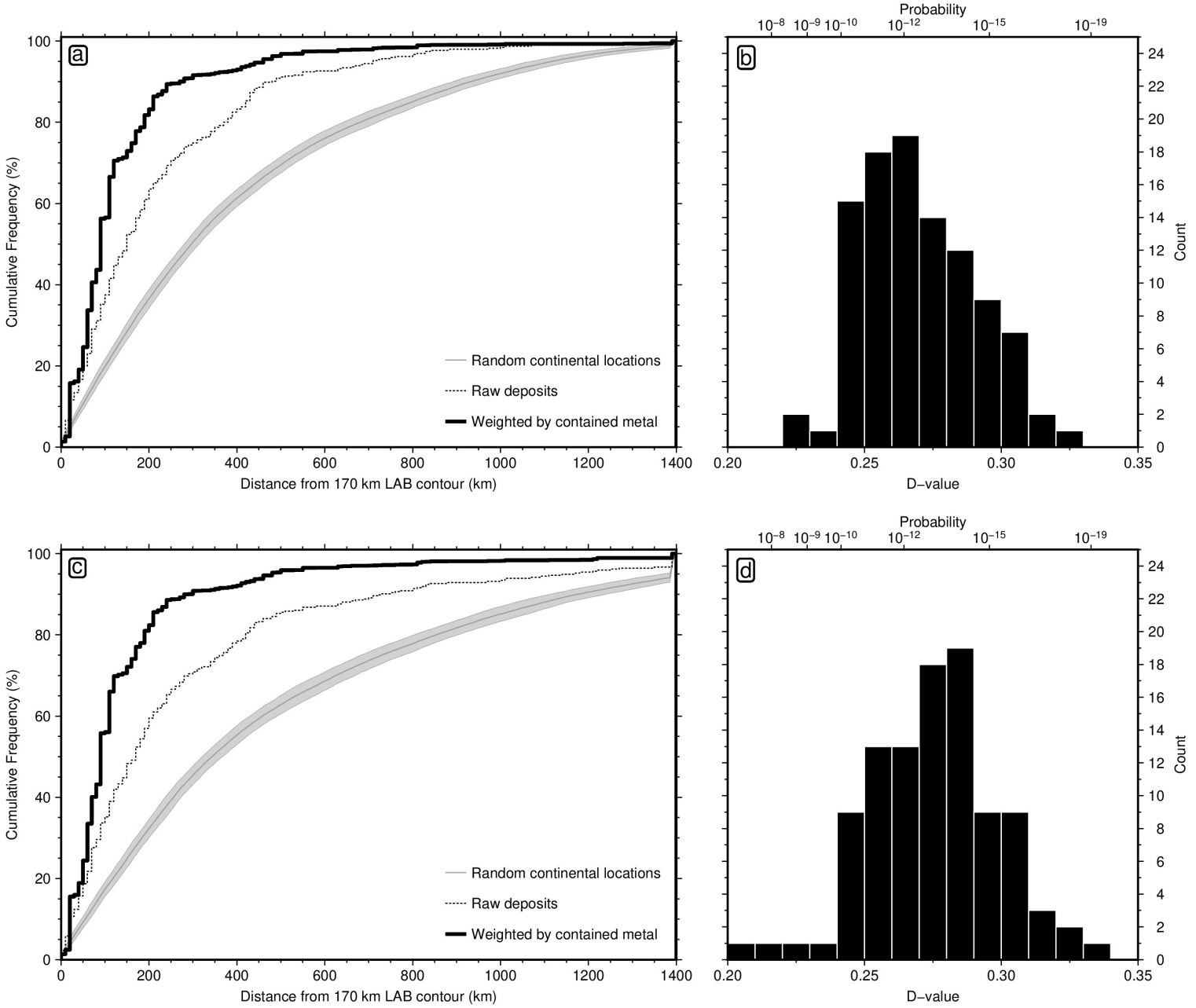

Figure S17: **Effect of removing potentially anomalous features in subduction zone settings on deposit statistics.** (a) Cumulative distribution functions for global sediment-hosted base metals with respect to all 170 km LAB thickness contours (green and red polygons in Figure S16); dotted line = simple count of number of deposits with increasing distance from the 170 km contour; solid black line = deposits weighted by mass of contained metal; grey line/bounds = mean and standard deviation of 100 sets of equivalent number of randomly drawn continental locations. (b) Histogram of D-values for ensemble of 100 random CDFs calculated for a random test set of continental points compared with the non-mass-weighted CDF. (c) and (d) same but using 170 km LAB thickness contours with potentially anomalous subduction zone features removed (only green polygons in Figure S16).

9 Rift modelling of continental lithosphere

To predict the subsidence and basal heat flow of a basin formed by rifting, we model the thermal evolution of the lithosphere during extension. Following McKenzie (1978), we assume thinning occurs by pure shear and that vertical heat transfer dominates. We start with the one-dimensional heat flow equation

$$\rho(T,P,X)C_P(T,X)\frac{\partial T}{\partial t} = \frac{\partial}{\partial z}\left[k(T,P,X)\frac{\partial T}{\partial z}\right] + H(X) \tag{22}$$

where t is time, z is depth, T is temperature, P is pressure, X is composition, ρ is density, C_P is the isobaric specific heat capacity, k is the thermal conductivity, and H is the internal radiogenic heat production.

We solve Equation (22) numerically using an unconditionally stable time- and space-centered Crank-Nicholson finite-difference scheme with a predictor-corrector step (Press *et al.*, 1992). Equation (22) is recast as

$$\begin{aligned} &-k^{n+1}_{j-\frac{1}{2}}T^{n+1}_{j-1} + \left[k^{n+1}_{j-\frac{1}{2}} + k^{n+1}_{j+\frac{1}{2}} + \frac{\left(\Delta z^{n+1}\right)^2}{\Delta t}\left(\rho^n_j C^n_{Pj} + \rho^m_j C^m_{Pj}\right)\right]T^{n+1}_j - k^{n+1}_{j+\frac{1}{2}}T^{n+1}_{j+1} = \\ &\frac{(\Delta z^m)^2}{(\Delta z^n)^2}\left\{k^n_{j-\frac{1}{2}}T^n_{j-1} - \left[k^n_{j-\frac{1}{2}} + k^n_{j+\frac{1}{2}} - \frac{(\Delta z^n)^2}{\Delta t}\left(\rho^n_j C^n_{Pj} + \rho^m_j C^m_{Pj}\right)\right]T^n_j + k^n_{j+\frac{1}{2}}T^n_{j+1} + 2(\Delta z^n)^2 H_j\right\} \end{aligned} \tag{23}$$

where Δt is the time step, Δz is the depth spacing between nodes, and n and j are the time and depth indices, respectively. Equation (23) is solved by tridiagonal elimination (Press *et al.*, 1992). For the initial predictor phase of each time step, $m = n$, whilst in the subsequent corrector phases, $m = n + 1$. We use a Lagrangian reference frame, whereby Δz is initially set to 1 km and updates using the strain rate for each timestep. Timesteps are calculated using a Courant-Friedrichs-Lewy condition with the Courant number set equal to five, such that

$$\Delta t = \min_j\left[\frac{5\Delta z^2 \rho_j C_{Pj}}{k_j}\right] \tag{24}$$

and T^{n+1} typically convergences to within a tolerance of 0.001°C after two corrector phases. The strain rate is constant during rifting and is set by rift duration and a stretching factor, β, which is the ratio of initial to final crustal thickness.

For the crustal layer, we adopt constant thermal parameters of $C_P = 750$ J kg^{-1} K^{-1} and $k = 2.5$ W m^{-1} K^{-1}. Crustal density is $\rho = 2800$ kg m^{-3} for regular continental lithosphere and is $\rho = 2900$ kg m^{-3} for cratonic lithosphere, in accordance with expectations for an increase in bulk density with increasing crustal thickness (Christensen & Mooney, 1995). For the mantle, we use temperature and pressure dependent parameters that have been derived from experimental data on olivine. Density is calcuated according to Equation (14), with $\rho_\circ = 3330$ kg m^{-3} in regular lithospheric mantle, and 3280 kg m^{-3} in cratonic lithosphere, which has been chemically depleted by melt extraction. The effect of pressure on heat capacity is minimal throughout the upper $\sim$ 300 km of the mantle (Hofmeister, 2007). We therefore use the Korenaga & Korenaga (2016) purely temperature-dependent parameteristaion

$$C_P(T) = c_0 - \frac{c_1}{\sqrt{T}} - \frac{c_2}{T^3} \tag{25}$$

where $c_0 = 1580$, $c_1 = 12230$ and $c_2 = 1694 \times 10^6$. Mantle conductivity is pressure- and temperature-dependent and includes contributions from both phonons (lattice conductivity, k_{lat}) and photons (radiative conductivity, k_{rad}, which is poorly constrained by experimental data). Total conductivity is expressed using

$$k(T,P) = \kappa_{lat}(T)\rho(T,P)C_P(T)\exp\left[\frac{\partial ln\,(k)}{\partial P}P\right] + k_{rad}(T) \tag{26}$$

where $\frac{\partial ln(k)}{\partial P} = 0.05$ W m^{-1} K^{-1} GPa^{-1} (Hofmeister, 2007). $\kappa_{lat}(T)$ is the temperature-dependent lattice diffusivity and is given by

$$\kappa_{lat}(T) = \left[\kappa_0 + \kappa_1 \exp\left(-\frac{T - T_0}{\kappa_2}\right) + \kappa_3 \exp\left(-\frac{T - T_0}{\kappa_4}\right)\right] \times 10^{-6} \tag{27}$$

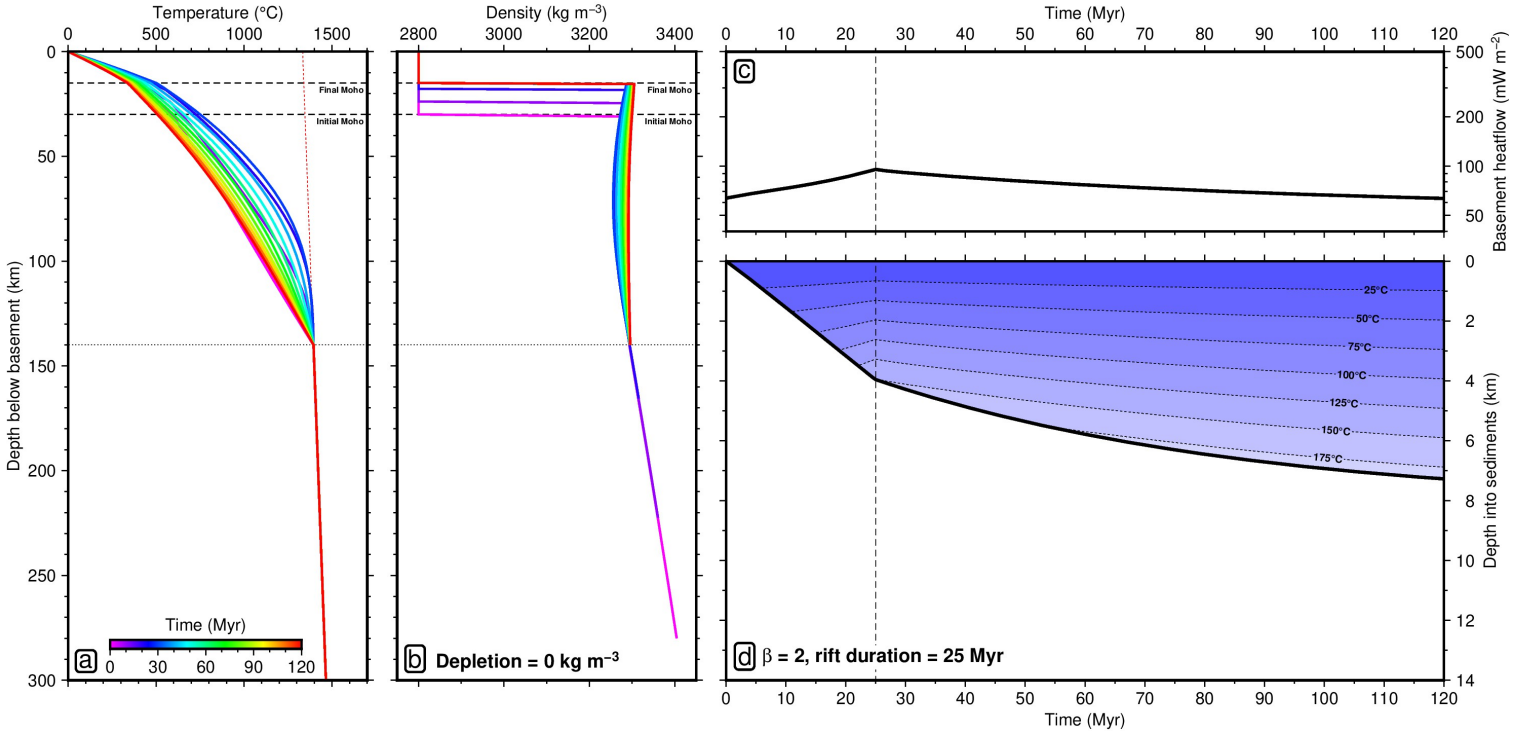

Figure S18: **Regular continental lithosphere with $\beta = 2$ and 25 Myr rift duration.** (a) Thermal evolution of the lithosphere. (b) Density evolution of the lithosphere. (c) Heat flow through the top of the crust. (d) Sediment-loaded subsidence of the basin, coloured by temperature structure of the sedimentary pile.

where $\kappa_0 = 0.565$, $\kappa_1 = 0.67$, $\kappa_2 = 590$, $\kappa_3 = 1.4$, $\kappa_4 = 135$, and $T_0 = 273$ K (Pertermann & Hofmeister, 2006). The parameterisation for k_{rad} is taken from Grose & Afonso (2013), based on earlier work by Hofmeister (2005), and is given by

$$k_{rad}(T) = A_r \exp\left[-\frac{(T - T_A)^2}{2x_A^2}\right] + B_r \exp\left[-\frac{(T - T_B)^2}{2x_B^2}\right] \tag{28}$$

where

$$A_r = 1.8\left[1 - \exp\left(\frac{-d^{1.3}}{0.15}\right)\right] - \left[1 - \exp\left(\frac{-\sqrt{d}}{5}\right)\right] \tag{29}$$

$$B_r = 11.7 \exp\left(\frac{-d}{0.159}\right) + 6 \exp\left(\frac{-d^3}{10}\right) \tag{30}$$

$$T_A = 490 + 1850 \exp\left(\frac{-d^{0.315}}{0.825}\right) + 875 \exp\left(\frac{-d}{0.18}\right) \tag{31}$$

$$T_B = 2700 + 9000 \exp\left(\frac{-\sqrt{d}}{0.205}\right) \tag{32}$$

$$x_A = 167.5 + 505 \exp\left(\frac{-\sqrt{d}}{0.85}\right) \tag{33}$$

$$x_B = 465 + 1700 \exp\left(\frac{-d^{0.94}}{0.175}\right) \tag{34}$$

and d is the grain size in centimeters, assumed to be $d = 0.5$ cm.

For the finite difference scheme boundary conditions, we fix the surface node to have $T_0^n = T_0 = 273$ K, whilst the initial basal node has an adiabatic value of $(1606 + 0.44z)$ K, equivalent to a potential temperature of 1333°C. In cratonic areas, the lithospheric mantle is thicker than standard continental lithosphere and has been chemically depleted. During the rift phase, this basal node shallows through time and non-depleted asthenospheric mantle rises adiabatically beneath. If this basal node becomes shallower than the initial thickness of standard continental lithosphere, we update the index at which this lower boundary condition is applied to the node closest to this standard depth. Heat flow

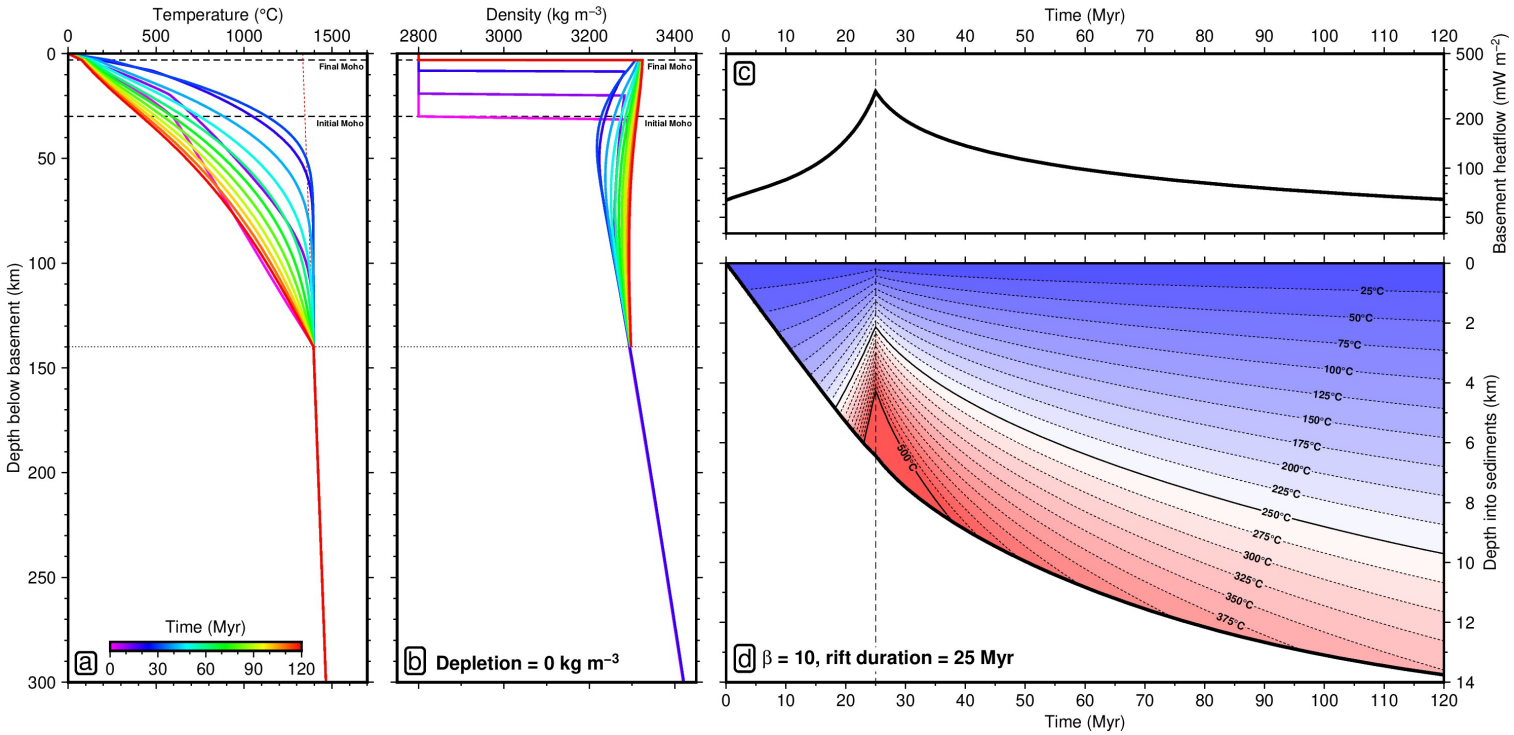

Figure S19: **Regular continental lithosphere with $\beta = 10$ and 25 Myr rift duration.** (a) Thermal evolution of the lithosphere. (b) Density evolution of the lithosphere. (c) Heat flow through the top of the crust. (d) Sediment-loaded subsidence of the basin, coloured by temperature structure of the sedimentary pile.

through the top of the crust, $Q_H(t)$, and subsidence, $S(t)$, are calculated according to

$$Q_H^n = \frac{(k_0^n + k_1^n)(T_1^n - T_0^n)}{2\Delta z} \tag{35}$$

$$S^n = \frac{\sum_j \rho_j^n \Delta z^n - \sum_j^{\mathrm{J}} \rho_j^0 \Delta z^0}{\rho_{\mathrm{J}} - \rho_{infill}} \tag{36}$$

where J is the index of the node at the depth of the original lithospheric thickness, ρ_{J} is the adiabatic density of standard mantle at this depth, and $\rho_{infill} = 2200$ kg m^{-3} is the density of material that infills the basin, which we assume to be

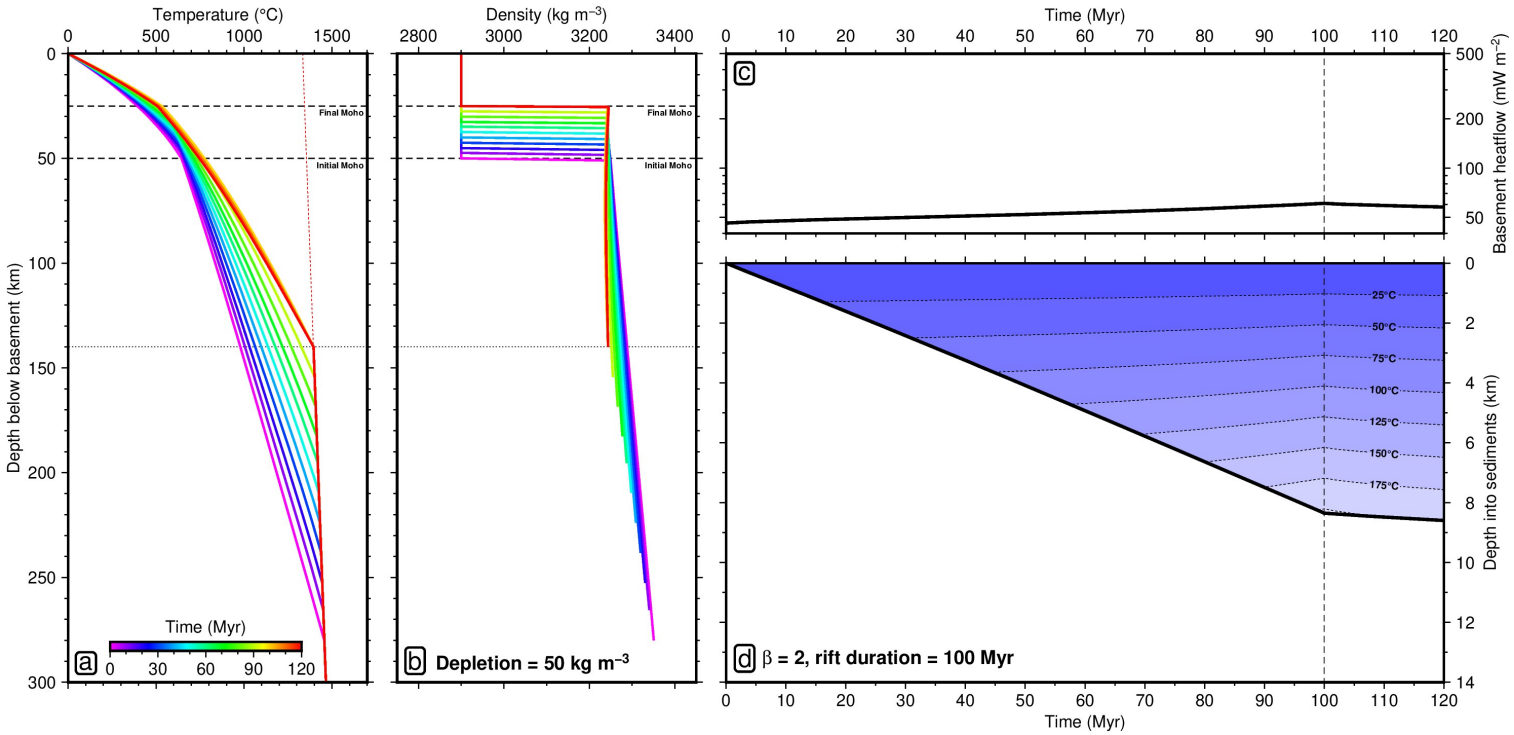

Figure S20: **Cratonic continental lithosphere with $\beta = 2$ and 100 Myr rift duration.** (a) Thermal evolution of the lithosphere. (b) Density evolution of the lithosphere. (c) Heat flow through the top of the crust. (d) Sediment-loaded subsidence of the basin, coloured by temperature structure of the sedimentary pile.

sediments. Figures S18–S20 show the results of thermal modelling of rifting continental lithosphere on basin subsidence and temperature of the sedimentary pile.

10 Regional deposit maps

Regional maps of Africa, Europe, Asia, Australia, Antarctica, North and South America are provided, showing the global SL2013sv LAB model (except for Australia) with known sediment-hosted base metal deposits.

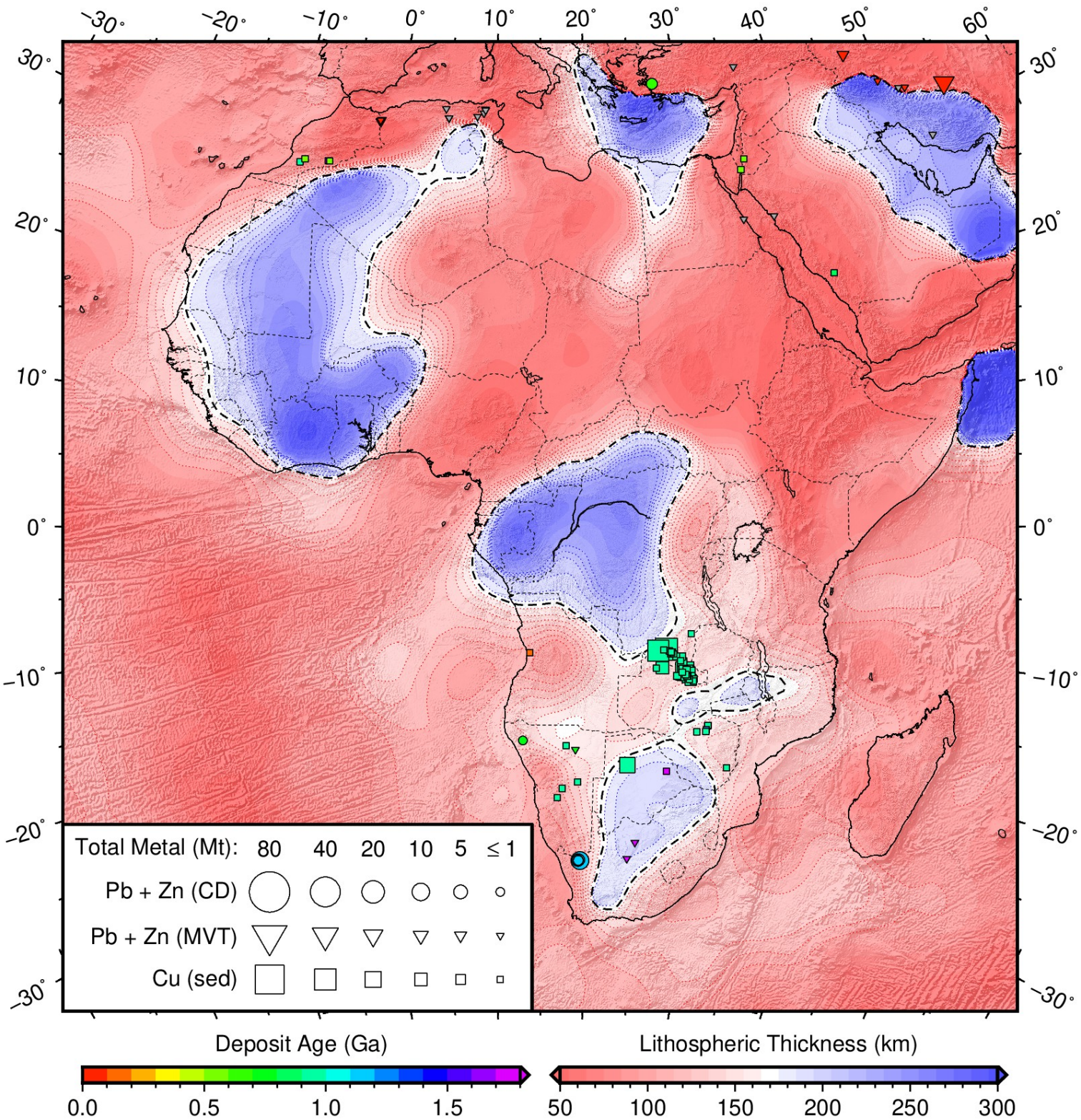

Figure S21: **Distribution of sediment-hosted base metal deposits as a function of lithospheric thickness in Africa.** Global LAB derived from SL2013sv tomography model using a calibrated anelasticity parameterisation (Schaeffer & Lebedev, 2013; Yamauchi & Takei, 2016); black dashed contour = 170 km LAB thickness; symbols = deposit locations; area proportional to estimate of total contained mass of metal (Mt = megatonnes); unknown deposit size given 1 Mt symbol; colour = ore body formation age (billion years); unknown age plotted in grey; circles = clastic-dominated lead-zinc (PbZn-CD); triangles = Mississippi Valley type lead-zinc (PbZn-MVT); squares = sedimentary copper (Cu-sed).

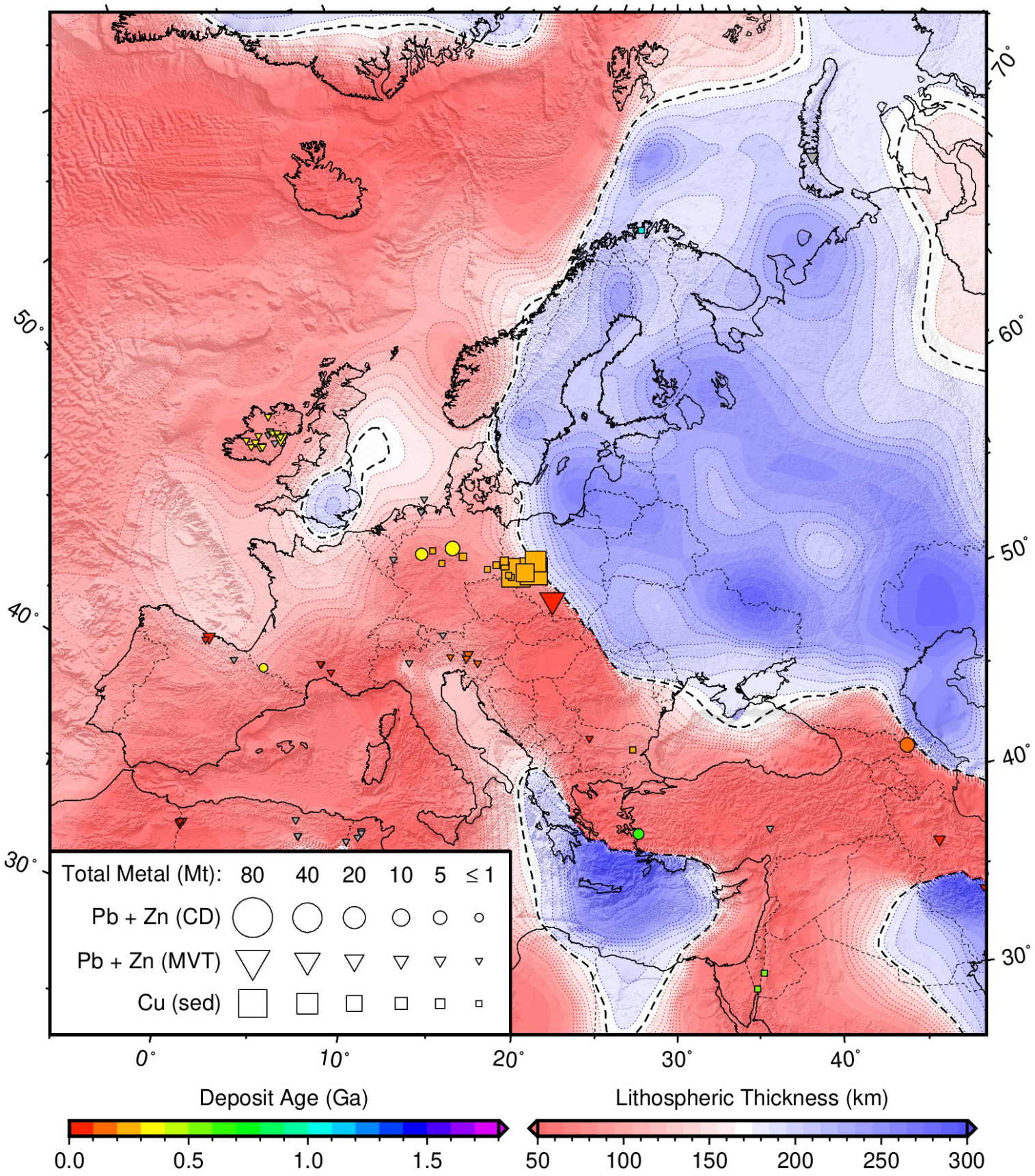

Figure S22: **Distribution of sediment-hosted base metal deposits as a function of lithospheric thickness in Europe.** Global LAB derived from SL2013sv tomography model using a calibrated anelasticity parameterisation (Schaeffer & Lebedev, 2013; Yamauchi & Takei, 2016); black dashed contour = 170 km LAB thickness; symbols = deposit locations; area proportional to estimate of total contained mass of metal (Mt = megatonnes); unknown deposit size given 1 Mt symbol; colour = ore body formation age (billion years); unknown age plotted in grey; circles = clastic-dominated lead-zinc (PbZn-CD); triangles = Mississippi Valley type lead-zinc (PbZn-MVT); squares = sedimentary copper (Cu-sed).

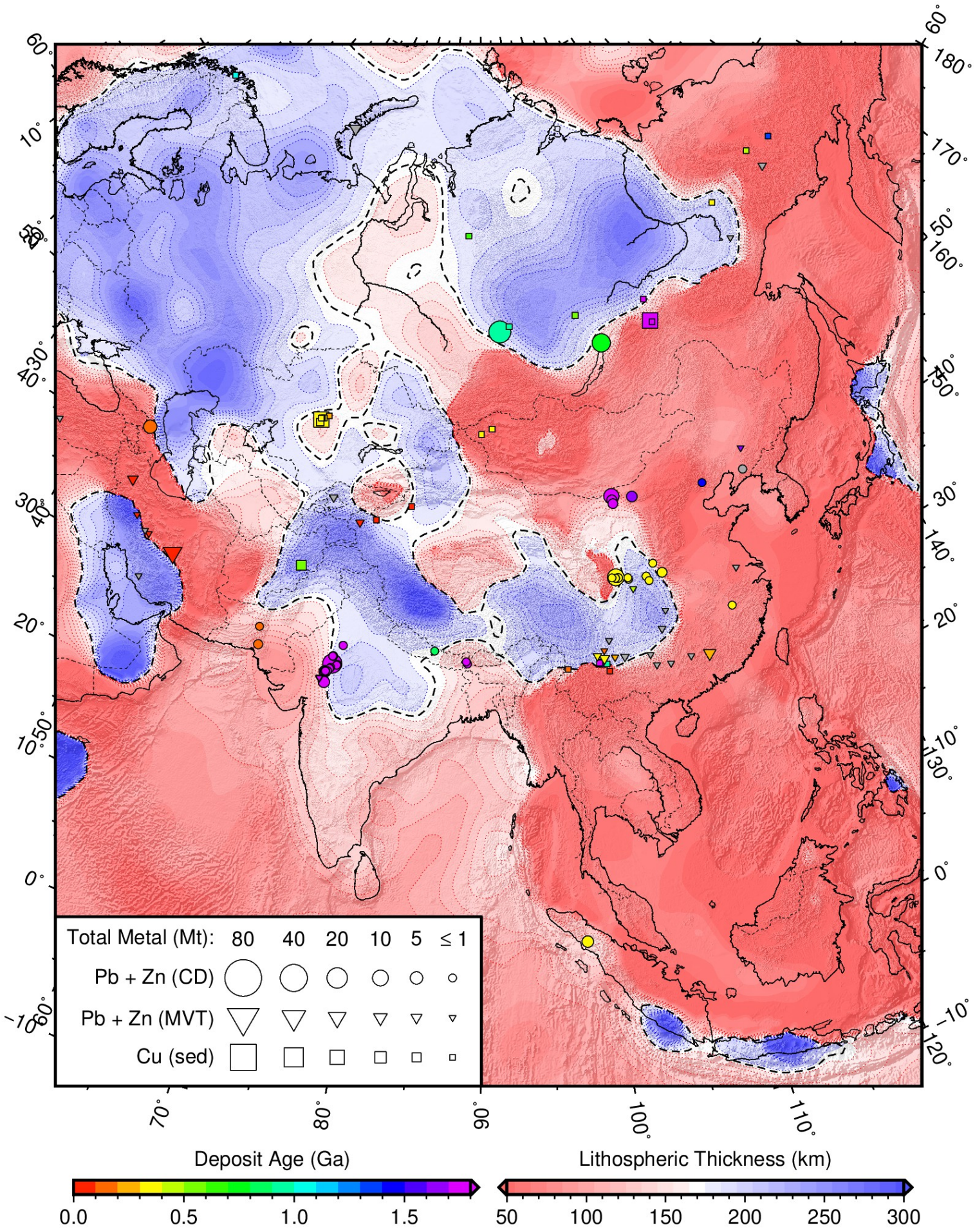

Figure S23: **Distribution of sediment-hosted base metal deposits as a function of lithospheric thickness in Asia.** Global LAB derived from SL2013sv tomography model using a calibrated anelasticity parameterisation (Schaeffer & Lebedev, 2013; Yamauchi & Takei, 2016); black dashed contour = 170 km LAB thickness; symbols = deposit locations; area proportional to estimate of total contained mass of metal (Mt = megatonnes); unknown deposit size given 1 Mt symbol; colour = ore body formation age (billion years); unknown age plotted in grey; circles = clastic-dominated lead-zinc (PbZn-CD); triangles = Mississippi Valley type lead-zinc (PbZn-MVT); squares = sedimentary copper (Cu-sed).

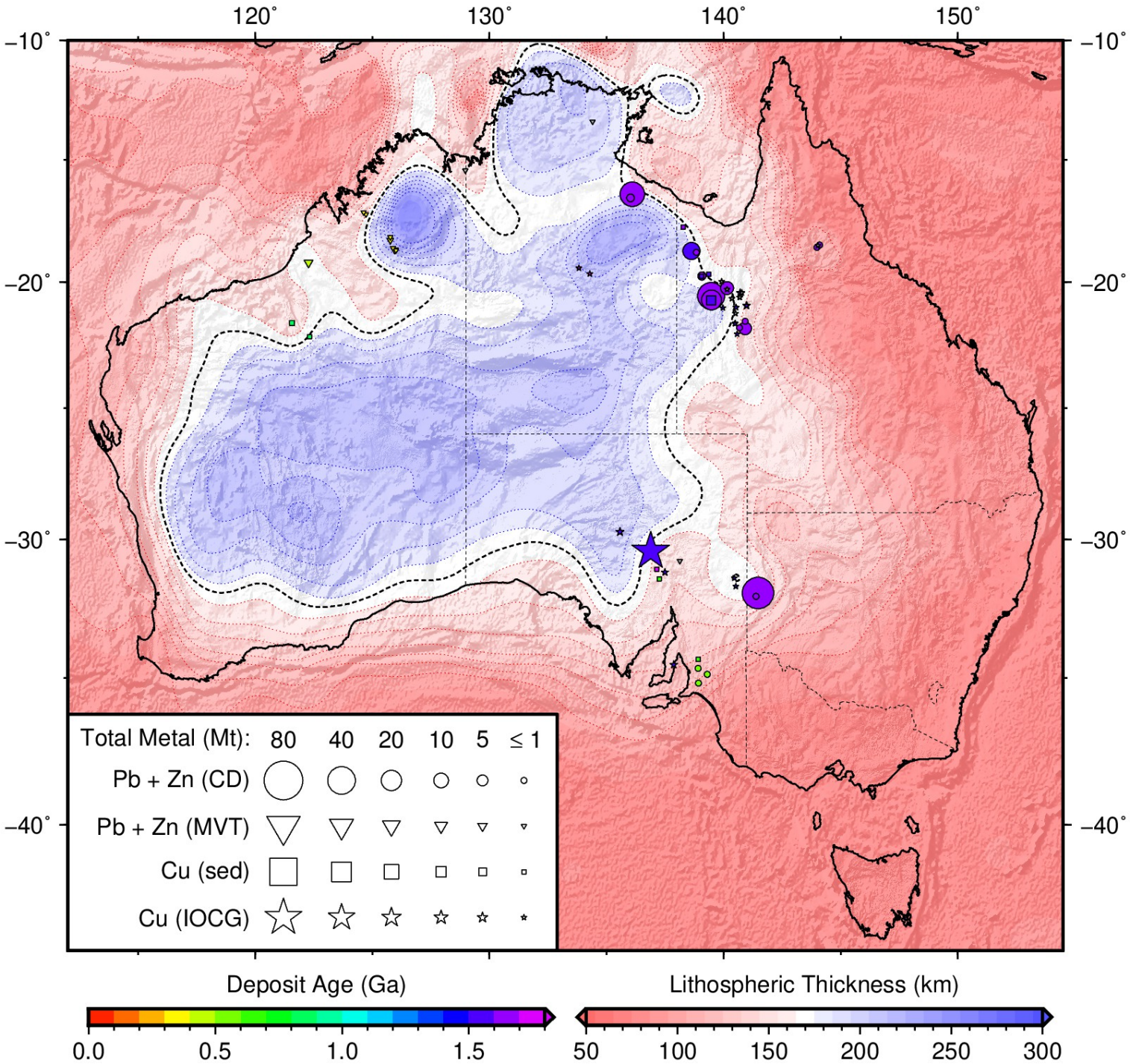

Figure S24: **Distribution of sediment-hosted and IOCG base metal deposits as a function of lithospheric thickness in Australia.** Regional LAB derived from FR12 tomography model using a calibrated anelasticity parameterisation (Fishwick & Rawlinson, 2012; Yamauchi & Takei, 2016); black dashed contour = 170 km LAB thickness; symbols = deposit locations; area proportional to estimate of total contained mass of metal (Mt = megatonnes); unknown deposit size given 1 Mt symbol; colour = ore body formation age (billion years); unknown age plotted in grey; circles = clastic-dominated lead-zinc (PbZn-CD); triangles = Mississippi Valley type lead-zinc (PbZn-MVT); squares = sedimentary copper (Cu-sed); stars = iron-oxide-copper-gold (IOCG).

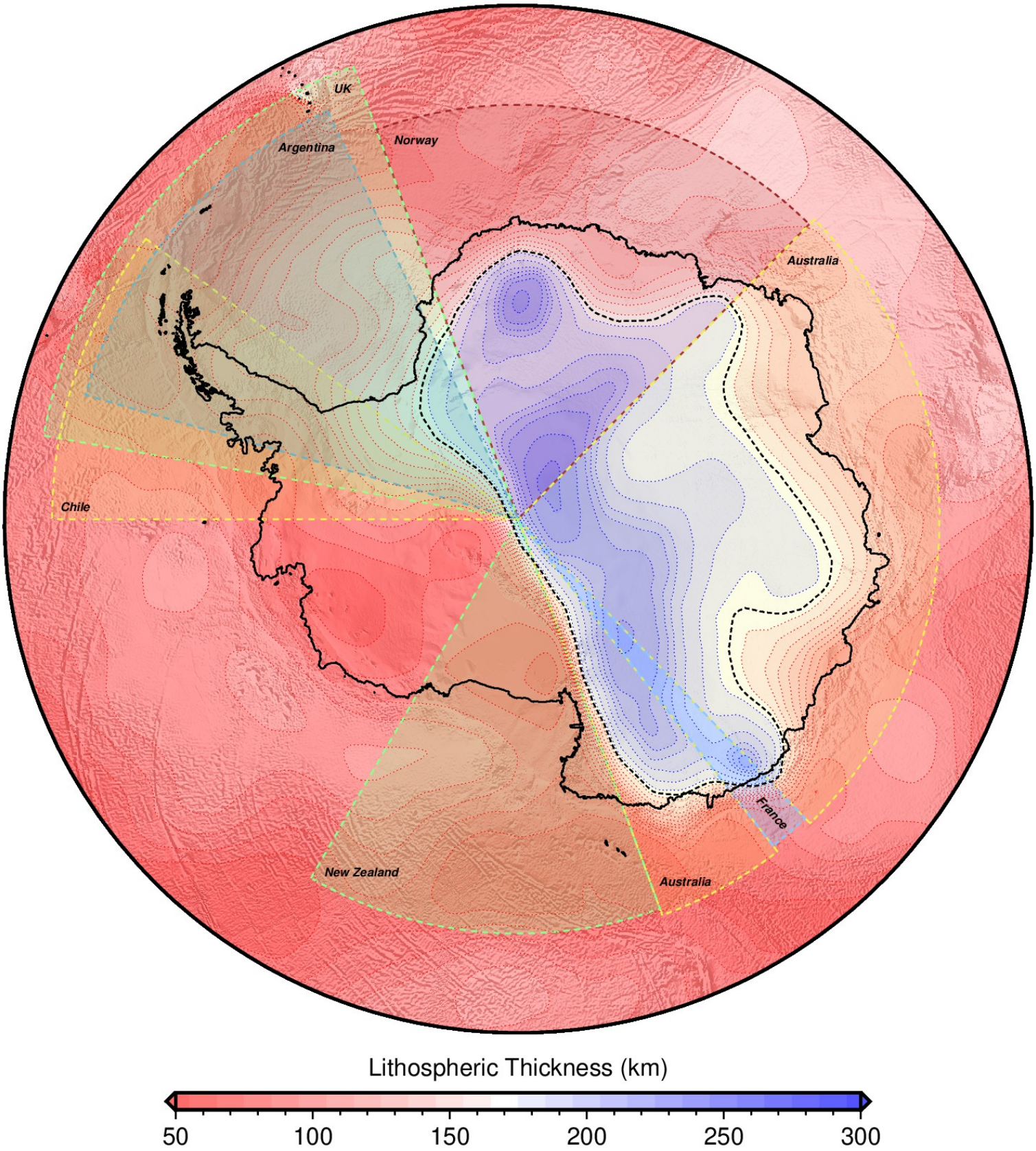

Figure S25: **Lithospheric thickness in Antarctica.** Global LAB derived from SL2013sv tomography model using a calibrated anelasticity parameterisation (Schaeffer & Lebedev, 2013; Yamauchi & Takei, 2016); black dashed contour = 170 km LAB thickness; coloured segments = approximate extent of principal territorial claims by sovereign states.

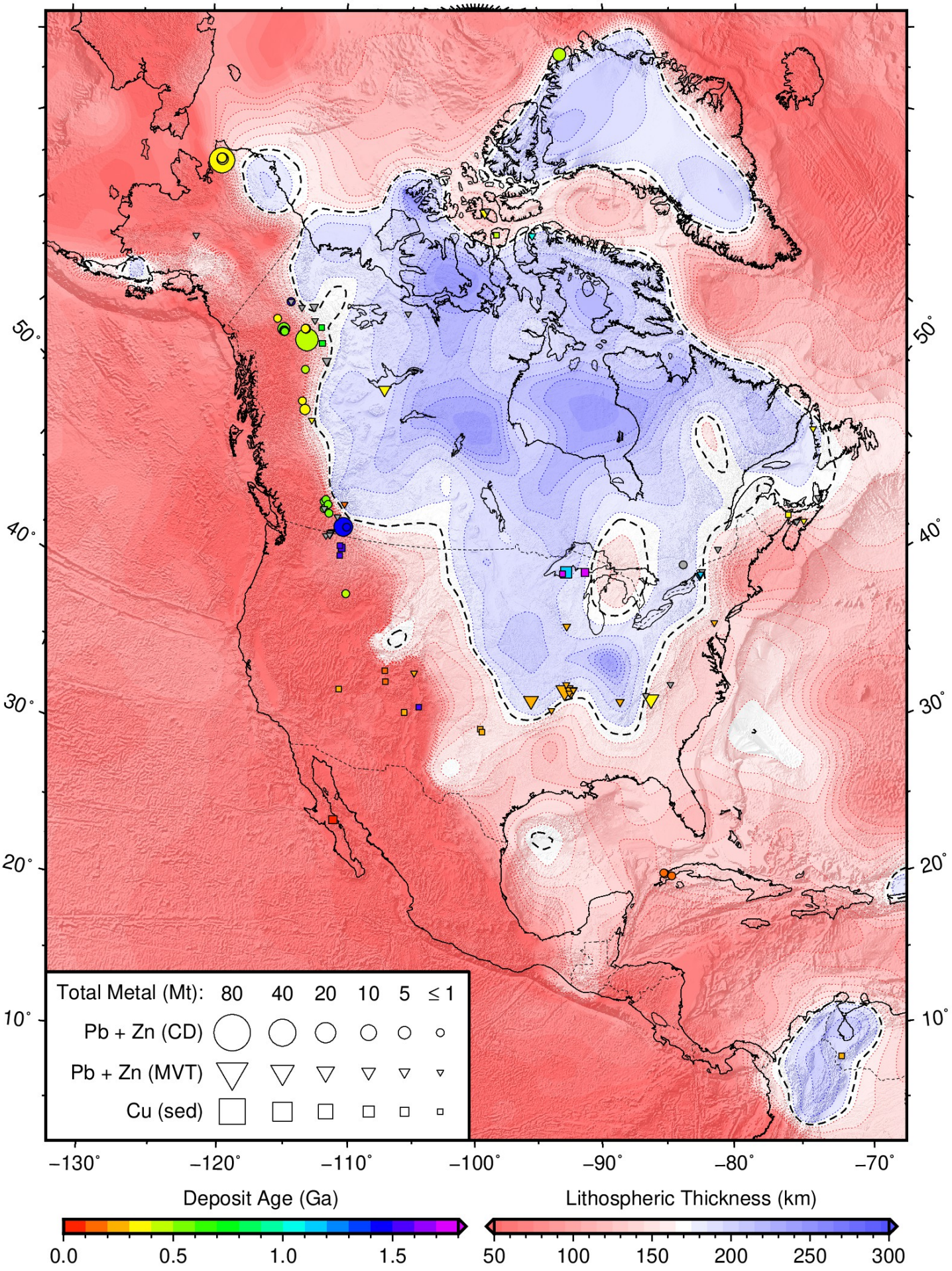

Figure S26: **Distribution of sediment-hosted base metal deposits as a function of lithospheric thickness in North America.** Global LAB derived from SL2013sv tomography model using a calibrated anelasticity parameterisation (Schaeffer & Lebedev, 2013; Yamauchi & Takei, 2016); black dashed contour = 170 km LAB thickness; symbols = deposit locations; area proportional to estimate of total contained mass of metal (Mt = megatonnes); unknown deposit size given 1 Mt symbol; colour = ore body formation age (billion years); unknown age plotted in grey; circles = clastic-dominated lead-zinc (PbZn-CD); triangles = Mississippi Valley type lead-zinc (PbZn-MVT); squares = sedimentary copper (Cu-sed).

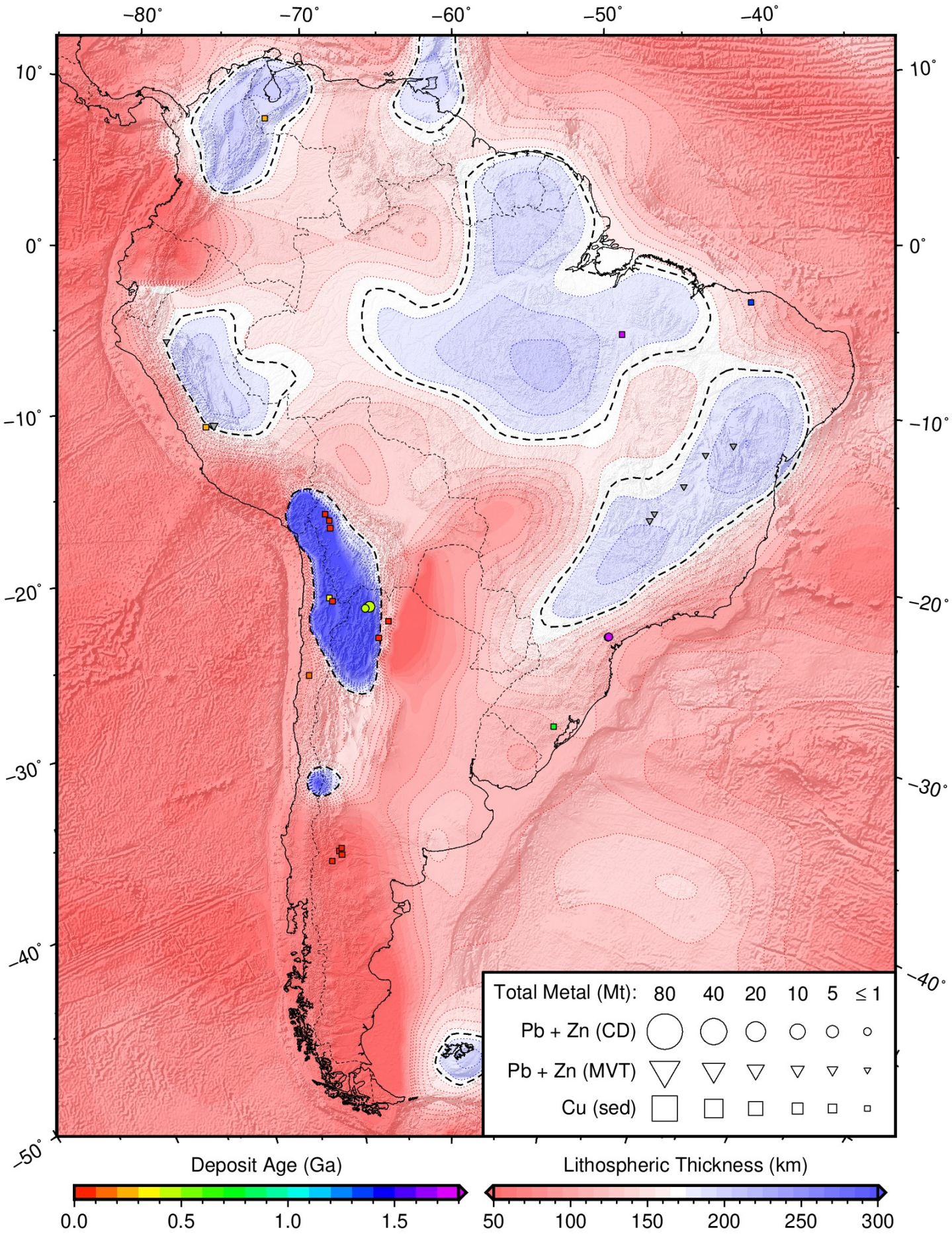

Figure S27: **Distribution of sediment-hosted base metal deposits as a function of lithospheric thickness in South America.** Global LAB derived from SL2013sv tomography model using a calibrated anelasticity parameterisation (Schaeffer & Lebedev, 2013; Yamauchi & Takei, 2016); black dashed contour = 170 km LAB thickness; symbols = deposit locations; area proportional to estimate of total contained mass of metal (Mt = megatonnes); unknown deposit size given 1 Mt symbol; colour = ore body formation age (billion years); unknown age plotted in grey; circles = clastic-dominated lead-zinc (PbZn-CD); triangles = Mississippi Valley type lead-zinc (PbZn-MVT); squares = sedimentary copper (Cu-sed).

11 Inventory of base metal deposits

Figures S30–S32 show deposit locations, age distributions with respect to lithospheric thickness, and Kolmogorov-Smirnov statistical test results for each individual deposit type compiled in this study (Methods). These are followed by tabulated information and associated references for each individual deposit, which is also available as a spreadsheet through the online Supplementary Information.

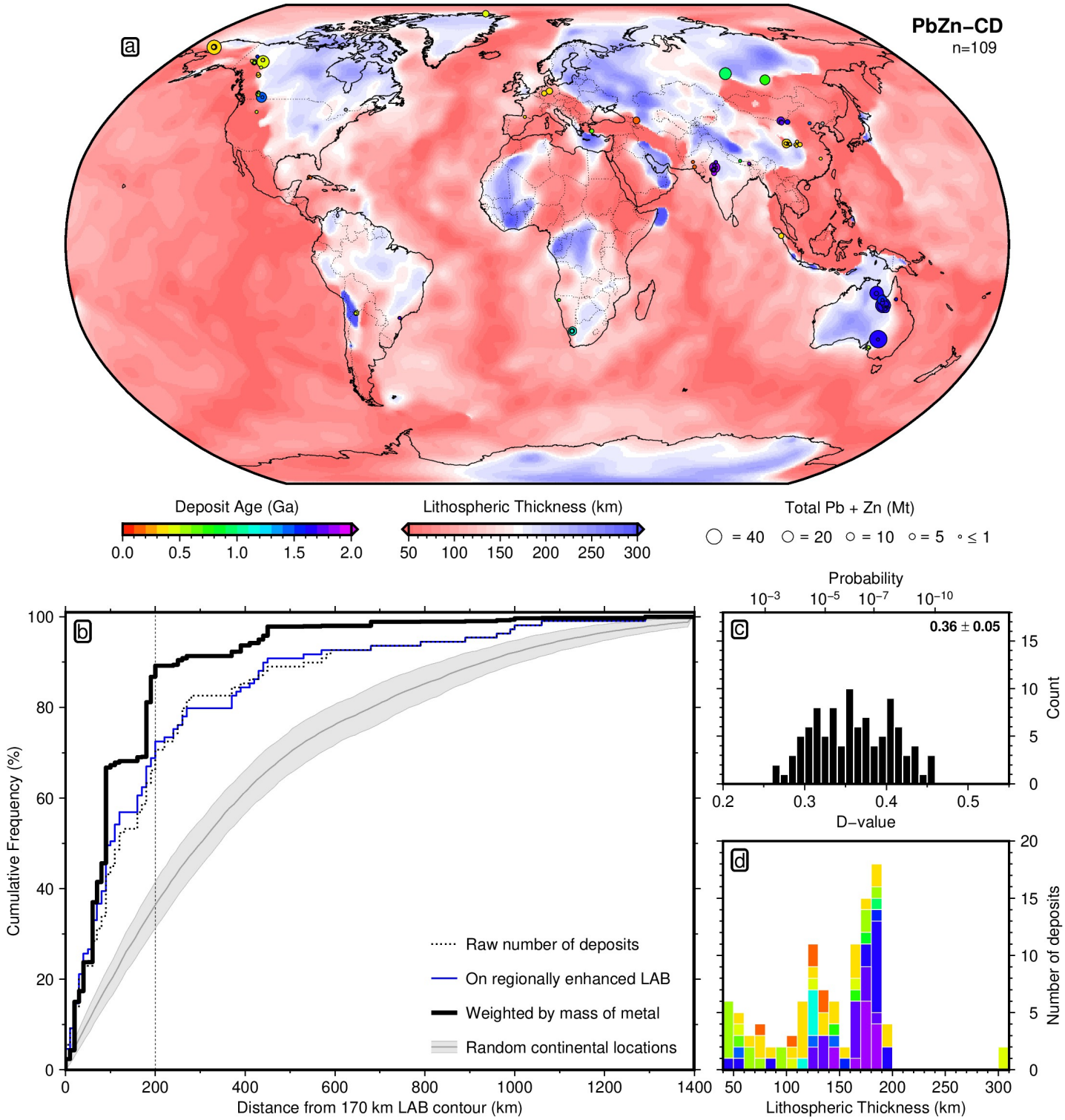

Figure S28: **109 clastic-dominated lead-zinc deposits from Table 2.** (a) LAB derived from SL2013sv tomography model using a calibrated anelasticity parameterisation (Schaeffer & Lebedev, 2013; Yamauchi & Takei, 2016). Circles = deposit locations; area proportional to estimate of total contained mass of metal (Mt = megatonnes); unknown deposit size given 1 Mt symbol; colour = ore body formation age (billion years); unknown age plotted in grey. (b) Different approaches for generating cumulative distribution functions. Dotted line = simple count of number of deposits with increasing distance from the 170 km contour in global LAB map; blue line = simple count where Australian LAB has been replaced with regionally enhanced map (Figure S11a); solid black line = deposits weighted by mass of contained lead and zinc on regionally enhanced map; grey line/bounds = mean and standard deviation of 100 sets of equivalent number of randomly drawn continental locations, with respect to regionally enhanced LAB. (c) Histogram of 100 D-values calculated for each random test set and a non-mass-weighted, locally enhanced CDF (blue CDF); inset lists mean and standard deviation of D-values; associated probabilities shown across top. (d) Histogram of deposit occurrence as a function of lithospheric thickness, coloured by deposit age.

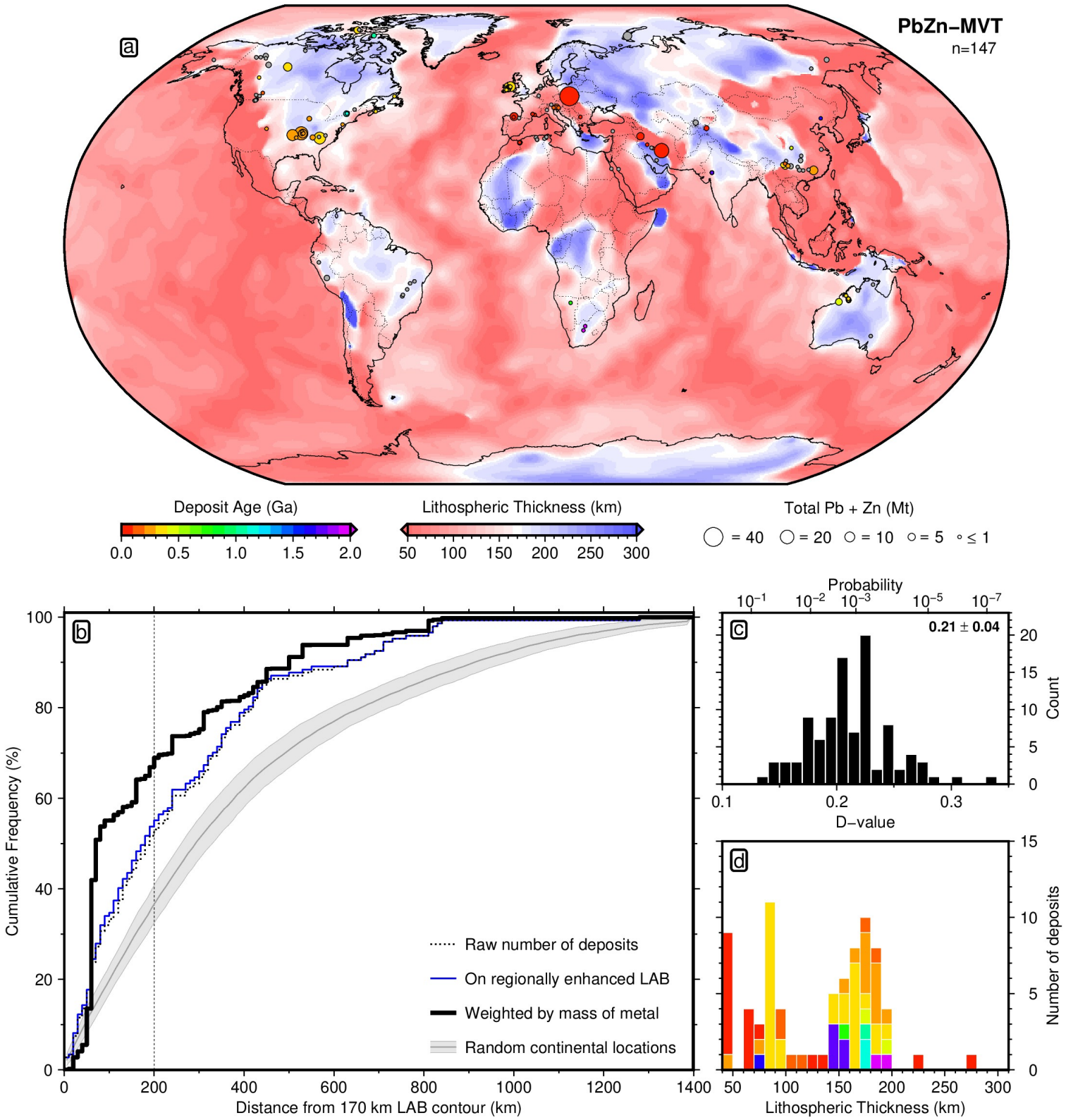

Figure S29: **147 Mississippi Valley-type lead-zinc deposits from Table 3.** (a) LAB derived from SL2013sv tomography model using a calibrated anelasticity parameterisation (Schaeffer & Lebedev, 2013; Yamauchi & Takei, 2016). Circles = deposit locations; area proportional to estimate of total contained mass of metal (Mt = megatonnes); unknown deposit size given 1 Mt symbol; colour = ore body formation age (billion years); unknown age plotted in grey. (b) Different approaches for generating cumulative distribution functions. Dotted line = simple count of number of deposits with increasing distance from the 170 km contour in global LAB map; blue line = simple count where Australian LAB has been replaced with regionally enhanced map (Figure S11a); solid black line = deposits weighted by mass of contained lead and zinc on regionally enhanced map; grey line/bounds = mean and standard deviation of 100 sets of equivalent number of randomly drawn continental locations, with respect to regionally enhanced LAB. (c) Histogram of 100 D-values calculated for each random test set and a non-mass-weighted, locally enhanced CDF (blue CDF); inset lists mean and standard deviation of D-values; associated probabilities shown across top. (d) Histogram of deposit occurrence as a function of lithospheric thickness, coloured by deposit age.

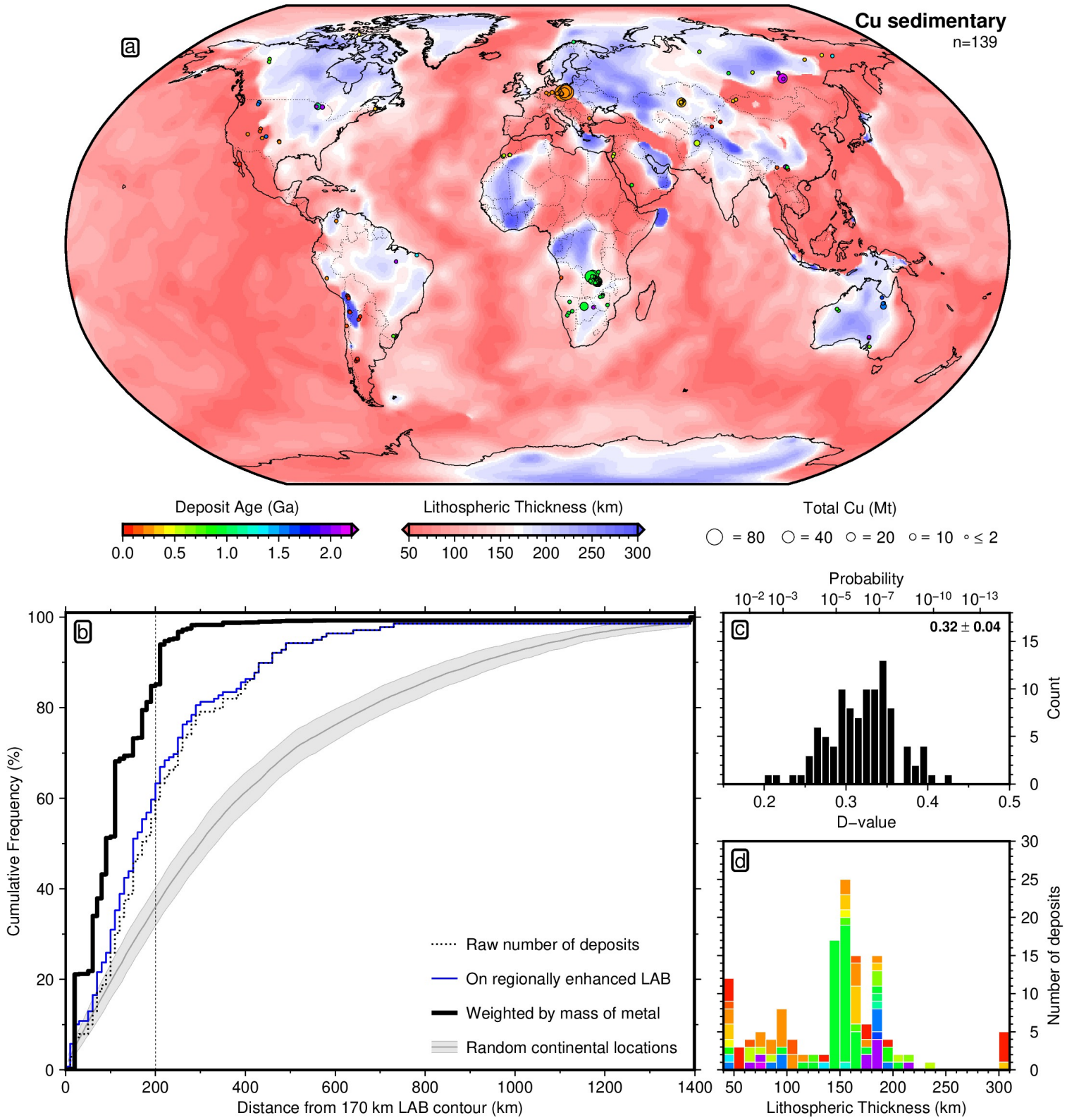

Figure S30: **139 sedimentary copper deposits from Table 4.** (a) LAB derived from SL2013sv tomography model using a calibrated anelasticity parameterisation (Schaeffer & Lebedev, 2013; Yamauchi & Takei, 2016). Circles = deposit locations; area proportional to estimate of total contained mass of metal (Mt = megatonnes); unknown deposit size given 2 Mt symbol; colour = ore body formation age (billion years); unknown age plotted in grey. (b) Different approaches for generating cumulative distribution functions. Dotted line = simple count of number of deposits with increasing distance from the 170 km contour in global LAB map; blue line = simple count where Australian LAB has been replaced with regionally enhanced map (Figure S11a); solid black line = deposits weighted by mass of contained copper on regionally enhanced map; grey line/bounds = mean and standard deviation of 100 sets of equivalent number of randomly drawn continental locations, with respect to regionally enhanced LAB. (c) Histogram of 100 D-values calculated for each random test set and a non-mass-weighted, locally enhanced CDF (blue CDF); inset lists mean and standard deviation of D-values; associated probabilities shown across top. (d) Histogram of deposit occurrence as a function of lithospheric thickness, coloured by deposit age.

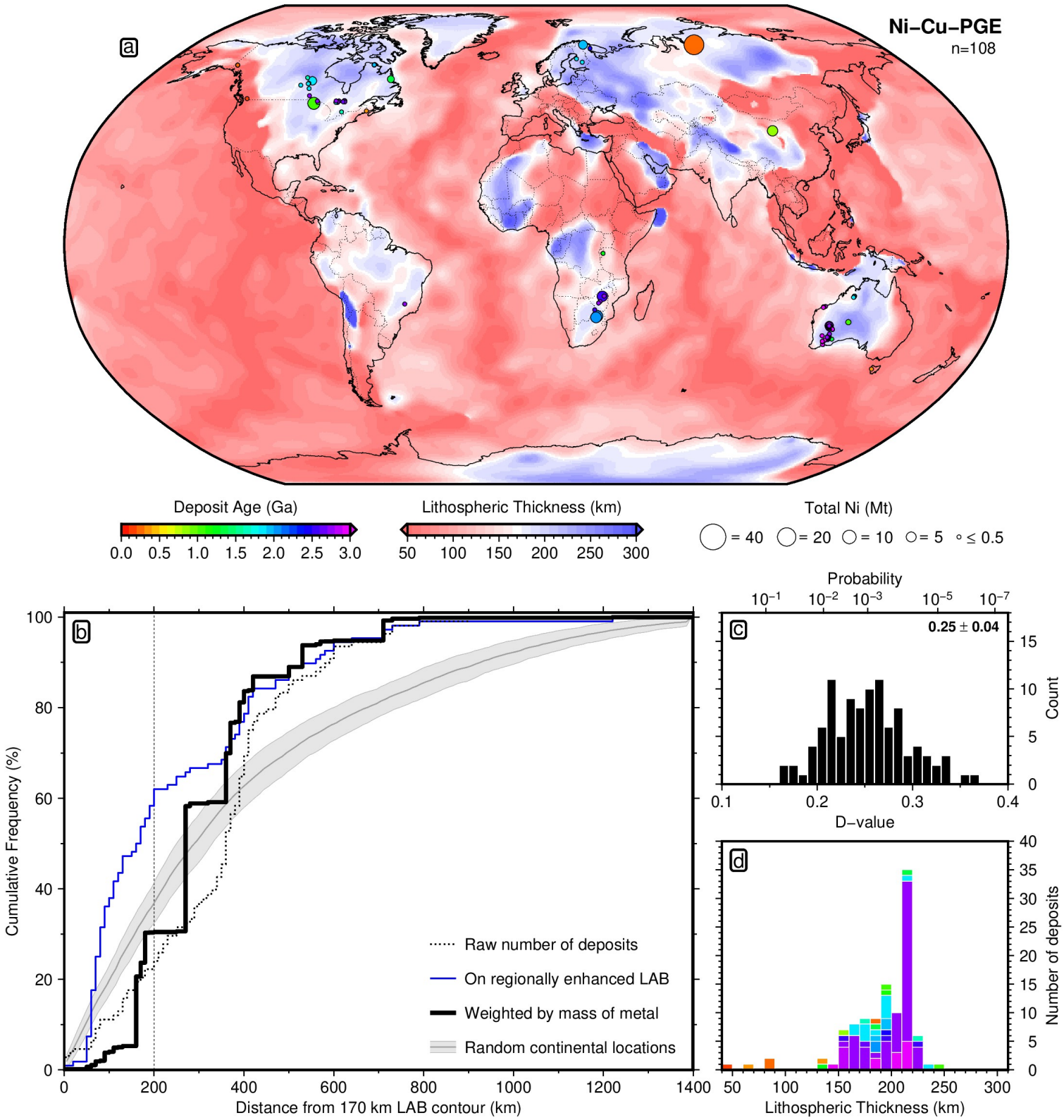

Figure S31: **108 magmatic nickel-copper-platinum group element deposits from Table 5.** (a) LAB derived from SL2013sv tomography model using a calibrated anelasticity parameterisation (Schaeffer & Lebedev, 2013; Yamauchi & Takei, 2016). Circles = deposit locations; area proportional to estimate of total contained mass of metal (Mt = megatonnes); unknown deposit size given 0.5 Mt symbol; colour = ore body formation age (billion years); unknown age plotted in grey. (b) Different approaches for generating cumulative distribution functions. Dotted line = simple count of number of deposits with increasing distance from the 170 km contour in global LAB map; blue line = simple count where Australian LAB has been replaced with regionally enhanced map (Figure S11a); solid black line = deposits weighted by mass of contained nickel on regionally enhanced map; grey line/bounds = mean and standard deviation of 100 sets of equivalent number of randomly drawn continental locations, with respect to regionally enhanced LAB. (c) Histogram of 100 D-values calculated for each random test set and a non-mass-weighted, locally enhanced CDF (blue CDF); inset lists mean and standard deviation of D-values; associated probabilities shown across top. (d) Histogram of deposit occurrence as a function of lithospheric thickness, coloured by deposit age.

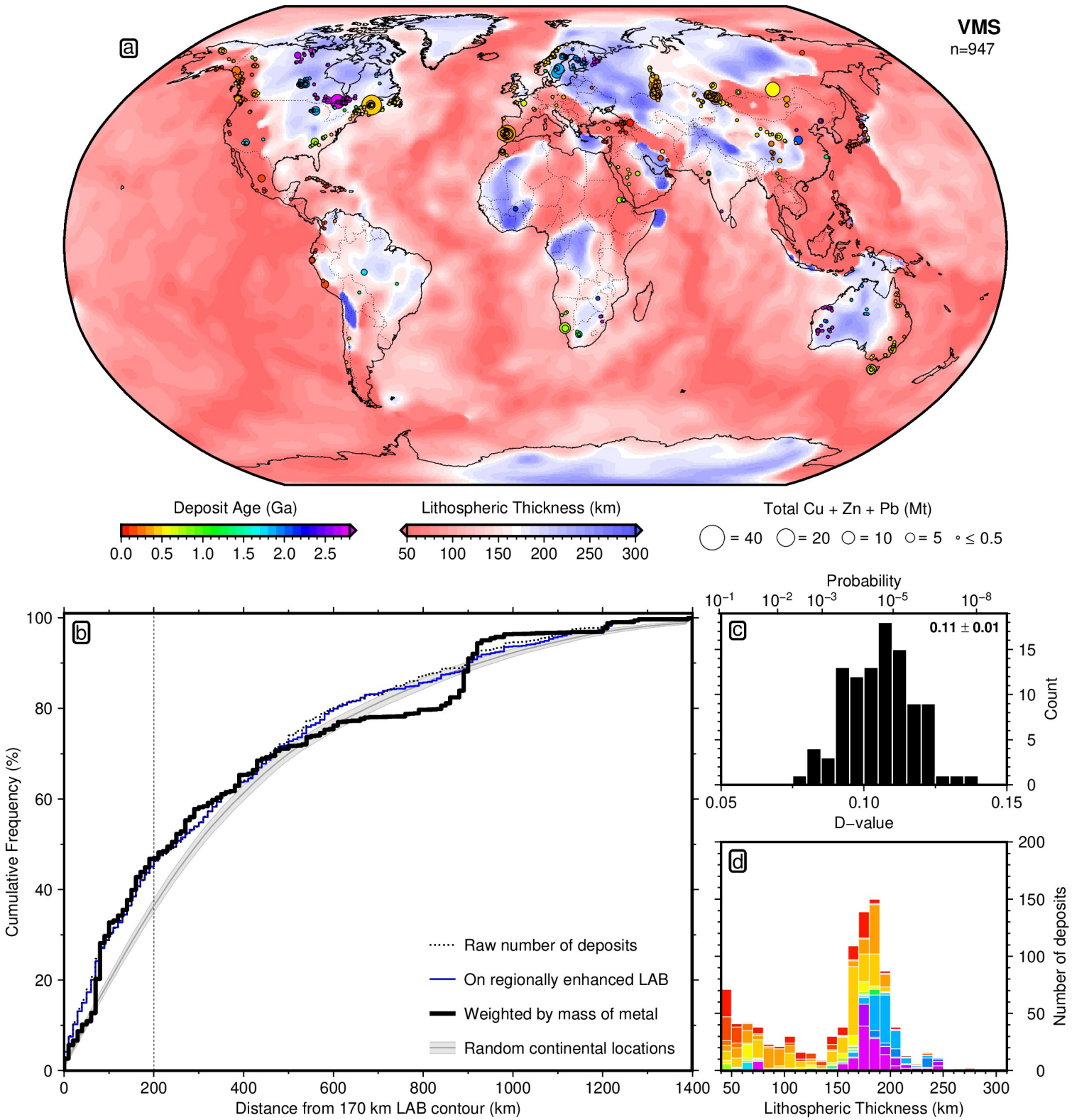

Figure S32: **947 volcanogenic massive sulphide deposits from Table 6.** (a) LAB derived from SL2013sv tomography model using a calibrated anelasticity parameterisation (Schaeffer & Lebedev, 2013; Yamauchi & Takei, 2016). Circles = deposit locations; area proportional to estimate of total contained mass of metal (Mt = megatonnes); unknown deposit size given 0.5 Mt symbol; colour = ore body formation age (billion years); unknown age plotted in grey. (b) Different approaches for generating cumulative distribution functions. Dotted line = simple count of number of deposits with increasing distance from the 170 km contour in global LAB map; blue line = simple count where Australian LAB has been replaced with regionally enhanced map (Figure S11a); solid black line = deposits weighted by mass of contained copper, lead and zinc on regionally enhanced map; grey line/bounds = mean and standard deviation of 100 sets of equivalent number of randomly drawn continental locations, with respect to regionally enhanced LAB. (c) Histogram of 100 D-values calculated for each random test set and a non-mass-weighted, locally enhanced CDF (blue CDF); inset lists mean and standard deviation of D-values; associated probabilities shown across top. (d) Histogram of deposit occurrence as a function of lithospheric thickness, coloured by deposit age.

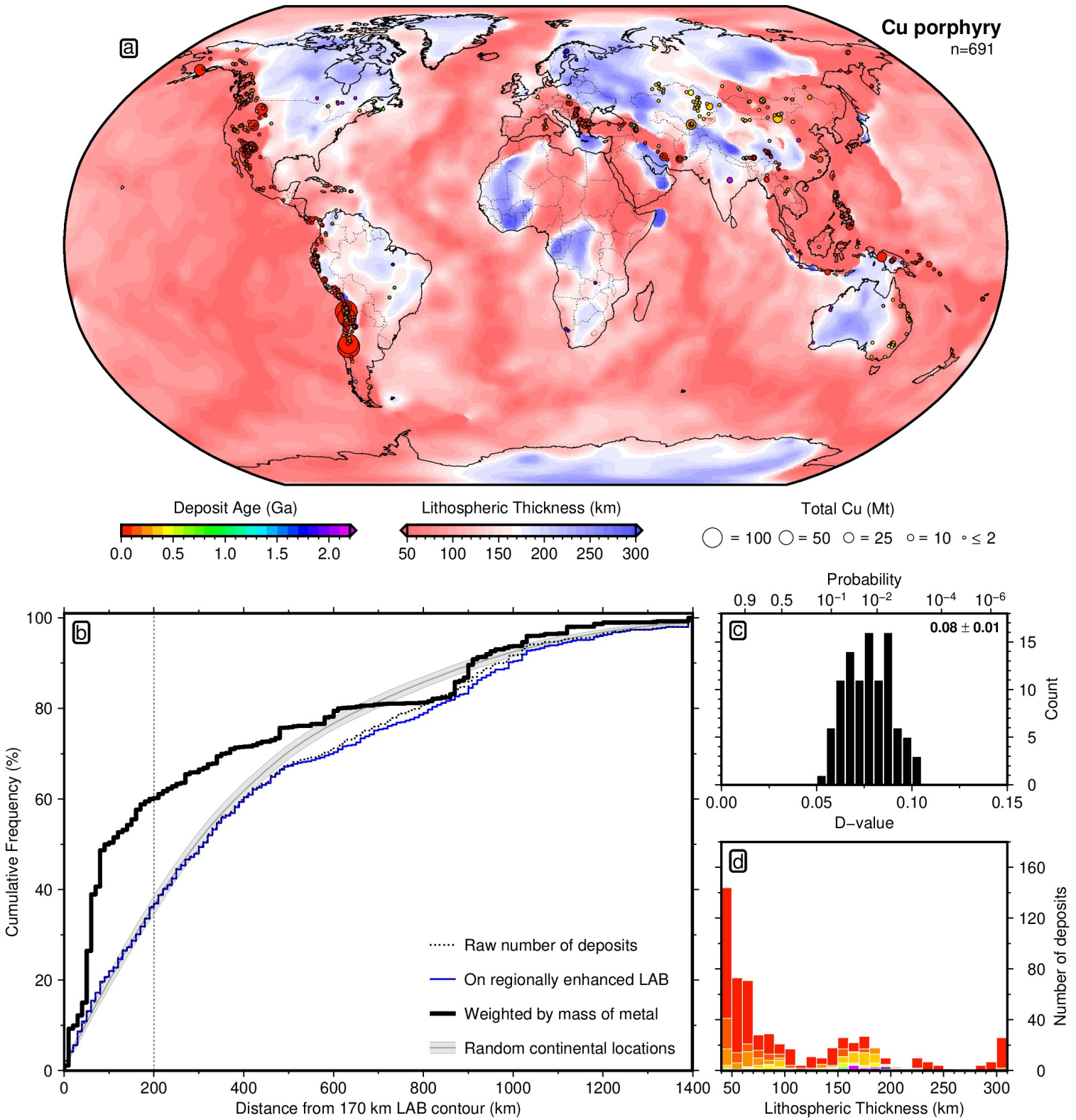

Figure S33: **691 copper porphyry deposits from Table 7.** (a) LAB derived from SL2013sv tomography model using a calibrated anelasticity parameterisation (Schaeffer & Lebedev, 2013; Yamauchi & Takei, 2016). Circles = deposit locations; area proportional to estimate of total contained mass of metal (Mt = megatonnes); unknown deposit size given 2 Mt symbol; colour = ore body formation age (billion years); unknown age plotted in grey. (b) Different approaches for generating cumulative distribution functions. Dotted line = simple count of number of deposits with increasing distance from the 170 km contour in global LAB map; blue line = simple count where Australian LAB has been replaced with regionally enhanced map (Figure S11a); solid black line = deposits weighted by mass of contained copper on regionally enhanced map; grey line/bounds = mean and standard deviation of 100 sets of equivalent number of randomly drawn continental locations, with respect to regionally enhanced LAB. (c) Histogram of 100 D-values calculated for each random test set and a non-mass-weighted, locally enhanced CDF (blue CDF); inset lists mean and standard deviation of D-values; associated probabilities shown across top. (d) Histogram of deposit occurrence as a function of lithospheric thickness, coloured by deposit age.

Table 2: Global compilation of 109 clastic-dominated Pb-Zn deposits shown in Figure S28, building extensively on Taylor *et al.* (2009). Ga = billion years; Mt = million tonnes; ND = no data.

Deposit	State/Region	Country	Lon.[a]	Lat.[a]	Age (Ga)	Ore (Mt)	Cu (%)	Zn (%)	Pb (%)	Cu (Mt)	Zn (Mt)	Pb (Mt)	References
Aguilar	Jujuy	Argentina	-65.70	-23.20	0.483	30.0	ND	6.20	5.50	ND	1.9	1.7	Sureda & Martin (1990); Gemmell *et al.* (1992); Singer *et al.* (2009)
Esperanza	Jujuy	Argentina	-66.00	-23.29	0.483	0.0	ND	ND	ND	ND	ND	ND	Sureda & Martin (1990); Gemmell *et al.* (1992); Singer *et al.* (2009)
HYC (McArthur River)	Northern Territory	Australia	136.10	-16.43	1.637	227.0	0.20	9.25	4.10	0.5	21.0	9.3	Smith & Croxford (1973); Williams (1978a,b); Rye & Williams (1981); Logan *et al.* (1990); Eldridge *et al.* (1993); Cooke *et al.* (1998); Page *et al.* (2000); Carr *et al.* (2001); Ireland *et al.* (2004); Symons (2007)
Myrtle	Northern Territory	Australia	136.03	-16.58	1.639	43.6	ND	4.09	0.95	ND	1.8	0.4	Rox Resources (2020)
Cannington	Queensland	Australia	140.92	-21.87	1.665	43.8	ND	4.40	11.60	ND	1.9	5.1	Walters & Bailey (1998); Bodon (1998); Carr *et al.* (2001)
Century	Queensland	Australia	138.63	-18.75	1.573	94.6	ND	13.10	1.80	ND	12.4	1.7	Broadbent *et al.* (1998); Carr *et al.* (2001)
Chloe-Jackson-Stella (Mt Misery)	Queensland	Australia	143.99	-18.61	1.673	4.6	0.20	4.80	2.00	0.0	0.2	0.1	Kositcin *et al.* (2009)
Dugald River	Queensland	Australia	140.15	-20.25	1.662	53.0	ND	12.50	1.90	ND	6.6	1.0	Connor (1990); Davidson & Dixon (1992); Dixon & Davidson (1996); Carr *et al.* (2001); MMG (2020)
Einasleigh barite	Queensland	Australia	144.10	-18.51	1.686	ND	ND	ND	ND	ND	ND	ND	Denaro *et al.* (1997); Evins *et al.* (2007); Lees & Buckle (2009); Kositcin *et al.* (2009)
Hilton-George Fisher	Queensland	Australia	139.47	-20.57	1.655	227.0	ND	11.31	5.40	ND	25.7	12.3	Page *et al.* (2000); Carr *et al.* (2001); Chapman (2004)
Kamarga	Queensland	Australia	138.84	-18.81	1.614	10.4	ND	2.70	0.20	ND	0.3	0.0	Jones *et al.* (1999); Carr *et al.* (2001); Geological Survey of Queensland (2020)
Lady Loretta	Queensland	Australia	139.07	-19.77	1.633	12.7	ND	14.20	4.80	ND	1.8	0.6	Carr & Smith (1977); Carr (1984); Hancock & Purvis (1990); Carr *et al.* (2001); Glencore (2020)
Maramungee	Queensland	Australia	140.92	-21.58	1.675	1.8	ND	4.40	ND	ND	0.1	ND	Williams & Heinemann (1993); Carr *et al.* (2001)
Mount Isa	Queensland	Australia	139.48	-20.73	1.652	150.0	ND	7.00	6.00	ND	10.5	9.0	Smith *et al.* (1978); Forrestal (1990); Painter *et al.* (1999); Page *et al.* (2000); Carr *et al.* (2001)
Pegmont	Queensland	Australia	140.68	-21.84	1.664	8.6	ND	3.50	7.70	ND	0.3	0.7	Vaughan & Stanton (1986); Williams *et al.* (1998); Carr *et al.* (2001); Pegmont (2020)
Broken Hill	South Australia	Australia	141.47	-31.97	1.685	280.0	0.14	8.50	10.00	0.4	23.8	28.0	Lawrence & Rafter (1962); Both & Smith (1975); Plimer (1977, 1986); Page *et al.* (2005); Parr *et al.* (2004); Huston *et al.* (2006); Groves *et al.* (2008)
Mount Torrens	South Australia	Australia	139.30	-34.88	0.518	0.7	ND	1.60	6.40	ND	0.0	0.0	Belperio *et al.* (1998); Haines *et al.* (2009); Skwarnecki & Fitzpatrick (2003)
Pinnacles	South Australia	Australia	141.39	-32.09	1.695	0.8	ND	2.50	11.00	ND	0.0	0.1	Parr (1994); Parr *et al.* (2004)
Wheal Ellen	South Australia	Australia	138.93	-35.19	0.518	0.1	ND	25.00	20.00	ND	0.0	0.0	Belperio *et al.* (1998); Both (1990); Seccombe *et al.* (1985); Haines *et al.* (2009)
Filizchai	Zaqatala	Azerbaijan	46.47	41.79	0.181	100.0	0.64	4.50	2.00	0.6	4.5	2.0	Singer *et al.* (2009); Taylor *et al.* (2009)
Canoas	Paran	Brazil	-48.95	-24.83	1.700	1.3	ND	3.26	3.02	ND	0.0	0.0	Daitx (1996); Misi *et al.* (1999); Singer *et al.* (2009); Taylor *et al.* (2009)
Perau	Paran	Brazil	-49.00	-24.85	1.700	3.3	ND	1.88	4.13	ND	0.1	0.1	Daitx (1996); Singer *et al.* (2009); Taylor *et al.* (2009)
Big Ledge	British Columbia	Canada	-118.05	50.48	0.560	6.5	ND	3.00	3.00	ND	0.2	0.2	Höy (1975); Kuiper *et al.* (2011); British Columbia Geological Survey (2020a); StratDB (2020)
Cirque	British Columbia	Canada	-125.15	57.51	0.366	22.1	ND	9.40	2.80	ND	2.1	0.6	Goodfellow (2007); Paradis *et al.* (1998); British Columbia Geological Survey (2020b)
Cottonbelt	British Columbia	Canada	-118.82	51.45	0.560	0.7	ND	6.00	5.00	ND	0.0	0.0	Kuiper *et al.* (2011); British Columbia Geological Survey (2020c); StratDB (2020)
Driftpile	British Columbia	Canada	-125.95	58.05	0.366	2.4	ND	11.90	3.10	ND	0.3	0.1	Goodfellow (2007); Paradis *et al.* (1998); Thorpe (2008); British Columbia Geological Survey (2020d)
Kingfisher (Colby)	British Columbia	Canada	-118.73	50.73	0.560	1.7	ND	2.60	0.58	ND	0.0	0.0	Kuiper *et al.* (2011); British Columbia Geological Survey (2020e); StratDB (2020)
Kootenay King	British Columbia	Canada	-115.61	49.74	1.470	0.0	ND	6.65	5.36	ND	0.0	0.0	Kuiper *et al.* (2011); British Columbia Geological Survey (2020f); StratDB (2020)
River Jordan	British Columbia	Canada	-118.41	51.13	0.560	2.6	ND	5.60	5.10	ND	0.1	0.1	Kuiper *et al.* (2011); British Columbia Geological Survey (2020g)
Ruddock Creek	British Columbia	Canada	-118.98	51.27	0.560	3.8	ND	7.29	1.47	ND	0.3	0.1	Kuiper *et al.* (2011); British Columbia Geological Survey (2020h); StratDB (2020)
Sullivan	British Columbia	Canada	-116.01	49.71	1.468	150.5	0.00	5.28	5.59	0.0	7.9	8.4	Campbell *et al.* (1978); Lydon (2007); Anderson & Parrish (2000); Thorpe (2008); British Columbia Geological Survey (2020i)

Continued overleaf...

Table 2 – continued

Deposit	State/Region	Country	Lon.[a]	Lat.[a]	Age (Ga)	Ore (Mt)	Cu (%)	Zn (%)	Pb (%)	Cu (Mt)	Zn (Mt)	Pb (Mt)	References
Cadieux	Ontario	Canada	-76.71	45.41	ND	0.8	ND	10.00	1.00	ND	0.1	0.0	Singer *et al.* (2009); MDIO (2020)
Blende	Yukon	Canada	-134.67	64.40	1.540	19.6	ND	3.04	2.80	ND	0.6	0.5	Robinson & Godwin (1995); Yukon Geological Survey (2008); Moroskat *et al.* (2015)
Clear Lake	Yukon	Canada	-135.14	62.78	0.372	7.7	ND	7.60	1.08	ND	0.6	0.1	Goodfellow (2007); Thorpe (2008); Yukon Geological Survey (2008); Redtail Metals (2020)
Faro	Yukon	Canada	-133.37	62.36	0.521	57.6	ND	4.70	3.40	ND	2.7	2.0	Goodfellow (2007); Yukon Geological Survey (2008); StratDB (2020)
Grizzly (Dy)	Yukon	Canada	-133.14	62.23	0.521	17.2	ND	6.39	4.85	ND	1.1	0.8	Goodfellow (2007); Yukon Geological Survey (2008); StratDB (2020)
Grum	Yukon	Canada	-133.22	62.27	0.521	18.6	ND	4.43	2.68	ND	0.8	0.5	Goodfellow (2007); Thorpe (2008); Yukon Geological Survey (2008)
Howards Pass (XY + Anniv)	Yukon	Canada	-129.18	62.45	0.436	388.5	ND	4.90	1.60	ND	19.0	6.2	Goodfellow (2007); Thorpe (2008); Singer *et al.* (2009)
Jason	Yukon	Canada	-130.26	63.15	0.378	12.5	ND	6.62	4.40	ND	0.8	0.5	Gardner & Hutcheon (1985); Irwin & Orchard (1989); Goodfellow (2007); Thorpe (2008); Yukon Geological Survey (2008); Singer *et al.* (2009)
Mel	Yukon	Canada	-127.40	60.35	0.490	6.8	ND	7.10	2.03	ND	0.5	0.1	Thorpe (2008); Yukon Geological Survey (2008)
Swim	Yukon	Canada	-133.03	62.21	0.521	4.3	ND	4.70	3.80	ND	0.2	0.2	Goodfellow (2007); Yukon Geological Survey (2008); StratDB (2020)
Tom	Yukon	Canada	-130.14	63.17	0.378	18.5	ND	6.67	3.45	ND	1.2	0.6	Large (1980); Gardner & Hutcheon (1985); Irwin & Orchard (1989); Goodfellow (2007); Thorpe (2008); Yukon Geological Survey (2008); Singer *et al.* (2009)
Vangorda	Yukon	Canada	-133.18	62.25	0.521	7.1	ND	4.30	3.40	ND	0.3	0.2	Goodfellow (2007); Yukon Geological Survey (2008); StratDB (2020)
Changba-Lijiagou	Gansu	China	105.50	34.00	0.389	142.5	ND	7.20	1.30	ND	10.3	1.9	Ma *et al.* (2004); Singer *et al.* (2009); Taylor *et al.* (2009); Wang *et al.* (2014)
Gaobanhe	Hebei	China	118.23	40.78	1.475	38.8	ND	2.00	0.20	ND	0.8	0.1	Li & Kusky (2007); Singer *et al.* (2009); Taylor *et al.* (2009); Wang *et al.* (2014)
Dongshengmiao	Inner Mongolia	China	106.72	41.65	1.700	238.0	ND	3.11	0.78	ND	7.4	1.9	Ding & Jiang (2000); Peng & Zhai (2004); Singer *et al.* (2009); Taylor *et al.* (2009); Wang *et al.* (2014)
Huogeqi	Inner Mongolia	China	106.68	41.28	1.700	97.8	1.10	1.10	1.40	1.1	1.1	1.4	Peng & Zhai (2004); Zhu *et al.* (2006); Singer *et al.* (2009); Taylor *et al.* (2009); Wang *et al.* (2014)
Jiashengpan	Inner Mongolia	China	109.25	41.23	1.680	61.6	ND	3.80	1.30	ND	2.3	0.8	Ding & Jiang (2000); Peng & Zhai (2004); Zhu *et al.* (2006); Singer *et al.* (2009); Taylor *et al.* (2009); Fu *et al.* (2010); Wang *et al.* (2014); StratDB (2020)
Tanyaokou	Inner Mongolia	China	106.73	40.93	1.700	63.3	0.74	3.30	0.21	0.5	2.1	0.1	Ding & Jiang (2000); Peng & Zhai (2004); Singer *et al.* (2009); Taylor *et al.* (2009); Wang *et al.* (2014)
Dengjiashan	Jiangxi	China	105.75	33.91	0.389	25.0	ND	4.77	1.27	ND	1.2	0.3	Ma *et al.* (2007); Singer *et al.* (2009); Taylor *et al.* (2009); Wang *et al.* (2014)
Lehua	Jiangxi	China	117.30	28.84	0.320	15.0	ND	1.90	1.30	ND	0.3	0.2	Gu *et al.* (2007)
Qingchengzi	Liaoning	China	123.59	40.73	ND	27.6	ND	1.90	2.60	ND	0.5	0.7	Singer *et al.* (2009); Taylor *et al.* (2009); Wang *et al.* (2014)
Bafangshan	Shaanxi	China	106.88	33.59	0.375	9.4	ND	1.55	5.10	ND	0.1	0.5	Singer *et al.* (2009); Taylor *et al.* (2009); Wang *et al.* (2014)
Qiandongshan	Shaanxi	China	110.79	33.59	0.388	25.0	ND	7.80	1.80	ND	2.0	0.5	Zhang (1991); Singer *et al.* (2009); Taylor *et al.* (2009); Wang *et al.* (2014)
Tongmugou	Shaanxi	China	109.98	34.62	0.388	2.3	ND	21.70	1.98	ND	0.5	0.0	Jiang *et al.* (1995); Singer *et al.* (2009); Taylor *et al.* (2009); Wang *et al.* (2014)
Xidonggou	Shaanxi	China	109.15	33.10	0.388	22.5	ND	3.30	0.90	ND	0.7	0.2	Singer *et al.* (2009); Taylor *et al.* (2009); Wang *et al.* (2014)
Yindongliang	Shaanxi	China	106.84	33.75	0.388	4.4	ND	7.44	1.98	ND	0.3	0.1	Singer *et al.* (2009); Taylor *et al.* (2009); Wang *et al.* (2014)
Yindongzi	Shaanxi	China	108.93	33.54	0.388	10.0	0.56	2.00	10.00	0.1	0.2	1.0	Jiang *et al.* (1995); Singer *et al.* (2009)
Yinmusi	Shaanxi	China	106.85	33.75	0.388	4.4	0.08	7.40	2.00	0.0	0.3	0.1	USGS (2020a); World Mineral Deposits (2020)
Luoba	Sichuan	China	105.07	34.00	0.389	17.4	ND	4.61	1.44	ND	0.8	0.3	Singer *et al.* (2009); Taylor *et al.* (2009); Wang *et al.* (2014)
Bijiashan	Yunnan	China	105.46	33.92	0.389	10.5	0.65	5.24	5.23	0.1	0.6	0.5	Singer *et al.* (2009); Taylor *et al.* (2009); Wang *et al.* (2014)
Castellanos	Pinar del Rio	Cuba	-84.05	22.72	0.163	12.0	ND	2.40	3.20	ND	0.3	0.4	Valdés-Nodarse *et al.* (1993); Whitehead *et al.* (1996); Valdés-Nodarse (1998); Singer *et al.* (2009)
Matahambre	Pinar del Rio	Cuba	-83.43	22.43	0.163	14.8	4.39	0.51	0.24	0.6	0.1	0.0	Valdés-Nodarse *et al.* (1993); Whitehead *et al.* (1996); Valdés-Nodarse (1998); Singer *et al.* (2009)

Continued overleaf...

Table 2 – continued

Deposit	State/Region	Country	Lon.[a]	Lat.[a]	Age (Ga)	Ore (Mt)	Cu (%)	Zn (%)	Pb (%)	Cu (Mt)	Zn (Mt)	Pb (Mt)	References
Santa Lucia	Pinar del Rio	Cuba	-83.98	22.65	0.163	19.4	ND	5.70	1.83	ND	1.1	0.4	Valdés-Nodarse *et al.* (1993); Whitehead *et al.* (1996); Valdés-Nodarse (1998); Thorpe (2008); Singer *et al.* (2009)
Arrens	Hautes Pyrnes	France	-0.22	42.95	0.375	4.0	ND	6.60	0.90	ND	0.3	0.0	Escande & Majesté-Menjoulas (1985); Pouit & Bois (1986)
Rammelsberg	Lower Saxony	Germany	10.42	51.88	0.395	29.1	ND	14.57	6.76	ND	4.2	2.0	Anger *et al.* (1966); Large & Walcher (1999); Mueller (2008); StratDB (2020)
Meggen	North Rhine-Westphalia	Germany	8.08	51.13	0.389	44.7	ND	7.70	0.75	ND	3.4	0.3	Buschendorf *et al.* (1963); Mueller (2005); StratDB (2020)
Citronen Fjord	Northeast Greenland	Greenland	-28.25	83.08	0.444	131.1	ND	4.10	0.50	ND	5.4	0.7	Kragh *et al.* (1997); Ironbark (2020)
Bajta Central	Rajasthan	India	75.27	25.83	1.800	0.6	ND	3.37	1.45	ND	0.0	0.0	Bhawan (2006)
Bamnia Kalan	Rajasthan	India	74.18	25.04	1.799	5.1	ND	4.90	3.10	ND	0.2	0.2	Deb & Pal (2004); Thorpe (2008)
Bethumni	Rajasthan	India	74.18	25.07	1.799	0.2	ND	1.00	1.64	ND	0.0	0.0	Deb & Pal (2004)
Devpura	Rajasthan	India	74.63	25.45	1.800	17.5	ND	1.84	0.44	ND	0.3	0.1	Raghu Nundan *et al.* (1981); Deb & Thorpe (2004); Thorpe (2008)
Ganeshpura	Rajasthan	India	75.25	25.80	1.800	0.8	ND	4.60	1.15	ND	0.0	0.0	Geological Survey of India (1994)
Kankariya	Rajasthan	India	74.65	26.51	1.780	9.0	ND	3.22	2.56	ND	0.3	0.2	Ramakrishnan & Vaidyanathan (2008)
Kayar	Rajasthan	India	74.69	26.53	1.780	10.0	ND	13.10	2.22	ND	1.3	0.2	Ramakrishnan & Vaidyanathan (2008); Thorpe (2008)
Madarpura	Rajasthan	India	74.67	26.50	1.780	6.6	ND	5.51	ND	ND	0.4	ND	Ramakrishnan & Vaidyanathan (2008)
Mokanpura North	Rajasthan	India	74.13	25.00	1.799	63.0	ND	2.20	0.70	ND	1.4	0.4	Deb & Pal (2004)
Rajpura-Dariba	Rajasthan	India	74.13	24.98	1.799	45.0	ND	6.50	2.40	ND	2.9	1.1	Deb (1986); Deb *et al.* (1989); Deb & Sarkar (1990); Deb & Pal (2004); Deb & Thorpe (2004); Ramakrishnan & Vaidyanathan (2008)
Rampura-Agucha	Rajasthan	India	74.73	25.83	1.804	107.4	ND	13.94	1.96	ND	15.0	2.1	Deb *et al.* (1989); Deb & Sarkar (1990); Deb & Thorpe (2004); Roy *et al.* (2004); Shah (2004); Ramakrishnan & Vaidyanathan (2008)
Rewara	Rajasthan	India	74.37	25.10	1.800	2.5	0.38	0.66	3.42	0.0	0.0	0.1	Bhawan (2006)
Saladipura	Rajasthan	India	75.53	27.65	1.780	115.0	ND	1.00	ND	ND	1.2	ND	Deb *et al.* (1989); Deb & Sarkar (1990); Ramakrishnan & Vaidyanathan (2008); Thorpe (2008)
Samodi	Rajasthan	India	74.55	25.35	1.800	3.7	ND	1.85	1.37	ND	0.1	0.1	Raghu Nundan *et al.* (1981)
Sawar	Rajasthan	India	75.22	25.75	1.800	0.9	ND	1.45	2.54	ND	0.0	0.0	Raghu Nundan *et al.* (1981); Deb & Thorpe (2004)
Sindesar Kalan East	Rajasthan	India	74.17	25.00	1.799	94.0	ND	2.10	0.60	ND	2.0	0.6	Deb & Pal (2004)
Sindesar Khurd	Rajasthan	India	74.23	24.01	1.800	37.2	ND	5.80	3.82	ND	2.2	1.4	Deb & Thorpe (2004); Ameta & Sharma (2008)
South Dedwas	Rajasthan	India	74.57	25.35	1.800	18.4	ND	1.30	0.79	ND	0.2	0.1	Raghu Nundan *et al.* (1981); Geological Survey of India (1994)
Tikhi	Rajasthan	India	75.24	25.76	1.800	1.5	ND	2.59	1.90	ND	0.0	0.0	Raghu Nundan *et al.* (1981); Geological Survey of India (1994); Thorpe (2008)
Tiranga	Rajasthan	India	74.54	25.34	1.800	1.2	ND	1.13	1.75	ND	0.0	0.0	Raghu Nundan *et al.* (1981); Deb *et al.* (1989); Thorpe (2008)
Rangpo	Sikkim	India	88.53	27.17	1.850	0.6	1.10	2.60	1.10	0.0	0.0	0.0	Borodaev *et al.* (2002); Long *et al.* (2011); Raghu Nundan *et al.* (1981); Sarkar *et al.* (2000)
Gorubathan	West Bengal	India	88.65	26.97	1.850	2.8	0.10	4.23	4.00	0.0	0.1	0.1	Anonymous (1985); Long *et al.* (2011); Raghu Nundan *et al.* (1981); Saha (1985); Sarkar *et al.* (2000)
Sopokomil	North Sumatra	Indonesia	98.17	2.83	0.329	24.3	ND	10.30	6.00	ND	2.5	1.5	Reynolds & Geerdts (2012); Middleton (2004, 2020)
Tsongoari	Kunene	Namibia	13.41	-18.78	0.700	5.8	0.40	0.80	6.40	0.0	0.0	0.4	Hoffman *et al.* (1996); Gauert (2005); Singer *et al.* (2009)
Ganesh Himal	Bagmati Pradesh	Nepal	85.18	28.07	0.875	2.3	ND	16.91	2.87	ND	0.4	0.1	Ghosh *et al.* (2005); Thorpe (2008); Singer *et al.* (2009)
Duddar	Balochistan	Pakistan	66.82	26.09	0.180	15.8	ND	8.50	3.10	ND	1.3	0.5	Ahsan & Quraishi (1997); Ahsan & Mallick (1999); Singer *et al.* (2009); PorterGeo (2020a)
Gunga	Balochistan	Pakistan	66.48	27.73	0.180	6.9	ND	4.00	0.74	ND	0.3	0.1	Ahsan & Quraishi (1997); Ahsan & Mallick (1999); Husain *et al.* (2002); Singer *et al.* (2009)
Gorevsk	Krasnoyarsk Krai	Russia	93.31	58.08	0.920	300.0	ND	1.36	6.50	ND	4.1	19.5	Khiltova & Pleskach (1997); PorterGeo (2020b); Smirnov & Gorzhevsk (1977)
Kholodninskoye	Republic of Buryatia	Russia	109.80	55.85	0.760	307.0	ND	4.33	0.68	ND	13.3	2.1	Karpenko *et al.* (1981); Seltmann *et al.* (2010); PorterGeo (2020c)
Big Syncline	Northern Cape	South Africa	18.83	-29.20	1.197	100.0	0.09	2.45	1.01	0.1	2.5	1.0	Ryan *et al.* (1986); Reid *et al.* (1997); McClung *et al.* (2007)
Black Mountain (Swartberg)	Northern Cape	South Africa	18.73	-29.23	1.197	83.2	0.63	0.69	2.52	0.5	0.6	2.1	Ryan *et al.* (1986); Reid *et al.* (1997); McClung *et al.* (2007)
Broken Hill	Northern Cape	South Africa	18.78	-29.23	1.197	37.9	0.45	2.87	6.35	0.2	1.1	2.4	Ryan *et al.* (1986); Reid *et al.* (1997); McClung *et al.* (2007)

Continued overleaf...

Table 2 – continued

Deposit	State/Region	Country	Lon.[a]	Lat.[a]	Age (Ga)	Ore (Mt)	Cu (%)	Zn (%)	Pb (%)	Cu (Mt)	Zn (Mt)	Pb (Mt)	References
Broken Hill Deeps	Northern Cape	South Africa	18.81	-29.24	1.197	18.8	0.74	3.94	3.98	0.1	0.7	0.7	McClung *et al.* (2007)
Gamsberg	Northern Cape	South Africa	18.97	-29.25	1.197	199.3	ND	5.51	ND	ND	11.0	ND	Rozendaal (1986); Reid *et al.* (1997); Stalder & Rozendaal (2005); McClung *et al.* (2007); Cornell *et al.* (2009)
Bayindir	Izmir	Turkey	27.35	38.17	0.600	27.6	ND	7.50	1.50	ND	2.1	0.4	Dora (1977); Taylor *et al.* (2009)
Anarraaq	Alaska	USA	-162.96	68.16	0.338	18.0	ND	18.00	5.40	ND	3.2	1.0	Ayuso *et al.* (2004); Kelley *et al.* (2004a); Johnson *et al.* (2004); Young (2004)
Lik	Alaska	USA	-163.20	68.17	0.338	23.9	ND	2.76	8.44	ND	0.7	2.0	Young (2004); Singer *et al.* (2009); Taylor *et al.* (2009)
Red Dog	Alaska	USA	-162.80	68.07	0.338	165.0	ND	16.60	4.60	ND	27.4	7.6	Ayuso *et al.* (2004); Kelley *et al.* (2004b); Johnson *et al.* (2004); Morelli *et al.* (2004); Slack *et al.* (2004); Young (2004); Taylor *et al.* (2009)
Su (Lik South)	Alaska	USA	-163.21	68.16	0.338	20.1	ND	7.90	2.55	ND	1.6	0.5	Johnson *et al.* (2004); Young (2004); Singer *et al.* (2009); Taylor *et al.* (2009)
Triumph	Idaho	USA	-114.25	44.67	0.400	3.1	0.06	5.40	4.20	0.0	0.2	0.1	Hall (1985); Howe & Hall (1985); Turner & Otto (1995); Singer *et al.* (2009)

[a] In decimal degrees

Table 3: Global compilation of 147 Mississippi Valley-type Pb-Zn deposits shown in Figure S29, building on original database of Taylor *et al.* (2009). Ga = billion years; Mt = million tonnes; ND = no data.

Deposit	Country	Lon.[a]	Lat.[a]	Age (Ga)	Ore (Mt)	Cu (%)	Zn (%)	Pb (%)	Cu (Mt)	Zn (Mt)	Pb (Mt)	References
Ain Khala	Algeria	5.29	35.43	ND	7.1	ND	1.90	1.20	ND	0.1	0.1	Mosier *et al.* (2009); Taylor *et al.* (2009)
Boukdema-Kef Semmah	Algeria	4.89	36.21	ND	12.0	ND	6.50	2.07	ND	0.8	0.2	Singer *et al.* (2009); Taylor *et al.* (2009)
El Abed	Algeria	-1.63	34.52	0.008	30.0	ND	4.50	1.00	ND	1.4	0.3	Bouabdellah *et al.* (1999, 2012)
Kherzet Youcef	Algeria	5.28	35.46	ND	1.6	ND	18.40	3.60	ND	0.3	0.1	Singer *et al.* (2009); Taylor *et al.* (2009)
Admiral Bay	Australia	122.28	-19.23	0.420	72.0	ND	3.10	2.90	ND	2.2	2.1	McCracken *et al.* (1996); Kagara Ltd. (2008)
Bulman	Australia	134.41	-13.42	ND	0.4	ND	15.00	2.00	ND	0.1	0.0	Taylor *et al.* (2009)
Cadjebut Trend	Australia	125.96	-18.71	0.357	16.4	ND	8.90	5.00	ND	1.5	0.8	Tompkins *et al.* (1994); Vearncombe *et al.* (1995b); Tompkins *et al.* (1997)
Ediacara	Australia	138.13	-30.80	ND	29.0	ND	ND	1.07	ND	ND	0.3	USGS (2020b)
Fossil Downs	Australia	125.77	-18.19	0.357	2.2	ND	9.50	2.10	ND	0.2	0.0	Ltd. (2009)
Goongewa (Twelve Mile Bore)	Australia	125.88	-18.63	0.351	2.4	ND	10.10	2.70	ND	0.2	0.1	Brannon *et al.* (1996)
Kapok	Australia	126.01	-18.73	0.351	5.9	ND	7.80	8.70	ND	0.5	0.5	Symons & Arne (2003)
Napier Range (Narlarla)	Australia	124.73	-17.26	0.357	0.6	ND	8.50	8.00	ND	0.1	0.0	Ringrose (1984)
Pillara (Blendevale)	Australia	125.77	-18.32	0.357	19.3	ND	7.80	2.60	ND	1.5	0.5	Christensen *et al.* (1995); Vearncombe *et al.* (1995a); Gwatkin & Muccilli (2002); Symons & Arne (2005)
Sorby Hills	Australia	128.97	-15.45	ND	16.7	ND	0.70	4.50	ND	0.1	0.8	KBL Mining Ltd. (2017)
Wagon Pass	Australia	124.63	-17.18	0.357	0.5	ND	ND	ND	ND	ND	ND	Taylor *et al.* (2009)
Bleiberg	Austria	13.67	46.67	0.180	43.0	ND	5.88	1.09	ND	2.5	0.5	Schroll & Rantitsch (2005); Schroll *et al.* (2006)
Lafatsch	Austria	11.45	47.36	ND	1.0	ND	6.00	1.00	ND	0.1	0.0	Taylor *et al.* (2009)
Raibl	Austria	13.60	46.44	0.180	18.1	ND	5.97	1.22	ND	1.1	0.2	Taylor *et al.* (2009)
Schmalgraf	Belgium	6.02	50.42	ND	0.7	ND	24.00	2.10	ND	0.2	0.0	Taylor *et al.* (2009)
Fagundes	Brazil	-46.52	-16.87	ND	3.0	ND	4.50	ND	ND	0.1	ND	Taylor *et al.* (2009)
Januaria	Brazil	-44.75	-15.05	ND	0.1	ND	4.00	7.50	ND	0.0	0.0	Taylor *et al.* (2009)
Morro Agudo	Brazil	-46.80	-17.32	ND	17.0	ND	5.14	1.53	ND	0.9	0.3	Hitzman *et al.* (1995); Misi *et al.* (2005)
Nova Redencao	Brazil	-43.50	-13.00	ND	2.5	ND	0.50	6.30	ND	0.0	0.2	Misi *et al.* (2005)
Tres Irmas	Brazil	-41.80	-12.33	ND	7.0	ND	7.60	1.40	ND	0.5	0.1	Taylor *et al.* (2009)
Sedmochislenitsi	Bulgaria	23.54	43.15	0.043	16.7	0.30	1.11	1.41	0.1	0.2	0.2	Minčeva-Stefanova (1972); Taylor *et al.* (2009)
Bear-Twit	Canada	-129.42	64.03	ND	7.3	ND	5.42	2.60	ND	0.4	0.2	Paradis *et al.* (2007)
Blende	Canada	-134.67	64.40	ND	19.6	ND	3.04	2.80	ND	0.6	0.5	Paradis *et al.* (2007)
Colby	Canada	-118.73	50.73	ND	1.0	ND	ND	ND	ND	ND	ND	USGS (2020b)
Duncan	Canada	-116.95	50.37	ND	2.8	ND	3.10	3.30	ND	0.1	0.1	Taylor *et al.* (2009)
Eclipse	Canada	-96.20	75.57	ND	0.9	ND	11.31	ND	ND	0.1	ND	Taylor *et al.* (2009)
Esker	Canada	-113.43	66.97	ND	1.9	ND	3.50	1.20	ND	0.1	0.0	Paradis *et al.* (2007)

Continued overleaf...

Table 3 – continued

Deposit	Country	Lon.[a]	Lat.[a]	Age (Ga)	Ore (Mt)	Cu (%)	Zn (%)	Pb (%)	Cu (Mt)	Zn (Mt)	Pb (Mt)	References
Gayna River	Canada	-130.68	64.93	ND	50.0	ND	4.70	0.20	ND	2.4	0.1	Hewton (1982); Paradis *et al.* (2007)
Gays River	Canada	-63.36	45.03	0.303	5.1	ND	5.49	2.45	ND	0.3	0.1	Akande & Zentilli (1984); Kontak (1992); Kontak *et al.* (1994); Pan *et al.* (1993); Paradis *et al.* (2007)
Goz Creek	Canada	-132.52	64.43	ND	2.5	ND	11.00	ND	ND	0.3	ND	Paradis *et al.* (2007)
H.B.	Canada	-117.20	49.15	ND	6.5	ND	4.10	0.77	ND	0.3	0.0	Taylor *et al.* (2009)
Jersey	Canada	-117.22	49.10	ND	7.9	ND	3.49	1.63	ND	0.3	0.1	Taylor *et al.* (2009)
Jubilee	Canada	-60.96	45.98	ND	0.8	ND	5.20	1.40	ND	0.0	0.0	Fallara *et al.* (1998); Paradis *et al.* (2007)
Monarch-Kicking Horse	Canada	-116.45	51.43	0.100	0.8	ND	8.60	5.60	ND	0.1	0.0	Symons *et al.* (1998a); Paradis *et al.* (2007)
Nanisivik	Canada	-84.51	73.06	1.095	25.2	ND	7.20	0.34	ND	1.8	0.1	Olson (1984); Symons *et al.* (2000); Sherlock *et al.* (2004); Paradis *et al.* (2007); Hnatyshin *et al.* (2005)
Newfoundland Zinc (Daniel's Harbor)	Canada	-57.47	50.28	0.374	6.5	ND	8.00	ND	ND	0.5	ND	Hall *et al.* (1989); Pan & Symons (1993); Paradis *et al.* (2007)
Pine Point (district)	Canada	-114.58	60.78	0.362	79.3	ND	6.30	2.70	ND	5.0	2.1	Sasaki & Krouse (1969); Rhodes *et al.* (1984); Nakai *et al.* (1993); Symons *et al.* (1993); Hannigan (2007); Paradis *et al.* (2007)
Polaris	Canada	-96.93	75.40	0.367	26.0	ND	13.90	3.70	ND	3.6	1.0	Symons & Sangster (1992); Christensen *et al.* (1995); Randell & Anderson (1996); Dewing *et al.* (2007); Paradis *et al.* (2007)
Prairie Creek	Canada	-124.83	61.58	ND	11.9	0.40	12.50	10.10	0.0	1.5	1.2	Paradis *et al.* (2007)
Remac	Canada	-117.37	49.02	ND	5.8	ND	3.42	0.98	ND	0.2	0.1	Taylor *et al.* (2009)
Robb Lake	Canada	-123.71	56.93	0.350	7.1	ND	4.70	1.50	ND	0.3	0.1	Smethurst *et al.* (1999); Nelson *et al.* (2002); Paradis *et al.* (2007); Taylor *et al.* (2009)
Upton	Canada	-72.67	45.68	ND	1.0	0.15	0.60	1.90	0.0	0.0	0.0	Taylor *et al.* (2009)
Walton	Canada	-64.04	45.21	ND	4.9	0.04	0.11	0.32	0.0	0.0	0.0	Paradis *et al.* (2007)
Beishan	China	108.10	25.20	ND	23.9	ND	4.49	0.70	ND	1.1	0.2	Wang *et al.* (2014)
Daliangzi	China	102.88	26.63	0.366	40.0	ND	10.40	0.80	ND	4.2	0.3	Zheng & Wang (1991); Wang *et al.* (2014)
Dongjiahe	China	110.19	30.01	ND	20.0	ND	2.60	0.80	ND	0.5	0.2	Zeng & Li (2007); Wang *et al.* (2014)
Fankou	China	113.62	25.10	0.257	51.7	ND	9.97	4.90	ND	5.2	2.5	Wang *et al.* (2005, 2014)
Guanmenshan	China	124.32	42.66	1.620	3.8	ND	11.00	4.20	ND	0.4	0.2	Rui *et al.* (1991); Duan *et al.* (2008); Wang *et al.* (2014)
Houjiangqiao	China	111.72	25.30	ND	32.0	ND	1.50	0.50	ND	0.5	0.2	Li (2002); Wang *et al.* (2014)
Huayuan	China	109.41	28.41	ND	50.0	ND	3.40	ND	ND	1.7	ND	Liu *et al.* (2002); Schneider *et al.* (2002); Wang *et al.* (2014)
Jinshachang	China	103.63	28.22	ND	3.8	ND	5.00	4.10	ND	0.2	0.2	Wang *et al.* (2014)
Kuangshanchang and Qilinchang	China	103.98	26.60	0.224	7.9	ND	13.50	5.04	ND	1.1	0.4	Li *et al.* (2007b,c); Yin *et al.* (2009); Wang *et al.* (2014)
Maozu	China	102.98	27.35	0.196	10.0	ND	5.70	1.90	ND	0.6	0.2	Zhou *et al.* (2013a); Wang *et al.* (2014)
Mayuan	China	107.21	32.63	0.486	3.0	ND	4.50	4.00	ND	0.1	0.1	Li *et al.* (2007a); Wang *et al.* (2008, 2014)
Niujiaotang	China	107.66	26.24	ND	3.8	ND	6.00	ND	ND	0.2	ND	Ye *et al.* (2012); Wang *et al.* (2014)
Qixiashan	China	118.98	32.14	ND	13.7	ND	4.86	2.64	ND	0.7	0.4	Taylor *et al.* (2009); Wang *et al.* (2014)
Shanshulin	China	105.00	26.50	ND	13.1	ND	15.00	4.00	ND	2.0	0.5	Wang *et al.* (2014)
Siding	China	109.53	25.07	ND	4.5	ND	9.70	1.80	ND	0.4	0.1	Taylor *et al.* (2009)
Tianbaoshan	China	102.20	26.95	0.366	20.0	ND	10.40	1.40	ND	2.1	0.3	Wang *et al.* (2000); Zhou *et al.* (2013b); Wang *et al.* (2014)
Wulagen	China	75.12	39.35	0.054	52.8	ND	3.70	0.50	ND	2.0	0.3	Li *et al.* (2005, 2013); Wang *et al.* (2014)
Umm Gheig	Egypt	34.45	25.63	ND	1.5	ND	11.00	1.30	ND	0.2	0.0	Taylor *et al.* (2009)
Les Malines	France	4.28	43.89	0.045	12.5	ND	6.20	1.00	ND	0.8	0.1	Disnar (1996); Henry *et al.* (2001); Leach *et al.* (2001a,b, 2006); Singer *et al.* (2009)
Trves	France	3.39	44.13	0.045	0.1	ND	6.00	1.40	ND	0.0	0.0	Disnar (1996); Henry *et al.* (2001); Leach *et al.* (2001a,b, 2006); Singer *et al.* (2009)
Villemagne	France	3.45	44.13	0.045	0.6	ND	6.30	3.30	ND	0.0	0.0	Disnar (1996); Henry *et al.* (2001); Leach *et al.* (2001a,b, 2006); Singer *et al.* (2009)
Black Angel	Greenland	-51.75	71.17	ND	13.6	ND	12.30	4.00	ND	1.7	0.5	Pedersen (1980); Thomassen (2006); Taylor *et al.* (2009)
Nunngarut	Greenland	-51.70	71.13	ND	0.4	ND	8.80	3.90	ND	0.0	0.0	Taylor *et al.* (2009); Wang *et al.* (2014)
Ballaria (Mochia Balaria)	India	73.73	24.35	1.702	16.0	ND	5.85	1.17	ND	0.9	0.2	Deb *et al.* (1989); Deb & Sarkar (1990); Bhattacharya (2004); Deb & Thorpe (2004); Sarkar & Banerjee (2004); Ramakrishnan & Vaidyanathan (2008)

Continued overleaf...

Table 3 – continued

Deposit	Country	Lon.[a]	Lat.[a]	Age (Ga)	Ore (Mt)	Cu (%)	Zn (%)	Pb (%)	Cu (Mt)	Zn (Mt)	Pb (Mt)	References
Baroi (Baroi Magra)	India	73.68	24.32	1.710	7.0	ND	1.71	4.60	ND	0.1	0.3	Deb *et al.* (1989); Deb & Sarkar (1990); Bhattacharya (2004); Deb & Thorpe (2004); Sarkar & Banerjee (2004); Ramakrishnan & Vaidyanathan (2008)
Mochia	India	73.72	24.36	1.702	17.0	ND	4.26	1.75	ND	0.7	0.3	Deb *et al.* (1989); Deb & Sarkar (1990); Bhattacharya (2004); Deb & Thorpe (2004); Sarkar & Banerjee (2004); Ramakrishnan & Vaidyanathan (2008)
Paduna North Block	India	73.69	24.27	1.710	3.1	ND	3.25	0.67	ND	0.1	0.0	Deb *et al.* (1989); Deb & Sarkar (1990); Bhattacharya (2004); Sarkar & Banerjee (2004); Ramakrishnan & Vaidyanathan (2008)
Zawarmala	India	73.68	24.33	1.712	18.0	ND	3.72	2.16	ND	0.7	0.4	Deb *et al.* (1989); Deb & Sarkar (1990); Bhattacharya (2004); Deb & Thorpe (2004); Sarkar & Banerjee (2004); Ramakrishnan & Vaidyanathan (2008)
Angouran	Iran	47.41	36.62	0.021	19.3	ND	23.39	4.06	ND	4.5	0.8	Gilg *et al.* (2006)
Anjireh-Vejin	Iran	51.15	32.71	ND	1.2	ND	ND	ND	ND	ND	ND	Taylor *et al.* (2009)
Emarat	Iran	49.61	33.75	0.056	10.0	ND	6.00	2.26	ND	0.6	0.2	Ehya *et al.* (2010)
Irankuh	Iran	51.68	32.55	0.056	10.0	ND	7.40	2.40	ND	0.7	0.2	Ghazban *et al.* (1994)
Kuh-e-Surmeh	Iran	52.50	28.50	ND	0.9	ND	12.10	5.40	ND	0.1	0.0	Taylor *et al.* (2009)
Mehdiabad	Iran	54.99	31.73	0.056	394.0	ND	4.20	1.60	ND	16.5	6.3	Reichert (2007); Taylor *et al.* (2009)
Abbeytown	Ireland	-8.53	54.22	0.360	2.2	ND	3.80	1.50	ND	0.1	0.0	Taylor *et al.* (2009)
Allenwood West	Ireland	6.90	53.29	ND	10.1	ND	1.60	0.40	ND	0.2	0.0	Taylor *et al.* (2009)
Ballinalack	Ireland	-7.47	53.65	0.360	3.5	ND	5.90	1.10	ND	0.2	0.0	Taylor *et al.* (2009)
Boston Hill	Ireland	6.94	53.22	ND	0.8	ND	2.70	1.10	ND	0.0	0.0	Taylor *et al.* (2009)
Carrickittle	Ireland	-8.37	52.51	0.360	0.2	ND	6.06	ND	ND	0.0	ND	Taylor *et al.* (2009)
Courtbrown	Ireland	-8.98	52.64	0.360	1.0	ND	3.50	2.00	ND	0.0	0.0	Taylor *et al.* (2009)
Galmoy	Ireland	-7.59	52.80	0.360	10.9	ND	12.43	1.60	ND	1.4	0.2	Taylor *et al.* (2009)
Garrycam	Ireland	-7.72	53.65	0.360	1.4	ND	2.67	0.18	ND	0.0	0.0	Taylor *et al.* (2009)
Harberton Bridge	Ireland	-6.86	53.27	ND	3.9	ND	8.10	1.21	ND	0.3	0.0	Taylor *et al.* (2009)
Keel	Ireland	-7.73	53.65	0.360	1.9	ND	7.71	1.04	ND	0.1	0.0	Taylor *et al.* (2009)
Lisheen	Ireland	-7.75	52.75	0.350	22.0	ND	11.50	1.90	ND	2.5	0.4	Taylor *et al.* (2009)
Moyvoughly	Ireland	-7.68	53.45	ND	0.1	ND	6.90	1.10	ND	0.0	0.0	Taylor *et al.* (2009)
Navan	Ireland	-6.68	53.66	0.360	95.3	ND	8.30	2.10	ND	7.9	2.0	Blakeman *et al.* (2002)
Oldcastle	Ireland	-7.13	53.77	0.360	3.0	ND	4.30	0.60	ND	0.1	0.0	Taylor *et al.* (2009)
Rickardstown	Ireland	6.82	53.90	ND	3.5	ND	2.20	1.10	ND	0.1	0.0	Taylor *et al.* (2009)
Silvermines	Ireland	-8.27	52.79	0.360	17.7	ND	6.43	2.53	ND	1.1	0.4	Coomer & Robinson (1976)
Tatestown	Ireland	-6.74	53.69	0.360	3.6	ND	5.30	1.50	ND	0.2	0.1	Taylor *et al.* (2009)
Tynagh	Ireland	-8.34	53.16	0.360	9.2	0.52	5.00	6.19	0.0	0.5	0.6	Taylor *et al.* (2009)
Gorno	Italy	9.50	45.52	ND	6.2	ND	11.45	2.26	ND	0.7	0.1	Taylor *et al.* (2009)
Salafossa	Italy	12.40	46.34	0.180	11.0	ND	5.00	0.99	ND	0.5	0.1	Taylor *et al.* (2009)
Sumsar	Kyrgyzstan	71.34	41.22	ND	30.0	ND	3.00	5.00	ND	0.9	1.5	Taylor *et al.* (2009)
Beddiane	Morocco	-1.80	34.40	0.008	6.7	ND	0.00	16.60	ND	0.0	1.1	Bouabdellah *et al.* (1999, 2012)
Bou Beker	Morocco	-1.71	34.30	0.008	18.0	ND	4.00	3.50	ND	0.7	0.6	Bouabdellah *et al.* (1999, 2012)
Mekta	Morocco	-1.82	34.38	0.008	2.0	ND	0.00	13.00	ND	0.0	0.3	Bouabdellah *et al.* (1999, 2012)
Touissit	Morocco	-1.76	34.46	0.008	12.0	ND	3.50	3.00	ND	0.4	0.4	Bouabdellah *et al.* (1999, 2012)
Berg Aukas	Namibia	18.26	-19.57	0.750	3.2	ND	17.00	4.00	ND	0.5	0.1	Taylor *et al.* (2009)
Florida Canyon	Peru	-78.06	-5.92	ND	7.0	ND	ND	ND	ND	ND	ND	Basuki *et al.* (2008)
San Vicente	Peru	-75.35	-11.23	ND	20.0	ND	12.00	0.90	ND	2.4	0.2	Fontbote & Gorzawski (1990); Gunnesch *et al.* (1990); Schütfort (2001); Taylor *et al.* (2009)
Silesian-Crakow district	Poland	19.53	50.29	0.046	731.0	ND	4.24	1.34	ND	31.0	9.8	Symons *et al.* (1995); Leach *et al.* (1996, 2001a)
Pavlovskoye	Russia	55.17	72.92	ND	128.0	ND	3.90	1.53	ND	5.0	2.0	Taylor *et al.* (2009)
Sardana	Russia	136.48	60.19	ND	10.0	ND	6.00	3.00	ND	0.6	0.3	Nokleberg *et al.* (2005); Taylor *et al.* (2009)
Urultun	Russia	148.42	63.48	ND	23.0	ND	6.74	2.85	ND	1.6	0.7	Nokleberg *et al.* (2005); Taylor *et al.* (2009)
Jabal Dhaylan	Saudi Arabia	37.25	25.50	ND	1.2	ND	5.60	1.40	ND	0.1	0.0	Taylor *et al.* (2009)
Mezica	Slovenia	14.52	46.30	0.180	16.2	ND	2.47	4.94	ND	0.4	0.8	Taylor *et al.* (2009)
Bushy Park	South Africa	23.60	-28.88	2.049	10.0	ND	5.00	0.60	ND	0.5	0.1	Kesler & Reich (2006)
Pering	South Africa	24.27	-27.43	1.980	18.0	ND	3.60	0.60	ND	0.6	0.1	Huizenga *et al.* (2006)
Picos de Europa	Spain	-4.56	43.10	0.015	0.6	ND	13.00	2.00	ND	0.1	0.0	Fernández *et al.* (2000)

Continued overleaf...

Table 3 – continued

Deposit	Country	Lon.[a]	Lat.[a]	Age (Ga)	Ore (Mt)	Cu (%)	Zn (%)	Pb (%)	Cu (Mt)	Zn (Mt)	Pb (Mt)	References
Reocin	Spain	-4.41	43.28	0.015	62.5	ND	8.70	1.00	ND	5.4	0.6	Velasco *et al.* (2003); Symons *et al.* (2009)
Troya	Spain	-2.28	42.77	ND	3.5	0.20	13.10	1.00	0.0	0.5	0.0	Velasco *et al.* (1996); Singer *et al.* (2009); Taylor *et al.* (2009)
Bou Grine	Tunisia	8.94	36.11	ND	5.5	ND	12.00	2.50	ND	0.7	0.1	Sainfeld (1956); Orgeval (1995); Taylor *et al.* (2009); Jemmali *et al.* (2013)
Bou Jabeur	Tunisia	8.28	35.78	ND	8.8	ND	2.17	0.99	ND	0.2	0.1	Sainfeld (1956); Charef *et al.* (2009); Taylor *et al.* (2009)
Djebba	Tunisia	9.09	36.47	ND	4.0	ND	6.00	4.00	ND	0.2	0.2	Sainfeld (1956); Singer *et al.* (2009); Taylor *et al.* (2009)
Fedj-el Adoum	Tunisia	9.10	36.37	ND	3.0	ND	6.00	2.00	ND	0.2	0.1	Sainfeld (1956); Charef & Sheppard (1987); Singer *et al.* (2009); Taylor *et al.* (2009)
Yahyali (district)	Turkey	36.32	38.33	ND	2.4	ND	21.00	3.60	ND	0.5	0.1	Koptagel *et al.* (2007); Singer *et al.* (2009); Taylor *et al.* (2009)
Annapolis	USA	-90.68	37.36	0.273	1.1	ND	ND	2.30	ND	ND	0.0	Harper & Borrok (2007)
Austinville-Ivanhoe (district)	USA	-80.92	36.85	ND	22.6	ND	3.70	0.70	ND	0.8	0.2	Jones *et al.* (1996)
Balmat	USA	-75.40	44.25	1.150	31.7	ND	8.88	0.25	ND	2.8	0.1	Lea & Dill Jr. (1968); Fletcher & Farquhar (1977, 1982); Whelan *et al.* (1984); Steers (2003)
Central Tennesse (district)	USA	-85.93	36.20	0.255	71.0	ND	3.31	ND	ND	2.4	ND	Kesler *et al.* (1994); Harper & Borrok (2007)
Edwards	USA	-75.26	44.34	1.150	6.0	ND	10.80	0.31	ND	0.6	0.0	Lea & Dill Jr. (1968); Fletcher & Farquhar (1977, 1982); Steers (2003)
Fredricktown	USA	-90.27	37.55	0.273	13.6	ND	ND	3.90	ND	ND	0.5	Harper & Borrok (2007)
Friedensville	USA	-75.38	40.56	0.273	2.6	ND	6.50	ND	ND	0.2	ND	Harper & Borrok (2007)
Hyatt	USA	-75.33	44.30	ND	0.9	ND	8.60	ND	ND	0.1	ND	USGS (2020b)
Idol	USA	-83.41	36.37	ND	6.8	ND	3.00	ND	ND	0.2	ND	USGS (2020b)
Indian Creek	USA	-90.91	38.04	0.273	26.4	0.14	0.40	3.50	0.0	0.1	0.9	Harper & Borrok (2007)
Mascott-Jefferson City (East Tennessee) (district)	USA	-83.00	36.00	0.362	500.0	ND	3.00	ND	ND	15.0	ND	Harper & Borrok (2007)
Metaline (district)	USA	-117.36	48.87	ND	7.5	ND	2.77	1.34	ND	0.2	0.1	St Marie & Kesler (2000)
Northern Arkansas (district)	USA	-92.56	36.13	0.265	ND	ND	ND	ND	ND	ND	ND	Harper & Borrok (2007)
Old Lead Belt (district)	USA	-90.50	37.50	0.273	239.0	ND	0.30	2.90	ND	0.7	6.9	Harper & Borrok (2007)
Pend Oreille-Yellowhead	USA	-117.30	48.90	ND	8.8	ND	6.75	1.34	ND	0.6	0.1	Taylor *et al.* (2009)
Pierrepont	USA	-75.02	44.50	ND	2.3	ND	16.40	ND	ND	0.4	ND	USGS (2020b)
Reef Ridge	USA	-154.25	63.41	ND	11.8	ND	0.99	ND	ND	0.1	ND	Taylor *et al.* (2009)
Sherman	USA	-106.17	39.14	0.272	0.7	0.10	4.00	0.80	0.0	0.0	0.0	Taylor *et al.* (2009)
Tri-state (district)	USA	-94.50	37.00	0.258	453.6	ND	2.33	0.57	ND	10.6	2.6	Taylor *et al.* (2009)
Upper Mississippi Valley (district)	USA	-90.23	42.57	0.270	40.2	ND	2.73	1.86	ND	1.1	0.7	Brannon *et al.* (1992); Harper & Borrok (2007); Taylor *et al.* (2009)
Van Stone	USA	-117.76	48.76	ND	6.2	ND	4.16	0.04	ND	0.3	0.0	Taylor *et al.* (2009)
Viburnum Trend (distict)	USA	-91.13	37.58	0.273	276.3	0.20	1.05	5.72	0.6	2.9	15.8	Sverjensky (1981); Symons *et al.* (1998b); Harper & Borrok (2007); Taylor *et al.* (2009); Lori (2014)

[a] In decimal degrees

Table 4: Global compilation of 139 sedimentary copper deposits shown in Figure S30. Primarily compiled from Hitzman *et al.* (2005), cross-checked against Cox *et al.* (2007), with original references reported where available. Ga = billion years; Mt = million tonnes; ND = no data.

Deposit	State/Region	Country	Lon.[a]	Lat.[a]	Age (Ga)	Cu (Mt)	References
Aynak	Logar	Afganistan	69.30	34.27	0.570	7.00	Abdullah S. *et al.* (1977); Sillitoe (1980)
Cachoeiras de Binga	Cuanza Sul	Angola	14.09	-11.08	0.115	0.13	Van Eden (1978)
Martin Bronce	Jujuy	Argentina	-64.42	-24.17	0.090	0.09	Zappettini (1999)
Barda Gonzalez	Neuqun	Argentina	-68.98	-38.88	0.090	0.13	Northern Miner (1995)
Cerro Granito	Neuqun	Argentina	-69.82	-39.22	0.090	0.01	Yamana Resources Inc. (1996)
Sauzal Bonito	Neuqun	Argentina	-69.18	-38.63	0.090	0.25	Yamana Resources Inc. (1996)
Tordillos	Neuqun	Argentina	-68.97	-38.45	0.090	0.04	Northern Miner (1995)

Continued overleaf...

Table 4 – continued

Deposit	State/Region	Country	Lon.[a]	Lat.[a]	Age (Ga)	Cu (Mt)	References
Juramento	Salta	Argentina	-65.15	-25.22	0.090	0.09	Durieux & Brown (2001)
Redbank	Northern Territory	Australia	137.74	-17.19	1.600	0.14	Sexton (2011)
Gunpowder	Queensland	Australia	139.37	-19.70	1.550	0.27	Scott & Taylor (1977, 1982); Clark (2001)
Lady Annie	Queensland	Australia	139.04	-19.77	1.550	0.46	Sexton (2011)
Mt Isa Copper	Queensland	Australia	139.48	-20.74	1.523	7.43	Perkins (1984); Heinrich *et al.* (1995); Waring *et al.* (1998); Matthäi *et al.* (2004)
Walford Creek	Queensland	Australia	138.27	-17.78	1.600	0.20	Sexton (2011)
Emmie Bluff	South Australia	Australia	137.15	-31.11	2.050	0.33	Geological Survey of South Australia (2020)
Kapunda	South Australia	Australia	138.92	-34.35	0.650	0.12	Terramin Australia Ltd. (2018); Geological Survey of South Australia (2020)
Mount Gunson	South Australia	Australia	137.25	-31.45	0.630	0.31	Geological Survey of South Australia (2020)
Maroochydore	Western Australia	Australia	122.31	-22.20	0.820	0.39	Anderson *et al.* (2001)
Nifty	Western Australia	Australia	121.57	-21.65	0.822	1.68	Anderson *et al.* (2001)
Chacarilla	La Paz	Bolivia	-68.20	-17.58	0.028	0.06	Cox *et al.* (1992); Long (1992)
Corocoro	La Paz	Bolivia	-68.45	-17.16	0.040	0.50	Drummond (1996)
Azurita	Oruro	Bolivia	-68.15	-18.07	0.013	0.52	Northern Miner (1996a)
Thakadu	Central	Botswana	26.75	-21.08	2.050	0.18	Mining Magazine (1998a)
Ngwako Pan	Ngamiland	Botswana	23.10	-20.75	0.900	17.52	Anglo American Corp. (1989); Schwartz *et al.* (1995); Gencor (1995); Delta Gold (2000)
Pedra Verde	Cear	Brazil	-41.12	-3.50	1.300	0.12	Brizzi & Roberto (1988)
Bahia	Par	Brazil	-49.08	-5.67	2.050	0.79	Dayton & Sassos (1985)
Camaqua	Rio Grande do Sul	Brazil	-52.40	-30.78	0.700	0.08	Teixeira & Gonzalez (1988)
Venesta	Razgrad	Bulgaria	26.75	42.67	0.200	0.01	Todorov (1997)
Dorchester	New Brunswick	Canada	-64.48	45.93	0.300	0.05	Canerpa-Amax (1974)
Jay	Northwest Territories	Canada	-127.83	63.77	0.750	0.03	Ruelle (1982)
Redstone	Northwest Territories	Canada	-126.62	62.69	0.750	1.32	Gourlay (2003)
Storm	Nunavut	Canada	-94.07	73.62	0.450	0.10	Hitzman *et al.* (2005)
San Bartolo	Antofagasta	Chile	-68.23	-22.73	0.012	0.03	Camus (1986)
San Jose de Tuina	Antofagasta	Chile	-68.45	-22.52	0.300	0.12	Northern Miner (1997); Hitzman *et al.* (2005)
Teresita	Atacama	Chile	-70.23	-27.35	0.120	0.02	Hitzman *et al.* (2005)
LaoXue	Sichuan	China	102.33	26.29	2.050	0.50	Hitzman *et al.* (2005)
TangDan	Sichuan	China	102.67	26.25	1.500	3.60	Ren (1994); Hitzman *et al.* (2005)
Dishui	Xinjiang	China	81.25	41.50	0.013	0.09	Hitzman *et al.* (2005)
Jiashi	Xinjiang	China	77.08	39.83	0.004	0.15	Hitzman *et al.* (2005)
Jinman	Yunnan	China	99.05	26.05	0.170	ND	Hitzman *et al.* (2005)
Lanniping	Yunnan	China	103.07	26.10	0.900	ND	Hitzman *et al.* (2005)
LiuZu	Yunnan	China	103.25	25.42	0.070	0.85	Hitzman *et al.* (2005)
Dikulushi	Haut-Katanga	Democratic Republic of Congo	28.25	-9.17	0.900	0.15	Anvil Mining NL (2003); Northern Miner (2004a)
Etoile	Haut-Katanga	Democratic Republic of Congo	27.58	-11.65	0.900	4.16	Northern Miner (1996c); Hitzman *et al.* (2005)
Kamatanda	Haut-Katanga	Democratic Republic of Congo	26.78	-10.95	0.900	0.50	Hitzman *et al.* (2005)
Kambove	Haut-Katanga	Democratic Republic of Congo	26.61	-10.88	0.900	2.78	Northern Miner (1996b); Hitzman *et al.* (2005)
Kimbwe	Haut-Katanga	Democratic Republic of Congo	27.51	-11.14	0.900	2.00	Hitzman *et al.* (2005)
Kinsenda	Haut-Katanga	Democratic Republic of Congo	27.97	-12.28	0.900	1.75	U.S. Bureau of Mines (1974); Hitzman *et al.* (2005)
Lonshi	Haut-Katanga	Democratic Republic of Congo	28.94	-13.18	0.900	0.27	Northern Miner (2004b)
Lufua	Haut-Katanga	Democratic Republic of Congo	28.50	-12.75	0.900	1.02	Northern Miner (2004c)
Luishia	Haut-Katanga	Democratic Republic of Congo	27.01	-11.17	0.900	1.81	Hitzman *et al.* (2005)
Luiswishi	Haut-Katanga	Democratic Republic of Congo	27.42	-11.51	0.900	0.20	Hitzman *et al.* (2005)
M'Sesa	Haut-Katanga	Democratic Republic of Congo	26.61	-10.85	0.900	0.46	Hitzman *et al.* (2005)
Musoshi (see Konkola)	Haut-Katanga	Democratic Republic of Congo	27.71	-12.27	0.900	3.57	Hitzman *et al.* (2005)
Kakanda	Lualaba	Democratic Republic of Congo	26.41	-10.73	0.900	1.11	Hitzman *et al.* (2005)
Kalukundi	Lualaba	Democratic Republic of Congo	25.92	-10.63	0.900	0.51	Northern Miner (2004d)
Kamfundwa	Lualaba	Democratic Republic of Congo	26.59	-10.81	0.900	0.28	Hitzman *et al.* (2005)
Kolwezi	Lualaba	Democratic Republic of Congo	25.42	-10.73	0.900	39.40	Northern Miner (2002a); Hitzman *et al.* (2005)

Continued overleaf...

Table 4 – continued

Deposit	State/Region	Country	Lon.[a]	Lat.[a]	Age (Ga)	Cu (Mt)	References
Tenke-Fungurume	Lualaba	Democratic Republic of Congo	26.15	-10.58	0.900	43.15	Mining Magazine (1998b); Tenke Mining Corp. (2003)
Spremberg	Brandenburg	Germany	14.37	51.58	0.260	1.50	Hitzman *et al.* (2005)
Richelsdorf	Hesse	Germany	9.90	50.98	0.260	0.42	Walther (1986)
Marsberg	North Rhine-Westphalia	Germany	8.89	51.47	0.260	0.06	Walther (1986)
Mansfeld	Saxony-Anhalt	Germany	11.47	51.60	0.260	2.63	Hitzman *et al.* (2005)
Timna	Southern	Israel	34.95	29.77	0.530	0.29	Vered-Weiss *et al.* (1971)
Fenan	Tafilah	Jordan	35.42	30.60	0.560	0.78	U.S. Bureau of Mines (1984)
Dzhezkazgan	Karagandy	Kazakstan	67.39	48.12	0.320	22.00	Hitzman *et al.* (2005)
East Saryoba	Karagandy	Kazakstan	67.43	48.28	0.320	0.78	Hitzman *et al.* (2005)
Itauz	Karagandy	Kazakstan	67.33	48.27	0.300	0.87	Hitzman *et al.* (2005)
Karashoshak	Karagandy	Kazakstan	67.72	48.34	0.300	0.49	Hitzman *et al.* (2005)
Taskura	Karagandy	Kazakstan	68.33	48.63	0.270	0.01	Abdulin *et al.* (1998); Hitzman *et al.* (2005)
West Saryoba	Karagandy	Kazakstan	67.40	48.28	0.320	0.77	Hitzman *et al.* (2005)
Zhaman-Aibat	Karagandy	Kazakstan	67.30	47.87	0.320	2.90	Abdulin *et al.* (1998); Hitzman *et al.* (2005)
Boleo	Baja California Sur	Mexico	-112.50	27.17	0.003	4.04	Bailes *et al.* (2001)
Khatuugiin	Khovd	Mongolia	90.15	48.65	0.350	ND	Nokleberg *et al.* (2003)
Omnogobi	Uvs	Mongolia	91.68	49.13	0.350	ND	Nokleberg *et al.* (2003)
Bleida	Dra-Tafilalet	Morocco	-6.17	30.33	2.050	0.18	Hitzman *et al.* (2005)
Jbel Hassel	Dra-Tafilalet	Morocco	-6.00	30.33	0.510	0.05	Hitzman *et al.* (2005)
Talat N'Ouamane	Souss-Massa	Morocco	-8.35	30.09	0.530	0.02	Hitzman *et al.* (2005)
Tazalaght	Souss-Massa	Morocco	-8.75	29.77	0.900	0.03	Hitzman *et al.* (2005)
Klein Aub	Hardap	Namibia	16.63	-23.80	0.900	0.18	Hitzman *et al.* (2005)
Oamites	Khomas	Namibia	17.10	-22.98	0.900	0.08	Lee & Glenister (1976)
Witvlei	Omaheke	Namibia	18.53	-22.38	0.900	0.12	Hitzman *et al.* (2005)
Tschudi	Oshikoto	Namibia	17.51	-19.26	0.900	0.14	Hitzman *et al.* (2005)
Repparfjord	Troms og Finnmark	Norway	24.22	70.43	1.000	0.08	Bjørlykke *et al.* (1985); Stribrny (1985)
Negra Huanusha	Junn	Peru	-75.85	-11.30	0.260	ND	Kobe (1960)
Kaleje	Greater Poland	Poland	17.62	52.18	0.260	40.00	Hitzman *et al.* (2005)
Sulmierzyce	Greater Poland	Poland	17.62	51.65	0.260	74.00	Oszczepalski & Rydzewski (1997); Hitzman *et al.* (2005)
Borzecin- Janowo	Lower Silesia	Poland	16.90	51.48	0.260	28.00	Oszczepalski & Rydzewski (1997); Hitzman *et al.* (2005)
Konrad	Lower Silesia	Poland	13.72	51.25	0.260	0.67	Oszczepalski & Rydzewski (1997); Hitzman *et al.* (2005)
Lena	Lower Silesia	Poland	15.82	51.11	0.260	0.12	Hitzman *et al.* (2005)
Lubin	Lower Silesia	Poland	16.13	51.40	0.260	82.80	Wodzicki & Piestrzyński (1994); Przeniosło (2000); Piestrzyński & Wodzicki (2000)
Wartowice	Lower Silesia	Poland	15.58	51.18	0.260	0.70	Hitzman *et al.* (2005)
Zary Pericline	Lower Silesia	Poland	14.97	51.88	0.260	3.20	Oszczepalski & Rydzewski (1997)
Zary	Lubusz	Poland	15.09	51.64	0.270	3.20	Oszczepalski & Rydzewski (1997)
Lena	Irkutsk	Russia	106.50	58.77	0.520	1.35	Narkelyun *et al.* (1971)
Sakinskoye	Irkutsk	Russia	118.50	58.58	2.050	ND	Volodin *et al.* (1994); Nokleberg *et al.* (2003)
Graviisk	Krasnoyarsk Krai	Russia	87.55	66.52	0.600	ND	Rzhevskii *et al.* (1988); Dodin *et al.* (2000); Hitzman *et al.* (2005)
Kunshskoye	Krasnoyarsk Krai	Russia	94.97	58.50	0.900	0.02	Nokleberg *et al.* (2003)
Oroek	Magadan	Russia	152.80	64.90	1.300	ND	Nockleberg *et al.* (1997); Hitzman *et al.* (2005)
Agyndja	Sakha Republic	Russia	148.00	65.22	0.480	ND	Shpikerman (1990); Nockleberg *et al.* (1997)
Kurpandja	Sakha Republic	Russia	137.02	63.52	0.385	0.50	Nockleberg *et al.* (1997)
Pravo-Ingamakitsk	Zabaykalsky Krai	Russia	118.67	56.42	2.000	ND	Volodin *et al.* (1994); Nokleberg *et al.* (2003)
Udokan	Zabaykalsky Krai	Russia	118.43	56.59	2.100	24.00	Kirkham *et al.* (1994); Volodin *et al.* (1994); Nokleberg *et al.* (2003)
Jabal Murryyi	Al Bahah	Saudi Arabia	41.57	20.11	0.800	0.01	Hitzman *et al.* (2005)
Cashin	Colorado	USA	-108.95	38.30	0.170	0.06	Tanaka (2004)
Snowstorm	Idaho	USA	-115.72	47.48	1.500	0.03	Hitzman *et al.* (2005)
Kona Dolomite	Michigan	USA	-87.45	46.53	2.000	3.50	Wilband (1978); Hitzman *et al.* (2005)
Presque Isle	Michigan	USA	-89.98	46.68	2.050	1.18	Hitzman *et al.* (2005)

Continued overleaf...

Table 4 – continued

Deposit	State/Region	Country	Lon.[a]	Lat.[a]	Age (Ga)	Cu (Mt)	References
White Pine	Michigan	USA	-89.57	46.77	1.100	10.13	Mining Journal of London (1989); Seasor & Brown (1989); Hitzman *et al.* (2005)
Rock Creek	Montana	USA	-115.68	48.08	1.500	2.42	Northern Miner (2002b); Hitzman *et al.* (2005)
Spar Lake	Montana	USA	-115.90	48.23	1.500	0.46	Balla (1982); Hitzman *et al.* (2005)
Champion	New Mexico	USA	-105.50	36.50	1.500	0.25	Northern Miner (1996d); U.S. Bureau of Mines (1998)
Nacimiento	New Mexico	USA	-106.88	36.01	0.220	0.06	Ahlness & Pojar (1983)
Creta	Oklahoma	USA	-99.35	34.65	0.270	0.04	Hitzman *et al.* (2005)
Mangum	Oklahoma	USA	-99.50	34.88	0.270	0.07	Hitzman *et al.* (2005)
Lisbon Valley	Utah	USA	-109.10	39.15	0.130	0.58	Summo Minerals Corp. (2001)
Silver Reef	Utah	USA	-113.42	37.28	0.220	0.04	James & Newman (1986); Hitzman *et al.* (2005)
Seboruco	Los Andes	Venezuela	-72.00	8.00	0.200	0.18	Rodriguez (1990)
Baluba (see Luanshya)	Copperbelt	Zambia	28.38	-13.05	0.900	1.32	Lungu (1998); Hitzman *et al.* (2005)
Bwana Mkubwa	Copperbelt	Zambia	28.69	-13.02	0.900	0.35	Northern Miner (1998)
Chambishi	Copperbelt	Zambia	28.05	-12.68	0.900	10.40	Hitzman *et al.* (2005)
Chibuluma South	Copperbelt	Zambia	28.05	-12.83	0.900	0.34	McGregor (1991); Northern Miner (2000a)
Chibuluma-Chibuluma West	Copperbelt	Zambia	28.13	-12.83	0.900	0.74	McGregor (1991); Crew Development Corp. (1998)
Fituaola	Copperbelt	Zambia	27.88	-12.41	0.900	0.13	Hitzman *et al.* (2005)
Konkola-Kirila Bombwe	Copperbelt	Zambia	27.83	-12.39	0.900	27.22	Northern Miner (1998); Hitzman *et al.* (2005)
Luanshya	Copperbelt	Zambia	28.38	-13.13	0.900	7.41	Lungu (1998); Hitzman *et al.* (2005)
Mindola-Nkana N-S	Copperbelt	Zambia	28.17	-12.80	0.900	12.16	McGregor (1991); Northern Miner (2000c)
Mufulira	Copperbelt	Zambia	28.24	-12.52	0.900	8.14	McGregor (1991); Northern Miner (2000b)
Muliashi (see Luanshiya)	Copperbelt	Zambia	28.28	-13.08	0.900	0.21	McGregor (1991)
Mutundu North	Copperbelt	Zambia	27.62	-12.50	0.900	0.06	McGregor (1991)
Nchanga	Copperbelt	Zambia	27.87	-12.53	0.900	18.29	Hitzman *et al.* (2005)
Nkana West Limb	Copperbelt	Zambia	27.18	-12.83	0.900	1.88	McGregor (1991)
Chimiwungo-Lumwana	North-Western	Zambia	25.85	-12.18	0.900	10.00	Northern Miner (2004e)
Kalumbila	North-Western	Zambia	25.33	-12.25	0.900	0.26	Steven & Armstrong (2003)
Alaska area	Mashonaland West	Zimbabwe	30.01	-17.43	0.900	0.17	Maiden *et al.* (1984); Newham (1986)
Mangula	Mashonaland West	Zimbabwe	30.15	-16.88	0.900	0.74	Maiden *et al.* (1984); Newham (1986)
Norah	Mashonaland West	Zimbabwe	30.15	-16.93	0.900	0.12	Maiden *et al.* (1984); Newham (1986)
Shackleton	Mashonaland West	Zimbabwe	30.04	-17.27	1.250	0.04	Maiden *et al.* (1984); Newham (1986)
Umkondo	Masvingo	Zimbabwe	32.15	-20.32	0.900	0.03	Newham (1986)
Copper Queen	Midlands	Zimbabwe	29.22	-17.52	0.900	0.19	U.S. Bureau of Mines (1980)

[a] In decimal degrees

Table 5: Global compilation of 108 magmatic nickel deposits shown in Figure S31. Primarily compiled from Hoatson *et al.* (2006), with original references reported where available. Ga = billion years; Mt = million tonnes.

Deposit	State/Region	Country	Lon.[a]	Lat.[a]	Age (Ga)	Ore (Mt)	Ni (%)	Ni (Mt)	References
Avebury	Tasmania	Australia	145.25	-41.92	0.360	11.59	1.02	0.118	Newnham (2003)
Armstrong (formerly Moore)	Western Australia	Australia	121.53	-31.42	2.705	2.06	1.22	0.025	Nelson (1997a)
Beta	Western Australia	Australia	121.69	-31.24	2.705	7.60	3.63	0.276	Nelson (1997a)
Black Swan (incl. Silver Swan, Cygnet)	Western Australia	Australia	121.65	-30.39	2.706	11.10	1.93	0.214	Kositcin *et al.* (2008)
Blair	Western Australia	Australia	121.72	-30.91	2.705	1.33	2.64	0.035	Nelson (1997a)
Carnilya Hill	Western Australia	Australia	121.86	-31.05	2.705	0.52	2.68	0.014	Nelson (1997a)
Carr Boyd Rocks	Western Australia	Australia	121.63	-30.07	2.700	1.02	1.17	0.012	Groenewald *et al.* (2009)
Cliffs-Charterhall	Western Australia	Australia	120.55	-27.31	2.705	2.40	4.04	0.097	Nelson (1997a)
Copernicus	Western Australia	Australia	127.99	-17.66	1.844	0.24	1.50	0.004	Page & Hoatson (2000)
Corkwood	Western Australia	Australia	128.19	-17.30	1.844	0.23	0.65	0.001	Page & Hoatson (2000)
Cosmos	Western Australia	Australia	120.58	-27.60	2.705	1.02	7.77	0.079	Nelson (1997a)
East Scotia	Western Australia	Australia	121.46	-31.18	2.705	0.08	2.00	0.002	Nelson (1997a)

Continued overleaf...

Table 5 – continued

Deposit	State/Region	Country	Lon.[a]	Lat.[a]	Age (Ga)	Ore (Mt)	Ni (%)	Ni (Mt)	References
Emily Ann	Western Australia	Australia	120.48	-32.20	2.921	2.08	3.62	0.075	Wang *et al.* (1996)
Forrestania Nickel (incl. Cosmic Boy, Daybreak, Digger Rocks, Flying Fox, New Morning)	Western Australia	Australia	119.81	-32.72	3.000	7.57	1.91	0.145	Wang *et al.* (1996)
Gibb	Western Australia	Australia	121.68	-31.18	2.705	0.25	2.04	0.005	Nelson (1997a)
Honeymoon Well (incl. Harrier, Wedgetail)	Western Australia	Australia	120.38	-26.92	2.705	134.80	0.75	1.011	Nelson (1997a)
Jericho	Western Australia	Australia	120.58	-27.39	2.705	ND	ND	0.405	Nelson (1997a)
Kambalda (incl. Kambalda Dome St Ives-Tramways)	Western Australia	Australia	121.65	-31.18	2.705	42.06	3.30	1.388	Nelson (1997b)
Lanfranchi	Western Australia	Australia	121.84	-31.51	2.705	3.65	2.02	0.074	Nelson (1997b)
Long	Western Australia	Australia	121.68	-31.18	2.705	1.16	5.79	0.067	Nelson (1997b)
Maggie Hays	Western Australia	Australia	120.52	-32.22	2.921	12.27	1.41	0.173	Wang *et al.* (1996)
Mariners	Western Australia	Australia	121.66	-31.63	2.705	1.58	2.91	0.046	Nelson (1997a)
Marriott	Western Australia	Australia	120.99	-28.45	2.705	0.72	1.10	0.008	Nelson (1997a)
McEwen (formerly Mt Edwards 360N)	Western Australia	Australia	121.52	-31.40	2.705	0.73	0.86	0.006	Nelson (1997a)
Melon	Western Australia	Australia	120.73	-27.86	2.705	0.35	2.00	0.007	Nelson (1997a)
Miitel (incl. North)	Western Australia	Australia	121.64	-31.58	2.705	1.64	3.60	0.059	Nelson (1997a)
Miriam	Western Australia	Australia	121.09	-31.07	2.705	0.23	1.70	0.004	Nelson (1997a)
Mt Edwards (incl. Mt Edwards 14N)	Western Australia	Australia	121.54	-31.45	2.705	1.08	1.21	0.013	Nelson (1997a)
Mt Edwards 132N	Western Australia	Australia	121.54	-31.45	2.705	0.28	3.45	0.010	Nelson (1997a)
Mt Edwards 166N	Western Australia	Australia	121.53	-31.44	2.705	0.13	1.85	0.002	Nelson (1997a)
Mt Edwards 26N	Western Australia	Australia	121.54	-31.48	2.705	1.70	2.50	0.043	Nelson (1997a)
Mt Keith	Western Australia	Australia	120.54	-27.23	2.705	599.18	0.57	3.415	Nelson (1997a)
Mt Martin	Western Australia	Australia	121.68	-31.01	2.500	0.07	2.00	0.001	Nelson (1997a)
Mt Sholl	Western Australia	Australia	116.89	-20.92	2.892	3.03	0.75	0.023	Frick *et al.* (2001)
Mt Windarra	Western Australia	Australia	122.23	-28.49	2.900	12.71	1.42	0.181	Barley & Groves (1990)
Munda	Western Australia	Australia	121.53	-31.50	2.705	0.05	2.53	0.001	Nelson (1997a)
Munni Munni	Western Australia	Australia	116.83	-21.12	2.927	23.60	0.09	0.021	Hoatson & Sun (2002)
Nebo-Babel	Western Australia	Australia	127.73	-26.10	1.078	283.33	0.36	1.020	Huston *et al.* (2007)
Nepean	Western Australia	Australia	121.09	-31.16	2.705	1.55	3.16	0.049	Nelson (1997a)
Nova	Western Australia	Australia	123.19	-31.82	1.300	11.40	2.40	0.274	PorterGeo (2020d)
Panton	Western Australia	Australia	127.83	-17.75	1.856	33.60	0.16	0.054	Page & Hoatson (2000)
Perseverance (incl. Rocky's Reward, Leinster)	Western Australia	Australia	120.70	-27.79	2.705	236.45	1.05	2.483	Nelson (1997b)
Pioneer	Western Australia	Australia	121.64	-31.97	2.705	0.03	1.11	0.000	Nelson (1997a)
Prospero	Western Australia	Australia	120.58	-27.63	2.705	1.06	5.72	0.061	Nelson (1997a)
Radio Hill	Western Australia	Australia	116.86	-20.98	2.892	2.76	1.53	0.042	Frick *et al.* (2001)
Ratbat	Western Australia	Australia	119.74	-32.55	3.000	0.25	1.10	0.003	Wang *et al.* (1996)
Rav 8	Western Australia	Australia	120.30	-33.60	2.958	0.51	3.56	0.018	Nelson (1997a)
Ravensthorpe Nickel (incl. Rav 1, 4, 5, 4w)	Western Australia	Australia	120.40	-33.64	2.958	1.58	0.87	0.014	Nelson (1997a)
Redross	Western Australia	Australia	121.65	-31.68	2.705	0.77	3.99	0.031	Nelson (1997a)
Ruth Well	Western Australia	Australia	116.87	-20.87	2.876	0.03	2.00	0.001	Meisel *et al.* (2001)
Savannah (Sally Malay)	Western Australia	Australia	128.02	-17.35	1.844	3.74	1.74	0.065	Page & Hoatson (2000)
Scotia	Western Australia	Australia	121.46	-31.18	2.705	1.92	2.71	0.052	Nelson (1997a)
Seagull	Western Australia	Australia	119.74	-32.55	3.000	0.97	1.31	0.013	Wang *et al.* (1996)
Sherlock Bay	Western Australia	Australia	117.54	-20.81	2.866	25.42	0.40	0.102	Hoatson & Sun (2002)
South Windarra	Western Australia	Australia	122.24	-28.61	2.900	10.27	1.44	0.148	Barley & Groves (1990)
Spargoville (1a)	Western Australia	Australia	121.49	-31.32	2.705	1.02	2.45	0.025	Nelson (1997a)
Tapinos (formerly Anomaly 4 near Prospero)	Western Australia	Australia	120.58	-27.63	2.705	0.14	7.40	0.011	Nelson (1997a)
Trough Well	Western Australia	Australia	118.89	-30.67	3.000	0.02	2.50	0.001	Wang *et al.* (1996)
Victor	Western Australia	Australia	121.68	-31.14	2.705	0.36	5.71	0.021	Nelson (1997a)
Victor Shoot	Western Australia	Australia	121.68	-31.19	2.705	0.23	5.11	0.012	Nelson (1997a)
Wannaway	Western Australia	Australia	121.52	-31.60	2.705	0.57	2.81	0.016	Nelson (1997a)
Weebo Bore	Western Australia	Australia	120.82	-28.05	2.705	12.00	0.70	0.084	Nelson (1997a)

Continued overleaf...

Table 5 – continued

Deposit	State/Region	Country	Lon.[a]	Lat.[a]	Age (Ga)	Ore (Mt)	Ni (%)	Ni (Mt)	References
Widgie 3	Western Australia	Australia	121.59	-31.52	2.705	0.09	1.89	0.002	Nelson (1997a)
Widgie Townsite	Western Australia	Australia	121.57	-31.50	2.705	2.19	1.48	0.032	Nelson (1997a)
Yakabindie	Western Australia	Australia	120.58	-27.46	2.705	290.00	0.58	1.682	Nelson (1997a)
Zabel	Western Australia	Australia	121.51	-31.39	2.705	0.98	1.93	0.019	Nelson (1997a)
SelebiPhikwe	Central	Botswana	27.86	-21.95	2.500	49.44	1.04	0.514	Eckstrand (1995)
O'Toole	Minas Gerais	Brazil	-46.00	-20.00	2.700	6.60	2.20	0.145	Brenner *et al.* (1990)
Giant Mascot	British Columbia	Canada	-121.51	49.46	0.100	2.05	1.40	0.029	Eckstrand & Hulbert (2007)
Amax area 1 (Nose)	Manitoba	Canada	-81.89	48.16	1.880	7.30	1.33	0.097	Hulbert *et al.* (2005)
Bowden	Manitoba	Canada	-97.00	53.00	1.880	80.00	0.60	0.480	Hulbert *et al.* (2005)
Bucko	Manitoba	Canada	-98.66	54.88	1.880	2.50	2.23	0.056	Hulbert *et al.* (2005)
Lynn Lake	Manitoba	Canada	-101.04	56.86	1.600	20.15	1.02	0.206	Eckstrand & Hulbert (2007)
Manibridge	Manitoba	Canada	-98.84	54.72	1.880	1.41	2.55	0.036	Hulbert *et al.* (2005)
Namew Lake	Manitoba	Canada	-101.79	54.20	1.847	2.60	2.44	0.063	Cumming & Krstic (1991)
Thompson	Manitoba	Canada	-97.80	55.73	1.880	150.30	2.32	3.487	Hulbert *et al.* (2005)
St. Stephen (3 zones)	New Brunswick	Canada	-67.30	45.22	0.387	1.00	1.05	0.011	Paktunc (1987)
Voisey's Bay	Newfoundland and Labrador	Canada	-62.08	56.33	1.333	136.70	1.59	2.174	Amelin *et al.* (1999)
Alexo	Ontario	Canada	-80.81	48.66	2.707	0.06	3.58	0.002	Barrie *et al.* (1999)
Gordon Lake	Ontario	Canada	-94.93	50.46	2.724	1.07	1.62	0.017	Ayer *et al.* (2002)
Great Lakes	Ontario	Canada	-89.58	48.08	1.109	45.60	0.18	0.082	Davis & Sutcliffe (1985)
Langmuir (No. 1 and 2)	Ontario	Canada	-81.03	48.34	2.707	1.60	2.09	0.033	Ayer *et al.* (2002)
Macassa	Ontario	Canada	-77.72	44.87	1.600	1.80	0.91	0.016	Eckstrand & Hulbert (2007)
Montcalm	Ontario	Canada	-82.09	48.66	2.702	3.56	1.44	0.051	Barrie & Naldrett (1989)
Redstone	Ontario	Canada	-81.16	48.31	2.707	1.22	2.39	0.029	Ayer *et al.* (2002)
Shebandowan	Ontario	Canada	-90.24	48.59	2.724	15.00	1.50	0.225	Ayer *et al.* (2002)
Texmont	Ontario	Canada	-81.20	48.16	2.707	3.19	0.93	0.030	Ayer *et al.* (2002)
Dumont	Qubec	Canada	-78.44	48.65	2.710	150.00	0.50	0.750	Naldrett (1989)
Expo-Ungava	Qubec	Canada	-73.44	61.55	1.918	6.30	0.86	0.054	Parrish (1989)
Lorraine	Qubec	Canada	-78.94	48.36	2.694	0.66	0.39	0.003	Barnes *et al.* (1993)
Marbridge	Qubec	Canada	-78.18	48.34	2.715	0.77	2.82	0.022	Ayer *et al.* (2002)
Raglan	Qubec	Canada	-73.45	61.55	1.918	24.70	2.72	0.672	Parrish (1989)
Canalask	Yukon	Canada	-139.53	61.47	0.232	0.50	1.68	0.008	Hulbert (1997)
Wellgreen	Yukon	Canada	-139.52	61.46	0.232	0.67	2.04	0.014	Hulbert (1997)
Jinchuan	Gansu	China	102.16	38.46	0.827	515.00	1.06	5.459	Li *et al.* (2004)
Hitura	North Ostrobothnia	Finland	25.04	63.84	1.877	12.30	0.56	0.069	Papunen & Gorbunov (1985)
Kotalahti	North Savo	Finland	27.63	62.56	1.883	23.20	0.70	0.162	Papunen & Gorbunov (1985)
Noril'sk-Talnakh	Krasnoyarsk Krai	Russia	88.18	69.33	0.251	1257.00	1.84	23.129	Kamo *et al.* (2003)
Monchegorsk	Murmansk Oblast	Russia	32.95	67.92	2.493	47.00	0.70	0.329	Neradovsky *et al.* (1997)
Pechenga	Murmansk Oblast	Russia	29.73	69.33	1.977	339.00	1.18	4.000	Hanski *et al.* (1990)
Merensky Reef	Limpopo	South Africa	28.50	-24.49	2.060	4209.00	0.15	6.314	Kruger *et al.* (1986)
Platreef	Limpopo	South Africa	28.96	-24.08	2.060	1597.00	0.41	6.548	Kruger *et al.* (1986)
Kabanga	Kagera	Tanzania	30.57	-2.88	1.275	11.70	1.72	0.201	Deblond & Tack (1999)
Duluth	Minnesota	USA	-91.25	47.83	1.099	4000.00	0.20	8.000	Paces & Miller Jr. (1993)
Trojan	Mashonaland Central	Zimbabwe	31.33	-17.29	2.700	20.35	0.68	0.138	Prendergast (2003)
Great Dyke	Midlands	Zimbabwe	30.63	-17.39	2.587	2574.00	0.21	5.405	Mukasa *et al.* (1998)
Hunter's Road	Midlands	Zimbabwe	29.83	-19.16	2.700	30.00	0.70	0.210	Prendergast (2003)
Shangani	Midlands	Zimbabwe	29.25	-19.66	2.700	22.00	0.71	0.156	Prendergast (2003)

[a] In decimal degrees

Table 6: Global compilation of 947 volcanogenic massive sulphide deposits shown in Figure S32, revised starting from Franklin *et al.* (2005). Ga = billion years; Mt = million tonnes; ND = no data.

Deposit	Country	Lon.[a]	Lat.[a]	Age (Ga)	Cu (Mt)	Zn (Mt)	Pb (Mt)
Gjegjani	Albania	20.01	41.94	0.164	0.186	0.040	ND
Arroyo Rojo	Argentina	-68.10	-54.75	0.153	ND	ND	ND
Santa Elena	Argentina	-69.42	-31.33	0.444	ND	ND	ND
Anaconda	Australia	121.77	-28.97	ND	0.008	0.017	ND
Anomaly A	Australia	130.72	-13.61	1.862	0.014	0.076	0.001
Avoca Tank	Australia	146.84	-31.20	0.479	0.042	ND	ND
Ayshia	Australia	116.94	-21.07	3.114	0.003	0.018	ND
Balcooma	Australia	144.71	-18.77	0.480	0.095	0.106	0.050
Bentley	Australia	121.17	-28.48	2.692	0.041	0.226	0.014
Bernts	Australia	119.28	-21.23	3.238	0.002	0.047	0.010
Big Stubby	Australia	119.75	-21.22	3.465	0.000	0.028	0.009
Budgery	Australia	146.68	-31.53	0.479	0.021	ND	ND
Budgerygar	Australia	146.72	-31.38	0.479	0.033	ND	ND
Captains Flat	Australia	149.44	-35.59	0.424	0.028	0.400	0.240
Catalpa	Australia	116.96	-28.77	2.953	ND	0.259	0.021
Coles Hill	Australia	133.78	-23.06	1.809	ND	ND	ND
Commonwealth	Australia	149.05	-32.59	0.425	0.001	0.011	0.004
Coondamar Creek	Australia	120.67	-21.93	2.905	ND	ND	ND
Cow Flat	Australia	149.54	-33.57	0.425	0.082	0.190	ND
Currawang	Australia	149.50	-34.99	0.424	0.013	0.104	0.018
Currawong	Australia	147.91	-36.98	0.425	0.207	0.413	0.083
DeGrussa	Australia	119.25	-25.57	2.027	0.659	ND	ND
Dianne	Australia	144.52	-16.10	0.388	0.018	ND	ND
Discovery	Australia	118.78	-20.78	3.253	0.001	0.029	0.012
Dresser	Australia	119.44	-21.15	3.481	ND	ND	ND
Dry River South-Surveyor	Australia	144.69	-18.79	0.480	0.023	0.267	0.090
Edwards Creek	Australia	134.03	-23.01	1.802	ND	ND	ND
Fisher Well	Australia	122.27	-27.71	2.805	ND	ND	ND
Freddie Well	Australia	118.68	-28.75	2.814	0.001	0.050	ND
Gossan Hill	Australia	116.96	-28.78	2.953	0.413	0.865	0.132
Halls Peak	Australia	152.03	-30.75	0.285	0.000	0.005	0.003
Hammerhead	Australia	120.24	-21.04	3.465	0.003	0.085	0.022
Handcuff	Australia	146.21	-20.35	0.479	0.006	0.100	0.004
Hartman	Australia	146.85	-31.22	0.479	0.009	ND	ND
Hellyer	Australia	145.72	-41.57	0.500	0.063	2.294	1.188
Henty	Australia	145.56	-41.87	0.500	ND	ND	ND
Hercules	Australia	145.51	-41.85	0.503	0.013	0.576	0.183
Highway-Reward	Australia	146.20	-20.36	0.479	0.073	ND	ND
Home of Bullion	Australia	134.16	-21.51	1.728	0.045	0.050	0.030
Horseshoe Lights	Australia	118.62	-25.36	1.922	0.185	ND	ND
Jaguar	Australia	121.16	-28.44	2.692	0.050	0.187	0.012
John Fardy	Australia	149.42	-34.11	0.425	0.003	0.028	0.006
Kangaroo Caves	Australia	119.24	-21.21	3.238	0.032	0.208	ND
Kempfield	Australia	149.26	-33.79	0.425	ND	0.205	0.098
Larsens	Australia	146.85	-31.22	0.479	0.031	ND	ND
Lewis Ponds	Australia	149.25	-33.27	0.417	0.013	0.152	0.089
Liontown	Australia	146.07	-20.41	0.479	0.009	0.112	0.040
Magpie	Australia	146.74	-20.32	0.479	0.005	0.038	0.005
McPhillamys	Australia	149.32	-33.49	0.417	0.049	ND	ND
Mons Cupri	Australia	117.81	-20.88	2.954	0.053	0.062	0.026
Mount Ararat	Australia	142.93	-37.20	0.518	0.024	0.005	ND
Mount Bulga	Australia	149.20	-33.28	0.425	0.009	0.031	0.009
Mount Chalmers	Australia	150.65	-23.30	0.277	0.024	0.023	0.010
Mount Gibson	Australia	117.16	-29.78	2.934	ND	ND	ND
Mount Lyell - Cu-Au	Australia	145.58	-42.06	0.500	3.017	ND	ND
Mount Lyell - Tasman and Crown Lyell (Zn-Pb)	Australia	145.59	-42.05	0.500	0.001	0.014	0.012
Mount Molloy	Australia	145.34	-16.70	0.388	0.004	ND	ND
Mount Morgan	Australia	150.37	-23.64	0.381	0.374	0.052	ND
Mount Mulcahy	Australia	117.70	-27.05	2.752	0.006	0.004	ND
Murrawombie (Girilambone)	Australia	146.87	-31.26	0.479	0.209	ND	ND
Nimbus	Australia	121.65	-30.79	2.708	0.000	0.034	0.005
North East	Australia	146.85	-31.22	0.479	0.021	ND	ND
OK	Australia	144.25	-16.60	0.388	0.008	ND	ND
Onedin	Australia	127.54	-18.32	1.843	0.027	0.097	0.045
Oonagalabi	Australia	134.86	-23.13	1.765	0.125	0.250	ND
Orchard Tank-Acacia	Australia	118.80	-20.77	3.253	0.001	0.040	0.016
Peelwood	Australia	149.42	-34.12	0.425	0.001	0.007	0.003
Pincher Well	Australia	118.78	-28.72	2.814	0.041	0.446	ND
Que River	Australia	145.70	-41.60	0.500	0.023	0.439	0.244
Rosebery	Australia	145.54	-41.77	0.503	0.190	4.742	1.439
Salt Creek	Australia	117.70	-20.76	2.945	0.011	0.100	0.034
Sandiego	Australia	127.49	-18.36	1.843	0.035	0.127	0.018
Scuddles	Australia	116.94	-28.75	2.953	0.126	1.229	0.084

Continued overleaf...

Table 6 – continued

Deposit	Country	Lon.[a]	Lat.[a]	Age (Ga)	Cu (Mt)	Zn (Mt)	Pb (Mt)
South Hercules	Australia	145.51	-41.85	0.503	0.001	0.021	0.011
Sulphur Springs	Australia	119.21	-21.15	3.239	0.202	0.543	ND
Teutonic Bore	Australia	121.15	-28.41	2.692	0.076	0.244	0.017
Thalanga	Australia	145.77	-20.34	0.479	0.140	0.782	0.248
Tritton	Australia	146.72	-31.39	0.479	0.669	ND	ND
Tuff Hill	Australia	122.22	-27.64	2.805	ND	ND	ND
Waterloo	Australia	146.11	-20.38	0.479	0.013	0.073	0.010
Wet Lagoon	Australia	149.46	-34.81	0.425	0.008	0.083	0.045
Whim Creek	Australia	117.83	-20.85	2.948	0.041	0.003	ND
Whundo-West Whundo	Australia	116.93	-21.08	3.114	0.022	0.017	ND
Wickliffe	Australia	142.68	-37.69	0.501	ND	ND	ND
Wilga	Australia	147.89	-37.00	0.425	0.084	0.179	0.015
Woodlawn	Australia	149.57	-35.06	0.423	0.401	2.286	0.911
Walchen	Austria	14.07	47.43	0.475	0.035	0.052	0.048
Miguela A-zone	Bolivia	-63.04	-15.87	1.450	0.061	0.005	ND
Aripuan	Brazil	-60.67	-8.99	1.762	0.101	1.445	0.513
Palmierpolis	Brazil	-48.32	-12.92	1.300	0.049	0.186	0.029
Perkoa (Boromo)	Burkino Faso	-2.65	12.35	2.195	ND	1.254	0.019
777 (Triple Seven)	Canada	-101.88	54.78	1.889	0.567	0.962	0.002
Aldermac	Canada	-79.23	48.22	2.700	0.044	0.118	ND
Amulet 11	Canada	-79.07	48.31	2.698	0.016	0.011	ND
Amulet A - Upper and Lower	Canada	-79.08	48.32	2.698	0.243	0.255	ND
Amulet C	Canada	-79.07	48.31	2.698	0.013	0.048	ND
Amulet F Shaft	Canada	-79.05	48.33	2.698	0.009	0.023	ND
Anderson Lake	Canada	-99.99	54.86	1.895	0.086	0.003	0.000
Ansil	Canada	-79.12	48.35	2.698	0.114	0.015	ND
Armstrong A	Canada	-66.05	47.60	0.470	0.010	0.076	0.014
Armstrong B	Canada	-66.06	47.59	0.470	0.002	0.001	0.000
Austin Brook	Canada	-65.82	47.40	0.470	0.001	0.028	0.023
Barvalle	Canada	-77.66	48.43	2.725	0.002	0.012	ND
Barvue-Abcourt (incl. Peshcourt, Frebert)	Canada	-77.68	48.52	2.706	ND	0.487	ND
Bear	Canada	-112.39	62.89	2.705	ND	0.056	0.024
Belfort (Roymont)	Canada	-77.68	48.43	2.725	0.000	0.004	ND
Bell Allard	Canada	-77.73	49.69	2.726	0.045	0.491	ND
Bell Allard Sud	Canada	-77.69	49.69	2.726	0.003	0.021	ND
Big Bull	Canada	-133.55	58.67	0.327	0.003	0.048	0.020
Bigstone	Canada	-103.20	54.58	1.875	0.038	0.003	0.004
Birch Lake	Canada	-102.03	54.66	1.900	0.017	0.000	ND
Bob Lake	Canada	-101.04	55.16	1.853	0.077	0.065	ND
Bobby's Pond	Canada	-56.84	48.64	0.498	0.013	0.085	0.006
Bomber	Canada	-100.18	54.86	1.890	0.000	0.006	ND
Bonanza	Canada	-129.85	55.39	0.186	0.014	ND	ND
Boot Lake	Canada	-108.44	65.91	2.690	0.013	0.225	0.045
Boundary	Canada	-56.45	48.66	0.509	0.018	0.020	0.005
Bousquet 1	Canada	-78.47	48.25	2.698	0.028	ND	ND
Bousquet 2	Canada	-78.44	48.25	2.698	0.046	ND	ND
Boylen-Koke	Canada	-69.45	57.66	1.880	0.007	0.073	0.011
Brabant Lake	Canada	-103.70	56.12	1.850	0.028	0.300	0.007
Bracemac-McLeod	Canada	-77.66	49.67	2.726	0.088	0.496	ND
Britannia	Canada	-123.14	49.61	0.112	0.537	0.317	ND
Brompton	Canada	-72.11	45.48	0.504	0.011	ND	ND
Brunswick 12	Canada	-65.89	47.48	0.470	1.057	17.600	6.916
Brunswick 6	Canada	-65.82	47.41	0.470	0.084	0.758	0.296
Buchans	Canada	-56.86	48.83	0.465	0.009	0.094	0.048
Caber	Canada	-78.08	49.74	2.726	0.008	0.068	0.001
Caber North	Canada	-78.11	49.75	2.726	0.041	0.111	ND
Callinan	Canada	-101.88	54.78	1.889	0.106	0.311	0.004
Canadian Jamieson	Canada	-81.57	48.54	2.700	0.017	0.029	ND
Canoe Landing Lake	Canada	-66.11	47.41	0.470	0.118	0.354	0.126
Captain	Canada	-65.88	47.28	0.470	0.004	ND	ND
Captain North	Canada	-65.88	47.30	0.470	0.001	0.022	0.008
Caribou	Canada	-66.30	47.56	0.470	0.354	2.981	1.112
Centennial	Canada	-101.67	54.71	1.880	0.037	0.052	0.006
Champagne	Canada	-70.22	46.59	0.466	0.001	0.007	0.001
Chance	Canada	-81.39	48.70	2.714	ND	0.023	0.006
Chester	Canada	-66.22	47.10	0.470	0.121	0.189	0.082
Chisel Lake	Canada	-100.12	54.83	1.890	0.043	0.960	0.032
Chisel Lake North	Canada	-100.12	54.83	1.890	0.043	0.960	0.032
Chu Chua	Canada	-120.06	51.38	0.315	0.051	0.008	ND
Clinton River	Canada	-70.91	45.46	0.480	0.037	0.029	ND
Colchester	Canada	-56.08	49.64	0.505	0.013	ND	ND
Cold Lake	Canada	-101.10	55.14	1.853	0.018	0.035	ND
Coniagas	Canada	-76.17	49.50	2.725	0.000	0.077	0.007
Copper lode A and E	Canada	-92.91	50.97	2.739	0.010	0.013	ND
Copper Reef (Mink Narrows)	Canada	-101.59	54.62	1.905	0.007	0.002	0.000
Corbet	Canada	-79.10	48.30	2.698	0.081	0.045	ND

Continued overleaf...

Table 6 – continued

Deposit	Country	Lon.[a]	Lat.[a]	Age (Ga)	Cu (Mt)	Zn (Mt)	Pb (Mt)
Coronation	Canada	-102.00	54.58	1.900	0.054	0.003	ND
Cupra D'estrie	Canada	-71.31	45.77	0.460	0.067	0.080	0.005
Cuprus	Canada	-101.71	54.72	1.880	0.015	0.029	0.001
Daniel's Pond	Canada	-56.90	48.63	0.498	0.005	0.069	0.032
Deb	Canada	-111.23	64.00	2.701	0.008	0.030	0.002
Delbridge	Canada	-78.97	48.27	2.698	0.002	0.031	ND
Devils Elbow	Canada	-66.40	47.43	0.470	0.004	ND	ND
DH-FL Groups	Canada	-101.01	56.83	1.905	0.005	0.011	ND
Dickstone	Canada	-100.49	54.86	1.890	0.043	0.237	ND
Domergue-Lessard	Canada	-74.64	50.64	2.774	0.014	0.026	ND
Double Ed	Canada	-129.88	55.41	0.186	0.030	0.019	ND
Duck Pond	Canada	-56.49	49.63	0.509	0.168	0.310	0.057
Dumagami	Canada	-78.44	48.26	2.698	0.034	0.005	ND
Dunraine	Canada	-77.57	48.07	2.704	0.036	ND	ND
Dyce Siding-Sylvia	Canada	-100.15	54.41	1.890	0.009	0.012	0.004
East Cleaver Lake	Canada	-108.46	65.92	2.690	ND	0.315	0.004
East Sullivan	Canada	-77.71	48.07	2.704	0.172	0.117	ND
East Waite	Canada	-79.08	48.34	2.698	0.062	0.049	ND
Ecstall	Canada	-129.51	53.87	0.393	0.027	0.071	0.006
Empire-Le Tac	Canada	-76.14	49.43	2.725	0.001	0.007	ND
Errington	Canada	-81.26	46.54	1.848	0.069	0.311	0.090
Eskay Creek	Canada	-130.43	56.65	0.175	0.013	0.216	0.088
Esso West	Canada	-128.39	58.21	0.246	0.045	0.072	ND
Estrades	Canada	-79.20	49.45	2.720	0.008	0.092	0.008
Eustis	Canada	-71.92	45.32	0.460	0.108	ND	ND
F Group	Canada	-91.05	49.87	2.736	0.002	0.032	0.002
Farewell Lake	Canada	-100.05	54.49	1.890	0.005	ND	ND
Flat Landing Brook North	Canada	-65.88	47.38	0.470	0.000	0.071	0.016
Flexar	Canada	-102.03	54.68	1.900	0.012	0.002	0.000
Flin Flon	Canada	-101.88	54.77	1.889	1.381	2.568	0.006
FON	Canada	-102.50	54.75	1.890	0.013	0.174	0.000
Fox Lake	Canada	-101.65	56.63	1.905	0.218	0.213	0.001
Frederickson Lake	Canada	-66.27	55.05	1.880	0.002	0.012	ND
Fyre Lake	Canada	-131.49	61.34	0.365	0.185	ND	ND
Gallen	Canada	-78.95	48.33	2.698	0.006	0.272	ND
Garon Lake	Canada	-77.57	49.77	2.726	0.007	0.010	ND
Geco	Canada	-85.79	49.15	2.720	1.086	2.015	0.088
Gmini-Turgeon	Canada	-79.18	49.50	2.736	0.020	0.066	0.007
Genex (Mordey)	Canada	-81.57	48.48	2.699	0.015	0.029	ND
Ghost Lake and Lost Lake	Canada	-100.10	54.83	1.890	0.008	0.050	0.002
Goldstream	Canada	-118.43	51.63	0.510	0.067	0.007	ND
Gondor	Canada	-111.80	65.56	2.668	0.015	0.350	0.029
Gonzague-Langlois	Canada	-76.67	49.25	2.718	0.055	1.279	ND
GPF4	Canada	-131.51	61.45	0.363	0.002	0.096	0.047
Granduc	Canada	-130.35	56.21	0.223	0.449	0.025	0.005
Great Burnt Lake	Canada	-56.17	48.33	0.466	0.019	ND	ND
Gullbridge	Canada	-56.16	49.20	0.472	0.042	ND	ND
Hackett (Jo)	Canada	-108.36	65.92	2.690	0.002	0.034	ND
Hackett River A	Canada	-108.37	65.92	2.690	0.024	0.683	0.079
Halfmile Lake	Canada	-66.32	47.31	0.470	0.009	0.762	0.241
Handcamp	Canada	-56.08	49.28	0.472	0.059	ND	ND
Hanson Lake	Canada	-103.70	56.12	1.870	0.001	0.015	0.009
Harper Creek	Canada	-119.82	51.52	0.361	3.550	ND	ND
Hart River	Canada	-136.83	64.63	1.381	0.008	0.020	0.005
Headvue (Headway-Coulee)	Canada	-87.66	50.02	2.764	ND	0.013	0.000
Headway	Canada	-65.90	47.45	0.470	0.004	0.016	0.006
Heath Steele	Canada	-66.04	47.30	0.470	0.685	1.880	0.622
Heninga Gemex	Canada	-96.20	61.77	2.685	0.029	0.452	ND
Hidden Creek	Canada	-129.82	55.44	0.186	0.627	ND	ND
High Lake	Canada	-110.86	67.38	2.705	0.387	0.576	0.053
Homestake	Canada	-119.83	51.11	0.361	0.001	0.006	0.003
Hood River No 10	Canada	-112.75	66.06	2.700	0.096	0.112	ND
Hood River No 41	Canada	-112.75	66.06	2.700	0.004	0.011	0.001
Horne - H and G lenses	Canada	-79.01	48.26	2.702	1.205	ND	ND
Horne - No 5 zone	Canada	-79.02	48.23	2.702	0.150	1.350	ND
Hudvam (Vamp Lake)	Canada	-101.17	54.94	1.890	0.014	0.022	0.001
Huntington	Canada	-72.33	45.26	0.504	0.016	ND	ND
Hyers Island	Canada	-96.02	54.76	2.832	0.009	ND	ND
Ice	Canada	-131.42	61.88	0.275	0.067	ND	ND
Indian Mountain Lake (incl. BB, Kennedy Lake, Kennedy Lake West Copper)	Canada	-110.96	63.03	2.680	0.006	0.087	0.007
Isle Dieu	Canada	-77.74	49.73	2.726	0.031	0.544	ND
Izok Lake	Canada	-115.08	65.45	2.681	0.377	1.887	0.185
Jameland	Canada	-81.59	48.58	2.701	0.005	0.006	ND
Jay Copper (Conigo)	Canada	-78.06	48.60	2.700	0.014	0.012	ND
Joannie	Canada	-100.03	54.83	1.890	0.006	0.000	ND

Continued overleaf...

Table 6 – continued

Deposit	Country	Lon.[a]	Lat.[a]	Age (Ga)	Cu (Mt)	Zn (Mt)	Pb (Mt)
Joutel	Canada	-78.35	49.45	2.728	0.037	0.066	ND
Jungle Lake	Canada	-100.97	55.17	1.853	0.050	0.052	0.000
Kam Kotia	Canada	-81.59	48.60	2.701	0.071	0.063	ND
Kamad-7	Canada	-119.81	51.14	0.361	0.002	0.023	0.018
Kelly-Desmond	Canada	-78.32	49.43	2.725	0.007	0.069	ND
Kendon Copper	Canada	-87.59	50.42	2.739	0.027	0.094	ND
Key Anacon	Canada	-65.70	47.44	0.470	0.004	0.130	0.049
Kidd Creek	Canada	-81.37	48.69	2.714	3.416	9.139	0.325
Knobby-McBride	Canada	-99.98	56.87	1.800	0.006	0.160	0.001
Koff Zone	Canada	-100.21	54.06	1.890	0.006	ND	ND
Konuto	Canada	-102.06	54.66	1.900	0.069	0.027	0.000
Kudz Ze Kayah	Canada	-131.61	61.46	0.363	0.130	0.722	0.169
Kutcho Creek	Canada	-128.36	58.21	0.246	0.207	0.271	ND
La Gauchetiere (Phelps Dodge)	Canada	-78.18	49.78	2.725	0.017	0.076	ND
La Ronde-Penna	Canada	-78.44	48.25	2.698	0.194	1.275	ND
Lake Bond	Canada	-56.19	49.03	0.472	0.003	0.023	ND
Lalor	Canada	-100.14	54.87	1.890	0.117	1.392	0.000
Lar	Canada	-101.88	56.64	1.905	0.011	0.029	ND
Lara	Canada	-123.91	48.88	0.366	0.018	0.050	0.010
Lemarchant	Canada	-56.72	48.53	0.509	0.013	0.116	0.026
Lemoine	Canada	-74.12	49.75	2.728	0.032	0.072	ND
Linda	Canada	-99.93	54.83	1.895	0.035	0.094	ND
Lingwick	Canada	-71.38	45.66	0.460	0.002	0.020	0.000
Little Bay	Canada	-55.94	49.60	0.505	0.062	ND	ND
Little Deer	Canada	-56.02	49.59	0.505	0.125	ND	ND
Lockport	Canada	-55.50	49.46	0.486	0.004	0.007	ND
Long Lake	Canada	-57.17	48.43	0.511	0.016	0.106	0.013
Lost Lake	Canada	-101.08	55.13	1.853	0.019	0.061	ND
Louvem-Zinc	Canada	-77.52	48.10	2.704	0.005	0.132	0.002
Louvicourt	Canada	-65.93	47.39	0.470	0.001	0.001	0.002
Louvicourt	Canada	-77.50	48.10	2.704	0.598	0.328	ND
Lucky Strike	Canada	-56.87	48.82	0.465	0.118	1.478	0.744
Lyon Lake	Canada	-90.89	49.89	2.736	0.081	0.426	0.041
Maclean	Canada	-56.88	48.83	0.465	0.038	0.437	0.243
Mag Lake	Canada	-95.93	61.89	2.685	0.004	0.027	ND
Magusi River	Canada	-79.37	48.44	2.702	0.038	0.055	ND
Manitou-Barvue (Golden Manitou)	Canada	-77.61	48.09	2.704	0.010	0.050	0.010
Marg	Canada	-134.47	64.01	0.376	0.149	0.379	0.182
Marshall Lake (Billiton)	Canada	-87.58	50.41	2.739	0.024	0.084	ND
Mattabi	Canada	-90.98	49.88	2.736	0.084	0.944	0.097
Mattagami Lake	Canada	-77.72	49.72	2.726	0.144	2.102	ND
McIlvenna Bay	Canada	-102.85	54.68	1.888	0.132	0.882	0.058
McMaster	Canada	-66.24	47.61	0.470	0.002	ND	ND
Memphremagog	Canada	-72.31	45.15	0.489	0.030	ND	ND
Millenbach	Canada	-79.05	48.30	2.698	0.123	0.154	ND
Mobrun-Bouchard-Hebert	Canada	-78.87	48.38	2.696	0.155	0.695	ND
Mokoman Lake	Canada	-102.74	55.87	1.870	0.012	0.022	ND
Montauban (incl. Ttrault; Montauban Anacon and Au-rich zones)	Canada	-72.35	46.84	1.280	ND	0.124	0.041
Moulton Hill	Canada	-71.81	45.43	0.460	0.003	ND	ND
Murray Brook	Canada	-66.43	47.53	0.470	0.079	0.396	0.139
Musk	Canada	-107.60	65.32	2.689	0.004	0.034	0.005
Myra Falls Group	Canada	-125.59	49.57	0.366	0.537	1.833	0.161
Nash Creek	Canada	-66.10	47.88	0.416	ND	0.245	0.049
Nepisiguit	Canada	-66.03	47.38	0.470	0.014	0.099	0.021
New Calumet	Canada	-76.68	45.70	1.115	ND	0.219	0.065
New Hosco	Canada	-77.84	49.79	2.726	0.032	0.032	ND
New Insco (Fabie Bay)	Canada	-79.35	48.44	2.702	0.023	ND	ND
Newconex-Figuery	Canada	-78.17	48.48	2.706	ND	0.023	ND
Norbec	Canada	-79.06	48.35	2.698	0.123	0.212	ND
Norita	Canada	-77.66	49.78	2.726	0.071	0.153	ND
Norita East	Canada	-77.64	49.78	2.726	0.009	0.110	ND
Normtal	Canada	-79.37	49.00	2.725	0.215	0.512	ND
Normetmar	Canada	-79.37	49.00	2.725	ND	0.067	ND
North Star and Don Jon	Canada	-101.57	54.76	1.885	0.017	ND	ND
Old Waite	Canada	-79.09	48.34	2.698	0.053	0.033	0.000
Orchan	Canada	-77.71	49.71	2.726	0.046	0.444	ND
Orchan West	Canada	-77.74	49.72	2.726	0.005	0.048	ND
Oriental	Canada	-56.83	48.83	0.465	0.049	0.472	0.263
Orvan Brook	Canada	-66.12	47.63	0.470	0.010	0.160	0.046
Osbourne Lake	Canada	-99.72	54.95	1.895	0.088	0.042	0.000
Pabineau	Canada	-65.92	47.45	0.470	ND	0.004	0.001
PD1	Canada	-78.14	49.76	2.726	0.020	0.079	ND
Persvrance	Canada	-77.79	49.76	2.726	0.061	0.809	ND
Photo Lake	Canada	-100.10	54.86	1.890	0.032	0.044	0.004
Pic Lake	Canada	-87.39	48.97	2.723	0.012	0.220	ND

Continued overleaf...

Table 6 – continued

Deposit	Country	Lon.[a]	Lat.[a]	Age (Ga)	Cu (Mt)	Zn (Mt)	Pb (Mt)
Pilley's Island	Canada	-55.72	49.51	0.472	0.025	ND	ND
Pinebay	Canada	-101.61	54.77	1.880	0.020	0.001	0.000
Point Leamington (New Bay Pond)	Canada	-55.63	49.28	0.487	0.069	0.276	ND
Poirier	Canada	-80.75	48.32	2.728	0.138	0.189	ND
Potterdoal	Canada	-80.21	48.60	2.713	0.024	0.066	ND
Prud'Homme No 1	Canada	-69.91	58.26	1.880	0.086	0.109	0.011
Quandt (Ramsay; Keputch)	Canada	-102.75	54.74	1.870	0.016	0.013	0.004
Quemont	Canada	-79.01	48.26	2.702	0.200	0.300	0.003
Radiore No. 2	Canada	-77.56	49.74	2.726	0.002	0.002	ND
Rail Lake	Canada	-100.59	54.75	1.875	0.025	0.007	ND
Rambler Main	Canada	-56.06	49.90	0.487	0.007	0.012	ND
Rambler-Ming	Canada	-56.08	49.91	0.487	0.384	0.023	ND
Rea Gold	Canada	-119.82	51.15	0.361	0.001	0.009	0.008
Reed Lake	Canada	-100.55	54.64	1.875	0.083	0.013	0.000
Restigouche	Canada	-66.55	47.50	0.470	0.003	0.121	0.097
Rocky Turn	Canada	-66.07	47.63	0.470	0.000	0.011	0.004
Rod	Canada	-99.92	54.86	1.895	0.046	0.020	0.000
Rothermere	Canada	-56.88	48.82	0.465	0.038	0.416	0.252
Ruttan	Canada	-99.92	54.86	1.880	1.087	2.433	0.065
Samatosum	Canada	-119.81	51.14	0.361	0.005	0.015	0.008
Schist Lake and Mandy	Canada	-101.83	54.72	1.889	0.093	0.158	0.001
Schotts Lake	Canada	-102.23	55.10	1.870	0.012	0.027	0.000
Scotia	Canada	-129.67	54.08	0.393	0.001	0.038	0.004
Scott Lake	Canada	-74.63	49.86	2.728	0.068	0.297	ND
Selbaie	Canada	-78.96	49.80	2.729	0.619	0.930	ND
Seneca	Canada	-121.95	49.32	0.166	0.009	0.054	0.002
Sherridon	Canada	-101.11	55.14	1.853	0.183	0.176	0.002
Shunsby (Grandora)	Canada	-82.66	47.72	2.730	0.009	0.052	ND
Skidder	Canada	-56.92	48.73	0.465	0.018	0.018	ND
Solbec Copper	Canada	-71.27	45.81	0.460	0.162	0.442	0.056
Soucy	Canada	-69.87	58.32	1.880	0.081	0.098	0.011
Sourdough Bay	Canada	-101.62	54.76	1.880	0.004	0.005	0.000
South Bay	Canada	-92.68	51.11	2.739	0.035	0.223	ND
South Pond	Canada	-56.14	48.43	0.466	0.004	ND	ND
Spruce Point	Canada	-100.40	54.57	1.890	0.039	0.046	0.000
Stall Lake	Canada	-99.44	54.85	1.895	0.282	0.032	0.001
Stirling (Mindamar)	Canada	-60.44	45.73	0.681	0.009	0.079	0.018
Stralak	Canada	-81.71	46.80	2.730	0.003	0.022	0.003
Stratmat	Canada	-66.11	47.32	0.466	0.040	0.499	0.219
Strickland	Canada	-58.30	47.81	0.466	ND	0.010	0.010
Sturgeon Lake	Canada	-90.89	49.88	2.736	0.053	0.190	0.025
Suffield	Canada	-71.96	45.32	0.460	0.002	0.009	ND
Sunrise Lake	Canada	-112.38	62.90	2.670	0.004	0.245	0.096
Sunro	Canada	-124.03	48.45	0.045	0.014	ND	ND
Susu Lake	Canada	-110.79	63.01	2.680	0.001	ND	ND
Terra Nova	Canada	-56.23	49.92	0.487	0.011	ND	ND
Tilt Cove	Canada	-55.62	49.89	0.489	0.490	ND	ND
Trout Lake (Embury)	Canada	-101.82	54.83	1.870	0.376	1.074	0.013
Tulk's East	Canada	-57.13	48.54	0.498	0.015	0.093	0.007
Tulk's Hill	Canada	-57.20	48.51	0.498	0.009	0.040	0.014
Tulsequah Chief	Canada	-133.60	58.74	0.327	0.082	0.406	0.076
Turnback Lake (XL)	Canada	-112.64	62.73	2.680	0.004	0.011	0.003
Twin J	Canada	-123.79	48.87	0.366	0.005	0.023	0.002
Vauze	Canada	-79.08	48.36	2.698	0.010	0.003	ND
Vendme (Mogador)	Canada	-77.66	48.43	2.725	0.003	0.051	ND
Vermilion Lake	Canada	-81.36	46.52	1.848	0.040	0.138	0.035
Wedge	Canada	-66.13	47.40	0.470	0.053	0.052	0.019
Weedon	Canada	-71.37	45.70	0.460	0.043	0.007	0.001
Westarm	Canada	-101.84	54.64	1.875	0.045	0.021	0.001
Westwood	Canada	-78.44	48.25	2.698	ND	ND	ND
Whalesback	Canada	-56.01	49.60	0.505	0.036	ND	ND
White Lake	Canada	-101.72	54.71	1.880	0.017	0.039	0.002
Willecho	Canada	-85.88	49.18	2.720	0.010	0.087	0.004
Willroy	Canada	-85.83	49.16	2.720	0.065	0.112	0.012
Wim	Canada	-100.04	55.03	1.895	0.058	0.010	ND
Windy Craggy	Canada	-137.67	59.73	0.218	4.099	ND	ND
Winston Lake	Canada	-87.37	48.98	2.722	0.031	0.480	ND
Wolf (Hasselberg)	Canada	-131.49	61.34	0.350	ND	0.234	0.086
Wolverine	Canada	-130.13	61.43	0.348	0.073	0.747	0.099
Yava Lake	Canada	-107.93	65.60	2.690	0.013	0.064	0.021
York Harbour	Canada	-58.31	49.05	0.486	0.006	0.016	ND
Zenith	Canada	-87.36	48.98	2.722	0.027	0.506	ND
Pirn Alto	Chile	-73.10	-39.35	0.400	0.005	0.000	ND
Ashele (No. 1)	China	86.31	48.25	0.401	0.853	1.013	ND
Bizigou	China	124.98	42.15	2.980	0.007	0.026	ND
Chenjianiao	China	106.28	35.05	0.770	0.104	ND	ND

Continued overleaf...

Table 6 – continued

Deposit	Country	Lon.[a]	Lat.[a]	Age (Ga)	Cu (Mt)	Zn (Mt)	Pb (Mt)
Dadongguo	China	88.00	47.96	0.408	ND	ND	ND
Dahuanggou	China	124.76	42.20	2.980	0.003	0.038	ND
Dapingzhang (includes Dawaz)	China	100.52	22.78	0.429	0.563	0.216	0.086
Deerni	China	100.30	34.32	0.284	0.664	0.848	ND
Dongnanshan	China	124.63	42.11	2.980	0.008	0.013	ND
Gacun	China	99.53	31.18	0.217	0.018	0.216	0.148
Gayiqiong	China	99.30	31.57	0.219	ND	ND	ND
Guomisi	China	100.12	38.28	0.509	0.078	0.296	0.270
Honggou	China	101.02	37.37	0.478	0.135	ND	ND
Hongqishan	China	124.38	42.04	2.980	0.013	0.027	ND
Hongtoushan	China	124.53	42.02	2.980	0.700	0.960	ND
Huashugou (Jingtieshan)	China	97.93	39.32	0.770	0.226	ND	ND
Huoyanshan	China	104.25	36.68	0.503	0.260	ND	ND
Jiaolongzhang	China	106.07	35.32	0.503	ND	0.065	0.043
Keketale (Koktal)	China	89.20	47.35	0.409	0.002	0.095	0.045
Langlike	China	101.95	37.52	0.478	0.033	ND	ND
Liwu	China	101.80	28.60	0.402	0.775	0.155	ND
Shiqingdong	China	103.70	36.78	0.503	0.054	0.084	0.078
Shujigou	China	124.62	42.13	2.980	0.033	0.092	ND
Sigequan	China	104.25	36.68	0.503	0.120	0.157	0.062
Tiemurte	China	88.10	47.90	0.408	0.140	0.203	0.087
Tongchanggou	China	104.25	36.68	0.503	ND	ND	ND
Tongchangjie	China	99.75	24.33	0.329	0.008	ND	ND
Tongkuangyu	China	111.70	35.50	2.050	2.164	2.003	ND
Tongyu	China	110.30	34.53	0.490	0.065	ND	ND
Wutai	China	112.59	38.93	2.500	ND	ND	ND
Xiacun	China	99.85	31.10	0.201	0.077	0.677	0.418
Xiaorequanzi	China	89.52	42.28	0.320	0.005	0.002	ND
Xiaotieshan	China	104.25	36.68	0.503	0.428	1.812	1.153
Xibeishan	China	124.58	42.11	2.980	0.016	0.021	ND
Xiqiu	China	120.63	29.92	1.300	0.319	0.567	ND
Xitieshan	China	95.61	37.24	0.478	ND	0.486	0.416
Yargla	China	99.17	29.33	0.263	0.006	ND	ND
Zhanghugou	China	124.93	42.12	2.980	0.002	0.090	ND
Zheyaoshan	China	104.25	36.68	0.503	0.500	ND	ND
El Alacran	Columbia	-76.32	7.40	0.083	0.067	ND	ND
El Roble	Columbia	-76.42	6.10	0.083	0.057	ND	ND
Guadalupe	Columbia	-75.54	7.74	0.110	0.526	ND	ND
Santa Anita	Columbia	-75.73	5.67	0.083	0.013	ND	ND
Antonio	Cuba	-79.83	22.11	0.123	0.027	0.060	ND
Cacarajicara	Cuba	-83.28	22.81	0.113	0.007	ND	ND
Carlota	Cuba	-80.15	22.03	0.150	0.027	ND	ND
Cuba Libre	Cuba	-77.92	21.42	0.113	0.010	ND	ND
El Cobre-Zona Barita	Cuba	-75.93	20.02	0.052	0.164	ND	ND
Guachinango	Cuba	-80.12	22.07	0.150	0.041	ND	ND
Hierro Mantua	Cuba	-84.13	22.47	0.132	0.199	ND	ND
Infierno-El Pino-El Roble	Cuba	-76.33	20.02	0.052	0.280	0.636	0.176
Jcaro	Cuba	-83.28	22.86	0.113	0.008	ND	ND
La Victoria	Cuba	-80.15	22.08	0.150	0.005	ND	ND
San Fernando-Los Mangos	Cuba	-80.08	22.20	0.123	0.037	ND	ND
Agrokipia A	Cyprus	33.15	35.03	0.092	0.012	0.006	ND
Agrokipia B	Cyprus	33.15	35.03	0.092	0.018	0.027	ND
Alestos	Cyprus	33.02	35.04	0.092	0.012	ND	ND
Apliki	Cyprus	32.85	35.07	0.092	0.030	ND	ND
East Lefka	Cyprus	32.83	35.10	0.092	0.019	ND	ND
Kalavasos	Cyprus	33.75	34.80	0.092	0.060	0.030	0.001
Kambia (Kokkinonero)	Cyprus	33.28	35.00	0.092	ND	ND	ND
Kinousa (underground and open cut)	Cyprus	32.52	35.03	0.092	0.012	0.012	ND
Kokkinopezoula	Cyprus	33.12	35.03	0.092	0.007	ND	ND
Kokkinoyia	Cyprus	33.04	35.07	0.092	0.019	ND	ND
Limni	Cyprus	32.48	35.03	0.092	0.160	0.032	ND
Mangaleni	Cyprus	33.75	34.80	0.092	0.001	ND	ND
Mathiatis	Cyprus	33.35	34.97	0.092	0.006	0.028	ND
Mavrovouni	Cyprus	32.83	35.10	0.092	0.675	0.075	ND
Memi	Cyprus	33.04	35.04	0.092	0.002	ND	ND
Peristerka	Cyprus	33.23	34.99	0.092	0.003	0.001	ND
Phoenix (Skouriotissa)	Cyprus	32.88	35.08	0.092	0.160	ND	ND
Phoukasa (Skouriotissa)	Cyprus	32.88	35.08	0.092	0.135	0.004	ND
Pitharochoma	Cyprus	33.23	34.99	0.092	0.007	0.007	ND
Sha	Cyprus	34.95	33.37	0.092	0.004	ND	ND
Three Hills	Cyprus	32.90	35.09	0.092	0.023	ND	ND
West Apliki	Cyprus	32.83	35.07	0.092	0.012	ND	ND
Tisovi	Czech Republic	12.54	50.32	0.475	0.010	ND	ND
Zlate Hory	Czech Republic	17.41	50.27	0.380	0.170	0.595	0.145
Cerro de Maimn	Dominican Republic	-70.23	18.97	0.123	0.152	0.107	ND
El Anon - Anomaly B	Dominican Republic	-70.96	19.48	0.113	0.005	0.005	ND

Continued overleaf...

Table 6 – continued

Deposit	Country	Lon.[a]	Lat.[a]	Age (Ga)	Cu (Mt)	Zn (Mt)	Pb (Mt)
Loma Pesada	Dominican Republic	-70.36	19.09	0.123	0.024	0.008	0.000
San Antonio (Parcela)	Dominican Republic	-70.09	18.80	0.123	ND	ND	ND
La Plata	Ecuador	-78.90	-1.50	0.043	0.034	0.035	0.006
Mercedes	Ecuador	-79.10	-2.10	0.043	0.043	ND	ND
Um Samiuki	Egypt	34.41	27.01	0.712	0.003	0.035	0.003
Adi Nefas	Eritrea	39.03	15.33	0.750	0.038	0.229	ND
Bisha	Eritrea	37.50	15.40	0.750	0.262	1.513	0.053
Debarwa	Eritrea	39.00	15.12	0.750	0.020	0.038	ND
Emba Derho	Eritrea	38.88	15.42	0.750	0.449	0.863	ND
Aijala	Finland	23.36	60.19	1.895	0.013	0.006	ND
Attu	Finland	22.31	60.19	1.895	0.007	0.076	0.045
Hallaper	Finland	26.51	63.68	1.925	0.015	0.030	ND
Hllinmki	Finland	27.55	62.06	1.900	0.033	ND	ND
Hammaslahti	Finland	30.03	62.46	1.943	0.085	0.093	ND
Haveri	Finland	23.24	61.71	1.904	0.131	ND	ND
Kylylahti	Finland	29.35	62.86	1.926	0.051	0.015	ND
Luikonlahti	Finland	28.70	62.94	1.943	0.074	0.038	ND
Metsmonttu	Finland	23.34	60.19	1.895	0.004	0.050	0.011
Mullikkorme	Finland	26.16	63.70	1.921	0.011	0.277	0.029
Orijrvi	Finland	23.54	60.23	1.895	0.012	0.031	0.010
Outokumpu	Finland	28.99	62.72	1.943	1.083	0.305	0.001
Pahtavuoma	Finland	24.25	67.80	2.050	0.064	0.143	0.017
Perttilahti	Finland	29.19	62.79	1.943	0.028	0.021	ND
Pyhsalmi	Finland	26.05	63.66	1.932	0.518	1.424	0.039
Rauhala	Finland	24.79	64.06	1.905	0.023	0.081	0.016
Riihilathi	Finland	28.70	62.71	1.943	0.005	0.001	ND
Ruostesuo	Finland	26.36	63.59	1.925	0.011	0.054	ND
Salo-Issakka	Finland	28.78	61.10	1.895	0.006	0.030	ND
Saramki	Finland	29.13	62.94	1.943	0.024	0.021	ND
Svi	Finland	26.66	63.21	1.924	0.047	0.025	ND
Taivaljrvi	Finland	29.05	63.94	2.790	0.001	0.033	0.017
Tupala	Finland	23.55	60.61	1.881	ND	0.029	0.005
Vihanti	Finland	25.14	64.41	1.925	0.178	1.484	0.134
Vuohtojoki	Finland	25.93	63.99	1.925	0.002	0.018	ND
Vuonos	Finland	29.09	62.76	1.943	0.144	0.063	ND
Bodennec	France	-3.58	48.52	0.350	0.024	0.061	0.015
Chessy	France	4.61	45.90	0.360	0.137	0.479	0.021
Chizeuil	France	4.12	46.22	0.366	ND	ND	ND
La Port-aux-moines	France	-2.93	48.30	0.350	0.014	0.146	0.031
Rouez	France	-0.08	48.13	0.609	0.544	1.361	ND
Sain Bel	France	4.61	45.80	0.360	0.100	0.100	ND
Madneuli	Georgia	44.46	41.36	0.077	1.324	1.847	ND
Oxec	Guatemala	-89.44	15.53	0.125	0.027	ND	ND
Ambaji	India	72.85	24.33	0.987	0.236	0.626	0.451
Deri	India	72.83	24.38	0.987	ND	0.102	0.080
Kalyadi	India	76.50	11.50	3.352	0.007	ND	ND
Kali Kunning barite	Indonesia	126.28	-7.78	0.005	0.001	0.000	0.022
Lerokis and Kali Kunning pyrite	Indonesia	126.28	-7.78	0.005	0.281	0.022	0.026
Lerokis barite	Indonesia	126.28	-7.78	0.005	0.001	0.000	0.029
Barika	Iran	36.19	45.66	0.105	ND	ND	ND
Bavanat	Iran	30.46	53.59	0.191	0.180	0.030	ND
Chahgaz	Iran	54.70	29.45	0.176	0.060	0.900	0.600
Koushk (Kushk; Koushke)	Iran	55.76	31.75	0.528	ND	0.594	0.124
Sargaz	Iran	57.36	28.72	0.218	0.040	0.011	0.002
Avoca	Ireland	-6.22	52.87	0.457	0.096	ND	ND
Abeshiro	Japan	141.03	41.18	0.014	0.037	0.201	0.017
Ainai	Japan	140.75	40.38	0.012	0.065	0.164	0.053
Besshi	Japan	133.32	33.85	0.157	0.779	0.090	ND
Ezuri	Japan	140.60	40.24	0.012	0.027	0.303	0.100
Fukazawa	Japan	140.68	40.23	0.012	0.100	0.305	0.095
Furutobe	Japan	140.42	40.21	0.014	0.084	0.092	0.032
Hanaoka - Doyashiki	Japan	140.48	40.32	0.012	0.336	0.420	0.084
Hanaoka - Matsumine	Japan	140.48	40.32	0.013	0.780	0.690	0.180
Hanawa	Japan	140.87	40.13	0.012	0.053	0.116	0.032
Higashiyame	Japan	134.31	33.93	0.157	0.013	ND	ND
Hitachi	Japan	140.40	36.35	0.533	0.381	0.163	ND
Iimori	Japan	135.43	34.41	0.157	0.033	ND	ND
Iwami (Iwame and Iwame West)	Japan	132.44	35.18	0.012	0.023	0.332	0.068
Kamikita	Japan	140.92	40.73	0.014	0.034	0.020	ND
Kosaka - Motoyama	Japan	140.74	40.35	0.012	0.330	0.675	0.120
Kosaka - Uchinotai	Japan	140.75	40.33	0.011	0.227	0.386	0.118
Kosaka - Uwamuki	Japan	140.75	40.33	0.011	0.029	0.300	0.094
Kotsu	Japan	134.26	34.02	0.157	0.025	ND	ND
Kune	Japan	137.84	35.08	0.175	0.107	ND	ND
Kunitomi	Japan	140.70	43.03	0.012	0.005	0.032	0.001
Kurosawa	Japan	139.33	37.35	0.014	0.072	0.482	0.050

Continued overleaf...

Table 6 – continued

Deposit	Country	Lon.[a]	Lat.[a]	Age (Ga)	Cu (Mt)	Zn (Mt)	Pb (Mt)
Makimine	Japan	131.31	32.73	0.089	0.085	ND	ND
Matsuki	Japan	140.53	40.23	0.012	0.057	0.102	0.032
Nurukawa	Japan	140.79	40.50	0.012	0.007	0.079	0.039
Oshio	Japan	139.48	37.40	0.014	0.040	0.105	0.026
Sazare	Japan	133.57	33.90	0.158	0.065	0.015	ND
Shakanai	Japan	140.32	40.18	0.016	0.147	0.427	0.127
Shimokawa	Japan	142.98	43.90	0.048	0.182	0.107	ND
Shingu	Japan	133.68	33.94	0.157	0.006	ND	ND
Shirataki	Japan	133.47	33.82	0.157	0.031	0.008	ND
Taisho (including Nishimata)	Japan	140.91	41.46	0.014	0.045	0.154	0.022
Takaura	Japan	138.83	35.58	0.175	0.003	ND	ND
Tashiro	Japan	139.45	37.42	0.014	0.033	0.045	0.012
Terano	Japan	132.75	33.69	0.157	0.001	ND	ND
Yanahara	Japan	132.50	35.20	0.265	0.272	ND	ND
Yoshino	Japan	140.42	38.33	0.014	0.063	0.200	ND
50 Let Oktyrbrya	Kazakhstan	59.11	50.49	0.388	0.837	0.216	ND
Abyz	Kazakhstan	76.24	49.33	0.375	0.124	0.325	ND
Akbastau	Kazakhstan	77.79	48.61	0.475	0.343	0.211	ND
Anisimov Klyuch	Kazakhstan	83.00	50.68	0.375	0.061	0.105	0.014
Artemievskoe	Kazakhstan	82.81	50.60	0.375	0.964	3.278	1.011
Avangard	Kazakhstan	59.03	50.61	0.388	0.195	0.180	ND
Belousovskoye	Kazakhstan	82.50	50.13	0.395	0.330	1.422	0.345
Chekmar	Kazakhstan	83.62	50.64	0.395	0.267	2.273	0.832
Dolinnoye-Obruchev	Kazakhstan	83.60	50.33	0.395	0.095	0.220	0.110
Gabrielevskoe	Kazakhstan	83.25	50.32	0.390	0.041	0.074	0.013
Grekhovskoe	Kazakhstan	84.31	49.73	0.392	0.236	1.652	0.826
Irtyshskoe	Kazakhstan	82.37	50.15	0.395	0.648	1.536	0.213
Kamyshinskoe	Kazakhstan	81.78	50.60	0.375	0.396	0.416	0.158
Karchiga	Kazakhstan	85.51	48.44	0.530	0.190	0.043	ND
Kosmurun	Kazakhstan	77.79	48.60	0.475	0.745	0.192	ND
Krasnoyarskoe	Kazakhstan	82.43	50.36	0.380	0.045	0.202	0.061
Kunduzdy	Kazakhstan	58.61	49.16	0.388	0.329	0.350	ND
Limannoe	Kazakhstan	58.78	49.81	0.388	0.591	0.643	ND
Maikain cluster	Kazakhstan	75.80	51.48	0.490	ND	ND	ND
Maiskoe	Kazakhstan	84.15	49.43	0.390	0.030	0.449	0.172
Maleevskoe	Kazakhstan	84.29	49.89	0.390	1.150	3.750	0.650
Mizek	Kazakhstan	77.42	48.95	0.451	ND	ND	ND
Nikolayevskoe	Kazakhstan	81.88	50.53	0.376	0.967	1.306	0.173
Novo-Berezovskoe	Kazakhstan	82.24	50.27	0.388	0.088	0.195	0.006
Novo-Leningorskoe	Kazakhstan	83.57	50.36	0.395	0.085	2.157	0.764
Orlovskoe	Kazakhstan	81.36	50.93	0.392	2.256	1.536	0.432
Priorskoye	Kazakhstan	59.00	50.54	0.388	0.380	1.406	ND
Putintsevskoe	Kazakhstan	84.26	49.88	0.388	0.016	0.027	0.018
Ridder-Sokolnoye	Kazakhstan	83.54	50.35	0.400	0.876	3.727	1.751
Rulikha	Kazakhstan	81.97	50.49	0.371	ND	ND	ND
Shemonaikha	Kazakhstan	81.87	50.68	0.375	0.095	0.192	0.036
Shubinskoe	Kazakhstan	83.68	50.39	0.388	0.057	0.113	0.017
Snegirikha	Kazakhstan	82.98	50.68	0.375	0.203	0.197	0.030
Starkovskoe	Kazakhstan	83.82	50.42	0.388	0.046	0.184	0.027
Strezhanskoe	Kazakhstan	83.67	50.53	0.388	0.085	0.212	0.038
Suvenir	Kazakhstan	75.18	50.89	0.490	ND	ND	ND
Tesiktas	Kazakhstan	76.43	47.09	0.490	ND	ND	ND
Tishinskoye	Kazakhstan	83.37	50.28	0.395	0.300	3.180	0.540
Vavilonskoe	Kazakhstan	81.36	50.41	0.371	0.132	0.027	ND
Vesennee	Kazakhstan	59.45	50.63	0.401	0.367	0.325	ND
Zyryanovskoe	Kazakhstan	84.30	49.74	0.395	0.500	5.625	3.375
West Sualog	Malaysia	117.31	5.87	0.067	0.079	0.005	0.000
Azulaquez	Mexico	-99.70	18.57	0.140	0.002	0.042	0.015
El Cuale-La Prieta	Mexico	-105.08	20.38	0.154	0.006	0.080	0.025
El Largo	Mexico	-100.13	18.19	0.145	0.025	0.093	0.017
El Rey	Mexico	-100.13	18.21	0.145	0.018	0.088	0.020
La Esmerelda	Mexico	-100.40	19.05	0.132	ND	0.009	0.005
La Minita	Mexico	-103.08	18.59	0.123	ND	0.180	0.018
La Suriana	Mexico	-100.12	18.22	0.145	0.002	ND	0.027
Los Gavilanes	Mexico	-116.17	32.17	0.146	ND	ND	ND
Naranjo	Mexico	-100.14	18.19	0.145	0.074	0.184	0.049
Reforma	Mexico	-100.13	18.21	0.145	0.084	0.245	0.089
Rey de Plata	Mexico	-99.90	18.33	0.145	0.015	0.261	0.063
San Nicolas	Mexico	-102.00	22.65	0.148	1.353	1.632	0.149
Tizapa	Mexico	-100.40	19.08	0.132	0.032	0.356	0.081
Tumurtii-Ovoo	Mongolia	113.70	47.40	0.380	ND	0.886	ND
Ulaan	Mongolia	115.20	49.50	0.380	ND	1.360	0.816
Bleida	Morocco	-6.44	30.38	0.788	0.160	0.060	ND
Douar Lahjar	Morocco	-8.20	31.55	0.332	0.144	1.520	0.448
Hajar	Morocco	-8.18	31.51	0.332	0.100	1.600	0.600
Kettara	Morocco	-8.18	31.87	0.332	0.210	ND	ND

Continued overleaf...

Table 6 – continued

Deposit	Country	Lon.[a]	Lat.[a]	Age (Ga)	Cu (Mt)	Zn (Mt)	Pb (Mt)
Koudiat Acha	Morocco	-8.21	31.89	0.332	0.027	0.122	0.054
Tazakourt (Draa Sfar)	Morocco	-8.14	31.71	0.332	0.033	0.590	0.225
Gorob	Namibia	15.33	-23.47	0.755	0.027	ND	ND
Matchless	Namibia	16.75	-22.83	0.755	0.056	ND	ND
Otjihase	Namibia	17.25	-22.50	0.755	0.355	0.046	ND
Rosh Pinah	Namibia	16.76	-27.95	0.752	0.026	1.964	0.510
Skorpion	Namibia	16.66	-27.82	0.752	ND	6.843	0.604
soren	Norway	9.44	61.79	0.450	0.010	0.010	ND
Bjrksen	Norway	16.78	68.33	0.595	0.027	0.060	0.007
Bleikvassli	Norway	13.88	65.92	0.595	0.009	0.240	0.120
Bossmo	Norway	14.27	66.38	0.470	0.008	0.008	ND
Bursi	Norway	16.00	67.15	0.437	0.027	0.008	0.001
Charlotta	Norway	16.06	67.14	0.437	0.060	0.017	ND
Fahlbands	Norway	9.62	59.63	1.800	0.050	0.050	ND
Fjellsj	Norway	11.27	62.69	0.488	ND	ND	ND
Folldal	Norway	10.00	62.14	0.488	0.057	0.033	ND
Fosdalen	Norway	11.21	64.08	0.465	0.021	ND	ND
Giken	Norway	16.09	67.13	0.437	0.236	0.074	ND
Gjersvik	Norway	13.43	64.86	0.488	0.034	0.010	ND
Grimeli	Norway	5.08	61.44	0.443	0.030	0.015	ND
Grimsdallen	Norway	9.83	62.11	0.488	0.041	0.191	ND
Hammarfjell stre	Norway	17.16	68.36	0.595	ND	ND	ND
Hankabakken	Norway	16.11	67.14	0.437	0.035	0.010	ND
Hersjgruva	Norway	11.13	62.68	0.488	0.051	0.042	ND
Jacobsbakken	Norway	15.70	67.07	0.437	0.072	0.108	ND
Joma	Norway	13.88	64.85	0.488	0.335	0.326	ND
Killingdal	Norway	11.47	62.80	0.488	0.060	0.193	0.014
Kisgruva	Norway	9.61	59.60	1.320	0.006	0.007	ND
Kongens gruve	Norway	11.30	62.67	0.488	0.066	0.207	0.015
Lergruvbakken	Norway	11.34	62.65	0.488	0.009	0.088	0.004
Lillebo	Norway	5.47	59.79	0.430	0.009	0.009	0.009
Lkken	Norway	9.70	63.12	0.487	0.690	0.540	0.006
Mofjell	Norway	14.16	66.30	0.475	0.017	0.193	0.038
Mons Petter	Norway	16.03	67.14	0.437	0.044	0.012	ND
Mos	Norway	14.20	66.32	0.510	0.006	0.014	0.000
Muggruva	Norway	11.29	62.72	0.488	0.013	0.002	ND
Nordre Geitryggen	Norway	10.09	62.15	0.488	0.033	0.080	0.005
Ny-Sulitjelma	Norway	16.14	67.14	0.437	0.052	0.014	ND
Nye/Gamle Storwartz	Norway	11.54	62.63	0.488	0.031	0.206	0.015
Olavsgruva	Norway	11.56	62.63	0.488	0.041	0.033	ND
Quintus	Norway	11.55	62.63	0.488	0.007	ND	ND
Rieppe	Norway	21.59	69.74	0.439	0.015	0.060	ND
Rdhammeran	Norway	11.42	62.95	0.488	0.003	ND	ND
Rdkleiv	Norway	5.23	59.35	0.493	0.022	0.065	ND
Sagmo	Norway	16.01	67.12	0.437	0.038	0.005	ND
Skiftesmyr	Norway	12.61	64.48	0.488	0.034	0.051	ND
Skorovas	Norway	13.10	64.63	0.488	0.079	0.187	ND
Stord	Norway	5.42	59.79	0.430	ND	0.025	ND
Tverrfjellet	Norway	9.51	62.23	0.475	0.190	0.228	0.038
Undal	Norway	10.05	62.82	0.510	0.012	0.019	ND
Vaddas	Norway	21.58	69.81	0.439	0.019	0.000	ND
Vigsnes	Norway	5.22	59.35	0.493	0.057	0.072	ND
Visletten	Norway	13.20	64.79	0.488	0.007	0.030	ND
Ytterya	Norway	11.18	63.80	0.475	0.010	0.012	0.002
Aarja	Oman	56.42	24.33	0.095	0.048	0.029	0.000
Al Ajal	Oman	57.95	23.50	0.264	0.008	0.003	0.000
Al Bishara	Oman	56.54	23.66	0.095	0.033	ND	ND
Aswad	Oman	56.40	24.94	0.095	0.055	ND	ND
Bayda	Oman	56.38	24.55	0.095	0.028	0.013	0.000
Daris East	Oman	57.44	23.59	0.095	0.006	ND	ND
Ghuzayn	Oman	57.04	23.82	0.095	0.175	ND	ND
Hatta	Oman	56.44	25.00	0.095	0.028	0.008	ND
Hayl-As-Safil	Oman	56.55	23.66	0.095	0.104	0.048	0.001
Khaznah	Oman	56.45	24.99	0.095	0.004	ND	ND
Lasail	Oman	56.44	24.45	0.095	0.252	0.005	ND
Mahab 4	Oman	56.71	24.05	0.095	0.031	ND	ND
Mandoos	Oman	56.44	24.79	0.095	0.112	ND	ND
Maqail South	Oman	56.56	24.12	0.095	0.006	ND	ND
Rakah	Oman	56.62	23.65	0.095	0.031	0.005	0.000
Safwa	Oman	56.42	24.60	0.095	0.037	ND	ND
Shinas	Oman	56.38	24.76	0.095	0.055	ND	ND
Laloki	Papua-New Guinea	147.33	-9.43	0.041	0.015	0.009	ND
Cerro Lindo	Peru	-75.98	-13.08	0.100	0.668	2.460	0.270
Perubar	Peru	-76.58	-11.91	0.106	ND	0.552	0.078
Tambo Grande 1	Peru	-80.42	-4.92	0.104	0.899	0.562	0.169
Tambo Grande 3	Peru	-80.42	-4.93	0.104	0.820	1.148	0.246

Continued overleaf...

Table 6 – continued

Deposit	Country	Lon.[a]	Lat.[a]	Age (Ga)	Cu (Mt)	Zn (Mt)	Pb (Mt)
Ayala	Philippines	122.13	7.28	0.020	0.029	0.259	0.162
Bagacay	Philippines	125.27	11.80	0.020	0.168	0.129	ND
Canatuan	Philippines	121.78	7.80	0.138	0.042	0.033	ND
F	Philippines	119.96	15.99	0.044	0.044	0.051	ND
Hixbar	Philippines	124.19	13.19	0.084	0.017	0.028	ND
Marcos	Philippines	120.68	18.04	0.020	0.066	ND	ND
Ungay-Malobago	Philippines	124.13	13.19	0.084	0.087	0.145	ND
Aljustrel	Portugal	-8.16	37.86	0.352	0.690	1.176	0.662
Lagoa Salgada	Portugal	-8.48	38.45	0.356	0.013	0.164	0.119
Lousal	Portugal	-8.45	38.05	0.352	0.350	0.700	0.400
Neves Corvo	Portugal	-7.97	37.60	0.354	4.167	6.798	ND
Sao Domingos	Portugal	-7.47	37.67	0.359	0.360	0.900	ND
Zambujal-Lombador	Portugal	-7.97	37.60	0.350	0.462	1.271	ND
Aidyrlinskoe	Russia	59.85	52.07	0.386	0.110	0.140	ND
Aleksandrinskoe	Russia	59.37	53.52	0.391	0.448	0.550	0.052
Amurskoe	Russia	59.62	52.56	0.380	0.034	0.824	0.019
Bakr-Tau	Russia	58.18	52.44	0.396	0.034	0.061	0.009
Bakr-Uzayk	Russia	58.24	52.88	0.396	0.030	0.050	ND
Balta Tau	Russia	58.36	52.36	0.396	0.105	0.179	ND
Barsuchy Log	Russia	60.26	51.17	0.388	0.368	0.603	ND
Blyavinskoe	Russia	57.67	51.45	0.438	0.300	0.500	ND
Burubaiskoe	Russia	58.16	51.96	0.398	0.570	0.360	0.030
Chebach'e	Russia	59.40	54.10	0.388	0.241	0.327	ND
Dal'nee	Russia	95.60	52.02	0.531	0.008	0.150	0.015
Degtyarkskoe	Russia	60.09	56.71	0.413	1.690	3.510	0.130
Dergamish	Russia	58.09	51.76	0.420	ND	ND	ND
Dzerzhinskoe	Russia	60.20	55.49	0.386	0.191	0.173	ND
Dzhusinskoe	Russia	59.52	51.27	0.386	0.218	0.163	ND
Gaiskoe	Russia	58.49	51.46	0.398	6.566	2.814	0.281
Ishkinino	Russia	58.21	51.41	0.420	0.064	0.000	0.000
Ivonovskoe	Russia	57.92	52.45	0.430	0.108	0.030	ND
Kainooja	Russia	32.57	61.73	2.945	ND	0.018	0.022
Kaluginskoe	Russia	60.20	58.63	0.431	0.036	0.026	ND
Kamenushinskoe	Russia	85.81	54.38	0.431	0.109	ND	ND
Karabash	Russia	60.22	55.52	0.365	0.153	0.162	ND
Kasarginskoe	Russia	61.87	55.83	0.388	0.080	0.100	ND
Khotoidokh	Russia	141.14	66.45	0.154	0.042	0.894	0.309
Komsomolskoe	Russia	56.97	51.23	0.438	0.390	0.438	0.043
Korbalikhinskoe	Russia	82.32	51.28	0.377	0.365	2.453	0.503
Krasnogvardeyskoe	Russia	60.06	58.37	0.430	0.305	0.103	ND
Kyzyl-Tashtg	Russia	95.59	52.02	0.531	0.085	1.339	0.371
Leschevskoe	Russia	36.10	63.10	2.690	ND	ND	ND
Letnee	Russia	59.48	50.93	0.431	0.218	0.102	0.003
Levikhinskoe	Russia	59.92	57.58	0.431	0.227	0.227	ND
Lindolampi	Russia	33.93	62.10	2.000	0.130	ND	ND
Maiskoe (Maysk)	Russia	58.22	52.32	0.398	0.011	0.044	ND
Makanskoe	Russia	58.30	52.00	0.397	0.085	0.025	ND
Maukskoe	Russia	60.29	56.00	0.438	0.047	0.049	ND
Molodezhnoe	Russia	59.42	54.09	0.388	0.352	0.560	ND
Novo-Shermuskoe (Shermskoye Novy)	Russia	59.95	60.56	0.431	0.490	0.525	ND
Oktyabrskoe	Russia	58.26	52.02	0.397	0.454	0.239	ND
Osennee	Russia	59.54	50.92	0.431	0.342	0.018	ND
Ozernoe	Russia	111.70	52.93	0.531	ND	11.160	2.160
Pervomaiskoe	Russia	60.21	55.44	0.386	0.098	0.113	ND
Podolskoe	Russia	58.45	52.05	0.396	2.145	1.699	0.114
Rubtsovskoe	Russia	81.18	51.43	0.388	ND	0.560	0.326
Rybozero	Russia	35.48	63.07	2.600	ND	ND	ND
Rybozerskoe	Russia	35.47	63.08	2.690	ND	ND	ND
Safyanovka	Russia	61.53	57.38	0.390	0.767	0.312	ND
Salairskoe	Russia	85.78	54.24	0.530	0.150	2.100	0.435
Semenov East	Russia	58.21	51.51	0.365	0.011	0.075	ND
Sibaiskoe (Sibay)	Russia	58.64	52.70	0.391	1.150	1.794	0.046
Stepnoe	Russia	81.95	51.42	0.388	ND	0.743	0.374
Sultanovskoe	Russia	61.71	55.63	0.388	0.229	0.099	ND
Sumskoe	Russia	34.13	64.03	3.000	0.050	ND	ND
Talganskoe	Russia	59.37	54.14	0.388	0.113	0.084	ND
Talovskoe	Russia	81.91	51.45	0.388	ND	1.100	0.535
Talpus-1	Russia	33.72	62.82	2.690	0.080	ND	ND
Tarnyerskoe	Russia	59.92	60.82	0.430	0.144	0.386	0.061
Tash Tau	Russia	58.22	52.44	0.400	0.136	0.042	ND
Uchalinskoe (incl. Uchaly, Uchaly Novy)	Russia	59.43	54.31	0.391	2.305	7.232	ND
Urskoe	Russia	85.40	54.45	0.530	0.254	0.870	0.020
Uzelginskoe	Russia	59.34	54.13	0.388	1.142	2.856	ND
Valentorskoe	Russia	59.62	59.82	0.431	0.116	0.087	ND
Verhne-Vozhma	Russia	36.25	63.27	2.875	0.065	ND	ND
Vostochno-Povenetz	Russia	34.87	62.83	2.000	0.020	ND	ND

Continued overleaf...

Table 6 – continued

Deposit	Country	Lon.[a]	Lat.[a]	Age (Ga)	Cu (Mt)	Zn (Mt)	Pb (Mt)
Vostochno-Semenovskoe	Russia	58.33	52.51	0.400	0.011	0.075	ND
XIX Partsiezda	Russia	59.37	54.15	0.388	0.745	0.508	ND
Yaman Kasey	Russia	57.57	51.38	0.438	0.059	0.128	ND
Yubileinoe	Russia	58.13	52.17	0.400	2.033	1.284	0.107
Yubileinoe	Russia	81.57	50.87	0.377	0.070	0.387	0.103
Yulalinskoe	Russia	58.31	52.42	0.400	0.031	0.009	ND
Zakharovskoe	Russia	81.67	51.82	0.377	0.079	0.412	0.232
Zalomaevskoe	Russia	35.15	63.31	2.913	ND	ND	ND
Zapadno-Ashchebutakskoe	Russia	58.87	51.30	0.388	0.030	0.069	ND
Zapadno-Ozernoe (Ozernoe West)	Russia	59.28	54.19	0.390	0.459	0.561	ND
Zapadno-Rybozero	Russia	35.37	63.07	2.913	ND	ND	ND
Zarechenskoe	Russia	82.12	51.18	0.390	0.013	0.059	0.043
Zimnee	Russia	59.92	50.98	0.039	0.151	0.109	ND
Zmeinogorskoe	Russia	82.18	51.15	0.390	0.040	0.280	0.200
Zolotoporozhskoe	Russia	35.96	63.17	2.875	ND	ND	ND
Zolutushinskoe	Russia	81.44	50.99	0.388	0.290	2.176	0.462
Al Gehab	Saudi Arabia	41.40	20.68	0.700	0.020	0.012	ND
As Safra	Saudi Arabia	41.88	24.18	0.680	0.058	0.036	0.018
Jabal ash Shizm	Saudi Arabia	37.54	26.46	0.700	0.029	0.007	0.004
Jabal Sayid	Saudi Arabia	40.85	22.92	0.720	0.534	0.020	ND
Khnaiguiyah	Saudi Arabia	45.08	24.28	0.700	0.032	1.036	ND
Nuqrah	Saudi Arabia	41.44	25.64	0.680	0.011	0.080	0.023
Annex	South Africa	22.41	-30.23	1.285	0.023	0.008	ND
Areachap	South Africa	22.28	-29.92	1.250	0.042	0.199	ND
Bien Venue	South Africa	31.23	-25.67	3.259	0.009	0.120	0.045
Kantienpan	South Africa	21.54	-29.09	1.250	0.025	0.205	ND
Kielder K3	South Africa	22.34	-29.98	1.285	0.004	0.056	ND
Kielder K6	South Africa	22.34	-29.98	1.285	0.004	0.089	ND
LCZ (Letaba)	South Africa	30.81	-23.87	2.975	0.011	0.066	0.000
Maranda J	South Africa	30.52	-23.99	2.964	0.033	0.253	0.000
Preiska	South Africa	22.30	-29.93	1.285	0.691	1.819	ND
Romotshidi	South Africa	30.50	-23.99	2.970	0.005	0.069	0.003
Aguas Teidas	Spain	-6.82	37.77	0.350	0.023	ND	ND
Aguas Teidas Este	Spain	-6.85	37.78	0.350	0.951	2.357	1.134
Arinteiro	Spain	-8.32	42.88	0.471	0.084	ND	ND
Aznalcollar-Los Frailes	Spain	-6.28	37.53	0.346	0.664	4.267	2.244
Bama	Spain	-8.35	42.88	0.471	0.100	ND	ND
Concepcin	Spain	-6.68	37.78	0.350	0.322	0.322	0.087
Cueva de la Mora	Spain	-6.83	37.78	0.350	0.063	0.029	0.013
Forns	Spain	-8.49	42.85	0.471	0.015	ND	ND
Herrerias	Spain	-7.29	37.62	0.350	0.045	0.020	0.025
La Romanera	Spain	-7.35	37.68	0.350	0.136	0.782	0.408
La Zarza	Spain	-6.88	37.72	0.350	2.059	4.118	1.716
Las Cruces	Spain	-5.97	37.51	0.354	1.266	1.266	0.518
Lomero-Poyatos	Spain	-6.93	37.81	0.350	0.025	0.143	0.086
Monte Romero	Spain	-6.81	37.78	0.350	0.016	0.040	0.022
Rio Tinto	Spain	-6.60	37.70	0.350	9.198	6.433	3.452
San Miguel	Spain	-6.75	37.76	0.350	0.039	ND	ND
San Platn	Spain	-6.67	37.76	0.350	0.037	0.037	0.006
San Telmo	Spain	-6.96	37.80	0.350	0.048	0.480	0.016
Sierracilla	Spain	-7.29	37.67	0.350	0.015	0.120	0.050
Sotiel-Migollas	Spain	-6.85	37.61	0.350	0.970	3.674	1.611
Tharsis (Filon Norte and San Guillermo)	Spain	-7.10	37.58	0.350	0.575	3.105	0.690
Valverde	Spain	-6.83	37.54	0.350	0.400	1.188	0.584
Vuelta Falsa	Spain	-7.44	37.69	0.350	0.013	0.207	0.088
Adak-Lindskld	Sweden	18.63	65.37	1.889	0.114	ND	ND
kulla Vastra	Sweden	20.25	64.91	1.889	0.010	ND	ND
Alfrida-Hllefors	Sweden	14.48	59.85	1.889	ND	ND	ND
mmeberg-Zinkgruvan	Sweden	15.10	58.81	1.891	0.101	4.459	2.027
sen	Sweden	19.88	64.93	1.889	0.008	0.011	0.001
Bjurtrsk Norra	Sweden	19.73	64.99	1.889	0.002	0.009	0.000
Boliden	Sweden	20.37	64.87	1.894	0.118	0.075	0.025
Falun	Sweden	15.50	60.60	1.891	0.100	0.900	0.500
Garpenberg	Sweden	16.21	60.32	1.891	0.088	4.422	2.034
Holmtjrn nya	Sweden	19.57	65.11	1.889	0.002	0.018	0.002
Horntrskviken	Sweden	18.52	65.09	1.889	0.006	0.031	0.004
Kankberg	Sweden	20.27	64.92	1.889	0.016	0.021	0.003
Kedtrsk	Sweden	19.89	64.95	1.889	0.002	0.017	0.002
Kimheden	Sweden	18.60	65.09	1.889	0.001	0.000	ND
Kristineberg	Sweden	18.57	65.06	1.889	0.380	2.102	0.090
Lngdal	Sweden	20.23	64.83	1.889	0.008	0.241	0.063
Lngsele	Sweden	20.27	64.83	1.889	0.058	0.435	0.019
Maurliden Norra	Sweden	19.56	65.05	1.889	0.001	0.009	0.001
Maurliden stra	Sweden	19.55	65.05	1.889	0.021	0.018	ND
Maurliden Vstra	Sweden	19.52	65.06	1.889	0.010	0.172	0.020
Nsliden	Sweden	19.10	65.10	1.889	0.048	0.116	0.011

Continued overleaf...

Table 6 – continued

Deposit	Country	Lon.[a]	Lat.[a]	Age (Ga)	Cu (Mt)	Zn (Mt)	Pb (Mt)
Norrliden Norra	Sweden	19.59	65.02	1.889	0.019	0.183	0.016
Petikns Norra	Sweden	20.05	64.94	1.889	0.016	0.055	0.006
Petikns Sdra	Sweden	20.04	64.93	1.889	0.049	0.265	0.049
Rakkejaur	Sweden	19.12	65.13	1.889	0.002	0.009	0.002
Rvliden	Sweden	18.47	65.07	1.889	0.016	0.066	0.012
Rvlidmyran	Sweden	18.50	65.08	1.889	0.068	0.284	0.039
Renstrm	Sweden	20.09	64.92	1.889	0.124	1.111	0.220
Rudtjebcken	Sweden	18.50	65.37	1.889	0.045	0.135	0.001
Saxberget	Sweden	14.94	60.14	1.891	0.058	0.457	0.142
Stekenjokk-Levi	Sweden	14.46	65.10	0.488	0.376	0.778	0.081
Svansele	Sweden	19.82	64.98	1.889	0.009	0.009	0.003
Tjokkola	Sweden	14.40	65.10	0.488	0.020	0.112	0.016
Udden	Sweden	19.84	64.96	1.889	0.024	0.272	0.018
Akarsen	Turkey	29.68	41.48	0.077	0.115	ND	ND
Akkoy	Turkey	38.98	40.93	0.091	0.008	0.051	ND
Asikoy (Kre)	Turkey	33.70	41.80	0.169	0.175	ND	ND
Cayeli (Madenky)	Turkey	42.12	41.38	0.091	0.579	0.831	0.021
Cerateppe	Turkey	41.90	41.40	0.077	0.141	0.018	ND
Ergani (Anatatak; Mihrapdag)	Turkey	39.73	38.28	0.045	0.211	ND	ND
Harky	Turkey	40.93	38.88	0.091	0.022	0.037	0.010
Irsahan	Turkey	41.81	41.29	0.077	0.004	0.031	0.013
Kayabasi (Kankoy)	Turkey	39.00	40.97	0.091	0.037	ND	ND
Killik	Turkey	38.68	40.82	0.091	0.009	0.002	ND
Kizilkaya	Turkey	38.75	40.90	0.091	0.041	0.051	0.001
Kprbai (Tirebolu)	Turkey	38.72	41.00	0.083	0.039	0.277	0.188
Kotarak Dere	Turkey	40.11	40.87	0.091	0.013	0.026	ND
Kutlular	Turkey	40.88	40.07	0.091	0.030	0.018	0.000
Kuvarshan	Turkey	40.68	41.80	0.077	0.018	0.036	0.007
Lahanos	Turkey	38.70	40.75	0.091	0.154	0.174	0.012
Madenkoy-Siirt	Turkey	42.14	38.05	0.045	0.531	0.240	ND
Murgul (Anayatak; Cakmakkaya)	Turkey	41.57	41.22	0.091	0.920	0.078	0.039
Seyitler	Turkey	41.86	41.22	0.077	0.024	0.035	ND
Sinkot	Turkey	41.84	41.22	0.077	0.020	ND	ND
Tunca	Turkey	41.15	41.17	0.091	0.005	0.003	0.000
Yenipazar	Turkey	35.02	39.43	0.298	0.074	0.367	0.241
Kerry Road	United Kindom	-5.71	57.73	1.950	ND	ND	ND
Parys Mountain	United Kindom	-4.42	53.38	0.436	0.151	0.345	0.168
Afterthought	USA	-122.07	40.77	0.248	0.005	0.024	0.003
Alder Pond	USA	-70.21	45.36	0.484	0.011	0.046	0.003
Andersonville No Zone 18	USA	-78.56	37.44	0.471	0.004	0.034	0.004
Andersonville No Zone 24	USA	-78.51	37.44	0.471	0.005	0.024	0.003
Arctic	USA	-156.37	67.19	0.376	1.174	1.667	0.278
Balaklala	USA	-122.50	40.73	0.400	0.031	0.014	ND
Bald Mountain	USA	-68.73	46.74	0.467	0.309	0.336	0.015
Barite Hill	USA	-82.29	33.88	0.566	ND	ND	ND
Barrett	USA	-67.23	44.97	0.430	0.007	0.008	ND
Beatson	USA	-147.85	60.03	0.059	0.090	ND	ND
Bend	USA	-90.60	45.29	1.870	0.066	ND	ND
Big Hill	USA	-67.22	44.97	0.430	0.001	0.023	0.008
Binghampton-Copper Queen	USA	-112.19	34.46	1.745	0.011	ND	ND
Black Hawk	USA	-68.77	44.43	0.504	0.024	0.200	0.081
Blue Hill	USA	-68.48	44.39	0.504	0.009	0.069	ND
Blue Moon	USA	-120.20	37.60	0.154	0.025	0.289	0.016
Bruce-Old Dick	USA	-113.23	34.55	1.740	0.048	0.160	ND
BT	USA	-155.76	67.15	0.382	0.060	0.091	0.032
Catwillow	USA	-88.55	45.63	1.870	0.040	0.069	ND
Chestatee	USA	-83.88	34.55	0.850	0.011	0.008	ND
CL Zone	USA	-68.74	46.74	0.467	0.018	0.117	ND
Copper Chief	USA	-112.09	34.70	1.739	0.001	ND	ND
Crandon	USA	-88.92	45.48	1.875	0.685	3.665	0.316
Davis	USA	-72.87	42.70	0.464	0.006	0.050	0.000
DD	USA	-144.24	63.27	0.359	0.038	0.172	0.083
Dry Creek	USA	-147.37	63.92	0.357	0.006	0.128	0.055
Duchess	USA	-147.92	60.02	0.059	0.019	0.006	ND
Ducktown	USA	-84.37	35.01	0.758	1.633	1.470	ND
DW-LP	USA	-144.09	63.25	0.372	0.035	0.393	0.148
Eisenbrey (Thornapple)	USA	-91.12	45.44	1.870	0.021	0.027	ND
Elizabeth	USA	-72.33	43.82	0.405	0.052	0.015	ND
Ellamar	USA	-146.70	60.89	0.059	0.009	ND	ND
Flambeau	USA	-91.14	45.51	1.870	0.267	0.065	ND
Gossan Lead	USA	-80.75	36.82	0.750	0.050	0.200	0.010
Gray Eagle	USA	-123.37	41.86	0.153	0.041	ND	ND
Greens Creek	USA	-134.63	58.08	0.221	0.070	3.057	1.121
Harborside	USA	-68.81	44.35	0.504	0.010	0.044	0.004
Hawk	USA	-89.76	45.45	1.870	0.011	0.037	ND
Horse Shoe	USA	-89.62	45.44	1.870	0.016	0.036	0.006

Continued overleaf...

Table 6 – continued

Deposit	Country	Lon.[a]	Lat.[a]	Age (Ga)	Cu (Mt)	Zn (Mt)	Pb (Mt)
Iron Dyke	USA	-116.86	45.03	0.285	0.014	ND	ND
Iron King	USA	-111.74	34.50	1.745	0.009	0.360	0.123
Iron Mountain	USA	-122.53	40.68	0.400	0.156	0.063	ND
Jenny Stone	USA	-84.92	33.78	0.850	0.006	0.004	ND
Jones Hill	USA	-81.40	36.29	1.720	0.434	0.497	ND
Keystone-Union	USA	-122.51	40.72	0.400	0.007	0.009	ND
Ledge Ridge	USA	-70.96	45.19	0.440	0.035	0.085	0.031
Lookout	USA	-132.14	55.05	0.565	0.071	0.125	ND
Lynne	USA	-89.97	45.69	1.870	0.024	0.473	0.087
Mammoth	USA	-122.46	40.76	0.400	0.122	0.142	ND
Midas	USA	-146.39	61.01	0.083	0.002	ND	ND
Milan	USA	-71.25	44.57	0.465	0.011	0.036	0.008
Mount Chase	USA	-68.46	46.14	0.467	0.042	0.326	0.140
Orange Point	USA	-137.00	58.55	0.270	0.052	0.190	0.002
Ore Knob	USA	-81.33	36.38	0.750	0.034	0.007	ND
Pecos	USA	-105.67	35.77	1.720	0.002	0.259	0.080
Pelican River	USA	-89.29	45.60	1.870	0.020	0.090	ND
Penn	USA	-120.87	38.23	0.154	0.018	0.069	0.049
PP2	USA	-144.08	63.24	0.372	0.021	0.247	0.113
Pyriton	USA	-85.55	33.36	0.470	0.033	0.014	0.001
Red Ledge	USA	-116.67	45.23	0.285	0.152	0.371	ND
Rising Star-Bully Hill	USA	-122.20	40.80	0.248	0.024	0.019	ND
Ritchie Creek	USA	-90.06	45.49	1.870	0.017	0.003	ND
Rua Cove	USA	-147.63	60.35	0.059	0.012	ND	ND
Shasta King	USA	-122.50	40.73	0.400	0.002	0.006	ND
Smucker	USA	-157.19	67.29	0.382	0.064	0.544	0.184
Standard Copper	USA	-146.54	60.85	0.059	0.000	ND	ND
Stone Hill	USA	-85.55	33.49	0.900	0.008	0.013	ND
Sumdum	USA	-133.45	57.78	0.360	0.138	0.090	ND
Sun	USA	-155.04	67.08	0.386	0.351	0.820	0.217
Threeman	USA	-146.54	60.85	0.059	0.018	ND	ND
Trio	USA	-132.13	55.05	0.565	0.025	0.039	ND
TRIO	USA	-144.03	63.26	0.372	0.001	0.012	0.002
Turner Albright	USA	-123.77	42.00	0.164	0.044	0.103	ND
United Verde	USA	-112.13	34.76	1.739	1.425	1.284	0.245
United Verde Extended	USA	-112.11	34.58	1.739	0.361	ND	ND
Verde Central	USA	-112.12	34.74	1.739	0.005	ND	ND
WTF	USA	-147.33	63.92	0.363	0.003	0.168	0.070
Bailadores	Venezuela	-71.85	8.20	0.340	0.022	0.377	0.102
Sunyati	Zimbabwe	29.15	-17.83	2.000	0.235	0.519	0.139

[a] In decimal degrees

Table 7: Global compilation of 691 porphyry copper deposits shown in Figure S33, drawn primarily from Sillitoe (2010). Ga = billion years; Mt = million tonnes; ND = no data.

Deposit	Country	Lon.[a]	Lat.[a]	Age (Ga)	Cu (Mt)
Agua Rica	Argentina	-66.28	-27.37	0.006	7.40
Alcaparrosa	Argentina	-69.37	-31.30	0.267	ND
Arroyo Chita	Argentina	-69.75	-30.50	0.012	ND
Bajo de Agua Tapado	Argentina	-66.65	-27.27	0.009	ND
Bajo de la Alumbrera	Argentina	-66.61	-27.33	0.008	4.27
Bajo de la Leona	Argentina	-67.31	-48.08	0.200	ND
Bajo de San Lucas	Argentina	-66.55	-27.40	0.007	ND
Bajo El Durazno	Argentina	-66.57	-27.28	0.008	0.64
Betito	Argentina	-67.90	-26.30	0.014	ND
Campana Mahuida	Argentina	-70.58	-38.25	0.074	0.95
Carrizal	Argentina	-69.17	-30.00	0.261	ND
Cerro Mercedario	Argentina	-70.05	-31.95	0.013	ND
El Oculto	Argentina	-66.60	-24.13	ND	ND
El Salado	Argentina	-69.63	-30.93	ND	ND
Filo Colorado	Argentina	-66.22	-27.38	ND	ND
Inca Viejo	Argentina	-66.76	-25.14	0.015	ND
La Voluntad	Argentina	-70.63	-39.18	0.281	0.38
Los Azules	Argentina	-70.18	-31.24	ND	ND
Nevados de Famatina	Argentina	-67.75	-29.00	0.004	1.11
Pancho Arias	Argentina	-65.87	-24.20	0.015	ND
Paramillos Norte	Argentina	-69.08	-32.42	0.014	1.08
Paramillos Sur	Argentina	-69.10	-32.48	0.014	0.99
Quebrada del Bronce	Argentina	-70.47	-37.43	0.045	ND
San Jorge	Argentina	-69.43	-32.25	0.260	1.49
Taca Taca Alto	Argentina	-67.78	-24.57	0.029	ND
Taca Taca Bajo	Argentina	-67.73	-24.58	0.031	2.99

Continued overleaf...

Table 7 – continued

Deposit	Country	Lon.[a]	Lat.[a]	Age (Ga)	Cu (Mt)
Yalguaraz	Argentina	-69.44	-32.14	0.264	ND
Agarak	Armenia	46.19	38.92	0.040	0.70
Ankavan	Armenia	44.52	40.63	0.033	ND
Dastakert	Armenia	46.02	39.38	0.022	ND
Kadjaran	Armenia	46.14	39.14	0.022	4.59
Shikahoh	Armenia	46.47	39.10	0.144	ND
Teghout	Armenia	44.86	41.10	0.121	1.62
Anabama Hill	Australia	140.24	-32.77	0.440	ND
Andromache River	Australia	148.26	-20.57	0.265	ND
Boddington	Australia	116.36	-32.74	2.620	0.80
Cadia Hill/Ridgeway	Australia	149.00	-33.47	0.449	3.87
Cargo	Australia	148.85	-33.62	0.416	ND
Chinaman Creek	Australia	151.62	-25.24	0.250	ND
Coalstoun	Australia	151.92	-25.68	0.235	0.25
Copper Hill	Australia	148.87	-33.05	0.447	0.45
Copper Hills	Australia	119.96	-21.66	0.470	0.28
Coppin Gap	Australia	120.11	-20.89	3.234	0.79
Dogwood	Australia	148.01	-37.57	0.410	ND
Endeavour	Australia	148.03	-32.92	0.442	1.44
Frogmore	Australia	148.84	-34.27	0.430	ND
Kelly	Australia	119.87	-21.79	2.630	ND
Kiwi Carpet	Australia	150.88	-24.67	0.235	ND
Limonite Hill	Australia	150.63	-23.69	0.246	ND
Mandamah	Australia	147.42	-33.97	0.445	ND
Marsden	Australia	147.53	-33.72	0.470	0.58
Moonmera	Australia	150.40	-23.60	0.245	ND
Mount Cannindah	Australia	151.37	-24.82	0.235	ND
Mt. Abbot	Australia	147.95	-20.20	ND	ND
Mt. Leslie	Australia	140.17	-20.34	ND	ND
Mt. Poole	Australia	152.37	-29.84	ND	ND
Mt. Robin	Australia	146.98	-20.58	0.285	ND
Mt. Turner	Australia	143.42	-18.25	0.310	ND
Peak Hill	Australia	148.22	-32.75	ND	ND
Struck Oil	Australia	150.46	-23.61	0.250	ND
Thursdays Gossan	Australia	142.61	-37.61	0.505	0.06
Town Creek	Australia	146.78	-20.42	0.285	ND
Whitewash	Australia	150.87	-24.81	0.235	ND
Yeoval	Australia	148.67	-32.77	0.390	ND
Yeppoon	Australia	150.69	-23.00	0.220	ND
Damirli	Azerbaijan	46.75	40.02	0.135	ND
Garadag	Azerbaijan	45.85	40.63	0.135	ND
Goshgarchai	Azerbaijan	46.15	40.53	0.135	ND
Kedabek	Azerbaijan	45.79	40.56	1.141	ND
Misdag	Azerbaijan	46.05	39.05	0.040	ND
Herzogenhugel	Belgium	5.92	50.28	0.419	0.03
Bom Jardim	Brazil	-51.60	-17.53	0.840	ND
Chapada	Brazil	-49.37	-14.25	0.840	0.59
Estrela	Brazil	-49.62	-6.40	1.880	0.15
Assarel	Bulgaria	23.98	42.58	0.090	1.56
Byrdtseto	Bulgaria	27.53	41.97	0.081	ND
Elatsite	Bulgaria	24.03	42.75	0.092	1.37
Medet	Bulgaria	24.09	42.72	0.090	0.90
Plana	Bulgaria	23.42	42.48	0.076	ND
Prohorovo	Bulgaria	26.30	42.34	0.081	ND
Spahievo	Bulgaria	25.25	42.12	0.033	ND
Tsar Assen	Bulgaria	24.34	42.36	0.090	0.03
Vlaykov Vruh	Bulgaria	24.23	42.35	0.086	0.05
Afton	Canada	-120.52	50.66	0.206	1.11
Ajax	Canada	-120.53	50.61	0.206	0.65
Axe	Canada	-120.53	49.65	0.179	0.50
Beidelman Bay	Canada	-91.00	49.83	2.500	ND
Bell Copper	Canada	-126.23	55.00	0.053	1.78
Berg	Canada	-127.44	53.80	0.050	0.95
Bethlehem	Canada	-121.00	50.49	0.200	3.05
Big Onion	Canada	-126.89	54.81	0.053	0.40
Brenda	Canada	-120.01	49.88	0.143	0.36
Bronson	Canada	-131.09	56.67	0.195	0.15
Cash	Canada	-137.62	62.42	ND	0.10
Casino	Canada	-138.83	62.74	0.073	2.12
Catface	Canada	-125.98	49.26	0.036	1.14
Chibougamau	Canada	-74.23	49.87	2.715	ND
Chuchi	Canada	-124.54	55.26	0.188	ND
Coles Creek	Canada	-127.23	53.53	0.086	ND
Copper Canyon	Canada	-131.35	57.12	0.212	0.58
Copper Mountain	Canada	-120.56	49.34	0.199	1.53
Coxheath	Canada	-60.37	46.08	0.621	ND

Continued overleaf...

Table 7 – continued

Deposit	Country	Lon.[a]	Lat.[a]	Age (Ga)	Cu (Mt)
Don Rouyn	Canada	-79.00	48.27	2.700	0.05
Dorothy	Canada	-126.17	55.25	0.050	0.12
Eaglehead	Canada	-129.11	58.48	0.186	0.12
Fish Lake	Canada	-123.63	51.46	0.079	2.53
Galaxy	Canada	-120.42	50.64	ND	0.03
Galore Creek	Canada	-131.45	57.13	0.208	3.00
Gambier Island	Canada	-123.42	49.50	ND	0.33
Gaspe	Canada	-65.52	48.97	0.348	1.86
Giant Copper	Canada	-121.03	49.17	ND	0.66
Gibraltar	Canada	-122.29	52.52	0.210	3.69
Gnat Lake	Canada	-129.83	58.25	ND	0.12
Granisle	Canada	-126.16	54.95	0.051	0.37
Highmont	Canada	-120.92	50.43	ND	0.70
Huckleberry	Canada	-127.18	53.68	0.082	0.77
Hushamu	Canada	-127.86	50.68	0.170	1.46
Island Copper	Canada	-127.48	50.60	0.171	1.55
Jogran	Canada	-84.62	47.04	1.070	0.04
Katie	Canada	-117.33	49.13	ND	ND
Kemess North	Canada	-126.76	57.06	0.203	1.24
Kemess South	Canada	-126.75	57.01	0.200	0.55
Kerr	Canada	-130.27	56.47	0.194	1.06
Kinaskan	Canada	-130.24	57.65	0.205	0.59
Krain	Canada	-120.97	50.58	ND	0.22
Kwanika	Canada	-125.30	55.50	0.121	0.07
Lennac Lake	Canada	-126.33	54.75	0.078	ND
Lornex	Canada	-121.04	50.45	0.197	2.19
Lorraine	Canada	-125.43	55.93	0.184	0.21
Louise Lake	Canada	-127.68	54.78	ND	0.15
Maggie	Canada	-121.42	50.92	0.061	0.51
McIntyre	Canada	-81.25	48.50	2.575	ND
Misty	Canada	-125.51	55.92	0.172	ND
Morrison	Canada	-126.32	55.19	0.050	1.03
Mt. Milligan	Canada	-124.03	55.12	0.186	0.96
Mt. Polly	Canada	-121.64	52.55	0.202	0.67
O.K.	Canada	-124.65	50.05	0.036	0.34
Ox Lake	Canada	-127.06	53.67	0.084	0.07
Pine	Canada	-126.73	57.23	0.197	0.06
Poison Mountain	Canada	-122.61	51.13	0.057	1.94
Poplar	Canada	-126.99	54.02	0.074	0.87
Primer	Canada	-120.46	49.76	ND	0.05
Rayfield	Canada	-121.09	51.31	ND	ND
Red Bluff	Canada	-131.10	56.67	0.195	0.09
Red Chris	Canada	-129.81	57.70	0.203	1.83
Red Dog	Canada	-127.97	50.71	ND	0.14
Schaft Creek	Canada	-130.99	57.36	0.220	3.59
Stancop	Canada	-80.75	47.97	2.633	ND
Sulphurets	Canada	-130.26	56.50	0.194	1.55
Taseko	Canada	-123.40	51.10	0.085	0.08
Tribag	Canada	-84.48	47.09	1.055	0.25
Trojan	Canada	-121.00	50.57	ND	ND
Valley	Canada	-121.05	50.49	0.196	3.60
Whipsaw	Canada	-120.76	49.29	ND	ND
Whiting Creek/Rusty Zone	Canada	-127.22	53.76	0.083	ND
Willa	Canada	-117.37	49.88	0.183	ND
Williams Creek	Canada	-136.69	62.34	ND	ND
Andacollo	Chile	-71.42	-30.25	0.112	2.43
Angelina	Chile	-69.61	-24.40	ND	ND
Antucoya	Chile	-69.92	-22.53	0.142	2.13
Centinela	Chile	-69.17	-23.16	0.044	ND
Cerro Casale	Chile	-69.23	-27.78	0.014	4.50
Cerro Colorado	Chile	-69.26	-20.04	0.052	4.92
Chimborazo	Chile	-69.08	-24.13	0.037	1.42
Chuquicamata	Chile	-68.90	-22.28	0.033	125.96
Collahuasi	Chile	-68.71	-20.96	0.032	26.66
Conchi	Chile	-68.74	-21.95	0.036	2.49
Copaquire	Chile	-68.89	-20.90	0.035	ND
Dos Hermanos	Chile	-69.72	-18.29	0.013	ND
El Abra	Chile	-68.83	-21.92	0.036	8.79
El Loa	Chile	-68.73	-21.12	0.252	ND
El Salvador	Chile	-69.55	-26.25	0.042	17.15
El Telagrafo	Chile	-69.08	-22.99	0.029	4.04
El Teniente	Chile	-70.46	-34.09	0.005	128.53
Escondida	Chile	-69.07	-24.27	0.037	85.81
Esperanza	Chile	-69.06	-22.97	0.041	7.32
Gaby	Chile	-68.82	-23.41	0.042	11.97
Inca de Oro	Chile	-69.87	-26.77	0.063	ND

Continued overleaf...

Table 7 – continued

Deposit	Country	Lon.[a]	Lat.[a]	Age (Ga)	Cu (Mt)
La Fortuna	Chile	-69.88	-28.63	0.034	5.10
La Planada	Chile	-69.08	-20.18	0.031	ND
Lilian	Chile	-68.75	-22.67	0.275	ND
Lomas Bayas	Chile	-69.51	-23.45	0.058	3.43
Los Bronces/Rio Blanco	Chile	-70.27	-33.13	0.005	101.06
Los Pelambres - El Pachon, AGTN	Chile	-70.50	-31.71	0.010	46.02
Mana	Chile	-69.24	-22.56	0.064	ND
Mansa Mina	Chile	-68.91	-22.38	0.034	13.00
Mocha	Chile	-69.28	-19.81	0.058	ND
Opache	Chile	-68.97	-22.47	0.036	1.81
Polo Sur	Chile	-69.23	-23.30	ND	ND
Potrerillos	Chile	-69.42	-26.49	0.037	10.05
Puntillas	Chile	-69.83	-21.92	0.132	ND
Quebrada Blanca	Chile	-68.80	-21.00	0.036	7.85
Queen Elizabeth	Chile	-68.97	-19.87	0.036	ND
Regalito	Chile	-69.60	-28.22	ND	3.68
Relincho	Chile	-70.30	-28.50	0.064	2.50
Rio Frio	Chile	-69.23	-25.22	0.292	ND
Sierra Gorda	Chile	-69.34	-22.88	0.064	0.66
Spence	Chile	-69.30	-22.84	0.057	4.57
Ticnamar	Chile	-69.45	-18.59	ND	1.00
Toki	Chile	-68.95	-22.42	0.038	11.99
Turbio	Chile	-72.15	-46.03	ND	ND
Ujina	Chile	-68.64	-20.99	0.035	9.22
Vizcachitas	Chile	-70.23	-32.88	0.011	4.42
Anjishan	China	119.10	32.07	0.115	ND
Bainamiao	China	112.55	41.72	0.450	0.51
Beiya	China	100.20	26.15	0.037	ND
Changaan	China	103.00	22.80	0.036	ND
Chengmenshan	China	115.83	29.68	0.142	3.07
Chihu	China	92.97	42.20	0.350	ND
Chonjiang	China	90.00	29.58	0.014	0.50
Dexing	China	117.73	29.02	0.173	8.38
Dongga	China	88.38	29.38	0.014	2.73
Duobaoshan	China	125.69	50.17	0.260	4.37
Duoxiasongduo	China	97.87	31.08	0.036	0.90
Fengshandong	China	115.45	29.81	0.144	0.40
Gegongnong	China	98.50	30.47	0.044	0.51
Habo	China	102.58	22.88	0.037	ND
Hengxingcuo	China	97.35	31.48	0.042	ND
Jiama	China	91.75	29.69	0.015	ND
Jicuo	China	98.58	29.92	0.041	ND
Jiru	China	88.93	29.68	ND	ND
Kalatage	China	91.92	42.53	0.348	ND
Lakangae	China	91.48	29.58	0.014	ND
Linglong	China	92.85	42.17	0.350	ND
Machangqing	China	100.50	25.67	0.036	0.31
Malasongduo	China	97.95	31.00	0.037	1.03
Mamupu	China	98.53	29.83	0.038	ND
Mangzhong	China	97.80	31.20	0.038	0.25
Nanmu	China	90.82	29.47	0.015	ND
Pulang	China	99.83	28.03	0.213	0.29
Qulong	China	91.58	29.60	0.016	7.89
Ridanguo	China	96.77	32.15	0.042	ND
Saishitang	China	99.82	35.29	ND	0.57
Sanchakou	China	94.83	42.35	0.350	ND
Seli	China	98.52	30.03	0.036	ND
Shaxi	China	117.27	31.18	0.148	ND
Tinggong	China	90.05	29.55	0.016	ND
Tongchankou	China	114.80	30.17	0.136	0.42
Tongkuangyu	China	111.70	35.50	2.150	3.04
Tuwu	China	92.62	42.12	0.333	2.10
Wunugetushan	China	117.43	49.39	0.183	2.23
Xiariduo	China	97.13	31.68	0.046	ND
Xietongmen	China	88.57	29.52	0.162	0.95
Xifanping	China	101.13	27.40	0.032	0.18
Yandong	China	92.52	42.08	0.333	2.16
Yulong	China	97.73	31.40	0.041	7.14
Zhanaga	China	97.73	31.25	0.039	0.30
Zhunuo	China	87.53	29.43	ND	1.00
Zijinshan	China	116.40	25.05	0.105	1.74
Acandi	Colombia	-77.32	8.49	0.048	ND
California	Colombia	-72.87	7.32	0.144	ND
Dolores	Colombia	-75.03	3.52	0.166	ND
Infierno-Chile	Colombia	-75.30	4.18	0.131	ND
Mocoa	Colombia	-76.67	1.24	0.166	1.05

Continued overleaf...

Table 7 – continued

Deposit	Country	Lon.[a]	Lat.[a]	Age (Ga)	Cu (Mt)
Murindo	Colombia	-76.75	7.05	0.055	ND
Pantanos-Pegadorcito	Colombia	-76.50	6.70	0.043	ND
Piedrasentada	Colombia	-76.88	2.10	0.017	ND
Nari	Costa Rica	-83.36	9.70	ND	ND
Sukut	Costa Rica	-82.98	9.37	ND	ND
Arimao	Cuba	-80.03	22.12	ND	0.22
El Cobre	Cuba	-75.95	20.05	0.052	ND
Eureca	Cuba	-76.87	20.25	ND	ND
Majagual	Dominican Republic	-70.25	18.52	ND	ND
Balzapamba-Las Guardias	Ecuador	-79.15	-1.67	0.020	ND
Chaso Juan	Ecuador	-79.12	-1.38	0.020	ND
Chaucha	Ecuador	-79.42	-2.93	0.011	1.45
Cumay	Ecuador	-78.88	-4.02	0.141	ND
El Hito	Ecuador	-78.95	-4.25	0.154	ND
Fierro Urcu	Ecuador	-79.33	-3.58	0.010	0.11
Gaby-Papa Grande	Ecuador	-79.68	-3.05	0.019	0.20
Junin	Ecuador	-78.58	0.33	0.007	2.26
Los Linderos	Ecuador	-80.00	-4.33	0.013	ND
Mirador	Ecuador	-78.90	-4.65	0.154	4.98
Panantza	Ecuador	-78.50	-3.60	0.154	3.06
Rio Playas	Ecuador	-79.58	-4.20	0.014	ND
San Carlos	Ecuador	-78.42	-3.65	0.154	4.25
Telimbela	Ecuador	-79.13	-1.57	0.015	ND
Tumi	Ecuador	-79.25	-4.25	0.154	ND
Warintza	Ecuador	-78.60	-3.78	0.154	0.76
Namosi	Fiji	178.18	-18.04	0.006	4.19
Waivaka	Fiji	178.18	-18.11	0.006	0.17
Kopsa	Finland	25.23	63.77	1.850	ND
Fakos	Greece	25.19	39.81	0.021	ND
Kassiteres	Greece	25.79	41.02	0.024	ND
Maronia	Greece	25.56	40.87	0.029	ND
Pontokerassia	Greece	23.19	41.06	ND	ND
Skouries/Fisoka	Greece	23.70	40.47	0.019	1.99
Douvray	Haiti	-71.78	19.55	ND	1.44
Terre-Neuve	Haiti	-72.70	19.52	0.066	ND
Barzsany Mountains	Hungary	19.05	47.91	0.014	ND
Recsk	Hungary	20.10	47.93	0.036	4.62
Malanjkhand	India	80.72	22.02	2.490	6.62
Baroi	Indonesia	113.18	-0.50	ND	ND
Batu Hijau	Indonesia	116.87	-8.97	0.004	7.22
Bulagidun	Indonesia	121.77	0.95	0.009	ND
Ciemas	Indonesia	106.56	-7.22	0.003	ND
Grasberg	Indonesia	137.23	-3.82	0.003	24.00
Hila	Indonesia	128.09	-3.61	0.004	ND
Ibu	Indonesia	109.25	0.83	0.105	ND
Kaputusan	Indonesia	127.58	-0.52	ND	0.25
Mudik	Indonesia	101.25	-1.70	ND	ND
Sassak	Indonesia	119.48	-3.16	0.011	ND
Tangse	Indonesia	95.95	5.03	0.011	0.90
Tapadaa	Indonesia	123.22	0.52	0.004	0.23
Tombulilato	Indonesia	123.40	0.35	0.003	1.81
Ali-Abad	Iran	53.85	31.66	0.016	0.29
Dallil	Iran	49.27	34.55	0.015	ND
Darreh-Zerreshk	Iran	53.82	31.58	0.016	0.21
Darrehzar	Iran	55.90	29.88	0.015	0.23
Kale Kafi	Iran	54.54	33.54	ND	0.64
Meiduk	Iran	55.17	30.42	0.011	1.49
Raigan	Iran	57.23	28.90	0.012	ND
Sar Cheshmeh	Iran	55.86	29.95	0.013	14.40
Sungun	Iran	46.37	38.81	0.015	4.89
Calabona	Italy	8.37	40.53	0.031	0.13
Carbonia	Italy	8.50	39.17	0.030	ND
Ogliastra	Italy	9.52	39.82	0.285	ND
Aktogai	Kazakhstan	79.97	46.93	0.333	10.28
Almaly	Kazakhstan	73.70	48.68	0.310	ND
Baiskoe	Kazakhstan	75.60	49.16	0.310	ND
Bataly	Kazakhstan	61.42	52.88	0.301	ND
Benkala	Kazakhstan	61.75	51.77	0.312	1.30
Besshoky	Kazakhstan	76.27	48.23	0.310	ND
Borly	Kazakhstan	74.08	47.50	0.329	0.32
Boshchekul	Kazakhstan	74.18	51.82	0.479	6.70
Chatyrkul	Kazakhstan	74.26	43.62	0.401	0.54
Karatas	Kazakhstan	73.63	46.65	0.310	0.13
Kazkyrmyskoye	Kazakhstan	74.28	45.48	0.375	1.54
Kenkuduk	Kazakhstan	75.23	47.38	0.294	0.08
Kepcham	Kazakhstan	75.10	47.50	ND	0.12

Continued overleaf...

Table 7 – continued

Deposit	Country	Lon.[a]	Lat.[a]	Age (Ga)	Cu (Mt)
Koksai	Kazakhstan	78.43	44.45	0.422	1.76
Koktasdzhal	Kazakhstan	76.16	50.16	0.292	0.35
Kounrad	Kazakhstan	74.99	46.99	0.330	3.75
Kyzylkain	Kazakhstan	84.42	47.53	0.325	1.63
Kyzyltu	Kazakhstan	72.33	51.95	0.445	0.32
Nurbay	Kazakhstan	79.33	47.92	0.300	ND
Nurkazgan	Kazakhstan	76.73	50.03	0.410	1.73
Ozernoe	Kazakhstan	75.98	49.33	0.315	0.70
Saryshagan	Kazakhstan	73.20	46.26	0.310	0.87
Sokurkoiy	Kazakhstan	74.42	46.60	0.310	ND
Spiridonovskoe	Kazakhstan	62.18	52.33	ND	ND
Varvarinskoye	Kazakhstan	62.57	53.02	0.310	0.78
Yubileinoe	Kazakhstan	58.68	48.93	0.355	ND
Taldy-Bulak	Kyrgyzstan	75.65	42.70	0.420	1.46
Phu Kham	Laos	102.93	18.92	0.250	1.41
Buchim	Macedonia	22.60	41.51	0.023	0.45
Ilovitza	Macedonia	22.82	41.37	0.033	ND
Kadiica	Macedonia	22.88	41.62	0.034	ND
Osogovo	Macedonia	22.87	41.80	0.023	ND
Bongkud	Malaysia	116.75	6.03	ND	ND
Mamut	Malaysia	116.47	6.03	0.007	0.94
Mengpur	Malaysia	102.87	3.85	0.245	0.81
Nungkok	Malaysia	116.47	6.10	0.008	ND
Bahuerachi	Mexico	-108.34	27.05	0.066	2.40
Batopilas	Mexico	-107.70	27.03	0.052	ND
Caballo Blanco	Mexico	-96.45	19.68	0.004	ND
Cananea	Mexico	-110.32	30.95	0.059	23.13
Cerro Colorado	Mexico	-107.33	26.25	0.046	ND
Cuatro Hermanos	Mexico	-109.66	28.39	0.056	1.00
Cumobabi	Mexico	-109.96	29.87	0.059	0.18
El Arco	Mexico	-113.57	28.03	0.164	5.26
El Batamote	Mexico	-109.75	30.48	0.057	0.02
Inguaran	Mexico	-101.64	18.88	0.036	0.09
La Caridad	Mexico	-109.56	30.32	0.054	8.14
La Florida	Mexico	-109.73	30.38	0.052	0.45
La Reyna	Mexico	-106.07	23.33	0.075	0.17
La Verde	Mexico	-102.03	19.08	0.033	0.77
Luz del Cobre	Mexico	-109.38	28.43	0.075	0.11
Mariquita	Mexico	-110.42	31.06	0.063	0.48
Milpillas	Mexico	-110.45	31.12	0.063	1.96
Piedras Verdes	Mexico	-109.02	27.17	0.060	1.07
Pilares	Mexico	-109.63	30.33	0.053	1.53
Rodeo	Mexico	-100.85	18.62	0.075	ND
San Isidro	Mexico	-101.98	18.94	0.033	0.05
Santo Tomas	Mexico	-108.23	26.72	0.057	1.36
Suaqui Verde	Mexico	-109.80	28.41	0.057	0.37
Tameapa	Mexico	-107.35	25.67	0.054	0.13
Tepal	Mexico	-102.92	19.12	0.075	0.20
Tiamaro	Mexico	-100.68	19.38	0.135	ND
Toliman	Mexico	-92.33	15.32	0.006	ND
Tuligtic	Mexico	-97.85	19.70	0.018	ND
Avdartolgoi	Mongolia	114.84	49.67	0.154	ND
Bayan-Uul	Mongolia	104.88	46.68	0.222	ND
Erdenet	Mongolia	104.13	49.00	0.230	9.01
Kharmagtai	Mongolia	106.17	44.00	0.330	0.80
Khongoot	Mongolia	103.65	49.13	0.300	ND
Khongor	Mongolia	102.80	43.17	ND	ND
Naran Bulag	Mongolia	97.78	48.58	0.260	ND
Nariin Khudag	Mongolia	108.03	44.23	0.300	ND
Oyu Tolgoi	Mongolia	106.87	43.00	0.367	21.00
Oyuut Ulaar Ovoo	Mongolia	109.44	44.57	ND	ND
Saran Uul	Mongolia	100.60	45.78	0.327	ND
Shand	Mongolia	104.22	48.78	ND	ND
Shuteen	Mongolia	107.50	44.17	0.295	ND
Tsagaan-Suvarga	Mongolia	108.33	43.87	0.370	1.27
Zos Uul	Mongolia	98.34	48.71	0.250	ND
Zost Tolgoi	Mongolia	98.34	48.72	0.260	ND
Monywa	Myanmar	95.08	22.25	0.016	6.29
Shangalon	Myanmar	95.52	23.71	ND	ND
Haib	Namibia	17.85	-28.68	1.800	1.32
Lorelei	Namibia	16.90	-28.07	1.930	ND
Thames	New Zealand	175.56	-37.10	0.011	ND
Dasht-e-Kain	Pakistan	64.50	29.55	0.021	1.05
Koh-i-Dalil	Pakistan	62.19	29.12	0.015	ND
Reko Diq	Pakistan	62.08	29.12	0.012	12.34
Saindak	Pakistan	61.58	29.27	0.021	1.80

Continued overleaf...

Table 7 – continued

Deposit	Country	Lon.[a]	Lat.[a]	Age (Ga)	Cu (Mt)
Ziarat Pir Sultan	Pakistan	64.14	29.40	ND	ND
Cerro Azul	Panama	-79.38	9.28	0.057	ND
Cerro Chorcha	Panama	-82.20	8.63	0.003	0.65
Cerro Colorado	Panama	-81.78	8.50	0.005	14.55
Cerro Quema	Panama	-80.60	7.63	0.059	ND
Cobre Panama	Panama	-81.50	8.43	0.034	1.77
Petaquilla-Botija	Panama	-80.67	8.83	0.033	6.09
Rio Pito	Panama	-77.57	8.63	0.049	ND
Arie	Papua New Guinea	146.88	-2.02	0.015	0.53
Esis	Papua New Guinea	151.72	-5.17	0.025	ND
Frieda River	Papua New Guinea	141.78	-4.70	0.013	5.52
Legusulum	Papua New Guinea	151.65	-3.20	0.024	ND
Mount Bini	Papua New Guinea	147.58	-9.30	0.004	0.34
Mount Kren	Papua New Guinea	146.95	-2.12	0.014	ND
Mt. Nakru	Papua New Guinea	150.47	-5.98	0.024	ND
Ok Tedi	Papua New Guinea	141.13	-5.20	0.001	5.47
Panguna	Papua New Guinea	155.50	-6.32	0.003	6.60
Plesyumi	Papua New Guinea	150.38	-5.97	0.024	ND
Simuku	Papua New Guinea	150.02	-5.72	0.024	ND
Star Mt. Futik	Papua New Guinea	141.33	-5.07	0.004	0.35
Star Mt. Nong River	Papua New Guinea	141.22	-5.02	0.004	0.30
Wafi River	Papua New Guinea	146.45	-6.88	0.009	1.76
Wamum	Papua New Guinea	146.28	-6.75	ND	ND
Yandera	Papua New Guinea	145.17	-5.75	0.007	1.42
Acos	Peru	-74.45	-14.20	ND	ND
Aguila	Peru	-77.90	-8.56	0.005	0.29
Almacen	Peru	-75.92	-13.23	ND	ND
Alondra	Peru	-73.58	-15.82	ND	ND
Alto Dorado	Peru	-78.18	-8.17	ND	ND
Anita de Tibilos	Peru	-75.15	-14.18	ND	ND
Antapaccay	Peru	-71.35	-14.96	0.036	3.49
Canariaco	Peru	-79.28	-6.08	0.015	3.69
Cerro Colorado	Peru	-69.90	-17.68	0.059	2.22
Cerro Corona	Peru	-78.61	-6.76	0.011	0.90
Cerro Negro	Peru	-71.55	-16.55	0.057	0.37
Cerro Verde/Santa Rosa	Peru	-71.59	-16.54	0.062	12.51
Chalcobamba	Peru	-72.33	-14.03	0.036	ND
Chapi	Peru	-71.36	-16.77	ND	ND
Chavez N2, Concesion	Peru	-75.42	-14.23	ND	ND
Constancia	Peru	-71.77	-14.46	0.033	1.65
Coroccohuayco	Peru	-71.26	-14.95	0.031	2.43
Cotabambas	Peru	-72.35	-14.18	0.036	0.78
Cuajone	Peru	-70.71	-17.05	0.051	11.25
El Galeno	Peru	-78.32	-7.02	0.017	4.09
Eliana	Peru	-75.72	-13.77	ND	ND
La Granja	Peru	-79.12	-6.36	0.012	16.80
La Vega	Peru	-79.28	-5.70	ND	ND
Laguna Chamis	Peru	-78.58	-7.12	ND	ND
Lahuani	Peru	-72.99	-14.46	0.036	ND
Los Chancas	Peru	-73.13	-14.16	0.032	2.00
Los Pinos	Peru	-76.14	-12.98	ND	0.15
Magistral	Peru	-77.77	-8.22	0.015	1.38
Michiquillay	Peru	-78.32	-7.30	0.020	4.55
Minas Conga	Peru	-78.36	-6.92	0.016	1.92
Paramo	Peru	-79.21	-5.72	ND	ND
Pashpap	Peru	-78.00	-8.79	0.015	0.64
Puquio	Peru	-75.35	-13.93	ND	ND
Puy-Puy	Peru	-76.08	-11.48	0.007	ND
Quechua	Peru	-71.31	-14.98	0.038	2.04
Quellaveco	Peru	-70.62	-17.11	0.054	6.33
Rio Blanco	Peru	-79.31	-4.94	0.016	7.16
San Salvador de Patillani	Peru	-70.99	-15.63	0.005	ND
Tantahuatay	Peru	-78.67	-6.73	0.013	2.96
Tingo	Peru	-75.09	-13.69	ND	ND
Tintaya	Peru	-71.31	-14.91	0.033	ND
Toquepala	Peru	-70.61	-17.25	0.057	12.76
Toromocho	Peru	-76.13	-11.60	0.008	9.92
Amacan	Philippines	126.15	7.33	0.010	0.33
Atlas	Philippines	123.83	10.37	0.108	6.36
Aya Aya	Philippines	122.70	9.43	0.020	0.12
Balak-5	Philippines	124.25	10.13	ND	0.04
Basay	Philippines	122.68	9.49	0.030	1.15
Batong Buhay	Philippines	121.06	17.34	0.007	0.52
Boneng Lobo	Philippines	120.82	17.47	0.011	0.64
Botilao	Philippines	121.01	17.30	ND	0.43
Boyongan	Philippines	125.49	9.55	0.004	1.80

Continued overleaf...

Table 7 – continued

Deposit	Country	Lon.[a]	Lat.[a]	Age (Ga)	Cu (Mt)
Cadan	Philippines	126.17	7.55	0.010	ND
Dinkidi	Philippines	121.29	16.32	0.023	0.47
Dizon	Philippines	120.20	14.97	0.003	0.67
Far Southeast-Bato Tabio	Philippines	120.78	16.86	0.001	4.23
Guinaoang-Tirad	Philippines	120.80	16.79	0.004	1.40
Hale-Mayabo	Philippines	120.73	17.17	ND	0.18
Hinobaan	Philippines	122.57	9.75	0.018	1.59
Ino-Capayang	Philippines	121.88	13.50	ND	0.25
Kalamatan	Philippines	126.07	7.59	ND	0.09
Kennon SE/Black Mountain	Philippines	120.60	16.37	0.002	0.23
Kilongolao	Philippines	120.87	17.40	ND	0.18
Kingking	Philippines	125.99	7.17	0.010	2.90
Labangan	Philippines	123.30	7.93	ND	ND
Lingig	Philippines	126.38	8.05	ND	ND
Lumbay	Philippines	121.32	14.77	ND	0.31
Luna-Asiga	Philippines	125.52	9.26	0.004	0.09
Manag	Philippines	121.23	17.77	ND	0.10
Mapula	Philippines	126.02	7.35	0.010	0.31
Marcopper	Philippines	122.08	13.45	0.021	2.05
Marian	Philippines	121.35	16.75	0.025	0.23
Matanlang	Philippines	122.73	14.23	0.021	0.23
Pisumpan	Philippines	120.37	15.01	0.002	0.08
Salatan	Philippines	124.40	6.57	0.020	ND
San AntonioPhilex	Philippines	120.70	16.75	ND	0.75
San Fabian	Philippines	120.98	16.38	0.021	0.85
Santo Nirio	Philippines	120.66	16.49	0.010	0.99
Santo Tomas II	Philippines	120.62	16.26	0.002	1.68
Sinipsip	Philippines	120.77	16.73	ND	ND
Sipalay	Philippines	122.45	9.82	0.030	3.82
Suguibon	Philippines	122.63	9.57	ND	0.09
Sulat	Philippines	125.25	11.82	0.010	0.20
Tagpura-Maangob	Philippines	126.10	7.54	ND	0.33
Tampakan	Philippines	125.05	6.48	0.004	12.00
Tawi-Tawi	Philippines	120.87	16.45	0.005	0.62
Taysan	Philippines	121.13	13.80	0.007	1.86
Dolina Bedkowska	Poland	19.95	50.12	0.343	ND
Myszkow	Poland	19.37	50.62	0.298	0.70
Pilica	Poland	19.62	50.47	0.343	ND
Rio Vivi	Puerto Rico	-66.42	18.25	0.041	1.59
Tanama	Puerto Rico	-66.82	18.25	0.042	0.81
Bolcana	Romania	23.03	45.98	0.010	0.27
Bozovici	Romania	22.00	44.75	0.065	ND
Bucium Tarnita	Romania	23.20	46.23	0.015	1.68
Ciclova	Romania	21.78	44.98	0.065	ND
Cofu	Romania	22.35	45.55	0.065	ND
Deva	Romania	22.89	45.88	0.013	ND
Moldova Noua	Romania	21.70	44.74	0.065	1.75
Musariu	Romania	22.80	46.15	0.013	0.02
Oravita	Romania	21.82	45.10	0.065	ND
Rosia Poieni	Romania	23.17	46.33	0.009	2.37
Rovina	Romania	22.90	46.17	0.015	0.47
Sasca	Romania	21.72	44.87	0.065	ND
Sopot	Romania	21.95	44.75	0.065	ND
Talagiu	Romania	22.15	46.27	0.008	0.53
Tincova	Romania	22.23	45.57	0.065	ND
Valea Morii	Romania	22.85	46.15	0.011	0.25
Voia	Romania	22.97	46.06	0.011	ND
Aksug	Russia	96.67	53.43	0.515	2.48
Birgildinskoe	Russia	61.09	55.00	0.347	ND
Borgulikan	Russia	126.62	53.75	0.123	ND
Kiyalykh-uzen	Russia	89.57	54.05	0.347	0.30
Krasnogorskoe	Russia	157.38	53.92	0.015	ND
Kyzyk-Chadr	Russia	96.78	52.93	ND	ND
Lekyntelbei	Russia	66.33	67.87	0.315	ND
Lora	Russia	153.77	59.25	0.095	0.89
Miheevskoye	Russia	60.82	53.23	0.345	1.58
Nakhodka	Russia	164.73	66.48	0.142	ND
Novonikolaevsk	Russia	60.57	53.23	0.340	ND
Osennee	Russia	150.32	59.72	0.095	ND
Peschanka	Russia	164.57	66.60	0.142	4.79
Salavat	Russia	57.47	53.09	0.347	ND
Tominskoe	Russia	61.27	54.93	0.347	1.40
Tumannoe	Russia	157.67	54.28	0.015	ND
Viking	Russia	152.68	58.97	0.095	ND
Voznesenskoe	Russia	59.80	54.63	0.367	ND
Yaguzak	Russia	61.13	54.96	0.347	ND

Continued overleaf...

Table 7 – continued

Deposit	Country	Lon.[a]	Lat.[a]	Age (Ga)	Cu (Mt)
Zelenodolskoe	Russia	61.07	54.72	0.340	ND
Bor	Serbia	22.09	44.10	0.085	6.72
Majdanpek	Serbia	21.95	44.38	0.084	6.00
Rudnitsa	Serbia	20.72	43.23	0.014	ND
Veliki Krivelj	Serbia	22.10	44.13	0.084	3.30
Zlatno	Slovakia	18.86	48.44	0.015	0.22
Hidden Valley	Solomon Islands	159.73	-9.37	0.003	ND
Koloula	Solomon Islands	160.03	-9.78	0.002	0.09
Mase	Solomon Islands	157.52	-8.08	0.004	ND
Mbetilonga	Solomon Islands	159.91	-9.53	0.031	ND
Poha	Solomon Islands	159.83	-9.43	0.024	ND
Aitik	Sweden	20.96	67.07	1.890	5.36
Tallberg	Sweden	19.77	64.99	1.886	0.12
Vaikijaur	Sweden	19.81	66.53	1.880	ND
Chimei	Taiwan	121.45	23.43	0.022	ND
Phu Hin Lek Fai	Thailand	101.67	17.50	0.230	ND
Phu Lon	Thailand	102.08	18.12	0.231	1.02
Phu Thong Daeng	Thailand	101.50	17.33	0.230	ND
Bakircay	Turkey	35.44	40.93	0.038	0.40
Berta	Turkey	41.90	41.20	0.040	ND
Cevizlidere	Turkey	39.60	39.27	ND	ND
Derekoy	Turkey	27.32	41.91	0.071	0.53
Gamahane	Turkey	41.85	41.18	0.053	0.40
Gazelyayla	Turkey	39.65	40.86	0.059	0.56
Ikiztepe	Turkey	27.68	41.83	0.075	0.05
Sukrupasa	Turkey	27.45	41.93	0.082	ND
Tereoba	Turkey	27.15	39.60	0.025	ND
Uluta	Turkey	40.88	40.45	0.059	0.38
Ajo	USA	-112.87	32.36	0.063	4.27
Allard	USA	-108.09	37.41	0.068	0.80
Ann Mason	USA	-119.27	38.96	0.169	1.98
Bagdad	USA	-113.21	34.59	0.072	6.40
Baultoff	USA	-141.21	62.11	0.111	0.28
Bear-Lagomarsino	USA	-119.18	39.03	ND	1.82
Beavertown	USA	-112.08	46.34	0.100	0.25
Bee Creek	USA	-158.40	56.52	0.004	ND
Bingham	USA	-112.15	40.53	0.037	28.49
Bisbee	USA	-109.90	31.43	0.180	2.27
Bobcat Gulch	USA	-113.99	45.36	ND	0.27
Bond Creek	USA	-142.73	62.22	ND	1.50
Butte Valley	USA	-115.15	39.80	ND	ND
Caribou Mountain	USA	-111.32	43.09	0.050	ND
Carl Creek	USA	-141.58	62.03	ND	0.02
Casa Grande West	USA	-111.95	32.87	0.068	8.53
Castle Dome	USA	-110.95	33.40	0.059	4.75
Catheart Mt.	USA	-70.22	45.54	0.443	0.10
Chilito	USA	-110.80	33.07	ND	0.60
Christmas	USA	-110.75	33.06	0.064	0.53
Contact	USA	-114.77	41.77	0.150	0.43
Continental/Butte	USA	-112.51	46.02	0.061	35.13
Copper Basin	USA	-117.04	40.61	0.086	0.15
Copper Basin	USA	-112.58	34.50	0.064	0.91
Copper Canyon	USA	-117.13	40.55	0.038	0.27
Copper Creek	USA	-110.48	32.75	0.058	0.56
Copper Flat	USA	-108.12	32.81	0.075	0.22
Copper King	USA	-105.19	41.15	ND	0.07
Crescent Peak	USA	-115.13	35.48	0.073	ND
Elder Creek	USA	-117.08	40.69	0.038	ND
Ely	USA	-115.00	39.26	0.110	4.62
Esperanza-Sierrita	USA	-111.12	31.87	0.055	6.65
Fish Creek	USA	-117.22	40.42	0.089	ND
Gibson	USA	-110.94	33.33	0.061	0.08
Glacier Peak	USA	-120.98	48.20	0.021	5.71
Gold Mountain	USA	-121.33	48.22	ND	0.20
Hannover Mountains	USA	-108.09	32.85	0.064	4.78
Heddleston	USA	-112.36	47.03	0.046	1.09
Helvetia	USA	-110.76	31.83	0.059	5.26
Horsfield	USA	-141.22	62.05	ND	0.09
Ithaca Peak	USA	-114.15	35.37	0.073	1.25
Johnson Camp	USA	-110.07	32.10	0.053	1.22
Kelsey	USA	-119.48	49.00	0.179	0.80
Kennedy	USA	-117.75	40.27	0.029	ND
Kijik River	USA	-154.32	60.35	0.060	ND
Kirwin	USA	-109.31	43.88	0.040	0.90
Lakeshore	USA	-111.90	32.52	0.066	4.71
Lights Creek	USA	-120.85	40.20	0.100	1.08

Continued overleaf...

Table 7 – continued

Deposit	Country	Lon.[a]	Lat.[a]	Age (Ga)	Cu (Mt)
Lonesome Pine	USA	-110.90	33.34	0.061	0.07
MacArthur	USA	-119.24	39.05	0.161	0.18
Margaret	USA	-122.08	46.36	0.017	1.88
Margerie Glacier	USA	-137.08	59.02	0.034	0.29
Mazama	USA	-120.38	48.61	0.089	0.49
Miami-Inspiration	USA	-110.74	33.42	0.064	10.02
Middle Fork	USA	-121.37	47.50	0.025	0.38
Mineral Butte	USA	-111.58	33.11	0.070	0.05
Mission-Pima	USA	-111.07	31.98	0.058	4.68
Morenci-Metcalf	USA	-109.36	33.10	0.056	33.90
North Fork Snoqualmie River	USA	-121.64	47.68	0.018	0.87
Nunatak	USA	-136.10	58.99	ND	0.22
OK	USA	-113.30	38.48	0.028	0.05
Orange Hill	USA	-142.84	62.21	0.105	1.12
Park Premier	USA	-111.38	40.63	0.033	ND
Pebble Copper	USA	-155.30	59.90	0.090	31.24
Pine Flat	USA	-112.35	34.37	ND	0.09
Poston Butte	USA	-111.42	33.12	0.062	2.76
Pyramid	USA	-160.67	55.63	0.006	0.59
Ray	USA	-110.98	33.16	0.069	10.76
Red Hills	USA	-111.22	33.04	0.065	0.45
Red Hills	USA	-104.40	29.81	0.060	ND
Red Hills	USA	-118.43	38.62	0.105	ND
Red Mountain	USA	-110.72	31.49	0.060	3.59
Resolution	USA	-111.08	33.30	0.064	ND
Round Top	USA	-157.05	64.13	0.075	0.11
Royston	USA	-117.50	38.33	0.207	ND
Sacaton	USA	-111.82	32.95	0.063	0.35
Safford	USA	-109.60	32.93	0.053	32.02
Sally Mountain	USA	-70.33	45.60	0.443	ND
San Manuel-Kalamazoo	USA	-110.68	32.70	0.068	8.34
San Xavier North	USA	-111.02	31.97	0.056	1.12
Sanchez	USA	-109.53	32.88	ND	0.55
Santa Rita	USA	-108.07	32.79	0.056	14.18
SFS	USA	-118.08	38.49	0.105	0.73
Sheep Mountain	USA	-112.46	34.08	ND	3.15
Silver Bell	USA	-111.50	32.40	0.068	1.77
Silver Creek	USA	-109.68	44.03	0.040	0.17
Southwest Tintic	USA	-112.13	39.86	0.036	1.57
Squaw Peak	USA	-111.87	34.48	ND	0.07
Stinkingwater	USA	-109.60	44.03	0.029	0.21
Sullivan	USA	-117.95	38.78	0.081	0.08
Sunnyside	USA	-110.75	31.45	ND	1.10
Sunrise	USA	-121.50	48.01	0.028	0.22
Superior East	USA	-111.00	33.38	0.060	4.96
Taurus	USA	-141.32	63.52	0.069	2.25
Twin Buttes	USA	-111.04	31.89	0.058	4.72
Two Peaks	USA	-110.46	31.77	0.074	0.09
Tyrone	USA	-108.37	32.63	0.056	5.15
Vekol Hills	USA	-112.09	32.58	ND	0.53
Venus	USA	-149.33	67.63	0.390	ND
Yerington	USA	-119.20	38.98	0.167	4.77
Almalyk	Uzbekistan	69.65	40.81	0.290	23.71
Kyzata	Uzbekistan	69.71	40.80	0.290	5.95
Sarycheku	Uzbekistan	69.78	40.78	0.290	1.00
Tekeli	Uzbekistan	70.13	41.10	0.295	ND
Samba	Zambia	27.88	-12.61	1.964	0.25

[a] In decimal degrees

Table 8: Compilation of 25 Australian IOCG deposits drawn from the authors' own knowledge and other disparate sources, building on the Geoscience Australia OZMin database (Sexton, 2011). Ga = billion years; Mt = million tonnes; ND = no data.

Deposit	State	Lon.[a]	Lat.[a]	Age (Ga)	Ore (Mt)	Cu (%)	Cu (Mt)
Warrego	Northern Territory	133.82	-19.44	1.848	4.8	2.0	0.10
Peko	Northern Territory	134.28	-19.68	1.848	3.2	4.0	0.13
Ernest Henry	Queensland	140.70	-20.44	1.525	166.0	1.1	1.83
E1	Queensland	140.78	-20.44	ND	38.5	0.8	0.31
Roseby	Queensland	140.15	-20.31	ND	128.5	0.7	0.90
Rocklands	Queensland	140.36	-20.68	ND	25.0	2.0	0.50
Kuridala	Queensland	140.51	-21.28	ND	3.5	1.3	0.05
Starra (Selwyn)	Queensland	140.48	-21.68	1.568	37.4	1.1	0.41
Osborne	Queensland	140.57	-22.09	1.595	11.2	3.5	0.39
Monakoff	Queensland	140.69	-20.63	ND	1.9	1.6	0.03
Great Australia	Queensland	140.69	-20.63	ND	2.1	1.5	0.03
Eloise	Queensland	140.98	-20.95	1.522	3.5	3.1	0.11
Mount Elliott	Queensland	140.98	-20.95	1.513	478.3	0.5	2.39
Greenmount	Queensland	140.53	-21.03	ND	8.0	1.0	0.08
Mount Dore	Queensland	140.53	-21.03	1.508	80.0	0.6	0.48
Merlin	Queensland	140.49	-21.66	ND	13.0	0.2	0.03
Kalman	Queensland	139.97	-21.05	1.475	61.0	0.3	0.18
Mount Cuthbert	Queensland	139.91	-19.99	ND	8.3	1.0	0.08
Kaiser Bill	Queensland	144.04	-18.53	ND	15.6	0.9	0.14
Olympic Dam	South Australia	136.89	-30.44	1.598	10400.0	0.8	83.20
Prominent Hill	South Australia	135.57	-29.72	1.595	278.8	1.0	2.79
Carapeteena	South Australia	137.50	-31.21	1.595	134.0	1.5	2.01
Hillside	South Australia	137.87	-34.54	1.595	337.0	0.6	2.02
Kalkaroo	South Australia	140.53	-31.73	1.592	232.5	0.5	1.16
North Portia	South Australia	140.46	-31.43	1.595	11.4	0.9	0.10

[a] In decimal degrees

References

Abdulin, A. A., H. A. Bespaev, C. Z. Daukeev, L. A. Miroshnichenko, & E. S. Votsalevskiy (1998). *Copper deposits of Kazakhstan*. Ministry of Ecology and Natural Resources of the Republic of Kazakhstan, Almaty, Kazakhstan.

Abdullah S., V. M., Chmyriov, K. F. Stazhilo-Alekseev, V. I. Dronov, P. Gannon, B. K. Lubemov, A. K. Kafarskiy, & E. P. Malyarov (1977). *Mineral resources of Afghanistan*. Afghan Geological and Mines Survey, Ministry of Mines and Industries, Republic of Afghanistan, Kabul, Afghanistan, 2 edn.

Adenis, A., E. Debayle, & Y. Ricard (2017). Attenuation tomography of the upper mantle. *Geophysical Research Letters*, 44, 7715–7724.

Afonso, J. C., F. Salajegheh, W. Szwillus, J. Ebbing, & C. Gaina (2019). A global reference model of the lithosphere and upper mantle from joint inversion and analysis of multiple data sets. *Geophysical Journal International*, 217, 1602–1628.

Ahlness, J. K. & M. G. Pojar (1983). In situ copper leaching in the United States: Case histories of operations. *Tech. rep.*, U. S. Bureau of Mines, Washington DC, USA.

Ahsan, S. H. & K. A. Mallick (1999). Geology and genesis of barite deposits of Lasbela and Khuzdar districts, Balochistan, Pakistan. *Resource Geology*, 49, 105–111.

Ahsan, S. H. & I. H. Quraishi (1997). Mineral/rock resources of Lasbela and Khuzdar districts, Balochistan, Pakistan. *Geological Bulletin of the University of Peshawar*, 30, 41–51.

Akande, S. & M. Zentilli (1984). Geologic, fluid inclusion, and stable isotope studies of the Gays River lead-zinc deposit, Nova Scotia. *Economic Geology*, 79, 1187–1211.

Amelin, Y., C. Li, & A. J. Naldrett (1999). Geochronology of the Voisey's Bay intrusion, Labrador, Canada, by precise U–Pb dating of coexisting baddeleyite, zircon, and apatite. *Lithos*, 47 (1-2), 33–51.

Ameta, S. S. & B. B. Sharma (2008). Geology metallogeny and exploration of concealed lead-zinc deposit in Sindesar Khurd-Lathiyakheri area, Rajsamand district, Rajasthan,. *Journal of the Geological Society of India*, 72, 381–399.

Anderson, B. R., J. B. Gemmell, & R. F. Berry (2001). The geology of the Nifty copper deposit, Throssell Group, Western Australia: Implications for ore genesis. *Economic Geology*, 96 (7), 1535–1565.

Anderson, H. E. & R. R. Parrish (2000). U–Pb geochronological evidence for the geological history of the Belt-Purcell Supergroup, southeastern British Columbia. *Geological Association of Canada, Mineral Deposits Division Special Publication*, 1, 113–126.

Anger, G., H. Nielson, H. Puchelt, & W. Ricke (1966). Sulfur isotopes in the Rammelsberg ore deposit (Germany). *Economic Geology*, 61, 511–536.

Anglo American Corp. (1989). *Tech. rep.*, London, UK.

Anonymous (1985). Geological report on exploration for lead-zinc ore, Gorubathan (Mal Khola) block, District – Darjeeling, West Bengal. *Unpublished Mineral Exploration Corporation Limited Report*. URL `mecl.gov.in/Reports/Gorubathan\_F.pdf`.

Anvil Mining NL (2003). *Tech. rep.*, Montréal, Canada.

Artemieva, I. M. (2006). Global 1 x 1 thermal model TC1 for the continental lithosphere: Implications for lithosphere secular evolution. *Tectonophysics*, 416, 245–277.

Ayer, J., Y. Amelin, F. Corfu, S. Kamo, J. Ketchum, K. Kwok, & N. Trowell (2002). Evolution of the southern Abitibi greenstone belt based on U–Pb geochronology: Autochthonous volcanic construction followed by plutonism, regional deformation and sedimentation. *Precambrian Research*, 115 (1-4), 63–95.

Ayuso, R. A., K. D. Kelley, D. L. Leach, L. E. Young, J. F. Slack, J. F. Wandless, A. M. Lyon, & J. L. Dillingham (2004). Origin of the Red Dog Zn-Pb-Ag deposits, Brooks Range, Alaska: Evidence from regional Pb and Sr isotope sources. *Economic Geology*, 99, 1533–1553.

Bailes, R. J., J. E. Christoffersen, V. F. Escandon, & G. Peatfield (2001). Sediment-hosted deposits of the Boléo copper-cobalt-zinc district, Baja California Sur, Mexico. *Society of Economic Geologists Special Publication*, 8, 291–306.

Balla, J. C. (1982). Geology of the Troy deposit, Northwestern Montana. In: *Proceedings of the Denver Regional Exploration Geologists Society Symposium, The genesis of Rocky Mountain ore deposits: Changes with time and tectonics*, p. 29. Denver, USA.

Barley, M. E. & D. I. Groves (1990). Deciphering the tectonic evolution of Archaean greenstone belts: The importance of contrasting histories to the distribution of mineralization in the Yilgarn Craton, Western Australia. *Precambrian Research*, 46 (1–2), 3–20.

Barnes, S.-J., J.-F. Couture, E. W. Sawyer, & C. Bouchaib (1993). Nickel-copper occurrences in the Belleterre-Angliers Belt of the Pontiac Subprovince and the use of Cu–Pd ratios in interpreting platinum-group element distributions. *Economic Geology*, 88 (6), 1402–1418.

Barrie, C. T., F. Corfu, P. Davis, A. C. Coutts, & D. MacEachern (1999). Geochemistry of the Dundonald komatiite-basalt suite and genesis of Dundeal Ni deposit, Abitibi subprovince, Canada. *Economic Geology*, 94 (6), 845–866.

Barrie, C. T. & A. J. Naldrett (1989). Geology and tectonic setting of the Montcalm gabbroic complex and Ni-Cu deposit, Western Abitibi subprovince, Ontario, Canada. In: *Proceedings of the 5th Magmatic Sulphides Conference*, pp. 151–163.

Basuki, N. I., B. E. Taylor, & E. T. C. Spooner (2008). Sulfur isotope evidence for thermochemical reduction of dissolved sulfate in Mississippi Valley-type zinc-lead mineralization, Bongara area, northern Peru. *Economic Geology*, 103 (4), 783–799.

Behn, M. D., G. Hirth, & J. R. Elsenbeck (2009). Implications of grain size evolution on the seismic structure of the oceanic upper mantle. *Earth and Planetary Science Letters*, 282, 178–189.

Belperio, A., W. Priss, M. Fairclough, C. Gatehouse, J. Gum, J. Hough, & A. Burtt (1998). Tectonic and metallogenic framework of the Cambrian Stansbury Basin — Kanmantoo Trough, South Australia. *Australian Geological Survey Organisation Journal of Australian Geology and Geophysics*, 17, 183–200.

Bhattacharya, H. N. (2004). Analysis of the sedimentary succession hosting the Paleoproterozoic Zawar zinc-lead sulphide ore deposit, Rajasthan, India. In: *Sediment-hosted lead-zinc sulphide deposits — attributes and models of some major deposits in India, Australia and Canada* (edited by M. Deb & W. D. Goodfellow), pp. 350–361. New Delhi, Narosa Publishing House.

Bhawan, B. A. (2006). *Geological report on exploration for lead-zinc, Bajta (Central) block phase-I, District Ajmer, Rajasthan*. Unpublished Mineral Exploration Corporation Limited Report. URL `mecl.gov.in/Reports/BajtaCentralPh1\_F.pdf`.

Bird, P., Z. Liu, & W. K. Rucker (2008). Stresses that drive the plates from below: Definitions, computational path, model optimization, and error analysis. *Journal of Geophysical Research: Solid Earth*, 113 (B11406).

Bjørlykke, A., S. Olerud, & J. S. Sandstad (1985). Metallogeny of Finnmark, North Norway. *Norges Geologiske Undersøkelse Bulletin*, 403, 183–196.

Blakeman, R. J., J. H. Ashton, A. J. Boyce, A. E. Fallick, & M. J. Russell (2002). Timing of interplay between hydrothermal and surface fluids in the Navan Zn–Pb orebody, Ireland: Evidence from metal distribution trends, mineral textures, and δ34S analyses. *Economic Geology*, 97 (1), 73–91.

Bodon, S. B. (1998). Paragenetic relationships and their implications for ore genesis at the Cannington Ag-Pb-Zn deposit Mount Isa Inlier, Queensland, Australia. *Economic Geology*, 93, 1463–1488.

Borodaev, Y. S., N. N. Mozgova, S. V. Ezhov, S. M. Gandhi, & S. Mookherjee (2002). Textural and mineralogical features of metamorphosed ores from the Rangpo polymetallic deposit (Sikkim, India). *Moscow University Geology Bulletin*, 57 (3), 3953.

Both, R. A. (1990). Kanmantoo Trough — Geology and mineral deposits. *Australasian Institute of Mining and Metallurgy Monograph*, 14, 1195–1203.

Both, R. A. & J. W. Smith (1975). A sulfur isotope study of base metal mineralization in the Willyama Complex, western New South Wales, Australia. *Economic Geology*, 70, 308–318.

Bouabdellah, M., L. Fontboté, Y. Haeberlin, L. Llinares, D. Leach, & J. Spangenberg (1999). Zoned sulphur isotope signatures at the Mississippi Valley-type Touissit Bou Becker, El Abed district, Morocco, Algeria — Evidence for thermochemical sulphate reduction and mixing of sulphur sources. In: *Mineral deposits: Processes to processing*, pp. 821–824. Balkema, Amsterdam.

Bouabdellah, M., D. F. Sangster, D. L. Leach, A. C. Brown, C. A. Johnson, & P. Emsbo (2012). Genesis of the Touissit-Bou Beker Mississippi valley-type district (Morocco-Algeria) and its relationship to the Africa-Europe collision. *Economic Geology*, 107, 117–146.

Bouhifd, M. A., D. Andrault, G. Fiquet, & P. Richet (1996). Thermal expansion of forsterite up to the melting point. *Geophysical Research Letters*, 23 (10), 1143–1146.

Brannon, J. C., F. A. Podosek, & S. C. Cole (1996). Radiometric dating of Mississippi Valley-type ore deposits. *Society of Economic Geologists Special Publication*, 4, 536–545.

Brannon, J. C., F. A. Podosek, & R. K. McLimans (1992). Alleghenian age of the Upper Mississippi Valley zinc-lead deposit determined by Rb–Sr dating of sphalerite. *Nature*, 356 (6369), 509–511.

Brenner, T. L., N. A. Teixeira, J. A. L. Oliveira, N. D. Franke, & J. F. H. Thompson (1990). The O'Toole nickel deposit, Morro do Ferro greenstone belt, Brazil. *Economic Geology*, 85 (5), 904–920.

British Columbia Geological Survey (2020a). URL `minfile.gov.bc.ca/Summary.aspx?minfilno=082LSE012`.

British Columbia Geological Survey (2020b). URL `minfile.gov.bc.ca/Summary.aspx?minfilno=094F\%20\%20008`.

British Columbia Geological Survey (2020c). URL `minfile.gov.bc.ca/Summary.aspx?minfilno=082M\%20\%20086`.

British Columbia Geological Survey (2020d). URL `minfile.gov.bc.ca/Summary.aspx?minfilno=094K++066`.

British Columbia Geological Survey (2020e). URL `minfile.gov.bc.ca/Summary.aspx?minfilno=082LNE007`.

British Columbia Geological Survey (2020f). URL `minfile.gov.bc.ca/Summary.aspx?minfilno=082GNW009`.

British Columbia Geological Survey (2020g). URL `minfile.gov.bc.ca/Summary.aspx?minfilno=082M++001`.

British Columbia Geological Survey (2020h). URL `minfile.gov.bc.ca/Summary.aspx?minfilno=082M\%20\%20084`.

British Columbia Geological Survey (2020i). URL `minfile.gov.bc.ca/Summary.aspx?minfilno=082FNE052`.

Brizzi, A. S. & F. A. C. Roberto (1988). Jazida de cobre de Pedra Verde — Viçosa do Ceará, Ceará. In: *Principais Depósitos Minerais do Brasil — Metais Básicos Não Ferrosos, Ouro e Alumínio* (edited by C. Schobbenhaus & C. Coelho), vol. 3, pp. 71–80. DNPM and Companhia Vale do Rio Doce, Brasilia, Brazil.

Broadbent, G. C., R. E. Myers, & J. V. Wright (1998). Geology and origin of shale-hosted Zn-Pb-Ag mineralization at the Century deposit northwest Queensland, Australia. *Economic Geology*, 93, 1264–1294.

Buschendorf, F., H. Nielsen, H. Puchelt, & W. Ricke (1963). Schwefel-Isotopen-Untersuchungen am Pyrit-Sphalerit-Baryt-Lager Meggen/Lenne (Deutschland) und an verschiedenen Devon-Evaporiten. *Geochimica et Cosmochimica Acta*, 27, 501–523.

Campbell, F. A., V. G. Ethier, H. R. Krouse, & R. A. Both (1978). Isotopic composition of sulfur in the Sullivan orebody, British Columbia. *Economic Geology*, 73, 246–268.

Camus, F. (1986). Los yacimientos estratoligados de Cu, Zn-Pb y Ag de Chile. In: *Geologia y recursos minerales de Chile* (edited by J. Frutos, R. Oyarzun, & M. Pincheira), vol. 2, pp. 547–635. Editorial de la Universidad de Concepción, Concepción, Chile.

Canerpa-Amax (1974). Project Report 536. *Tech. rep.*

Carr, G. R. (1984). Primary geochemical and mineralogical dispersion in the vicinity of the Lady Loretta Zn-Pb-Ag deposit northwest Queensland. *Journal of Geochemical Exploration*, 22, 217–238.

Carr, G. R., G. J. Denton, M. J. Korsch, J. M. Parr, A. S. Andrew, D. Whitford, L. A. I. Wyborn, & S. S. Sun (2001). User friendly isotope technologies in mineral exploration: Northern Australian Proterozoic basins. *Australian Mineral Industry Research Association Final Report P480*, 313.

Carr, G. R. & J. W. Smith (1977). A comparative isotopic study of the Lady Loretta zinc-lead-silver deposit. *Mineralium Deposita*, 12, 105–110.

Celli, N. L., S. Lebedev, A. J. Schaeffer, & C. Gaina (2020a). African cratonic lithosphere carved by mantle plumes. *Nature Communications*, 11 (92).

Celli, N. L., S. Lebedev, A. J. Schaeffer, M. Ravenna, & C. Gaina (2020b). The upper mantle beneath the South Atlantic Ocean, South America and Africa from waveform tomography with massive data sets. *Geophysical Journal International*, 221, 178–204.

Chapman, L. H. (2004). Geology and mineralization styles of the George Fisher Zn-Pb-Ag deposit, Mt Isa. *Economic Geology*, 99, 233–255.

Charef, A., A. Guedes, F. Noronha, & M. Sousa (2009). Fossil and present-day hydrothermal fluids from North Tunisia: An example of a dynamic fluid evolution. *Cadernos Laboratorio Xeolooxico de Laxe Corunña*, 34, 43–58.

Charef, A. & S. M. F. Sheppard (1987). Pb-Zn mineralization associated with diapirism: Fluid inclusion and stable isotope (H, C, O) evidence for the origin and evolution of the fluids at Fedj-el-Adoum, Tunisia. *Chemical Geology*, 61, 113–134.

Christensen, J. N., A. N. Halliday, J. R. Vearncombe, & S. E. Kesler (1995). Testing models of large-scale crustal fluid flow using direct dating of sulfides: Rb-Sr evidence for early dewatering and formation of Mississippi Valley-type deposits, Canning Basin, Australia. *Economic Geology*, 90, 877–884.

Christensen, N. I. & W. D. Mooney (1995). Seismic velocity structure and composition of the continental crust: A global view. *Journal of Geophysical Research*, 100 (B7), 9761–9788.

Clark, D. J. (2001). *Geology and genesis of the Mammoth Cu deposit Mount Isa inlier, Australia*. Ph.D. thesis, University of Tasmania.

Connor, J. I. R. M. M. D., A. G. (1990). Dugald River zinc-lead deposit. *Australasian Institute of Mining and Metallurgy Monograph*, 14, 949–953.

Cook, F. A., A. J. Van Der Velden, K. W. Hall, & B. J. Roberts (1999). Frozen subduction in Canada's Northwest Territories: Lithoprobe deep lithospheric reflection profiling of the western Canadian Shield. *Tectonics*, 18 (1), 1–24.

Cooke, D. R., S. W. Bull, S. Donovan, & J. R. Rogers (1998). K-metasomatism and base metal depletion in volcanic rocks from the McArthur Basin, Northern Territory — Implications for base metal mineralization. *Economic Geology*, 93, 1237–1263.

Coomer, P. G. & B. W. Robinson (1976). Sulphur and sulphate-oxygen isotopes and the origin of the Silvermines deposits, Ireland. *Mineralium Deposita*, 11 (2), 155–169.

Cornell, D., Å. Pettersson, M. Whitehouse, & A. Scherstén (2009). A new chronostratigraphic paradigm for the age and tectonic history of the Mesoproterozoic Bushmanland ore district, South Africa. *Economic Geology*, 104, 385–404.

Cox, D. P., R. Carrasco, O. Andre-Ramos, A. Hinojosa-Velasco, & K. R. Long (1992). Copper in sedimentary rocks. *U.S. Geological Survey Bulletin*, 1975, 95–108.

Cox, D. P., D. A. Lindsey, D. A. Singer, B. C. Moring, & M. F. Diggles (2007). Sediment-hosted copper deposits of the world: Deposit models and database. *U.S. Geological Survey Open-File Report*, 03-107.

Crew Development Corp. (1998). Annual Report. *Tech. rep.*, Vancouver, Canada.

Cumming, G. L. & D. Krstic (1991). Geochronology at the Namew Lake Ni-Cu deposit, Flin Flon area, Manitoba, Canada: A Pb/Pb study of whole rocks and ore minerals. *Canadian Journal of Earth Sciences*, 28 (9), 1328–1339.

Czarnota, K., G. G. Roberts, N. J. White, & S. Fishwick (2014). Spatial and temporal patterns of Australian dynamic topography from river profile modeling. *Journal of Geophysical Research: Solid Earth*, 119, 1384–1424.

Daitx, E. C. (1996). *Origem e evolução dos depósitos sulfetados tipo-Perau (Pb-Zn-Ag), com base nas jazidas Canoas e Perau (Vale do Ribeira, Paraná)*. Ph.D. thesis, Universidade Estadual Paulista, Instituto de Geociências e Ciências Exatas. 453.

Dalton, C. A., G. Ekström, & A. M. Dziewonski (2009). Global seismological shear velocity and attenuation: A comparison with experimental observations. *Earth and Planetary Science Letters*, 284, 65–75.

Dannberg, J., Z. Eilon, U. Faul, R. Gassmöller, P. Moulik, & R. Myhill (2017). The importance of grain size to mantle dynamics and seismological observations. *Geochemistry, Geophysics, Geosystems*, 18, 3034–3061.

Davidson, G. J. & G. H. Dixon (1992). Two sulphur isotope provinces deduced from ores in the Mount Isa Eastern Succession, Australia. *Mineralium Deposita*, 27, 30–41.

Davies, D. R., N. Rawlinson, G. Iaffaldano, & I. H. Campbell (2015). Lithospheric controls on magma composition along Earth's longest continental hotspot track. *Nature*, 525, 511–514.

Davis, D. & R. Sutcliffe (1985). U–Pb ages from the Nipigon Plate and northern Lake Superior. *Geological Society of America Bulletin*, 96 (12), 1572–1579.

Dayton, S. H. & M. P. Sassos (1985). Carajás: A new district, new mines and a big future. *Engineering and Mining Journal*, 186 (11), 24–46.

Deb, M. (1986). Sulfur and carbon isotope compositions in the stratiform Zn-Pb-Cu sulfide deposits of the Rajpura-Dariba belt, Rajasthan, NW India: A model of ore genesis. *Mineralium Deposita*, 21, 313–321.

Deb, M. & T. Pal (2004). Geology and genesis of the base metal sulphide deposits of the Dariba-Rajpura-Bethumni belt, Rajasthan, India, in light of basin evolution. In: *Sediment-hosted lead-zinc sulphide deposits — Attributes and models of some major deposits in India, Australia and Canada* (edited by M. Deb & W. Goodfellow), pp. 304–327. Narosa Publishing House, New Delhi.

Deb, M. & S. C. Sarkar (1990). Proterozoic tectonic evolution and metallogenesis in the Aravalli-Delhi orogenic complex, northwestern India. *Precambrian Research*, 46, 115–137.

Deb, M. & R. I. Thorpe (2004). Geochronological constraints in the Precambrian geology of Rajasthan and their metallogenic implications. In: *Sediment-hosted lead-zinc sulphide deposits — Attributes and models of some major deposits in India, Australia and Canada* (edited by M. Deb & W. Goodfellow), pp. 246–263. Narosa Publishing House, New Delhi.

Deb, M., R. I. Thorpe, G. L. Cumming, & A. Wagner (1989). Age, source and stratigraphic implications of Pb isotope data for conformable, sediment-hosted, base-metal deposits in the Proterozoic Aravalli-Delhi orogenic belt, northwestern India. *Precambrian Research*, 43, 1–22.

Debayle, E., F. Dubuffet, & S. Durand (2016). An automatically updated S-wave model of the upper mantle and the depth extent of azimuthal anisotropy. *Geophysical Research Letters*, 43, 674–682.

Deblond, A. & L. Tack (1999). Main characteristics and review of mineral resources of the Kabanga-Musongati mafic-ultramafic alignment in Burundi. *Journal of African Earth Sciences*, 29 (2), 313–328.

Delta Gold (2000). Technical review of Ngamiland JV Botswana. *Tech. rep.*, Delta Gold NL, Sydney, Australia.

Denaro, T. J., I. W. Withnall, J. H. C. Bain, & D. E. Mackenzie (1997). Mineral resource assessment, Georgetown-Croydon area. *Queensland Minerals and Energy Review Series*, p. 228.

Dewing, K., R. J. Sharp, & E. Turner (2007). Synopsis of the Polaris Zn-Pb district, Canadian Arctic Islands, Nunavut. In: *Mineral deposits of Canada: A synthesis of major deposit types, district metallogeny, the evolution of geological provinces, and exploration methods* (edited by W. D. Goodfellow), pp. 655–672. Geological Association of Canada, Mineral Deposits Division, Special Publication No. 5.

Ding, T. & S. Y. Jiang (2000). Stable isotope study of the Langshan polymetallic mineral district, Inner Mongolia, China. *Resource Geology*, 50, 25–38.

Disnar, J. R. (1996). A comparison of mineralization histories for two MVT deposits, Trèves and Les Malines (Causses Basin, France), based on the geochemistry of associated organic matter. *Ore Geology Reviews*, 11, 133–156.

Dixon, G. & G. J. Davidson (1996). Stable isotope evidence for thermochemical sulfate reduction in the Dugald River (Australia) strata-bound shale-hosted zinc-lead deposit. *Chemical Geology*, 129, 227–246.

Dodin, D. A., N. M. Chernyshov, & B. A. Yatskevich (2000). *Platinum Metal Deposits of Russia*. Ministry of Natural Resources of the Russian Federation and Nauka, Moscow, Russia.

Dora, O. O. (1977). The strata-bound lead-zinc deposits from Menderes Massif in Bayindir (West-Anatolia). In: *Time- and strata-bound ore deposits* (edited by D. Klemm & H. Schneider), pp. 220–231. Springer, Berlin.

Drummond, A. D. (1996). Corocoro oxide copper deposit. *Tech. rep.*, Reward Mining Corporation and George Resource Company Ltd., Vancouver, Canada.

Duan, S. G., C. J. Xue, C. H. Yan, G. Y. Liu, Y. W. Song, & D. H. Zhang (2008). Comparison of Pb-Zn metallogenic characteristics between northern and southern margins of North China landmass. *Mineral Deposits*, 27, 383–398.

Durieux, C. G. & A. C. Brown (2001). Diagenetic stratiform copper-silver mineralization, Salta district, northwestern Argentina. In: *Mineral Deposits at the Beginning of the 21st Century, Proceedings of the Joint Sixth Biennial SGA-SEG Meeting, Kraków, Poland, 26–29 August 2001* (edited by A. Piestrzynski), pp. 227–230. A. A. Balkema, Lisse, Netherlands.

Eckstrand, O. (1995). Magmatic nickel-copper-platinum group elements. In: *Geology of Canadian Mineral Deposit Types*, vol. 8, pp. 583–605. Geological Society of America, Boulder, CO, USA.

Eckstrand, O. R. & L. J. Hulbert (2007). Magmatic nickel-copper-platinium group element deposits. *Geological Association of Canada Special Publication*, 5, 205–222.

Ehya, F., M. Lotfi, & I. Rasa (2010). Emarat carbonate-hosted Zn-Pb deposit, Markazi Province, Iran: A geological, mineralogical and isotopic (S, Pb) study. *Journal of Asian Earth Sciences*, 37 (2), 186–194.

Eldridge, C. S., N. William, & J. L. Walshe (1993). Sulfur isotope variability in sediment-hosted massive sulfide deposits as determined using the ion microprobe SHRIMP II: A study of the HYC deposit at McArthur River, Northern Territory, Australia. *Economic Geology*, 88, 1–26.

Escande, B. & C. Majesté-Menjoulas (1985). Age dévonien moyen à supeérieur de la succession calcaréo-détritique à minéralisations stratiformes de la région d'Arrens (Hautes-Pyrénées). *Bulletin de la Société Géologique de France*, 1, 277–279.

Evins, M., A. R. Wilde, D. R. W. Foster, S. W. McKnight, & T. G. Blenkinsop (2007). Significance of monazite EPMA ages from the Quamby Conglomerate, Queensland. *Australian Journal of Earth Sciences*, 54, 19–26.

Fallara, F., M. M. Savard, & S. Paradis (1998). A structural, petrographic, and geochemical study of the Jubilee Zn-Pb deposit, Nova Scotia, Canada and a new metallogenic model. *Economic Geology*, 93, 757–778.

Fernández, F. G., R. A. Both, J. Mangas, & A. Arribas (2000). Metallogenesis of Zn-Pb carbonate-hosted mineralization in the southeastern region of the Picos de Europa (central northern Spain) province: Geologic, fluid inclusion, and stable isotope studies. *Economic Geology*, 95, 19–40.

Fichtner, A., H. Igel, H.-P. Bunge, & B. L. N. Kennett (2009a). Simulation and inversion of seismic wave propagation on continental scales based on a spectral-element method. *Journal of Numerical Analysis, Industrial and Applied Mathematics*, 4 (1-2), 11–22.

Fichtner, A., B. L. N. Kennett, H. Igel, & H.-P. Bunge (2009b). Full seismic waveform tomography for upper-mantle structure in the Australasian region using adjoint methods. *Geophysical Journal International*, 179, 1703–1725.

Fichtner, A., B. L. N. Kennett, H. Igel, & H.-P. Bunge (2010). Full waveform tomography for radially anisotropic structure: New insights into present and past states of the Australasian upper mantle. *Earth and Planetary Science Letters*, 290, 270–280.

Fishwick, S., M. Heintz, B. L. N. Kennett, A. M. Reading, & K. Yoshizawa (2008). Steps in lithospheric thickness within eastern Australia, evidence from surface wave tomography. *Tectonics*, 27 (4009).

Fishwick, S. & N. Rawlinson (2012). 3-D structure of the Australian lithosphere from evolving seismic datasets. *Australian Journal of Earth Sciences*, 59, 809–826.

Fletcher, I. R. & R. M. Farquhar (1977). Lead isotopes in the Grenville and adjacent Palaeozoic formations. *Canadian Journal of Earth Sciences*, 14, 56–66.

Fletcher, I. R. & R. M. Farquhar (1982). Lead isotopic compositions of Balmat ores and their genetic implications. *Economic Geology*, 77, 464–473.

Fontbote, L. & H. Gorzawski (1990). Genesis of the Mississippi Valley-type Zn-Pb deposit of San Vicente, central Peru: Geologic and isotopic (Sr, O, C, S, Pb) evidence. *Economic Geology*, 85 (7), 1402–1437.

Forrestal, J. (1990). Mount Isa and Hilton silver-lead-zinc deposits. *Australasian Institute of Mining and Metallurgy Monograph*, 14, 927–934.

Forsyth, D. W. (1992). Geophysical constraints on mantle flow and melt generation beneath mid-ocean ridges. *Geophysical Monograph*, 71, 1–65.

Franklin, J. M., H. L. Gibson, I. R. Jonasson, & A. G. Galley (2005). Volcanogenic massive sulfide deposits. *Economic Geology 100th Anniversary Volume*.

Frick, L. R., D. D. Lambert, & D. M. Hoatson (2001). Re–Os dating of the Radio Hill Ni-Cu deposit, west Pilbara Craton, Western Australia. *Australian Journal of Earth Sciences*, 48 (1), 43–47.

Fu, C., J. Wang, R. M. Peng, J. J. Liu, Z. J. Liu, & Z. M. Liu (2010). Features of sulfur isotope of the Jiashengpan lead-zinc-sulfur deposit in inner Mongolia and its genesis significance. *Geoscience*, 24, 34–41.

Gardner, H. D. & I. Hutcheon (1985). Geochemistry, mineralogy, and geology of the Jason Pb-Zn deposits, Macmillan Pass, Yukon, Canada. *Economic Geology*, 80, 1257–1276.

Gauert, C. D. (2005). Stratiform coticule-barite-sulphide horizons in the sediment-hosted Tsongoari-Omupokko Pb-Cu-Ba-Zn-Ag prospects, Kaokoland, Namibia. *South African Journal of Geology*, 108, 87–118.

Gemmell, J. B., H. Zantop, & L. D. Meinert (1992). Genesis of the Aguilar zinc-lead-silver deposit, Argentina: Contact metasomatic vs. sedimentary exhalative. *Economic Geology*, 87, 2085–2112.

Gencor (1995). Technical review of Ngamiland JV Botswana, Geological Memorandum No. 22, Vol. 1. *Tech. rep.*, Gencor Mineral Resources Target Generation Unit, Johannesburg, South Africa.

Geological Survey of India (1994). Detailed information on copper-lead-zinc ores in Rajasthan-Gujarat (India). *Geological Survey of India*, p. 168.

Geological Survey of Queensland (2020). URL `qdexdata.dnrme.qld.gov.au`.

Geological Survey of South Australia (2020). South Australian Resources Information Gateway Selected Publications. URL `sarigbasis.pir.sa.gov.au/WebtopEw/ws/samref/sarig1`.

Ghazban, F., R. H. McNutt, & H. P. Schwarcz (1994). Genesis of sediment-hosted Zn-Pb-Ba deposits in the Irankuh district, Esfahan area, west-central Iran. *Economic Geology*, 89 (6), 1262–1278.

Ghosh, A. K., R. I. Thorpe, & C. K. Chakrabarti (2005). Interpretation of Pb and S isotope data for the Ganesh Himal metamorphosed stratiform Zn-Pb deposit, central Nepal Himalaya. *Journal of the Geological Society of India*, 65, 725–737.

Gilg, H. A., M. Boni, G. Balassone, C. R. Allen, D. Banks, & F. Moore (2006). Marble-hosted sulfide ores in the Angouran Zn-(Pb-Ag) deposit, NW Iran: Interaction of sedimentary brines with a metamorphic core complex. *Mineralium Deposita*, 41 (1).

Glencore (2020). URL `www.glencore.com.au/en/who-we-are/metals-and-minerals/Pages/zinc.aspx`.

Goodfellow, W. D. (2007). Base metal metallogeny of the Selwyn Basin, Canada. *Geological Association of Canada, Mineral Deposits Division Special Publication*, 5, 553–579.

Gourlay, A. W. (2003). Independent technical review of the Coates Lake copper deposit, Nahanni mining district, western Northwest Territories. *Tech. rep.*, CRS Copper Resources Corp. and First Trimark Ventures Inc., Vancouver, Canada.

Groenewald, P. B., M. G. M. Painter, I. R. Roberts, M. McCabe, & A. Fox (2009). East Yilgarn geoscience database, 1:100,000 geology Menzies to Norseman — An explanatory note. *Tech. Rep. 78*, Geological Survey of Western Australia.

Grose, C. J. & J. C. Afonso (2013). Comprehensive plate models for the thermal evolution of oceanic lithosphere. *Geochemistry, Geophysics, Geosystems*, 14 (9).

Groves, I. M., D. I. Groves, F. Bierlein, J. Broome, & J. Penhall (2008). Recognition of the hydrothermal feeder to the structurally inverted, giant Broken Hill deposit, New South Wales, Australia. *Economic Geology*, 103, 1389–1394.

Gu, L., K. Zaw, W. Hu, K. Zhang, *et al.* (2007). Distinctive features of Late Palaeozoic massive sulphide deposits in South China. *Ore Geology Reviews*, 31 (1), 107–138.

Gunnesch, K. A., A. Baumann, & M. Gunnesch (1990). Lead isotope variations across the central Peruvian Andes. *Economic Geology*, 85 (7), 1384–1401.

Gwatkin, C. & P. Muccilli (2002). Pillara mine — December 2001 resources and reserves report. *Tech. rep.*, Western Metals Ltd.

Haines, W., S. Turner, J. D. Foden, & J. B. Jago (2009). Isotopic and geochemical characterisation of the Cambrian Kanmantoo Group, South Australia: Implications for stratigraphy and provenance. *Australian Journal of Earth Sciences*, 56, 1095–1110.

Hall, C., D. York, C. Aunders, & D. Strong (1989). Laser $^{40}Ar/^{39}Ar$ dating of Mississippi Valley-type mineralization from western Newfoundland. In: *International Geological Congress*, vol. 28, pp. 2.10–2.11.

Hall, W. E. (1985). Stratigraphy of and mineral deposits in Middle and Upper Paleozoic rocks of the black-shale mineral belt, central Idaho. *United States Geological Survey Bulletin*, 1658AS, 118–131.

Hancock, M. C. & A. H. Purvis (1990). Lady Loretta silver-lead-zinc deposit. *Australasian Institute of Mining and Metallurgy Monograph*, 14, 943–948.

Hannigan, P. (2007). Metallogeny of the Pine Point Mississippi Valley-type zinc-lead district, southern Northwest Territories. *Mineral Deposits of Canada, Geological Association of Canada, Mineral Deposits Division, Special Publication*, 5, 609–632.

Hanski, E., H. Huhma, V. F. Smolkin, & M. Vaasjoki (1990). The age of the ferropicritic volcanics and comagmatic Ni-bearing intrusions at Pechenga, Kola Peninsula, USSR. *Bulletin of the Geological Society of Finland*, 62 (2), 123–133.

Harper, D. D. & D. M. Borrok (2007). Dolomie fronts and associated zinc-lead mineralization, USA. *Economic Geology*, 102, 1345–1352.

Hayes, G. P., G. L. Moore, D. E. Portner, M. Hearne, H. Flamme, M. Furtney, & G. M. Smoczyk (2018). Slab2, a comprehensive subduction zone geometry model. *Science*, 362, 58–61.

Heinrich, C. A., J. H. C. Bain, T. P. Mernagh, L. A. I. Wyborn, A. S. Andrew, & C. L. Waring (1995). Fluid and mass transfer during metabasalt alteration and copper mineralization at Mount Isa, Australia. *Economic Geology*, 90 (4), 705–730.

Henry, B., H. Rouvier, M. le Goff, D. Leach, J.-C. Macquar, J. Thibieroz, & M. Lewchuk (2001). Paleomagnetic dating of widespread remagnetization on the southeastern border of the French Massif Central and implications for fluid-flow and Mississippi Valley-type mineralization. *Geophysical Journal International*, 145, 368–380.

Hewton, R. S. (1982). Gayna River: A Proterozoic Mississipppi Valley-type zinc-lead deposit, Precambrian sulphide. *Geological Association of Canada Special Paper*, 25, 668–700.

Hirschmann, M. M. (2000). Mantle solidus: Experimental constraints and the effects of peridotite composition. *Geochemistry Geophysics Geosystems*, 1 (10).

Hitzman, M. W., R. Kirkham, D. Broughton, J. Thorson, & D. Selley (2005). The sediment-hosted stratiform copper ore system. *Economic Geology 100th Anniversary Volume*.

Hitzman, M. W., C. H. Thorman, G. Romagna, T. F. Oliviera, M. A. Dardennes, & L. Drew (1995). The Morro Agudo Zn-Pb deposit, Minais Gerais, Brazil: A Proterozoic Irish-type carbonate-hosted Sedex-replacement (Irish-type) deposit. In: *Geological Society of America, Annual Meeting, New Orleans, Abstracts with Program, Vol. 27*, 6.

Hnatyshin, D., R. Morden, E. Turner, D. Kontak, & R. A. Creaser (2005). Re-Os and fluid inclusion constraints on the timing and nature of sulfide mineralization at Nanisivik and Hawker Creek, Baffin Island, Nunavut. *Geological Society of America, Abstracts with Programs*, 43, 633.

Hoatson, D. M., S. Jaireth, & A. L. Jaques (2006). Nickel sulfide deposits in Australia: Characteristics, resources, and potential. *Ore Geology Reviews*, 29, 177–241.

Hoatson, D. M. & S.-S. Sun (2002). Archean layered mafic-ultramafic intrusions in the West Pilbara Craton, Western Australia: A synthesis of some of the oldest orthomagmatic mineralizing systems in the world. *Economic Geology*, 97 (4), 847–872.

Hoffman, F., D. Hawkins, C. E. Isachsen, & S. A. Bowring (1996). Precise U-Pb zircon ages for early Damaran magmatism in the Summas and Welwitschia inlier, northern Damara Belt, Namibia. *Communications of the Geological Survey of Namibia*, 11, 47–52.

Hofmeister, A. M. (2005). Dependence of diffusive radiative transfer on grain-size, temperature, and Fe-content: Implications for mantle processes. *Journal of Geodynamics*, 40, 51–72.

Hofmeister, A. M. (2007). Pressure dependence of thermal transport properties. *Proceedings of the National Academy of Sciences of the United States of America*, 104 (22), 9192–9197.

Howe, S. S. & W. E. Hall (1985). Light stable isotope characteristics of ore systems in central Idaho. *United States Geological Survey Bulletin*, 1658AS, 183–192.

Höy, T. (1975). Big Ledge (82L/8E). *Geology in British Columbia*, pp. G12–G18.

Huizenga, J.-M., J. Gutzmer, D. Banks, & L. Greyling (2006). The Paleoproterozoic carbonate-hosted Pering Zn–Pb deposit, South Africa. II: Fluid inclusion, fluid chemistry and stable isotope constraints. *Mineralium Deposita*, 40 (686).

Hulbert, L. J. (1997). *Geology and metallogeny of the Kluane mafic-ultramafic belt, Yukon Territory, Canada: Eastern Wrangellia, a new Ni-Cu-PGE metallogenic terrane*, vol. 506. Geological Survey of Canada.

Hulbert, L. J., M. A. Hamilton, M. F. Horan, & R. F. J. Scoates (2005). U–Pb zircon and Re–Os isotope geochronology of mineralized ultramafic intrusions and associated nickel ores from the Thompson Nickel Belt, Manitoba, Canada. *Economic Geology*, 100 (1), 29–41.

Husain, V., H. Khan, K. Germann, & K. Zak (2002). Geological investigations of stratbound Ganga barite deposits of Khuzday (Balochistan), Pakistan. *Resource Geology*, 52, 49–58.

Huston, D. L., P. Morant, F. Pirajno, B. Cummins, D. Baker, & T. P. Mernagh (2007). Paleoarchean mineral deposits of the Pilbara Craton: Genesis, tectonic environment and comparisons with younger deposits. *Developments in Precambrian Geology*, 15, 411–450.

Huston, D. L., B. Stevens, N. Southgate, P. Muhling, & L. Wyborn (2006). Australian Zn-Pb-Ag ore-forming systems: A review and analysis. *Economic Geology*, 101, 1117–1158.

Ireland, T., R. R. Large, P. McGoldrick, & M. Blake (2004). Spatial distribution patterns of sulfur isotopes, nodular carbonate, and ore textures in the McArthur (HYC) Zn-Pb-Ag deposit, Northern Territory, Australia. *Economic Geology*, 99, 1687–1710.

Ironbark (2020). URL `www.ironbark.gl`.

Irwin, S. E. B. & M. J. Orchard (1989). Conodont biostratigrapahy and constraints on Upper Devonian mineral deposits in the Earn Group, northern British Columbia and Yukon, Canada. *Geological Survey of Canada Paper*, 89–1E, 13–20.

Jain, C., J. Korenaga, & S. I. Karato (2018). On the grain size sensitivity of olivine rheology. *Journal of Geophysical Research: Solid Earth*, 123, 674–688.

James, L. P. & E. W. Newman (1986). Subsurface character of mineralization at Silver Reef, Utah, and a possible model for ore genesis. *Utah Geological Association Publication*, 15, 149–158.

Jemmali, N., F. Souissi, E. J. M. Carranza, & T. W. Vennemann (2013). Sulfur and lead isotopes of Guern Halfaya and Bou Grine deposits (Domes zone, northern Tunisia): Implications for sources of metals and timing of mineralization. *Ore Geology Reviews*, 54, 17–28.

Jiang, S. Y., M. R. Palmer, Y. H. Li, & C. J. Xue (1995). Chemical compositions of tourmaline in the Yindongzi-Tongmugou Pb-Zn deposits, Qinling, China: Implications for hydrothermal ore-forming processes. *Mineralium Deposita*, 30, 225–234.

Johnson, C. A., K. D. Kelley, & D. L. Leach (2004). Sulfur and oxygen isotopes in barite deposits of the western Brooks Range, Alaska, and implications for the origin of the Red Dog massive sulfide deposits. *Economic Geology*, 99, 1435–1448.

Jones, D., S. Bull, & P. McGoldrick (1999). The Kamarga Deposit: A large, low grade, stratabound zinc resource in the Proterozoic 'Carpentaria Zinc Belt' of northern Australia. In: *Mineral deposits: Processes to processing* (edited by C. J. Stanley, A. H. Rankin, R. J. Bodnar, J. Naden, B. W. D. Yardley, A. J. Criddle, R. D. Hagni, A. P. Gize, J. Pasava, A. J. Fleet, R. Seltmann, C. Halls, M. Stemprok, B. Williamson, R. J. Herrington, R. E. T. Hill, H. M. Prichard, F. Wall, C. T. Williams, I. McDonald, J. J. Wilkinson, D. Cooke, N. J. Cook, B. J. Marshall, P. Spry, Z. Khin, L. Meinert, K. Sundblad, P. Scott, S. H. B. Clark, E. Valsami-Jones, N. J. Beukes, H. J. Stein, J. L. Hannah, F. Neubauer, D. J. Blundell, D. H. M. Alderton, M. P. Smith, S. Mulshaw, & R. A. Ixer), pp. 873–876. A.A. Balkema, Rotterdam.

Jones, H. D., S. E. Kesler, F. C. Furman, & J. R. Kyle (1996). Sulfur isotope geochemistry of southern Appalachian Mississippi Valley-type deposits. *Economic Geology*, 91 (2), 355–367.

Kagara Ltd. (2008). Drilling update — Victoria Project near Chillagoe. *Tech. rep.* URL `www.kagara.com.au`.

Kamo, S. L., G. K. Czamanske, Y. Amelin, V. A. Fedorenko, D. Davis, & V. Trofimov (2003). Rapid eruption of Siberian flood-volcanic rocks and evidence for coincidence with the Permian–Triassic boundary and mass extinction at 251 Ma. *Earth and Planetary Science Letters*, 214, 75–91.

Karpenko, S., M. H. Delevaux, & B. R. Doe (1981). Lead isotope analyses of galenas from selected ore deposits of the USSR. *Economic Geology*, 76, 716–742.

KBL Mining Ltd. (2017). URL `www.kblmining.com.au`.

Kelley, K. D., J. A. Dumoulin, & S. Jennings (2004a). The Anarraaq Zn-Pb-Ag and barite deposit, northern Alaska: Evidence for replacement of carbonate by barite and sulfides. *Economic Geology*, 99, 1577–1591.

Kelley, K. D., D. L. Leach, C. A. Johnson, J. L. Clark, *et al.* (2004b). Textural, compositional, and sulfur isotope variations of sulfide minerals in the Red Dog Zn-Pb-Ag deposits, Brooks Range, Alaska: Implications for ore formation. *Economic Geology*, 99, 1509–1532.

Kennett, B. L. N., A. Fichtner, S. Fishwick, & K. Yoshizawa (2013). Australian seismological reference model (AuSREM): Mantle component. *Geophysical Journal International*, 192, 871–887.

Kennett, B. L. N., M. Salmon, E. Saygin, & A. W. Group (2011). AusMoho: The variation of Moho depth in Australia. *Geophysical Journal International*, 187 (2), 946–958.

Kesler, S. E., M. S. Appold, G. L. Cumming, & D. Krstic (1994). Lead isotope geochemistry of Mississippi Valley-type mineralization in the central Appalachians. *Economic Geology*, 89 (7), 1492–1500.

Kesler, S. E. & M. H. Reich (2006). Precambrian Mississippi Valley-type deposits: Relation to changes in composition of the hydrosphere and atmosphere. In: *Evolution of Early Earth's Atmosphere, Hydrosphere, and Biosphere – Constraints from Ore Deposits* (edited by S. E. Kesler & H. Ohmoto), *Geological Society of America Memoirs*, vol. 198, pp. 185–204. Geological Society of America, Boulder, USA.

Khiltova, V. Y. & G. P. Pleskach (1997). Yenisei fold belt. In: *Precambrian ore deposits of the East European and Siberian Cratons* (edited by D. V. Rundkvist & C. Gillen), pp. 289–316. Elsevier, Amsterdam.

Kirkham, R. V., J. J. Carrière, R. M. Laramée, & D. F. Garson (1994). Global distribution of sediment-hosted stratiform copper deposits and occurrences. *Tech. Rep. Open File Report 2915b*, Geological Survey of Canada. URL `geoscan.nrcan.gc.ca/starweb/geoscan/servlet.starweb?path=geoscan/fulle.web\&search1=R=207806`.

Kobe, H. W. (1960). Cu-Ag deposits of the red-bed type at Negra Huanusha in central Peru. *Schweizerische Mineralogische und Petrogrographische Mitteilungen*, 40, 163–176.

Kontak, D. J. (1992). A preliminary report on geological, geochemical, fluid inclusion and isotopic studies of the Gays River Zn-Pb deposit, Nova Scotia. *Tech. rep.*, Nova Scotia Department of Natural Resources.

Kontak, D. J., E. Farrar, & S. L. McBride (1994). $^{40}Ar/^{39}Ar$ dating of fluid migration in a Mississippi Valley-type deposit: The Gays River Zn-Pb deposit, Nova Scotia, Canada. *Economic Geology*, 89, 1501–1517.

Koptagel, O., U. Ulusoy, & A. E. Fallick (2007). Sulfur and lead isotope investigations of the carbonate-hosted Pb-Zn deposits in the Yahyali region, Kayseri, southern Turkey. *Turkish Journal of Earth Sciences*, 16, 57–76.

Korenaga, T. & J. Korenaga (2016). Evolution of young oceanic lithosphere and the meaning of seafloor subsidence rate. *Journal of Geophysical Research: Solid Earth*, 121, 6315–6332.

Kositcin, N., S. J. Brown, M. E. Barley, B. Krapež,, K. F. Cassidy, & D. C. Champion (2008). SHRIMP U–Pb zircon age constraints on the Late Archaean tectonostratigraphic architecture of the Eastern Goldfields superterrane, Yilgarn craton, Western Australia. *Precambrian Research*, 161, 5–33.

Kositcin, N., D. C. Champion, & D. L. Huston (2009). Geodynamic synthesis of the north Queensland region and implications for metallogeny. *Geoscience Australia Record*, 2009/30, 196.

Kragh, K., S. M. Jensen, & H. Fougt (1997). Ore geological studies of the Citronen Fjord zinc deposit, North Greenland: Project 'Resources of the sedimentary basins of North and East Greenland'. *Geology of Greenland Survey Bulletin*, 176, 44–49.

Kruger, F. J., R. G. Cawthorn, P. S. Meyer, & K. L. Walsh (1986). Sr-isotopic, chemical and mineralogical variations across the pyroxenite marker and in the upper zone of the western Bushveld Complex. In: *Proceedings of Geo-Congress 1986, 21st Congress*, pp. 609–612.

Kuiper, Y. D., C. Shields, & M. N. Turbrett (2011). Detrital age constraints on the and of deposition and provenance of the metasedimentary cover sequence of the Thor-Odin Dome, British Columbia. *Geological Society of America Abstracts with Programs*, 43 (5), 101.

Large, D. & E. Walcher (1999). The Rammelsberg massive sulphide Cu-Zn-Pb-Ba-Deposit, Germany, an example of sediment-hosted, massive sulphide mineralisation. *Mineralium Deposita*, 34, 522–538.

Large, D. E. (1980). *On the geology, geochemistry and genesis of the Tom Pb-Zn-barite deposit, Yukon Territory, Canada*. Ph.D. thesis, Institute of Geology and Palaeontology, Braunschweig, West Germany.

Lau, H. C., J. X. Mitrovica, J. Austermann, O. Crawford, D. Al-Attar, & K. Latychev (2016). Inferences of mantle viscosity based on ice age data sets: Radial structure. *Journal of Geophysical Research: Solid Earth*, 121 (10), 6991–7012.

Lawrence, L. J. & T. A. Rafter (1962). Sulfur isotope distribution in sulfides and sulfates from Broken Hill South, New South Wales. *Economic Geology*, 57, 217–225.

Lea, E. R. & D. B. Dill Jr. (1968). Zinc deposits of the Balmat-Edwards district, New York. In: *Ore deposits of the United States, 1933–1967 (Graton-Sales Volume)* (edited by J. D. Ridge), vol. 1, pp. 20–48. American Institute of Mining, Metallurgical and Petroleum Engineers, New York.

Leach, D., J. Viets, A. Kozlowski, & S. Kibitlewski (1996). Geology, geochemistry, and genesis of the Silesia-Cracow zinc-lead district, Southern Poland. *Society of Economic Geologists Special Publication*, 4, 144–170.

Leach, D. L., D. Bradley, M. T. Lewchuk, D. T. Symons, G. de Marsily, & J. Brannon (2001a). Mississippi Valley-type leadzinc deposits through geological time: Implications from recent age-dating research. *Mineralium Deposita*, 36, 711–740.

Leach, D. L., J. C. Macquar, V. Lagneau, J. Leventhal, P. Emsbo, & W. Premo (2006). Precipitation of lead-zinc ores in the Mississippi Valley-type deposit at Trèves, Cévennes region of southern France. *Geofluids*, 6, 24–44.

Leach, D. L., W. Premo, M. Lewchuk, B. Henry, M. le Goff, H. Rouvier, J. C. Macquar, & J. Thibieroz (2001b). Evidence for Mississippi Valley-type lead-zinc mineralization in the Cévennes region, southern France, during Pyrenees orogeny. In: *Mineral Deposits at the Beginning of the 21st Century* (edited by A. Piestrzynski), pp. 157–160. Balkema, Rotterdam.

Lee, J. E. & D. A. Glenister (1976). Stratiform sulfide mineralization at Oamites copper mine, South West Africa. *Economic Geology*, 71 (1), 369–383.

Lees, T. & P. Buckle (2009). Base metal deposits in the Einasleigh area. *Australian Institute of Geoscientists Bulletin*, 49, 75–78.

Li, F. S., W. Wang, & J. M. Yang (2005). Geological and geochemical characteristics and genesis of the Wulagen lead and zinc deposit in Wuqia County, Xinjiang. *Mineral Resources and Geology*, 17, 10–16.

Li, H. M., Y. C. Chen, D. H. Wang, & H. Q. Li (2007a). Geochemistry and mineralisation age of the Mayuan zinc deposit, Nanzheng, southern Shanxi, China. *Bulletin of China*, 26, 546–552.

Li, J. & T. M. Kusky (2007). World's largest known Precambrian fossil black smoker chimneys and associated microbial vent communities, north China, implications for early life. *Gondwana Research*, 12, 84–100.

Li, W., Z. Huang, & M. Yin (2007b). Dating of the giant Huize ZnPb ore field of Yunnan Province, southwest China: Constraints from the SmNd system in hydrothermal calcite. *Resource Geology*, 57, 90–97.

Li, W., Z. Huang, & M. Yin (2007c). Isotope geochemistry of the Huize Zn-Pb ore field, Yunnan Province, Southwestern China: Implication for the sources of ore fluid and metals. *Geochemical Journal*, 47, 65–81.

Li, X., L. Su, B. Song, & D. Liu (2004). SHRIMP U–Pb zircon age of the Jinchuan ultramafic intrusion and its geological significance. *Chinese Science Bulletin*, 49 (4), 420–422.

Li, X. N. (2002). Deposit genesis and geological characteristics of Houjiangqiao Pb-Zn deposit in Hunan. *Contributions to Geology and Mineral Resources Research*, 17, 41–46.

Li, Z. D., C. J. Xue, X. F. Dong, Z. R. Liu, T. Z. Zhong, & S. J. Qi (2013). Ore geology, S- and Pb-isotopic compositions of the Wulagen Zn-Pb deposit, Wuqia county, Xinjiang. *Earch Science Frontiers*, 20, 40–54.

Liu, J. S., Z. Q. Gao, G. Q. Deng, M. Liu, & Q. D. Liu (2002). One potential super-large Pb-Zn ore occurrence with Himalayan thermal brine genesis, Wuqia region, Xinjiang, China. *Journal of Central South University of Technology*, 9, 41–46.

Logan, R. G., W. J. Murray, & N. Williams (1990). HYC silver-lead-zinc deposit, McArthur River. *Australasian Institute of Mining and Metallurgy Monograph*, 14, 907–911.

Long, K. R. (1992). Mines, prospects and mineral occurrences, Altiplano and Cordillera Occidental, Bolivia. *U.S. Geological Survey Bulletin*, 1975, 243–272.

Long, S., N. McQuarrie, T. Tobgay, C. Rose, G. Gehrels, & D. Grujic (2011). Tectonostratigraphy of the Lesser Himalaya of Bhutan: Implications for the along-strike stratigraphic continuity of the northern Indian margin. *Geological Society of America Bulletin*, 123, 1406–1426.

Lori, J. (2014). Trend mining and production. *Society of Economic Geologists Guidebook Series*, 45, 11–16.

Ltd., M. M. (2009). Quarterly report – 1 January to 31 March. *ASX Release*, p. 16. URL `www.asx.com.au/asxpdf/20090430/pdf/31hcg6505p5qcy.pdf`.

Lungu, C. V. (1998). Zambian mining in transition. *Mining Magazine*, September, 116–117.

Lydon, J. W. (2007). Geology and metallogeny of the Belt-Purcell Basin. *Geological Association of Canada Mineral Deposits Division Special Publication*, 5, 581–607.

Ma, G., G. Beaudoin, S. Qi, & Y. Li (2004). Geology and geochemistry of the Changba SEDEX Pb-Zn deposit, Qinling orogenic belt, China. *Mineralium Deposita*, 39, 380–395.

Ma, G., G. Beaudoin, S. Zhong, Y. Li, & Z. Zeng (2007). Geology and geochemistry of the Dengjiashan SEDEX Zn-Pb deposit, Qinling Belt, China. *Canadian Journal of Earth Sciences*, 44, 479–492.

Maiden, K. J., A. H. Innes, M. J. King, S. Master, & I. Pettitt (1984). Regional controls on the localisation of stratabound copper deposits: Proterozoic examples from southern Africa and South Australia. *Precambrian Research*, 25, 99–118.

Mather, K. A., D. G. Pearson, D. P. McKenzie, B. A. Kjarsgaard, & K. Priestley (2011). Constraints on the depth and thermal history of cratonic lithosphere from peridotite xenoliths, xenocrysts and seismology. *Lithos*, 125, 729–742.

Matthäi, S. K., C. A. Heinrich, & T. Driesner (2004). Is the Mount Isa copper deposit the product of forced brine convection in the footwall of a major reverse fault? *Geology*, 32 (4), 357–360.

McClung, C. R., J. Gutzmer, N. J. Beukes, K. Mezger, H. Strauss, & E. Gertloff (2007). Geochemistry of bedded barite of the Mesoproterozoic Aggeneys-Gamsberg Broken Hill-type district, South Africa. *Mineralium Deposita*, 42, 537–549.

McCracken, S. R., H. Etiman, A. G. Connor, & V. A. Williams (1996). Geology of the Admiral Bay carbonate-hosted zinc-lead deposit, Canning Basin, Western Australia. *Society of Economic Geologists Special Publication*, 4, 330–349.

McGregor, I. A. (1991). Assessment of mineral exploration opportunities in Zambia. *Tech. rep.*, Vans, Griffis and McOuat.

McKenzie, D. (2000). Constraints on melt generation and transport from U-series activity ratios. *Chemical Geology*, 162, 81–94.

McKenzie, D. P. (1978). Some remarks on the development of sedimentary basins. *Earth and Planetary Science Letters*, 40, 25–32.

MDIO (2020). URL `www.geologyontario.mndm.gov.on.ca/mndmfiles/mdi/data/records/MDI31F07NE00063.html`.

Meisel, T., J. Moser, & W. Wegscheider (2001). Recognizing heterogeneous distribution of platinum group elements (PGE) in geological materials by means of the Re-Os isotope system. *Fresenius' Journal of Analytical Chemistry*, 370, 566–572.

Middleton, T. (2004). The Dairi zinc-lead project, north Sumatra, Indonesia — Discovery to feasibility. URL `www.smedg.org.au/Tiger/DairiZinc.htm`.

Middleton, T. W. (2020). URL `smedg.org.au/Tiger/DairiZinc.htm`.

Minčeva-Stefanova, J. (1972). Mineral composition and origin of the stratiform polymetallic ore deposits in the Balkanides compared with the stratiform lead-zinc deposits of the Alps. In: *Proceedings of second internation symposium on the mineral deposits of the Alps*, pp. 301–313. Ljubljana, Slovenia.

Mining Journal of London (1989). Fleck agreement on Dunka. 312 (8006), 104.

Mining Magazine (1998a). May, RSA 5.

Mining Magazine (1998b). May, RSA 6.

Misi, A., S. S. Iyer, C. E. S. Coelho, C. C. Tassinari, *et al.* (2005). Sediment hosted leadzinc deposits of the Neoproterozoic Bambuí Group and correlative sequences, São Francisco Craton, Brazil: A review and a possible metallogenic evolution model. *Ore Geology Reviews*, 26 (3), 263–304.

Misi, A., S. S. Iyer, C. C. Tassinari, J. R. Kyle, *et al.* (1999). Geological and isotopic constraints on the metallogenic evolution of the Proterozoic sediment-hosted Pb-Zn (Ag) deposits of Brazil. *Gondwana Research*, 2, 47–65.

MMG (2020). URL `www.mmg.com/our-business/dugald-river`.

Morelli, R. M., R. A. Creaser, D. Selby, K. D. Kelley, D. L. Leach, & A. R. King (2004). Re–Os sulfide geochronology of the Red Dog sediment-hosted Zn-Pb-Ag deposit, Brooks Range, Alaska. *Economic Geology*, 99, 1569–1576.

Moroskat, M., S. A. Gleeson, R. J. Sharp, A. Simonetti, & C. J. Gallagher (2015). The geology of the carbonate-hosted Blende Ag–Pb–Zn deposit, Wernecke Mountains, Yukon, Canada. *Mineralium Deposita*, 50 (1), 83–104.

Mosier, D., V. Berger, & D. A. Singer (2009). Volcanogenic massive sulfide deposits of the world — Database and grade and tonnage models. *Tech. rep.*, US Geological Survey. URL `pubs.usgs.gov/of/2009/1034`.

Mueller, A. G. (2005). *The sedimentary-exhalative Meggen, Zn-Pb sulfide and barite deposit, Germany: Geology and plate-tectonic setting*. SGA Web mineral deposit archive. URL `e-sga.org/publications/mineral-deposit-archive/the-meggen-deposit`.

Mueller, A. G. (2008). *The Rammelsberg shale-hosted Cu-Zn-Pb sulfide and barite deposit, Germany: Linking SEDEX and Kuroko-type massive sulfides*. SGA Web mineral deposit archive. URL `e-sga.org/publications/mineral-deposit-archive/the-rammelsberg-deposit`.

Mukasa, S. B., A. H. Wilson, & R. W. Carlson (1998). A multi-element geochronologic study of the Great Dyke, Zimbabwe: Significance of the robust and reset ages. *Earth and Planetary Science Letters*, 164, 353–369.

Nakai, S. I., A. N. Halliday, S. E. Kesler, H. D. Jones, J. R. Kyle, & T. E. Lane (1993). Rb–Sr dating of sphalerites from Mississippi Valley-type (MVT) ore deposits. *Geochimica et Cosmochimica Acta*, 57, 417–427.

Naldrett, A. J. (1989). Magmatic sulfide deposits. *Oxford Monographs on Geology and Geophysics*, 14, 186.

Narkelyun, L. F., A. M. Filin, Y. P. Bezrodnykh, & A. I. Trubachev (1971). Cupriferous shales in Poland and their analogues in eastern parts of the USSR. *International Geology Review*, 13 (11), 1600–1610.

Nelson, D. R. (1997a). Evolution of the Archaean granite-greenstone terranes of the Eastern Goldfields, Western Australia: SHRIMP U–Pb constraints. *Precambrian Research*, 83, 57–81.

Nelson, D. R. (1997b). SHRIMP U–Pb zircon chronological constraints on the evolution of the Eastern Goldfields granite-greenstone terranes. *Australian Geological Survey Organisation Record*, 41, 11–14.

Nelson, J., S. Paradis, J. Christensen, & J. Gabites (2002). Canadian Cordilleran Mississippi Valley-type deposits: A case for Devonian-Mississippian back-arc hydrothermal origin. *Economic Geology*, 97, 1013–1036.

Neradovsky, Y. N., V. V. Borisova, & V. V. Sholokhnev (1997). The Monchegorsk layered complex and related mineralization. In: *Ore Deposits of the Kola Peninsula, Northwestern Russia* (edited by T.-F. I. M. Mitrofanov, F.), vol. 45, pp. 13–17.

Newham, W. D. N. (1986). The Lomagund and Sabi metallogenic provinces of Zimbabwe. In: *Mineral deposits of Southern Africa* (edited by C. R. Anhaeusser & S. Maske), vol. 1–2, pp. 1351–1393. Johannesburg, South Africa.

Newnham, L. (2003). Development of Avebury nickel sulphide deposit. In: *Australian Nickel Conference*, p. 6.

Nickel, K. G. & D. H. Green (1985). Empirical geothermobarometry for garnet peridotites and implications for the nature of the lithosphere, kimberlites and diamonds. *Earth and Planetary Science Letters*, 73, 158–170.

Nimis, P. & W. R. Taylor (2000). Single clinopyroxene thermobarometry for garnet peridotites. Part I. Calibration and testing of a Cr-in-Cpx barometer and an enstatite-in-Cpx thermometer. *Contributions to Mineralogy and Petrology*, 139, 541–554.

Nockleberg, W. J., T. K. Bundtzen, K. M. Dawson, R. A. Eremin, *et al.* (1997). Significant metalliferous and selected non-metalliferous lode deposits and placer districts for the Russian Far East, Alaska, and the Canadian Cordillera. *Tech. Rep. 96–513-B*, U.S. Geological Survey.

Nokleberg, W. J., T. V. Bounaeva, R. J. Miller, Z. V. Seminskiy, & M. F. Diggles (2003). Significant metalliferous and selected non-metalliferous lode deposits and selected placer districts for northeast Asia. *Tech. Rep. 03–220*, U.S. Geological Survey.

Nokleberg, W. J., T. K. Bundtzen, R. A. Eremin, V. V. Ratkin, *et al.* (2005). *Metallogenesis and tectonics of the Russian Far East Alaska, and the Canadian Cordillera*, vol. 1697. U.S. Geological Survey, Menlo Park, USA.

Northern Miner (1995). Neuquen project in Argentina: Yamana, MIM explore 'red bed deposits. *The Northern Miner*. URL `www.northernminer.com/news/neuquen-project-in-argentina-yamana-mim-explore-red-bed-deposits/1000094461`.

Northern Miner (1996a). Latin American special: Bolivias mineral wealth attracts companies. *The Northern Miner*. URL `www.northernminer.com/news/latin-american-special-bolivia-s-mineral-wealth-attracts-companies/1000096396`.

Northern Miner (1996b). Optimism inflates Western indices. *The Northern Miner*. URL `www.northernminer.com/news/optimism-inflates-western-indices/1000096924`.

Northern Miner (1996c). South Atlantic submits proposals for African copper-cobalt projects. *The Northern Miner*. URL www.northernminer.com/news/south-atlantic-submits-proposals-for-african-copper-cobalt-projects/1000142539.

Northern Miner (1996d). Summo hits copper at Champion. *The Northern Miner*. URL www.northernminer.com/news/summo-hits-copper-at-champion/1000160510.

Northern Miner (1997). Yuma completes feasibility study: Delays caused by efforts to gain approvals for process water. *The Northern Miner*. URL www.northernminer.com/news/literature-review-yuma-completes-feasibility-study-delays-caused-by-efforts-to-gain-approvals-for/1000183032.

Northern Miner (1998). Zambia nears end of ZCCM privatization: Kafue Consortium snaps up Nchanga-Nkana copper-cobalt complex. *The Northern Miner*. URL www.northernminer.com/news/africa-zambia-nears-end-of-zccm-privatization-kafue-consortium-snaps-up-nchanga-nkana-copper-cobal/1000148084.

Northern Miner (2000a). Crew builds new Zambian mine. *The Northern Miner*. URL www.northernminer.com/news/crew-builds-new-zambian-mine/1000104001.

Northern Miner (2000b). First Quantum, Glencore close ZCCM deal. *The Northern Miner*. URL www.northernminer.com/news/first-quantum-glencore-close-zccm-deal/1000164063.

Northern Miner (2000c). Glencore bankrolls Zambian copper deal. *The Northern Miner*. URL www.northernminer.com/news/glencore-bankrolls-zambian-copper-deal/1000103556.

Northern Miner (2002a). Anglo American bids farewell to Kolwezi. *The Northern Miner*. URL www.northernminer.com/news/anglo-american-bids-farewell-to-kolwezi/1000115613.

Northern Miner (2002b). Noranda nixes Montana silver project. *The Northern Miner*. URL www.northernminer.com/news/noranda-nixes-montana-silver-project/1000169505.

Northern Miner (2004a). Anvil expands Dikulushi copper-silver mine. *The Northern Miner*. URL www.northernminer.com/news/anvil-expands-dikulushi-copper-silver-mine/1000191429.

Northern Miner (2004b). Bwana Mkubwa copper output soars. *The Northern Miner*. URL www.northernminer.com/news/bwana-mkubwa-copper-output-soars/1000159472.

Northern Miner (2004c). First Quantum proves up resource at Lufua. *The Northern Miner*. URL www.northernminer.com/news/first-quantum-proves-up-resource-at-Lufua/1000156355.

Northern Miner (2004d). Rubicon gains stake in African company. *The Northern Miner*. URL www.northernminer.com/news/rubicon-gains-stake-in-african-company/1000158730.

Northern Miner (2004e). Southern Cross to explore Ethiudna. *The Northern Miner*. URL www.northernminer.com/news/southern-cross-to-explore-ethiudna/1000157572.

Olson, R. (1984). Genesis of paleokarst and strata-bound zinc-lead sulfide deposits in a Proterozoic dolostone, northern Baffin Island, Canada. *Economic Geology*, 79, 1056–1103.

Orgeval, J. J. (1995). Peridiapiric metal concentration at Bou Grine (Tunisian Atlas): Some geochemical characteristics. In: *Mineral deposits: From their origin to the environmental impacts* (edited by J. Pasava, B. Kribek, & K. Zak), pp. 299–302. Balkema, Rotterdam.

Oszczepalski, S. & A. Rydzewski (1997). *Metallogenic atlas of Zechstein copper-bearing series in Poland*. Wydawnictwo Kartograficzne Polskiej Agencji Ekologicznej.

Paces, J. B. & J. D. Miller Jr. (1993). Precise U–Pb ages of Duluth complex and related mafic intrusions, northeastern Minnesota: Geochronological insights to physical, petrogenetic, paleomagnetic, and tectonomagmatic processes associated with the 1.1 Ga midcontinent rift system. *Journal of Geophysical Research: Solid Earth*, 98 (B8), 13,997–14,013.

Page, R. W., C. H. H. Conor, B. P. J. Stevens, G. M. Gibson, W. V. Preiss, & P. N. Southgate (2005). Correlation of Olary and Broken Hill Domains, Curnamona Province: Possible relationship to Mount Isa and other north Australian Pb-Zn-Ag-bearing successions. *Economic Geology*, 100, 663–676.

Page, R. W. & D. M. Hoatson (2000). Geochronology of the mafic-ultramafic intrusions. In: *Geology and Economic Potential of the Palaeoproterozoic Layered Maficultramafic Intrusions in the East Kimberley, Western Australia* (edited by D. M. Hoatson & D. H. Blake), vol. 246, pp. 163–172. Australian Geological Survey Organisation Bulletin, Canberra, Australia.

Page, R. W., M. J. Jackson, & A. A. Krassay (2000). Constraining sequence stratigraphy in north Australiam basins: SHRIMP U–Pb zircon geochronology between Mt Isa and McArthur River. *Australian Journal of Earth Sciences*, 47, 431–460.

Painter, M. G. M., S. G. Golding, K. W. Hanan, & M. K. Neudert (1999). Sedimentologic, petrographic, and sulfur isotope constraints on fine-grained pyrite formation at Mount Isa mine and environments, northwest Queensland, Australia. *Economic Geology*, 94, 883–912.

Paktunc, A. D. (1987). Nickel, copper, platinum and palladium relations in Ni-Cu deposits of the St. Stephen intrusion, New Brunswick. *Geological Survey of Canada*, 87-1A, 543–553.

Pan, H. & D. T. A. Symons (1993). Paleomagnetism of the Mississippi Valley-type Newfoundland zinc deposit: Evidence for Devonian mineralization in the northern Appalachians. *Journal of Geophysical Research*, 98, 22,415–22,427.

Pan, H., D. T. A. Symons, & D. F. Sangster (1993). Paleomagnetism of the Gays River zinc-lead deposit, Nova Scotia: Pennsylvanian ore genesis. *Geophysical Research Letters*, 20, 1159–1162.

Papunen, H. & G. I. Gorbunov (1985). Nickel-copper deposits of the Baltic Shield and Scandinavian Caledonides. *Bulletin-Geological survey of Finland*, 333.

Paradis, S., P. Hannigan, & K. Dewing (2007). Mississippi Valley-type lead-zinc deposits. *Mineral deposits of Canada, Geological Association of Canada, Mineral Deposits Division, Special Publication*, 5, 185–203.

Paradis, S., J. L. Nelson, & S. E. Irwin (1998). Age constraints on the Devonian shale-hosted Zn-Pb-Ba deposits, Gataga District, northeastern British Columbia, Canada. *Economic Geology*, 93, 184–200.

Parr, J. (1994). The preservation of pre-metamorphic colloform banding in pyrite from the Broken Hill-type Pinnacles deposit, New South Wales, Australia. *Mineralogical Magazine*, 58, 461–472.

Parr, J. M., B. P. J. Stevens, G. R. Carr, & R. W. Page (2004). Subseafloor origin for Broken Hill Pb-Zn-Ag mineralization, New South Wales, Australia. *Geology*, 32, 589–592.

Parrish, R. R. (1989). U–Pb geochronology of the Cape Smith Belt and Sugluk block, northern Quebec. *Geoscience Canada*, 16, 126–130.

Pasyanos, M. E., T. G. Masters, G. Laske, & Z. Ma (2014). LITHO1.0: An updated crust and lithospheric model of the Earth. *Journal of Geophysical Research: Solid Earth*, 119, 2153–2173.

Pedersen, F. (1980). Remobilization of the massive sulfide ore of the Black Angel Mine, central West Greenland. *Economic Geology*, 75 (7), 1022–1041.

Pegmont (2020). URL `www.pegmont.com.au`.

Peng, R. M. & Y. S. Zhai (2004). The characteristics of hydrothermal exhalative mineralization of the Langshan-Zhaertai belt, Inner Mongolia, China. *Earth Science Frontiers*, 11, 257–268.

Perkins, W. (1984). Mount Isa silica dolomite and copper orebodies: The result of a syntectonic hydrothermal alteration system. *Economic Geology*, 79 (4), 601–637.

Pertermann, M. & A. M. Hofmeister (2006). Thermal diffusivity of olivine-group minerals at high temperature. *American Mineralogist*, 91, 1747–1760.

Piestrzyński, A. & A. Wodzicki (2000). Origin of the gold deposit in the Polkowice-West mine, Lubin-Sieroszowice mining district, Poland. *Mineralium Deposita*, 35 (1), 37–47.

Plimer, I. R. (1977). The origin of albite-rich rocks enclosing the cobaltian pyrite deposit at Thackaringa, N.S.W., Australia. *Mineralium Deposita*, 12, 175–187.

Plimer, I. R. (1986). Sediment-hosted exhalative Pb-Zn deposits — products of contrasting ensialic rifting. *Transactions of the Geological Society of South Africa*, 89, 57–73.

PorterGeo (2020a). URL `www.portergeo.com.au/database/mineinfo.asp?mineid=mn252`.

PorterGeo (2020b). URL `www.portergeo.com.au/database/mineinfo.asp?mineid=mn1464`.

PorterGeo (2020c). URL `www.portergeo.com.au/database/mineinfo.asp?mineid=mn260`.

PorterGeo (2020d). URL `www.portergeo.com.au/database/mineinfo.asp?mineid=mn1574`.

Pouit, G. & J. P. Bois (1986). Arrens Zn (Pb), Ba Devonian deposit, Pyrénées, France: An exhalative-sedimentary-type deposit similar to Meggen. *Mineralium Deposita*, 21, 181–189.

Prendergast, M. D. (2003). The nickeliferous Late Archean Reliance komatiitic event in the Zimbabwe Craton — Magmatic architecture, physical volcanology, and ore genesis. *Economic Geology*, 98 (5), 865–891.

Press, W. H., S. A. Teukolsky, W. T. Vetterling, & B. P. Flannery (1992). *Numerical recipes in Fortran*. Cambridge University Press, 2 edn.

Priestley, K., D. McKenzie, & T. Ho (2018). A lithosphere-asthenosphere boundary - A global model derived from multimode surface-wave tomography and petrology. In: *Geophysical Monograph 239, Lithospheric Discontinuities* (edited by H. Yuan & B. Romanowicz), chap. 6, pp. 111–123. John Wiley and Sons, Washington D.C.

Priestley, K. & D. P. McKenzie (2013). The relationship between shear wave velocity, temperature, attenuation and viscosity in the shallow part of the mantle. *Earth and Planetary Science Letters*, 381, 78–91.

Przeniosło, S. (2000). *Mineral resources of Poland*. Polish Geological Institute, Warsaw, Poland.

Raghu Nundan, K. R., B. K. Dhruva Rao, & M. L. Sinhal (1981). Exploration for copper, lead and zinc ores in India. *Bulletin of the Geological Survey of India, Series A — Economic Geology*, 47, 222.

Ramakrishnan, M. & R. Vaidyanathan (2008). Geology of India. *Geological Society of India*, 1, 556.

Randell, R. & G. Anderson (1996). Geology of the Polaris Zn-Pb deposit and surrounding area, Canadian Arctic Archipelago. *Society of Economic Geologists Special Publication*, 4, 307–319.

Redtail Metals (2020). URL `www.redtailmetals.com`.

Reichert, J. (2007). *A metallogenetic model for carbonate-hosted non-sulphide zinc deposits based on observations of Mehdi Abad and Irankuh, central and southwestern Iran*. Ph.D. thesis, Martin-Luther-Universitt Halle-Wittenberg.

Reid, D. L., H. J. Welke, C. B. Smith, & J. M. Moore (1997). Lead isotope patterns in Proterozoic stratiform mineralization in the Bushmanland Group, Namaqualand Province, South Africa. *Economic Geology*, 92, 248–258.

Ren, Z. (1994). Geology of Dongchuan copper mine, Yunnan, China. *Tech. rep.*, Southwest Geological Exploration Bureau of China National Nonferrous Metals Industry Corporation.

Reynolds, N. E. & P. M. Geerdts (2012). Structural controls and modification of the Sopokomil SHMS Zn-Pb deposits, Dairi, Sumatra. *AIG Bulletin*, 56, 149.

Rhodes, D., E. A. Lantos, J. A. Lantos, R. J. Webb, & D. C. Owens (1984). Pine Point orebodies and their relationship to the stratigraphy, structure, dolomitization, and karstification of the Middle Devonian barrier complex. *Economic Geology*, 79, 991–1055.

Richards, F. D., M. J. Hoggard, L. R. Cowton, & N. J. White (2018). Reassessing the thermal structure of oceanic lithosphere with revised global inventories of basement depths and heat flow measurements. *Journal of Geophysical Research: Solid Earth*, 123, 9136–9161.

Richards, F. D., M. J. Hoggard, N. J. White, & S. Ghelichkhan (2020). Quantifying the relationship between short-wavelength dynamic topography and thermomechanical structure of the upper mantle using calibrated parameterization of anelasticity. *Journal of Geophysical Research: Solid Earth*.

Ringrose, C. R. (1984). The geology and genesis of the Narlarla lead-zinc deposits, Napier Range, W. A. In: *The Canning Basin* (edited by P. G. Purcell), pp. 455–462. Geological Society of Australia, Perth.

Robinson, M. & C. I. Godwin (1995). Genesis of the Blende carbonate-hosted Zn-Pb-Ag deposit, north-central Yukon Territory: Geological, fluid inclusion and isotopic constraints. *Economic Geology*, 90, 369–384.

Rodriguez, S. E. (1990). Mineral deposits in the Venezuelan Andes. In: *Geology of the Andes and its relation to hydrocarbon and mineral resources* (edited by G. E. Ericksen, M. T. Pinochet, & J. A. Reinemund), pp. 237–244. Circum-Pacific Council for Energy and Mineral Resources, Houston, USA.

Rox Resources (2020). URL `roxresources.com.au/wp-content/uploads/2012/09/RRL1158D-IM.pdf`.

Roy, A. B., S. Kumar, L. Vivek, & N. K. Chauhan (2004). Tectonostratigraphy of the lead-zinc-bearing metasedimentary rocks of the Rampucha-Agucha Mine and its neighbourhood, district Bhilwara, Rajasthan: Implications on metallogeny. In: *Sediment-hosted lead-zinc sulphide deposits — Attributes and models of some major deposits in India, Australia and Canada* (edited by M. Deb & W. D. Goodfellow), pp. 273–289. Narosa Publishing House, New Delhi.

Rozendaal, A. (1986). The Gamsberg zinc deposit, Namaqualand district. In: *Mineral deposits of Southern Africa* (edited by C. Anhaeusser & S. Maske), pp. 1477–1488. Geological Society of South Africa, Johannesburg.

Ruelle, J. C. L. (1982). Depositional environments and genesis of stratiform copper deposits of the Redstone copper belt, Mackenzie Mountains, N.W.T. *Geological Association of Canada Special Paper*, 25, 701–738.

Rui, Z. Y., N. Li, & L. S. Wang (1991). The Guanmenshan lead-zinc deposit: Its basin brine. In: *Ore-forming Process and Lead Isotopic Targeting*, pp. 28–79. Geological Publishing House.

Ryan, P. J., A. L. Lawrence, R. D. Lipson, J. M. Moore, A. Paterson, D. P. Stedman, & D. Van Zyl (1986). The Aggeneys base metal sulphide deposits, Namaqualand, South Africa. In: *Mineral deposits of Southern Africa* (edited by C. Anhaeusser & S. Maske), pp. 1447–1474. Geological Society of South Africa, Johannesburg.

Rye, D. & N. Williams (1981). Studies of the base metal sulfide deposits at McArthur River, Northern Territory, Australia: III. The stable isotope geochemistry of the H.Y.C., Ridge and Cooley deposits. *Economic Geology*, 76, 826–842.

Rzhevskii, V. F., I. F. Gablina, L. V. Vasilovskaya, & A. M. Luré (1988). Genetic features of the Graviisk copper deposit. *Lithology and Mineral Resources*, 23 (2), 174–183.

Saha, A. B. (1985). On the nature of lead-zinc-magnetite ore bodies in Daling Group of rocks in Gorubathan area, Darjeeling district, West Bengal. *Indian Minerals*, 39 (4), 37–40.

Sainfeld, P. (1956). The lead-zinc-bearing deposits of Tunisia. *Economic Geology*, 51, 150–177.

Sarkar, S. C. & S. Banerjee (2004). Carbonate-hosted lead-zinc deposits of Zawar, Rajasthan, in the context of the world scenario. In: *Sediment-hosted lead-zinc sulphide deposits — Attributes and models of some major deposits in India, Australia and Canada* (edited by M. Deb & W. Goodfellow), pp. 328–349. Narosa Publishing House, New Delhi.

Sarkar, S. C., I. V. Chernyshev, & H. Banerjee (2000). Mid-Proterozoic Pb–Pb ages for some Himalayan base-metal deposits and comparison to deposits in Rajasthan, NW India. *Precambrian Research*, 99, 171–178.

Sasaki, A. & H. R. Krouse (1969). Sulfur isotopes and the Pine Point lead-zinc mineralization. *Economic Geology*, 64, 718–730.

Schaeffer, A. J. & S. Lebedev (2013). Global shear speed structure of the upper mantle and transition zone. *Geophysical Journal International*, 194, 417–449.

Schaeffer, A. J. & S. Lebedev (2014). Imaging the North American continent using waveform inversion of global and USArray data. *Earth and Planetary Science Letters*, 402, 26–41.

Schneider, W., A. Geng, F. Lapponi, & T. Bechstadt (2002). Carbonate-hosted zinc-lead deposits in the lower Cambrian of Huayuan, South China, a radiogenic (Pb, Sr) isotope study. *Economic Geology*, 97, 1815–1827.

Schroll, E., V. Koppel, & I. Cerny (2006). Pb and Sr isotope and geochemical data from the Pb-Zn deposit Bleiberg (Austria): Constraints on the age of mineralization. *Mineralogy and Petrology*, 86, 129–156.

Schroll, E. & G. Rantitsch (2005). Sulphur isotope patterns from the Bleiberg deposit (Eastern Alps) and their implications for genetically affiliated leadzinc deposits. *Mineralogy and Petrology*, 84, 1–18.

Schütfort, E. G. (2001). *The genesis of the San Vicente lead zinc rhythmite deposit, Peru: A petrologic, geochemical, and sulfur isotope study.* Ph.D. thesis, Oregon State University.

Schwartz, M. O., P. Akanyang, K. Trippler, & T. H. Ngwisanyi (1995). The sediment-hosted Ngwako Pan copper deposit, Botswana. *Economic Geology*, 90 (5), 1118–1147.

Scott, K. M. & G. F. Taylor (1977). Geochemistry of the Mammoth copper deposit, northwest Queensland, Australia. *Journal of Geochemical Exploration*, 8, 153–168.

Scott, K. M. & G. F. Taylor (1982). Eastern Creek Volcanics as the source of copper at the Mammoth Mine, northwest Queensland. *BMR Journal of Australian Geology & Geophysics*, 7 (2), 93–98.

Seasor, R. W. & A. C. Brown (1989). Syngenetic and diagenetic concepts at the White Pine copper deposit, Michigan. *Geological Association of Canada Special Paper*, 36, 257–267.

Seccombe, P. K., P. G. Spry, R. A. Both, M. T. Jones, & J. C. Schiller (1985). Base metal mineralization in the Kanmantoo Group, South Australia: A regional sulfur isotope study. *Economic Geology*, 80, 1824–1841.

Seltmann, R., S. Soloviev, V. Shatov, F. Pirajno, E. Naumov, & S. Cherasov (2010). Metallogeny of Siberia: Tectonic, geologic and metallogenic settings of selected significant deposits. *Australian Journal of Earth Sciences*, 57, 655–706.

Sexton, J. (2011). Australian mineral occurrences collection. *Geoscience Australia Dataset*, eCat Id 73. URL `ecat.ga.gov.au/geonetwork`.

Shah, N. (2004). Rampura-Agucha: A remobilised SEDEX deposit, southeastern Rajasthan, India. In: *Sediment-hosted lead-zinc sulphide deposits — Attributes and models of some major deposits in India, Australia and Canada* (edited by M. Deb & W. Goodfellow), pp. 290–303. Narosa Publishing House, New Delhi.

Sherlock, R., J. Lee, & B. Cousens (2004). Geological and geochronological constraints on the timing of mineralization at the Nanisivik zinc-lead Mississippi Valley-type deposit, northern Baffin Island, Nunavut, Canada. *Economic Geology*, 99, 279–293.

Shpikerman, V. I. (1990). Stratiform and stratabound ore mineralization of central parts of northeastern Russia. *Tech. rep.*

Sillitoe, R. H. (1980). Strata-bound ore deposits related to Infra-Cambrian rifting along northern Gondwanaland. In: *Proceedings of the 5^{th} Quadrennial IAGOD Symposium*, vol. 1, pp. 163–171. Snowbird, USA.

Sillitoe, R. H. (2010). Porphyry copper systems. *Economic Geology*, 105, 3–41.

Singer, D. A., V. I. Berger, & B. C. Moring (2009). Sediment-hosted zinc-lead deposits of the world — Database and grade and tonnage models. *Tech. rep.*, U.S. Geological Survey.

Skwarnecki, M. S. & R. W. Fitzpatrick (2003). Regional geochemical dispersion in acid sulfate soils in relation to base-metal mineralisation of the Kanmantoo Group, Mt Torrens-Strathalbyn region, eastern Mt Lofty Ranges, South Australia. *Tech. rep.*, CRC LEME.

Slack, J. F., K. D. Kelley, V. M. Anderson, J. L. Clark, & R. A. Ayuso (2004). Multistage hydrothermal silicification and Fe-Tl-As-Sb-Ge-REE enrichment in the Red Dog Zn-Pb-Ag district, northern Alaska: Geochemistry, origin, and exploration applications. *Economic Geology*, 99, 1481–1508.

Smethurst, M., D. Symons, D. Sangster, & M. Lewchuk (1999). Paleomagnetic age for Zn-Pb mineralization at Robb Lake, northeastern British Columbia. *Bulletin of Canadian Petroleum Geology*, 47, 548–555.

Smirnov, V. I. & D. I. Gorzhevsk (1977). Deposits of lead and zinc. In: *Ore Deposits of the U.S.S.R.* (edited by V. I. Smirnov), vol. 2, pp. 182–256. Pitman, London.

Smith, J. W., M. S. Burns, & N. J. W. Croxford (1978). Stable isotope studies of the origins of mineralization at Mount Isa. *Mineralium Deposita*, 13, 369–381.

Smith, J. W. & N. J. W. Croxford (1973). Sulfur isotope ratios in the McArthur zinc-lead-silver deposit. *Nature*, 245, 10–12.

St Marie, J. & S. E. Kesler (2000). Iron-rich and iron-poor Mississippi Valley-type mineralization, Metaline district, Washington. *Economic Geology*, 95 (5), 1091–1106.

Stalder, M. & A. Rozendaal (2005). Distribution and geochemical characteristics of barite and barium-rich rocks associated with the Broken Hill-type Gamsberg Zn-Pb deposit, Namaqua Province, South Africa. *South African Journal of Geology*, 108, 35–50.

Steers, J. E. (2003). Resource and reserve audit, Balmat no. 4 mine, Balmat-Edwards mining district, Balmat, N.Y., USA. URL `instruct.uwo.ca/earth-sci/fieldlog/Grenville/balmat.htm`.

Steinberger, B. & T. W. Becker (2018). A comparison of lithospheric thickness models. *Tectonophysics*, 746, 325–338.

Steven, N. & R. Armstrong (2003). A metamorphosed Proterozoic carbonaceous shale-hosted Co-Ni-Cu deposit at Kalumbila, Kabompo Dome: The Copperbelt ore shale in northwestern Zambia. *Economic Geology*, 98 (5), 893–909.

StratDB (2020). URL `thera2.usask.ca:8091/\$`.

Stribrny, B. (1985). The conglomerate-hosted Repparfjord copper ore deposit, Finnmark, Norway. *Monograph Series on Mineral Deposits*, 24, 1–75.

Summo Minerals Corp. (2001). Annual Report. *Tech. rep.*

Sureda, R. J. & J. L. Martin (1990). El Aguilar Mine: An Ordovician sediment-hosted stratiform lead-zinc deposit in the central Andes. In: *Stratabound Ore Deposits in the Andes* (edited by F. L., G. C. Amstutz, M. Cardozo, E. Cedillo, & J. Frutos), pp. 161–174. Springer-Verlag, Berlin.

Sverjensky, D. A. (1981). The origin of a Mississippi Valley-type deposit in the Viburnum Trend, southeast Missouri. *Economic Geology*, 76 (7), 1848–1872.

Symons, D., M. Lewchuk, & D. Sangster (1998a). Laramide orogenic fluid flow into the Western Canada Sedimentary Basin: Evidence from paleomagnetic dating of the Kicking Horse Mississippi Valley-type ore deposit. *Economic Geology*, 93, 68–83.

Symons, D., T. Symons, & D. Sangster (2000). Paleomagnetism of the Society Cliffs dolostone and the age of the Nanisivik zinc deposits, Baffin Island, Canada. *Mineralium Deposita*, 35, 672–682.

Symons, D. T., M. T. Lewchuk, K. Kawasaki, F. Velasco, & D. L. Leach (2009). The Reocín zinc-lead deposit, Spain: Paleomagnetic dating of a late Tertiary ore body. *Mineralium Deposita*, 44, 867–880.

Symons, D. T. A. (2007). Paleomagnetism of the HYC Zn-Pb SEDEX deposit, Australia: Evidence of an epigenetic origin. *Economic Geology*, 102, 1295–1310.

Symons, D. T. A. & D. C. Arne (2003). Paleomagnetic dating of mineralization in the Kapok MVT deposit, Lennard Shelf, Western Australia. *Journal of Geochemical Exploration*, 78, 267–272.

Symons, D. T. A. & D. C. Arne (2005). Paleomagnetic constraints on Zn-Pb ore genesis of the Pillara Mine, Lennard Shelf, Western Australia. *Mineralium Deposita*, 39, 944–959.

Symons, D. T. A., H. Pan, D. F. Sangster, & E. C. Jowett (1993). Paleomagnetism of the Pine Point Zn-Pb deposits. *Canadian Journal of Earth Sciences*, 30, 1028–1036.

Symons, D. T. A., D. Sangster, & D. Leach (1995). A Tertiary age from paleomagnetism for the Mississippi Valley-type zinc-lead mineralization in Upper Silesia. *Economic Geology*, 90, 782–794.

Symons, D. T. A., D. Sangster, & D. Leach (1998b). Age and duration of the Mississippi Valley-type mineralizing fluid flow event in the Viburnum Trend, southeast Missouri, USA, determined from palaeomagnetism. *Geological Society of London Special Publications*, 144, 27–39.

Symons, D. T. A. & D. F. Sangster (1992). Late Devonian paleomagnetic age for the Polaris Mississippi Valley-type Zn-Pb deposit, Canadian Arctic Archipelago. *Canadian Journal of Earth Sciences*, 29, 15–25.

Takei, Y. (2017). Effects of partial melting on seismic velocity and attenuation: A new insight from experiments. *Annual Review of Earth and Planetary Sciences*, 45, 447–470.

Tanaka, W. (2004). The Cashin Copper Deposit, Colorado, USA. *Tech. rep.*, Summo USA Corp., Lakewood, USA.

Taylor, R. D., D. L. Leach, D. C. Bradley, & S. A. Pisarevsky (2009). Compilation of mineral resource data for Mississippi Valley-type and clastic-dominated sediment-hosted lead-zinc deposits. *Tech. Rep. 1297*, U.S. Geological Survey.

Taylor, W. R. (1998). An experimental test of some geothermometer and geobarometer formulations for upper mantle peridotites with application to the thermobarometry of fertile lherzolite and garnet websterite. *Neues Jahrbuch für Mineralogie - Abhandlungen*, 172 (2-3), 381–408.

Teixeira, G. & M. Gonzalez (1988). Minas do Camaqua, Municipio de Cacapava do Sul, RS. In: *Principais Depósitos Minerais do Brasil - Metais Básicos Não Ferrosos, Ouro e Alumínio* (edited by C. Schobbenhaus & C. Coelho), vol. 3, pp. 71–80. DNPM and Companhia Vale do Rio Doce, Brasilia, Brazil.

Tenke Mining Corp. (2003). *Tech. rep.*, Vancouver, Canada.

Terramin Australia Ltd. (2018). ISR copper resource at Kapunda. *Tech. Rep. ASX Announcement*, Fullarton, South Australia. URL `www.envirocopper.com.au/sites/envirocopper/media/banners/terramintzn-resource-feb-2018.pdf`.

Thomassen, B. (2006). The Black Angel lead-zinc mine at Maarmorilik in West Greenland. *Geology and Ore*, 2 (2), 1–12.

Thorpe, R. I. (2008). Release of lead isotope data in 4 databases: Canadian, Western Superior, Foreign, and Whole rock and feldspar. *Geological Survey of Canada*, Open File 5664, 42.

Todorov, T. (1997). Geochemistry of gold in 'Venesta' sandstone-hosted stratiform copper deposit in Bulgaria. In: *Mineral deposits: Research and exploration — Where do they meet?* (edited by H. Papunen), Proceedings of the 4th Biennial SGA Meeting, pp. 327–334. A.A. Balkema, Rotterdam.

Tompkins, L. A., B. Eisenlohr, D. I. Groves, & M. Raetz (1997). Temporal changes in mineralization style at the Cadjebut Mississippi Valley-type deposit, Lennard Shelf, W.A. *Economic Geology*, 92, 843–862.

Tompkins, L. A., V. A. Pedone, M. T. Roche, & D. I. Groves (1994). The Cadjebut deposit as an example of Mississippi Valley-type mineralization on the Lennard Shelf, Western Australia – single episode or multiple events? *Economic Geology*, 89, 450–466.

Turner, R. J. W. & B. R. Otto (1995). Structural and stratigraphic setting of the Triumph stratiform zinc-lead-silver deposit, Devonian Milligen Formation, central Idaho. *United States Geological Survey Bulletin*, 2064E, 27.

U.S. Bureau of Mines (1974). The Mineral Industry of Zaire. *Tech. rep.*

U.S. Bureau of Mines (1980). The Mineral Industry of Zimbabwe (Southern Rhodesia). *Tech. rep.*

U.S. Bureau of Mines (1984). The Mineral Industry of Jordan. *Tech. rep.*, U.S. Bureau of Mines.

U.S. Bureau of Mines (1998). The Mineral Industry of New Mexico. *Tech. rep.*, U.S. Bureau of Mines.

USGS (2020a). URL `mrdata.usgs.gov/sedznpb/show-sedznpb.php?rec\%20id=189`.

USGS (2020b). URL `mrdata.usgs.gov`.

Valdés-Nodarse, E. L. (1998). Pb-Zn "SEDEX" deposits and their copper stockwork roots, western Cuba. *Mineralium Deposita*, 33, 560–567.

Valdés-Nodarse, E. L., A. Díaz-Carmona, J. F. Davies, R. E. Whitehead, & L. Fonseca (1993). Cogenetic SEDEX Zn-Pb and stockwork Cu ores, western Cuba. *Exploration and Mining Geology*, 2, 297–305.

Van Eden, J. G. (1978). Stratiform copper and zinc mineralization in the Cretaceous of Angola. *Economic Geology*, 73 (6), 1154–1161.

Vaughan, J. P. & R. L. Stanton (1986). Sedimentary and metamorphic factors in the development of the Pegmont stratiform Pb-Zn deposit, Queensland, Australia. *Institute of Mining and Metallurgy Transactions*, 95 (B), B94–B121.

Vearncombe, J. R., J. N. Christensen, S. L. Dorling, N. J. McNaughton, & A. R. Reed (1995a). The Blendevale orebody: Zinc-lead mineralization on the southeast Lennard Shelf, Canning Basin, Western Australia. *Society of Economic Geologists Guidebook Series*, 23, 103–135.

Vearncombe, J. R., S. L. Dorling, & M. J. Rayner (1995b). The Cadjebut orebody: Zinc-lead mineralization on the southeast Lennard Shelf, Canning Basin, Western Australia. *Society of Economic Geologists Guidebook Series*, 23, 81–102.

Velasco, F., J. M. Herrero, I. Yusta, J. A. Alonso, I. Seebold, & D. Leach (2003). Geology and geochemistry of the Reocín zinc-lead deposit, Basque-Cantabrian Basin, northern Spain. *Economic Geology*, 98, 1371–1396.

Velasco, F., A. Pesquera, & J. M. Herrero (1996). Lead isotope study of Zn-Pb ore deposits associated with the Basque-Cantabrian Basin and Paleozoic basement, northern Spain. *Mineralium Deposita*, 31, 84–92.

Vered-Weiss, J., E. A. Graber, & J. Good (1971). How Timna copper mines increased output and raised worker efficiency. *World Mining*, 24, 36–41.

Volodin, R. N., V. S. Chechetkin, Y. V. Bogdanov, L. F. Narkelyun, & A. I. Trubachev (1994). The Udokan cupriferous sandstone deposit (eastern Siberia). *Geology of Ore Deposits*, 36 (1), 1–25.

Walters, S. & A. Bailey (1998). Geology and mineralization of the Cannington Ag-Pb-Zn deposit: An example of Broken Hill-Type mineralization in the Eastern Succession, Mount Isa Inlier, Australia. *Economic Geology*, 93, 1307–1329.

Walther, H. W. (1986). Federal Republic of Germany. In: *Mineral Deposits of Europe* (edited by F. W. Dunning & A. M. Evans), pp. 175–301. Institution of Mining and Metallurgy and the Mineralogical Society, London.

Wang, C., J. Deng, E. J. M. Carranza, & X. Lai (2014). Nature, diversity and temporal-spatial distributions of sediment-hosted Pb-Zn deposits in China. *Ore Geology Reviews*, 56, 327–351.

Wang, M. L., W. X. Xu, H. Li, & S. L. Peng (2005). Isotope geochemical evidence of the Fankou lead and zinc deposit. *Acta Geologica Sinica*, 26, 164–167.

Wang, Q., L. Schiøtte, & I. H. Campbell (1996). Geochronological constraints on the age of komatiites and nickel mineralisation in the Lake Johnston greenstone belt, Yilgarn Craton, Western Australia. *Australian Journal of Earth Sciences*, 43 (4), 381–385.

Wang, X. C., Z. R. Zhang, M. H. Zheng, & X. H. Xu (2000). Metallogenic mechanism of the Tianbaoshan Pb-Zn deposit, Sichuan. *Chinese Journal of Geochemistry*, 19, 121–133.

Wang, X. H., C. J. Xue, Z. M. Li, Q. Li, & R. J. Yang (2008). Geological and geochemical characteristics of Mayuan Pb-Zn ore deposit on northern margin of Yangtze landmass. *Mineralium Deposita*, 27, 37–48.

Waring, C. L., C. A. Heinrich, & V. J. Wall (1998). Proterozoic metamorphic copper deposits. *AGSO Journal of Australian Geology & Geophysics*, 17 (4).

Whelan, J. F., R. O. Rye, & W. DeLorraine (1984). The Balmat-Edwards zinc-lead deposits — Synsedimentary ore from Mississippi Valley-type fluids. *Economic Geology*, 79, 239–265.

Whitehead, R. E., J. F. Davies, E. L. Valdés-Nodarse, & A. Díaz-Carmona (1996). Mineralogical and chemical variations, Castellanos shale-hosted Zn-Pb-Ba deposit, northwestern Cuba. *Economic Geology*, 91, 713–722.

Wilband, J. T. (1978). The copper resources of northern Michigan. *Tech. Rep. Contract No. J0366067*, U.S. Bureau of Mines.

Williams, N. (1978a). Studies of base metal sulfide deposits at McArthur River, Northern Territory, Australia: I. The Cooley and Ridge deposits. *Economic Geology*, 73, 1005–1035.

Williams, N. (1978b). Studies of base metal sulfide deposits at McArthur River, Northern Territory, Australia: II. The sulfide-S and organic-C relationships of the concordant deposits and their significance. *Economic Geology*, 73, 1036–1056.

Williams, P. J. & M. Heinemann (1993). Maramungee: A Proterozoic Zn skarn in the Cloncurry District, Mount Isa Inlier, Queensland, Australia. *Economic Geology*, 88, 1114–1134.

Williams, P. J., W. J. Pendergast, & G. Dong (1998). Late orogenic alteration in the wall rocks of the Pegmont Pb-Zn deposit, Cloncurry District, Queensland, Australia. *Economic Geology*, 93, 1180–1189.

Wodzicki, A. & A. Piestrzyński (1994). An ore genetic model for the LubinSieroszowice mining district, Poland. *Mineralium Deposita*, 29 (1), 30–43.

World Mineral Deposits (2020). URL `freegisdata.org/record/urn:uuid:ee97878f-cfce-40d0-bf80-781c3bbb15cd-GSC:WORLD\_SedexDeposits`.

Yamana Resources Inc. (1996). Annual Report. *Tech. rep.*, Toronto, Canada.

Yamauchi, H. & Y. Takei (2016). Polycrystal anelasticity at near-solidus temperatures. *Journal of Geophysical Research: Solid Earth*, 121 (11), 7790–7820.

Ye, L., N. J. Cook, T. Liu, C. L. Ciobanu, W. Gao, & Y. Yang (2012). The Niujiaotang Cd-rich zinc deposit, Duyun, Guizhou province, southwest China: Ore genesis and mechanisms of cadmium concentration. *Mineralium Deposita*, 47, 683–700.

Yin, M., W. Li, & X. Sun (2009). Rb–Sr isotopic dating of sphalerite from the giant Huize Zn-Pb ore field, Yunnan Province, Southwestern China. *Chinese Journal of Geochemistry*, 28, 70–75.

Yoshizawa, K. (2014). Radially anisotropic 3-D shear wave structure of the Australian lithosphere and asthenosphere from multi-mode surface waves. *Physics of the Earth and Planetary Interiors*, 235, 33–48.

Yoshizawa, K. & B. L. N. Kennett (2004). Multimode surface wave tomography for the Australian region using a three-stage approach incorporating finite frequency effects. *Journal of Geophysical Research: Solid Earth*, 109 (B2), 1–19.

Young, L. E. (2004). A geologic framework for mineralization in the western Brooks Range, Alaska. *Economic Geology*, 99, 1281–1306.

Yukon Geological Survey (2008). *Yukon mineral deposits summary,*. Yukon Geological Survey, Yukon, Canada.

Zappettini, E. O. (1999). Clasificación de depósitos minerales de Argentina. In: *Recursos Minerales de la República Argentina* (edited by E. O. Zappettini), vol. Anales 35, pp. 75–103. Instituto de Geología y Recursos Minerales, Servicio Geológico Minero Argentino, Subsecretaría de Minería de la Nación, Buenos Aires, Argentina.

Zeng, Y. & C. J. Li (2007). Discussion on the geological characteristics and sources of ore-forming materials of Dongjiahe Pb-Zn deposit in western Hunan Province. *Geology and Mineral Resources of South China*, 3, 24–30.

Zhang, F. (1991). Exhalites associated with Pb-Zn mineralization in Devonian system and their prospecting implications, Qinling, China. *Chinese Journal of Geochemistry*, 10, 348–356.

Zheng, M. H. & X. C. Wang (1991). Genesis of the Daliangzi Pb-Zn deposit in Sichuan, China. *Economic Geology*, 86, 831–846.

Zhou, J., Z. Huang, & Z. Yan (2013a). The origin of the Maozu carbonate-hosted Pb-Zn deposit, southwest China: Constrained by C-O-S-Pb isotopic compositions and Sm-Nd isotopic age. *Journal of Asian Earth Sciences*, 73, 39–47.

Zhou, J. X., J. G. Gao, D. Chen, & X. K. Liu (2013b). Ore genesis of the Tianbaoshan carbonate-hosted Pb-Zn deposit, Southwest China: Geologic and isotopic (C-H-O-S-Pb) evidence. *International Geology Review*, 55, 1300–1310.

Zhu, X., Q. Zhang, Y. He, & C. Zhu (2006). Lead isotopic composition and lead source of the Huogeqi Cu-Pb-Zn deposit, Inner Mongolia, China. *Acta Geologica Sinica (English Edition)*, 80, 528–539.